Investigations into sensing abilities of two-dimensional materials to assess quality of food products: A computational study

Madhumita Kundu

Roll No: 206121020

Under the supervision of

Prof. Subhradip Ghosh

Department of Physics
Indian Institute of Technology Guwahati
Guwahati-781039, Assam, India

Investigations into sensing abilities of two-dimensional materials to assess quality of food products: A computational study

A thesis submitted by

Madhumita Kundu

to

Department of Physics

Indian Institute of Technology Guwahati

in partial fulfillment of the requirements for the award of the degree of

Doctor of Philosophy in Physics

Department of Physics
Indian Institute of Technology Guwahati
Guwahati-781039, Assam, India

Statement

The research presented in this thesis, titled **Investigations into sensing abilities of two-dimensional materials to assess quality of food products: A computational study** was conducted by me at the Department of Physics, Indian Institute of Technology Guwahati, under the supervision of Prof. Subhradip Ghosh.

I hereby declare that the content of this thesis is the result of my original work and has not been submitted, either in part or in full, for the award of any other degree or diploma. All material that is not my own has been properly cited and acknowledged within the thesis.

Madhumita Kundu
Roll no: 206121020
Department of Physics
Indian Institute of Technology Guwahati
Guwahati - 781039, India

Friday 20th March, 2026

Disclaimer

The bibliography presented in this thesis is by no means exhaustive, but it includes the sources that were thoroughly consulted during the course of this work. I sincerely apologize for any unintentional omission of relevant research papers, review articles, or other scientific documents that deserve citation.
Some figures have been reproduced from external sources for illustrative purposes and are duly cited.

Certificate

It is certified that the work contained in the thesis entitled **Investigations into sensing abilities of two-dimensional materials to assess quality of food products: A computational study** by Madhumita Kundu, a Ph.D. student of the Department of Physics, Indian Institute of Technology Guwahati is carried out under my supervision and has not been submitted elsewhere for the award of any other degree.

(Prof. Subhradip Ghosh)
Department of Physics
Indian Institute of Technology Guwahati
Guwahati-781039, Assam, India

Friday 20th March, 2026

Dedicated to my parents

Acknowledgement

I thank my supervisor, Prof. Subhradip Ghosh, for his guidance during my Ph.D. tenure. His continuous support helped me keep my motivation during the tough times I have faced during my Ph.D. I particularly appreciate his support to explore ideas, make mistakes, and grow from those experiences.

I would also like to extend my heartfelt gratitude to my doctoral committee members, Dr. Uday Narayan Maiti, Prof. Padma Kumar Padmanabhan, and Prof. Ramagopal V.S. Uppaluri, for their various constructive insights during the annual progress seminars. I'm sincerely thankful to the Heads of the Departments for their various assistance during my Ph.D. journey(Prof. Subhradip Ghosh, Prof. Perumal Alagarsamy, and Prof. Basanta Ranjan Boruah). I acknowledge the technical and other office staff of the Department of Physics, IIT Guwahati, whose help made various aspects of my research more efficient and smooth. I would also like to express my gratitude to Param Ishan and Param Kamrupa, IIT Guwahati, for granting access to high-performance computing resources , which was essential for conducting the computational aspects of this research.

I would like to thank my past and present group members, Dr. Ashis Kundu, Dr. Sheuly Ghosh, Dr. Mandira Das, Dr. Himangshu Sekhar Sarmah, Dr. Himanshu Murari, Swati Shaw, Arvind Rajbhar,and Dr. Mayuri Bora, for research discussions.

I would also like to thank my friends in IIT Guwahati, Rohan, Aindrila, Madhurima, Utsab and Dr. Arghni Bhattacharya, whose friendliness and warmth made this place a true home away from home. I heartily thank, Dr. Ambaresh Sahoo, who always supports me in every difficult situation and his constant support during this journey. I would also like to thank all my labmates for creating a healthy learning environment in the labs. I want to thank Dhansiri hostel's library facility for providing a peaceful and positive environment. I'm also grateful to all my teachers, from school through university, whose inspiration and encouragement have shaped my academic journey and fueled my passion for research.

Lastly, and most importantly, I extend my deepest gratitude and respect to my parents and brother for their unwavering love, patience, and support. Their faith in me has been my greatest strength throughout this journey.

Abstract

Volatile organic compounds (VOCs) are a diverse array of organic chemicals associated with industrial processes, vehicle emissions, and biological activities. The detection and monitoring of their evolution are crucial for applications in environmental monitoring, industrial safety, and healthcare diagnostics. Their presence in food products determines the quality and freshness of food. Thus, the detection and separation of VOCs emitted by food are intricately related to the assessment of spoilage through continuous monitoring of their concentrations.

The unique electrical properties and atomically thin layers of two-dimensional (2D) materials make them outstanding candidates in this field. Because of their chemical diversity, structural adaptability, quantum confinement, high surface-to-volume ratios, and ease of surface modification, large-surface-area 2D materials have drawn significant attention.

This thesis investigates these possibilities by computing the sensing capabilities of diverse 2D materials using first-principles density functional theory (DFT) and non-equilibrium Green's function (NEGF) theory for standard food products. The goal is to classify these 2D materials into different sensing mechanisms, namely chemiresistive sensors, work-function-based sensors, and optical sensors.

We find that while pristine graphene performs poorly as both a chemiresistive and work-function-based sensor, r-GO in either mode is able to differentiate between four out of six VOCs. It turns out that GO, on the other hand, performs at par with r-GO as a work-function-based sensor but is not useful as a chemiresistive one. The analysis based on electronic structures, structural parameters, and adsorption characteristics traces such behavior back to the hybridization of molecular orbitals driven by the adsorption geometry.

Subsequently, the sensing and electronic properties of silicene and F-silicene are explored. This study reveals how functionalization drastically changes the electronic properties of the material, which impacts the charge transfer and transport properties. Next, we investigate the sensing properties of MXene and MXene/TMDC heterostructures. We show that sensitivity increases upon the formation of heterostructures. By forming heterostructures, a large charge transfer occurs across the interface compared to the case of bare MXene. This, coupled with significant changes in the work function, leads to much better sensitivities in heterostructure-based sensors.

Finally, we investigate the role of MXenes in sensing the food quality of papaya fruit. MXene, a new class of 2D material, has drawn considerable attention due to its unique structural properties. Different functional groups on the MXene surface behave differently in sensing food quality by altering the electronic and optical properties of the sensor.

In summary, this thesis expands our understanding of how 2D materials and their functionalization impact sensing properties toward volatile organic compounds emitted from standard food products through changes in electronic structure, charge transfer, and optical properties.

Contents

List of Figures

List of Tables

Chapter 1

Introduction

1.1 Food Quality, Safety, Wastage and the Need for Advanced Monitoring

In the modern era, the concept of food quality encompasses far more than flavour or appearance. It incorporates safety, freshness, nutritional integrity, and authenticity. Consumers expect that the food they buy not only tastes good but is also free of harmful contaminants (microbial, chemical, or physical), retains its intended nutrients, and has been produced, handled, and transported in a way that preserves quality and authenticity.

At the same time, producers, processors, distributors, and retailers operate in a world of ever-longer, more complex, and highly globalized supply chains. Food may travel from farm to processor, to transporter, to storage facility, to retailer, and finally to the consumer-often crossing continents, changing hands multiple times, and being stored under widely varying conditions of temperature, humidity, light, and handling. At each point in the chain, there exist possibilities of spoilage, contamination, nutrient degradation, or adulteration.

The World Health Organization (WHO) estimates that each year about 600 million people-nearly one in ten globally-fall ill after consuming contaminated food, and around 420,000 people die as a result. Children under five are disproportionately affected, with approximately 125,000 deaths annually in this age group from foodborne illnesses [1].

Beyond human health, the consequences of poor food quality and safety are also economic and societal. Unsafe food undermines consumer trust in brands and supply chains, triggers recalls and the destruction of product batches, imposes healthcare costs and productivity losses, and reduces the effective value of food production. For example, the World Health Organization (WHO) reports that unsafe food costs low and middle-income countries up to US 110 billion dollar per year in productivity losses and medical expenses. [2].

Parallel to these safety concerns is the challenge of food wastage (and loss) on a grand scale. According to the United Nations Environment Programme (UNEP) Food Waste Index Report, in 2022 the world wasted roughly 1.05 billion tonnes of food at retail and consumption levels alone-amounting to nearly 19% of all food available to consumers [3].In addition, about 13% of food is lost earlier in the supply chain (post-harvest, pre-retail)[4]. Breaking down the 1.05 billion tonnes figure, households generate approximately 60% of the waste ($\approx$ 631 million tonnes),food services about 28%($\approx$ 290 million tonnes) and retail about 12% ($\approx$ 131 million tonnes). On a per-person basis, the average household

wastes around 79 kg of food each year globally.

The environmental and resource-use implications of such wastage are profound. Food production is resource-intensive:land, water, energy, labour. When food is wasted, those inputs are effectively squandered. Food loss and waste also account for an estimated 8-10% of global greenhouse-gas emissions, contributing to climate change and ecosystem stress. Moreover, the data show that food waste is not exclusively a high-income country problem: the difference in per-capita household food waste between high-income, upper-middle-income, and lower-middle-income countries is only about 7 kg per year. These interlinked challenges-food safety risks, quality degradation, and large-scale food wastage-underscore a compelling need for more sophisticated and pervasive monitoring throughout the food supply chain.

Without such advanced monitoring capability, many quality failures will remain undetected until it is too late-resulting in spoilage, waste, recall, loss of nutritional value or health hazard. For instance, early detection of spoilage-related volatile organic compounds (VOCs), gases from microbial activity, contaminant ions or small-molecule markers could allow food producers or distributors to take corrective action (such as adjusting storage conditions, diverting product, increasing inspection) well before a full failure occurs.

1.2 Volitile Organic Compounds (VOCs) and their role in food quality and degradation

Volatile organic compounds (VOCs) are low-molecular weight chemicals (typically <300 Da) that readily evaporate at ambient conditions and diffuse through the headspace surrounding food. They include alcohols, aldehydes, ketones, esters, organic acids, sulfur compounds, terpenes, and hydrocarbons, each originating from specific biochemical processes within the food matrix. Because VOC profiles change systematically during ripening, fermentation, oxidation, and microbial spoilage, they serve as powerful chemical fingerprints of food quality and freshness.

1.2.1 Origin of VOCs in Food Products

VOCs arise from a variety of molecular pathways. In enzymatic reactions, enzymes such as lipoxygenase, alcohol dehydrogenase, and esterases break down lipids, carbohydrates, and amino acids, generating characteristic VOCs such as hexanal (from lipid oxidation) and esters (associated with fruit ripening). Ethanol and organic acids (produced by yeasts), amines (from protein decomposition), and sulfur-containing VOCs (associated with rotting meat and dairy products) are produced during bacterial and fungal growth in the food spoilage process [5, 6]. During cooking or processing, Maillard reactions and caramelization form hundreds of new VOCs.Volatile organic compounds serve as sensitive, reliable indicators of food quality and spoilage. Their origins-enzymatic activity, microbial metabolism, and chemical oxidation-produce unique chemical signatures that evolve as food progresses from freshness to degradation.

1.2.2 VOCs as Indicators of Food Quality

1.2.2.1 Freshness Indicators

VOCs play a vital role in defining aroma, flavor, and consumer acceptance. Specific compounds signify specific quality attributes. For example, Esters (e.g., ethyl acetate,methyl butanoate) in food mainly indicate freshness by pleasant fruity aroma, which describes the optimal ripeness of the food. Terpenes (limonene, 3-carene) provide the characteristic aromas of citrus and herbs and are markers of fresh produce. Aldehydes like trans-2-hexenal are associated with fresh-cut vegetables [7, 8].

1.2.2.2 Quality Attributes

VOCs also play a key role in quality control. In cheese, wine, coffee, spices, VOCs contribute to unique sensory profiles. VOC signatures distinguish species, cultivars, or processing methods. Deviations in VOC profiles reveal adulteration of oils, honey, or dairy products.

1.2.3 VOCs as Indicators of Food Degradation

As food degrades, its VOC emissions shift in predictable ways, making VOC monitoring a powerful freshness assessment tool. Lipid products such as hexanal(primary marker of rancidity), Heptanal, nonanal(secondary oxidation markers) and 2-butanone, 2-pentanone(advanced-rancidity indicators) are produced mainly in meats, fish, dairy, nuts, and oils [9, 10]. Microorganisms release distinct VOCs depending on species such as amines (putrescine, cadaverine)produces protein degradation in meat and fish. Sulfur VOCs (dimethyl sulfide, hydrogen sulfide) are strong markers of bacterial spoilage[11]. Short-chain organic acids (acetic, butyric acid) are responsible for sour odors from fermentation. Aldehydes and alcohols are produced due to yeast metabolism. Besides,fermentation produces ethanol, acetaldehyde in fruits during their over-ripening. Off-flavors from excessive lactic acid bacteria activity are seen in dairy products.

1.2.4 Reasons VOCs are Important for Food Monitoring

VOC detection allows sensing without cutting or chemically modifying the food. Continuous observation during storage, transport, and retail reduces the food waste. VOC changes occur before visual or textural changes, allowing early intervention. In quality control and safety assurance VOCs helps identifing the contamination, adulteration, improper storage conditions and temperature abuse. VOC-sensing indicators on packaging help consumers and distributors monitor freshness.

1.3 Techniques for VOC detection in food

In this section, we briefly discuss a conventional and an emerging advanced technique for detection of VOCs, profiling and monitoring of them.

1.3.1 Conventional Techniques for VOC Detection in Food: Gas Chromatography-Mass Spectrometry (GC-MS)

The detection and quantification of volatile organic compounds (VOCs) in food have long relied on a set of well-established, conventional analytical techniques. These methods remain the "gold standard" for comprehensive aroma profiling, freshness evaluation, spoilage assessment, and food authentication. The standard workflow typically involves: (i) sample preparation / VOC extraction, (ii) separation of components, (iii) identification and/or quantification, and (iv) sensory or odor-impact analysis [12]. Among all analytical methods, gas chromatography coupled with mass spectrometry (GC-MS) remains the most widely used and accepted technique for VOC analysis in foods, beverages, meats, fruits, etc [13, 14]. GC-MS combines the separation power of gas chromatography (GC)-which resolves complex mixtures into individual constituents - with the identification and structural elucidation capability of mass spectrometry (MS), thereby allowing both qualitative and quantitative analyses of VOCs [15]. It has high specificity and selectivity which can identify and quantify individual VOCs even in complex mixtures. It can detect a wide range of chemical classes (aldehydes, ketones, esters, alcohols, sulfur compounds, terpenes, etc.). Detection limits in low ppb to ppt range are achievable in this technique. However, the processes are time consuming; sample preparation along with chromatographic run times make analysis slow,not suitable for real-time monitoring.Secondly, it requires trained personnel, costly instrumentation and maintenance.Thus, it is not practical for in-field or on-packaging freshness monitoring.It only provides a “one-time” VOC profile and does not allow continuous monitoring during storage or transport. As a result, while GC-MS and its variants remain indispensable for detailed food VOC analysis, they are not ideally suited for rapid, in-line, or consumer-level freshness monitoring.

1.3.2 Emerging technique: Sensors

Sensor-based techniques are highly advantageous over conventional techniques for food sensing because they provide faster, more accurate, and non-destructive detection of food quality and safety. Sensors can continuously monitor parameters such as freshness, spoilage, contamination, moisture, temperature, and chemical composition in real time, unlike traditional methods that often require laboratory analysis, long processing times, or destructive sampling. They minimize human error, reduce the need for chemical reagents, and allow on-site or in-line monitoring during food processing and storage. Sensors play a crucial role in modern food quality monitoring due to their ability to rapidly detect volatile organic compounds (VOCs) associated with freshness, ripeness, spoilage, and adulteration. Gas-sensing technologies-including metal-oxide semiconductor (MOS) sensors, conducting polymer sensors, electrochemical sensors, quartz crystal microbalance (QCM) sensors, and integrated electronic nose (e-nose) systems-are increasingly being adopted as fast, non-destructive, and cost-effective alternatives to traditional laboratory-based analytical techniques [16, 17]. Additionally, sensor technologies integrate easily with smart packaging and IoT-based food monitoring systems, enabling better traceability and control throughout the supply chain. VOC (volatile organic compound) detection is performed using several different sensor technologies, each based on a distinct physical or chemical principle. Below is a complete, organized list of all major VOC sensor types, from the most common commercial sensors to advanced research technologies.

- Chemiresistive Sensors: These detect VOCs by measuring changes in electrical resistance when molecules are adsorbed on the sensing layer. The materials used generally are metal oxides (SnO_2, ZnO, WO_3, TiO_2), 2D materials (graphene, MoS_2, h-BN, MXenes), conductive polymers (PANI, PEDOT:PSS, PPy), carbon nanotubes[18, 19]. The advantages of this class of sensors is their high sensitivity, simple, low cost and fast response time. However, they have limited selectivity and often need high operating temperature[20, 21].

- Electrochemical Sensors: They mainly detect VOCs through redox reactions at electrodes, measuring current or potential. The main advantages of electrochemical sensor are that they can be operated in low power at room temperature and they are highly selective for specific gases[22, 23]. But they are not ideal for complex VOC mixtures. The degradation of electrolyte over time also poses problem.

- Optical Sensors: They detect VOCs via changes in light absorption, emission, scattering, or refractive index. There are different types of optical sensors: Colorimetric, Fluorescence-based sensors, Infrared absorption (NDIR), Surface plasmon resonance (SPR), Fiber-optic sensors, Photonic crystal and interference devices[24, 25, 26]. The main advantages are that they are higly selective, and real-time food freshness monitoring can be achieved at room temperature with them. The drawbacks are high cost and requirement of light sources or detectors.

- Calorimetric (Catalytic Heat) Sensors: This sensors detect VOCs by measuring the heat released when VOCs oxidize on a catalytic surface. The main advantanges of these sensor are their fast response and ability to detect VOCs at low ppb[27, 28]. But they need a microheater and are less selective unless catalyst is tailored.

- Acoustic / Piezoelectric Sensors: VOC adsorption changes mass or elastic properties in this case which shifts the resonant frequency of the material, thus detect VOCs.The main advantages of them are their nanogram-level sensitivity and good selectivity upon using polymer coatings. However, they are sensitive to humidity which can hamper the VOC detection[29, 30].

- Photoionization Detectors (PID): This kind of sensor is operated by using ultraviolate(UV) lamps to ionize VOCs; ion current is then measured. They are very sensitive and can detect VOC over a wide- spectrum[31, 32].

- Field-Effect Transistor (FET) Sensors: Here the VOC adsorption modulates the channel current of a semiconductor [33, 34]. This kind of sensor can operate at room-temperature with high sensitivity. But they have fabrication complexities and drift issues.

- Metal-Organic Framework (MOF) Sensors: MOFs selectively adsorb specific VOCs and produce signals via resistance change, mass change, fluorescence quenching and optical interference. The main advantages are high selectivity and tunable chemical affinity. But they often need hybridization with transducers[35, 36].

- Biosensors: They use enzymes or biological molecules to detect specific VOCs. An example is the enzyme-based ethanol sensors. But they have stability issue at high temperature or in long-term[37].

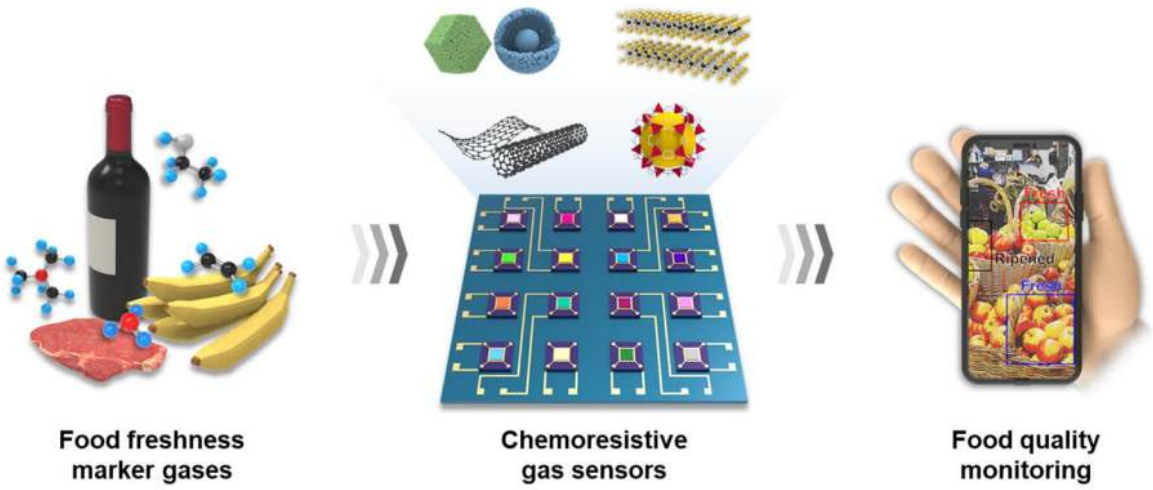

Figure 1.1: Schematic diagram of gas sensors for food quality monitoring.(Used with permission from [17])

One of the most significant applications of gas sensors is in the monitoring of meat and fish freshness[38]. During spoilage, proteins degrade and produce VOCs such as ammonia, trimethylamine, hydrogen sulfide, and various short-chain amines. These compounds are strong indicators of microbial activity. Gas sensors, especially Metal Oxide Semiconductor(MOS) sensor arrays used in e-nose systems, can detect these spoilage gases at very low concentrations. Studies have shown that e-noses, an array of sensors making up an electronic machine consisting of a signal pre-processing module and a pattern recognition engine[39], can distinguish between fresh, semi-spoiled, and spoiled meat with high accuracy by analyzing VOC patterns rather than single compounds[40]. For fish, the rapid detection of trimethylamine is particularly important, as it is a hallmark of marine fish spoilage. Gas sensors have thus enabled real-time assessment during processing, transport, and storage, helping reduce waste and ensure food safety. Gas sensors are also widely applied in the assessment of fruit ripeness and post-harvest quality. Fruits emit a range of volatiles including ethanol, ethylene, acetaldehyde, and esters as they ripen or deteriorate. Ethylene in particular is a critical hormone that regulates ripening processes in climacteric fruits such as bananas, apples, and tomatoes. Sensors like chemiresistive and piezoelectric sensors can detect ethylene and other VOCs at trace levels, enabling accurate prediction of ripening stages . This is especially valuable in supply chains where proper timing of distribution is essential to minimize losses. Additionally, e-noses have shown strong abilities to classify different stages of fruit ripeness based on complex aroma profiles, providing an advantage over chemical tests that focus on single indicators.

Another important area of application is the monitoring of dairy product quality. Dairy products such as milk, cheese, and yoghurt are highly susceptible to chemical oxidation and microbial spoilage, resulting in the release of aldehydes, ketones, alcohols, and sulfur-based compounds. Gas sensors can detect these changes early, providing rapid indicators of spoilage or contamination. Electronic nose systems have been successfully used to differentiate between fresh and spoiled milk, evaluate fermentation levels in yoghurt, and classify cheese varieties based on VOC emission patterns [41]. This capability is valuable not only for ensuring safety but also for supporting quality control during production.Gas sensors also play a significant role in detecting food adulteration, a widespread issue that affects consumer safety and market integrity. Many adulterated foods-such as

diluted milk, impure honey, blended olive oils, or counterfeit spices-exhibit different VOC profiles from authentic products. Sensor arrays can capture these subtle differences and identify adulteration quickly. For instance, e-nose systems have demonstrated the ability to distinguish pure olive oil from samples adulterated with cheaper oils, and to detect fraudulent additives in honey or wine[42]. This enables fast screening, reducing reliance on expensive chromatographic methods. In addition to product-level monitoring, gas sensors are increasingly integrated into smart packaging systems. Modified atmosphere packaging (MAP) and active packaging technologies aim to extend shelf life by controlling oxygen, carbon dioxide, humidity, and other environmental conditions. Embedded gas sensors can monitor changes in these atmospheric gases or detect VOCs produced during spoilage, offering real-time data to manufacturers and consumers[43]. For example, an oxygen sensor can detect seal failures, while VOC sensors warn of early spoilage. When paired with wireless communication modules, such smart packaging solutions contribute to Internet of Things (IoT)-based food monitoring, supporting traceability and real-time supply chain management.The use of gas sensors in food quality monitoring offers several advantages, including rapid results, portability, low cost, and the ability to perform non-destructive testing. Their sensitivity to low concentrations of VOCs makes them ideal for early detection of spoilage before it becomes visible or detectable through smell. However, challenges remain. Sensor drift, cross-sensitivity to multiple gases, and environmental influences such as humidity and temperature can reduce accuracy. These limitations are being addressed through improved sensor materials, advanced calibration methods, and the integration of artificial intelligence to enhance pattern recognition and compensate for sensor variability[44].

Overall, gas sensors have become indispensable tools in modern food safety and quality assurance. Sensors capable of detecting small changes in the food environment (volatile organic compounds (VOCs) released during spoilage or ripening, gases emitted by microbial activity, small molecules or ions signalling contamination or degradation) are emerging as key enablers for smarter food-quality systems. In particular, materials that form the active sensing layer must meet demanding criteria: large accessible surface for adsorption, strong interaction with target analytes, fast and measurable transduction of that interaction (e.g., shift in electrical conductivity, optical signal, electrochemical response), and stable operation in potentially harsh environments (moisture, humidity, complex food matrices).

1.4 Three dominant approaches for VOC profiling and monitoring: Chemiresistive, Work-function and Optical Sensing

The development of gas sensing technologies has significantly advanced in recent years, with each technology offering distinct advantages and challenges. The choice of sensing technology depends on the specific application requirements, including sensitivity, selectivity, cost, and environmental conditions.Volatile organic compound (VOC) sensing technologies have evolved significantly to support real-time, non-destructive food quality monitoring. Among these technologies, work-function (WF) sensors[45], chemiresistive sensors[46], and optical sensors[47] represent the three dominant approaches, each offering distinct advantages and limitations in terms of sensitivity, selectivity, stability, and

integration potential. Chemiresistive sensors provide a cost-effective and simple solution for gas detection but suffer from cross-sensitivity and require high operating temperatures. Work function-based sensors offer high selectivity and sensitivity, particularly for specific gases, but are often more complex and expensive. Optical sensors, especially NDIR sensors, provide excellent sensitivity and long-term stability, though they require more sophisticated equipment and are typically costlier.In this thesis, we have explored materials that can be utilized as one of these three sensors.

1.4.1 Chemiresistive VOC Sensors

Chemiresistive VOC sensors measure changes in electrical resistance of a semiconducting layer (metal oxides, graphene, CNTs, polymers) upon VOC adsorption. Chemiresistive sensors detect gas concentrations by measuring changes in the electrical resistance of a sensing material upon exposure to the gas. The most widely used materials for these sensors are semiconducting oxides, conductive polymers, and carbon-based nanomaterial. The fundamental principle behind chemoresistive sensors is the alteration in the material's electrical resistance due to the adsorption of gas molecules onto the sensor surface. When a gas interacts with the sensor material, it either donates or accepts electrons, which modulates the charge carrier concentration in the material. This change in carrier concentration leads to a measurable change in the electrical resistance of the material. The resistance change (ΔR) can be described as: $\Delta R = R_{\text{gas}} - R_{\text{air}}$ where,R_{gas} is the resistance in the presence of the gas and R_{air} is the resistance in ambient air. In many cases, the change in resistance is exponential and can be modeled by an Arrhenius-type equation, indicating that the temperature and energy required for gas adsorption play a key role in the sensor's sensitivity [48]. Chemoresistive sensors are widely used for air quality monitoring, industrial gas detection, and wearable health monitors. Despite their advantages, they suffer from cross-sensitivity to multiple gases and often require high operating temperatures. Moreover, the sensors' performance can degrade over time due to material fatigue and poisoning. In the area of food technology, chemiresistive sensors are widely used to detect hexanal, a primary marker of rancidity in meat, nuts, and oils; Ethanol, acetaldehyde during fruit over-ripening; Ammonia and amines in fish spoilage.

1.4.2 Work-Function-Based VOC Sensors

Work-function VOC sensors operate by detecting changes in the work function ($\Delta\phi$) of a material when VOC molecules are adsorbed onto it. VOC adsorption modifies dipole orientation, charge transfer, or surface states, leading to measurable changes in work function [49]. The work function is the minimum energy required to remove an electron from the surface of a material into the vacuum. The interaction of gas molecules with the sensor surface causes either the donation or acceptance of electrons, leading to a shift in the material's work function. This shift is indicative of the gas concentration and can be measured using techniques such as Kelvin Probe Force Microscopy (KPFM) or Surface Potential Measurements (SPM)[50]. The relationship between work function change ($\Delta\phi$) and gas concentration can be described by the equation: $\Delta\phi = \phi_{\text{gas}} - \phi_{\text{vacuum}}$; $|\phi_{\text{gas}}|$ is the work function in the presence of the gas and $|\phi_{\text{vacuum}}|$ is the work function in the absence of it . Work function-based sensors are ideal for high-selectivity applications where precise detection of specific gases is needed. Capable of detecting even weakly interacting VOCs (physisorption-dominated) and provide direct insight into sur-

face electronic interactions with analytes.However, they are often more complex, requires stable reference electrode or probe and costly compared to chemiresistive sensors. Work function sensors are particularly effective in detecting aldehydes (hexanal, nonanal) and esters that appear during lipid oxidation and fruit ripening, as these molecules strongly perturb surface dipoles even at low concentrations.

1.4.3 Optical VOC Sensors

Optical sensors detect VOCs by measuring changes in light absorption, photoluminescence, colorimetry, surface plasmon resonance (SPR), or Raman scattering. Optical gas sensors detect gases by measuring changes in the optical properties of a medium caused by the interaction between gas molecules and light. These sensors typically use infrared (IR) absorption or scattering to quantify gas concentrations. In optical gas sensors, gases absorb light at specific wavelengths, particularly in the infrared (IR) region. This absorption is proportional to the gas concentration and can be quantified using techniques such as Non-Dispersive Infrared (NDIR) spectroscopy. Optical sensors are particularly useful in applications requiring high sensitivity and selectivity, such as environmental monitoring of greenhouse gases and industrial emission monitoring. The strength of optical sensors lie in their extremely high selectivity due to specific spectral signatures, non-destructive nature (ideal for remote or inline sensing), high chemical stability and suitability for integration with smart packaging (colorimetric indicators)[51, 52]. However, they tend to be more expensive and require more complex instrumentation compared to chemiresistive sensors. Furthermore, optical sensors may be affected by environmental factors such as humidity and dust. In the area of food technology, optical methods excel in detecting carbonyl VOCs via colorimetric Schiff-base reactions, fruit ester VOCs via fluorescence quenching, spoilage amines through pH-sensitive dyes or plasmonic shifts. Optical sensors are widely used in intelligent packaging and real-time freshness labels.

1.5 Nanosensors for food detection

Nanomaterials are preferred for VOC detection because they provide more adsorption sites due to high surface area, large electronic response to molecular adsorption, faster reaction and diffusion kinetics, tunable chemical affinity for different VOCs, improved selectivity through functionalization, lower operating temperature, higher sensitivity and lower detection limits and compatibility with miniaturized, low-power devices. Together, these advantages make nanomaterials the dominant choice for modern VOC sensors used in food quality assessment[53]. Because of these advantages, nanosensors are particularly well-suited to meet the stringent requirements of food VOC sensing: high sensitivity to trace VOCs, selectivity amid complex mixtures, rapid response, stable operation in humid/variable environments, and low-cost scalability. The evolution of nanosensors for VOC detection in food can be traced through several “generations” of technological development[54, 55]. Early gas sensors for food used metal-oxide semiconductors (MOS), electrochemical cells, or colorimetric dyes. While useful, they suffered from relatively poor sensitivity to low VOC concentrations typical of early-stage spoilage, limited selectivity in complex food headspace, and requirement of high operating temperatures or significant preprocessing steps. With advances in nanotechnology, researchers began integrating nanomaterials - such as carbon nanotubes (CNTs), graphene, metal nanoparticles, and nanowires - into sensor platforms. The high surface area and tunable surface

chemistry permitted lower detection limits, faster response times, and somewhat improved discrimination. Combining different nanomaterials (e.g., metal-oxide nanostructures with carbon nanomaterials, polymers, or MOFs) improves sensitivity and selectivity. For example, sensors based on $ZnFe_2O_4$ spinel nanoparticles have shown promise for VOC detection relevant to food spoilage. A 2023 review summarizes the performance of spinel-ferrite nanosensors for VOC detection, emphasizing their sensitivity, applicability to food industry VOCs (e.g., ethanol, acetone), and potential for real-time monitoring[56]. A 2023 experimental study reported a 3D graphene film grown on a nano-porous SiC backbone for aging/rancidity detection in hazelnuts. The large surface-to-volume ratio and abundant edge/dangling bonds provided many active sites for VOC adsorption; the chemiresistive sensor successfully discriminated between fresh and spoiled nuts[57]. Recent reviews consolidate the state-of-the-art in nanomaterial-based VOC sensing for food/environment/health, highlighting the increasing maturity and broadening scope of nanosensor technologies [55].

1.6 Two dimensional (2D) material based nanosensors for food VOC detection: Graphene, Transition metal dichalcogenides (TMDC) and MXenes.

Two-dimensional (2D) materials have generated significant interest lately. These atomically thin sheets have higher lateral dimensions than thickness, resulting in high surface-to-volume ratios, active surface/edge locations, and tunable electronic, optical, and chemical characteristics. Furthermore, 2D materials have been used in a variety of sensor designs (chemiresistive, electrochemical, optical, and biosensing) for food quality monitoring. Most 2D materials have a greater specific surface area than zero-dimensional (0D), one-dimensional (1D), and three-dimensional (3D) nanomaterials, allowing for easier analyte loading and thereby improving the sensitivity of sensors based upon them. The comparatively large lateral dimensions of 2D materials can be in close contact with electrodes, thus gaining wide attention in applications as electrochemical sensors[58, 59, 60]. Graphene and its derivatives, transition metal dichalcogenides (TMDCs), and transition metal-carbonitrides (MXene) are some of the prominent 2D materials. Particularly in the areas of food safety and biomolecular detection, these two-dimensional (2D) materials has caused a paradigm shift in the architecture and operation of electrochemical sensors and biosensors. In the next subsection, we discuss some of the attributes of these 2D materials with regard to their usage as sensors in food safety and biomolecular detection.

1.6.1 Graphene Based Sensors

Graphene exhibits exceptional properties, including high transparency (97.7% visible light transmittance), high thermal conductivity ($3 \times 10^{3-5} \times 10^3$ W m^{-1} K^{-1}), electrical conductivity ($10^4\omega^{-1}$) at room temperature, high Young's modulus (130.5 GPa), and high specific surface area (2630 m^2 g^{-1})[61, 62, 63, 64]. In addition, graphene also has a special $\pi - \pi^*$ energy band structure, in which carbon atoms form a single-layer honeycomb lattice through sp^2 hybridisation. Its bandgap and conductivity are correlated with the number of layers; as the number of layers increases, these parameters get closer to those of graphite[65].These unusual structures offer exceptional electrochemical performance,

as well as optical and medicinal applications. Graphene has considerable potential in electrochemical sensing because of its huge specific surface area, strong electrical conductivity, plentiful surface atoms, high mechanical strength, and possibility for wide-scale manufacture[66, 67]. First, graphene has unusually high carrier mobility and density at room temperature, making it a desirable material for the fabrication of high-performance electrical devices[68, 69]. Second,Graphene's electronic characteristics, such as electrical conductivity, are affected by transfer and covalent bonding[70, 71]. The electron density within graphene-based materials can be concentrated at its edges. Combined with structural defects, this results in quicker electron transfer rates than on the substrate plane, highlighting graphene's flexible capabilities as an electrocatalyst for electrochemical sensing applications[72]. Third,Graphene has a high specific surface area, with each carbon atom acting as a surface atom. As a result, charge transport in graphene is highly sensitive to its chemical environment[73, 74].Fourth,Graphene's high mechanical strength and flexibility make it ideal for wearable electronics[75, 76]. For all those reason graphene's unique features make it the most promising 2D material for sensors. Because the graphene surface is critical in intermolecular interactions, adjusting the surface chemistry of graphene materials is the most important and direct way to improve sensing performance. The graphene surface is typically altered by different doping techniques to improve the interaction with the surrounding environment. To improve sensing performance in sensing devices, functional groups or dopants can be added after synthesis. Additionally, structural and defect control can be achieved by modifying the reactive sites of adsorbed molecules. Gas sensors made from graphene oxide (GO) with defects and oxygen-containing functional groups exhibit higher selectivity and sensitivity than pristine graphene[77, 78, 79]. Graphene and its derivatives, such as graphene oxide (GO) and reduced graphene oxide (rGO), are some of the most commonly employed 2D materials in biosensors because of their excellent conductivity, large surface area, and the ability to easily functionalise their surface for specific molecular interactions. In the following, we list few usages of Graphene based systems as VOC sensors.

1. Chemiresistive Sensors: Graphene and its derivatives (graphene oxide - GO, reduced graphene oxide - rGO) function as high-sensitivity chemiresistors.Adsorption of VOC molecules perturbs carrier concentration or mobility through charge transfer and dipole scattering, producing measurable resistance shifts. Local doping or functionalization (e.g., oxygen groups, metal nanoparticle decoration) enhances selective interaction with classes of food VOCs such as ethanol, acetone and hexanal and lowers detection limits to ppm-ppb ranges [80, 81]. Hybrid architectures (rGO + metal oxide or noble-metal nanoparticles) combine catalytic activation and high conductivity to improve response amplitude and recovery for food-related VOCs (e.g., rancidity markers).

2. Work-function (WF) sensors: Graphene's WF is sensitive to physisorbed and chemisorbed molecules. VOC adsorption shifts the local electrostatic potential and hence the WF, which can be obtained using Kelvin probe or via contact potential difference in diode/FET configurations. WF readout is advantageous in packaging or contact-type sensors because it can be made highly surface-specific and exploited in differential (two-sided) measurement geometries to reduce background drift [80, 82].

3. Optical Sensors: Graphene's optical transduction modes include surface plasmon enhancement (when coupled with metal films), fluorescence quenching of indicator dyes, and change in Raman features upon adsorption. For food VOCs, graphene-based optical

sensors often appear in hybrid colorimetric/graphene e-nose arrays where graphene improves signal transport or dye immobilization but the primary chemical selectivity derives from chromogenic indicators [83, 84].

1.6.2 TMDC-Based Sensors

TMDC have been favoured by researchers due to their superior electrical qualities and architectures[85]. TMDCs physical properties are very different from graphene. TMDCs have a layered structure (X-M-X) with transition metal atoms (M) sandwiched between two layers of chalcogen atoms (X) in a stoichiometric ratio of MX_2. These materials have covalently bonded atoms in the same layer and weak Van der Waals interactions between layers, which can lead to stacking or thinning.[86, 87]. TMDCs can exhibit a broad spectrum of polymorphisms[88, 89, 90]. As an example, MoS_2 has four distinct crystal structures: 2H, 1T, 1T', and 3R, depending on the coordination pattern of Mo and S atoms, as well as the stacking order between layers[91]. The electrical conductivity of bulk TMDCs also has diverse characteristics ranging from insulator (HfS_2) to semiconductor (MoS_2) to conductor (NbS_2). The characteristics of TMDCs differ greatly from those of the bulk because to the fracture of the interlayer coupling[92, 93]. Exfoliating TMDCs into 2D nanosheets exposes both basal planes and prism edges, revealing unique structural and electrical features. TMDCs are mostly made up of chalcogenides on their basal surface, with metal or chalcogen atoms present on the edges. These 2D materials are attractive options for sensing applications because of the benefits of TMDs, such as their great thermal/chemical stability and abundance of metal sites[94]. For instance, MoS_2 is a great option for creating electronic devices due to its larger bandgap following exfoliation from bulk materials into nanosheets[95]. MoS_2 undergoes a phase transition that turns it from a semiconducting to a metallic material, which boosts its electrical conductivity, and further optimizes its electrochemical properties[96, 97]. Furthermore, the vast surface area of the single-layer TMD nanosheets allows them to adsorb gas molecules in significant amounts. Among TMDCs, MoS_2, WS_2, and $MoSe_2$ have received substantial attention for their significant sensitivities in adsorption of gas molecules. Their semiconducting properties allow for easy functionalization with biorecognition molecules and enable effective signal amplification upon the binding of target analytes. In the following, we list few usages of TMDC based systems as gas sensors.

1. Chemiresistive Sensors: TMDC monolayers and few-layer films provide semiconducting channels with bandgaps and strong surface reactivity at defect sites and edges. Adsorption of polar VOCs (e.g., alcohols, aldehydes) modifies the carrier density and mobility. In FET geometries this yields large ON/OFF or threshold-voltage shifts, enabling room-temperature operation and low power. Surface treatments (UV-ozone, plasma, metal nanoparticle decoration) are commonly used to tune selectivity for food VOCs such as ethanol and toluene [98, 99].

2. Work-function sensors: TMDCs exhibit surface dipoles and edge-dependent WF. Asymmetric functionalization or heterostructuring (e.g., Janus or vertically stacked layers) creates measurable WF contrasts upon adsorption. WF readout using scanning Kelvin probe microscopy or contact work-function detectors has been demonstrated to detect gas-induced potential shifts that correlate with VOC concentration and species [98, 49].

3. Optical Sensors: TMDCs have strong excitonic resonances in the visible region that are sensitive to dielectric environment and charge transfer. Adsorption of VOC molecules shifts exciton energy, linewidth and photoluminescence intensity, enabling optical detection modalities for non-invasive sensing of headspace VOCs. Moreover, TMDCs integrated into photonic cavities or on optical fibers amplify these changes for improved sensitivity [100, 101].

1.6.3 MXene Based Sensors

MXene is a recent discovered family of 2D transition metal-carbonitrides, with a quasi-2D structure [102, 103, 104]. In 2011, Naguib et al. [105] successfully synthesised Ti_3C_2, the first MXene nanosheets with layered morphology by selectively etching the Al atomic layer in Ti_3AlC_2, a ternary layered cermet material.During the preparation process of MXene, functional groups like -OH, -F, and -O passivated its surface, resulting in an unusual structure, excellent electrical conductivity, and environmental protection. This has sparked interest in research and exploration of this materials family[106]. MXene is typically made by using concentrated hydrofluoric acid to selectively etch its precursor MAX phase [107, 108]. The standard formula for the MAX phase, a ceramic material with a distinct ternary layered structure, is $M_{n+1}AX_n$, where M is a transition metal element, A is a group III or group IV element (mostly Al or Si), and X is C or N;$1 \leq n \leq 3$[109]. The M atom and A atom form a metallic relationship in the MAX phase, whereas the M atom and X atom form a mixed bond with a greater binding force that mostly consists of covalent, ionic, and metallic bonds. MXene produced by the liquid etching approach has a very high surface activity and can react quickly with oxygen, water, and fluoride ions in the solution to lower the system's overall energy. Consequently, functional groups like -OH, -F, and -O are typically found on MXene surfaces[110, 111]. MXene materials can be converted from conductors to semiconductors by altering the surface functional groups. Theoretical simulations indicate that etching the A atomic layer in the MAX phase alters the d-orbital electrons of the M atoms, leading to increased metallic conductivity in MXene nanosheet materials. When functional groups like -OH and -F occupy the surface of the MXene nanosheet, novel physical properties are observed. In the following, we list few usages of MXene-based systems as VOC sensors.

1. Chemiresistive Sensor: MXenes ($Ti_3C_2T_x$, Nb_2CT_x, etc.) combine metallic conductivity and abundant surface terminations (-O, -OH, -F) that form specific interactions with VOCs. Their layered, hydrophilic surfaces enable rapid adsorption of polar VOCs and large resistance modulation, often at room temperature. MXene-polymer composites and MXene-MOF hybrids have demonstrated sensitive detection of ammonia, alcohols and other compounds relevant to food spoilage [112, 113].

2. Work-function sensors: Surface terminations and redox-active transition metals make MXene WF highly tunable. Adsorption or intercalation of VOCs alters surface dipole and WF substantially, allowing WF-based readouts (Kelvin probe or contact potential devices) to be used for selective sensing of certain food VOCs in humid conditions [114, 113].

3. Optical Sensor: MXenes exhibit broadband optical absorption and plasmonic-like behavior in the NIR. Functionalized MXene films can be used in optical transduction (absorbance/reflectance changes, fluorescence quenching) to detect VOC adsorption. Some

works show MXene fluorescence quenching of indicator dyes for optical VOC sensing [115, 116].

1.7 Need for computational modeling and the role of first principles Electronic Structure Methods

There have been quite a few experimental studies to detect and profile VOCs from food materials using nanosensors [117, 118, 119, 120] . A variety of issues like VOC profiling in sugarcane juice, monitoring of fish freshness, evolution of VOCs during fermentation process for products like vinegar, black tea and fruit drinks, meat and vegetables and integration to smart packaging have been addressed in these works. On the other hand, there are recent experiments that indentified the prominent VOCs that are bio-markers for papaya, a fruit consumed worldwide due to its rich nutritional values[121]. Naturally, appropriate nanosensors need to be discovered for efficient sensing of these VOCs to monitor the ripening stages of this important fruit. In general, there has been a need of discovering new sensors from the family of 2D materials due to the tunabilities offered by them. Such discovery can not run on the basis of trial and error. Understanding of the roles of surface chemistry, structure and composition of a 2D material are few of the crucial parameters that need to be understood at the electronic level before putting it into a device form in a laboratory. Computational modeling based upon parameter-free first principles electronic structure methods can come out to be extemely useful in this context. With the advent of Density Functional Theory [122] and its developments, understanding materials properties at the microscopic level has become possible. Thus modeling a complex system and performing extensive computational study at the electronic level to assess sensing abilities of materials is the way to go. This powerful strategy can even predict new sensors in a reliable way. In the area of sensor materials for food VOC detection, there have been a few studies by adoptiong this strategy that provided impotant insights [123, 124, 125, 126]. However, these studies lacked in modeling a real sensor device with the 2D material they investigated from electronic structure point of view. Device modeling at nanoscale can be done using Non-Equilibrium Green's function(NEGF) method[127]. An integration of DFT and NEGF turned out to be immensely successful in detecting VOCs as diverse as various hazaradous gases in the enviroment and biomarker of lung cancer[128, 129, 130, 131, 132, 133, 134, 135, 136, 137, 138, 139, 140, 141, 142]. However, no such device modeling following this route has been done in the area of food quality assessment. Thus, the real potentials of 2D sensors in the area have not been exploited. This leaves one with a huge scope of exploring materials from 2D families as sensors for quality assessment of generic as well as specific items computationally such that microscopic mechanism of gas-surface interaction and simulation of the nanodevice can be done simultaneously. So, in gernerally we try to explore different type of 2D materials like graphene and it's derivative, metallins(Borophene, Silicene, Germanene), MXene and MXene-TMDC heterostructure for food sensing application.

1.8 Outline of the thesis

In this thesis, Density functional theory (DFT)[122] in conjunction with Non-Equillibrium Green's Function (NEGF) method [127] has been used to compute the sensing abilities of

various 2D materials upon exposure to the VOCs emitted by different food products. Understanding of the molecular adsorption on different 2D surfaces and their consequences on the sensing characteristics have been investigated in detail by analysing the electronic structures, charge distributions, variations in work functions and optical absorbances of the VOC-2D material complexes. This is followed up by modeling the sensor and computations of sensitivities and selectivities, quantities that can be compared directly with experiments. A comparative analysis on usefulness of a particular 2D material as chemiresistive and work function based sensor has been made in several cases. We have chosen our systems carefully based upon the following criteria: a) systems that have been investigated experimentally such as Graphene and reduced Graphene oxide, b) systems which have been investigated towards their sensing capabilities with regard to various gases but have not been tried in the area of food quality assessment and c) the representative systems for this study should include materials from different 2D families that satisfy criteria b). Thus, we have chosen Graphene, and its oxides under criteria a), pristine and functionalized silicene, MXene and its heterostructure with TMDC satisfying criteria b) and c).The chapters in this thesis are organized as follows:

Chapter I begins with the overview of importance of VOCs from food in determining it's stages of degradation and corresponding significance in food technology. This is followed by a detailed discussion on importance of nanotechnology towards food quality and safety. Special emphasis is given on the role of 2D materials and their potential application in sensing. This chapter also introduces different gas sensing technologies.

In **Chapter II** the computational methodologies adapted throughout the thesis are described. Density Functional Theory (DFT) is used in the thesis to obtain the structural and electronic properties of the isolated VOC molecules, isolated 2D materials considered for sensing applications and the VOC-2D complexes upon adsorption of VOC on the 2D material. The NEGF formalism as implemented in conjunction with DFT to simulate the sensing device is discussed in detail next.Formalisms to evaluate the current-voltage (I-V) characteristics curves of nanoscale devices and computations of sensitivity, selectivity and relaxation times, the key parameters of a gas sensor are discussed thereafter.A short overview of the procedures used to determine work-function, charge density difference and optical characteristics are also included in this chapter.

In **Chapter III** results on a comparative assessment of pristine graphene and its two derivatives, graphene oxide (GO) and reduced graphene oxide (r-GO) as chemiresistive and work function based sensors to detect VOCs emitted by standard food products are shown. The work is motivated by a recent experiment on assessing capabilities of r-GO sensor in selecting six prominent VOCs emitted by standard food products like meat, vegetables and fruit during various stages of their degradation. The experiment inferred that unless r-GO is polymerized, discrimination of the VOCs is not possible. The computational study presented in this chapter however finds that while pristine graphene performs poorly as a chemiresistive and work function based sensor, r-GO in either mode is able to differentiate between four, out of six VOCs. It turns out that GO, on the other hand performs at par with r-GO as work function based sensor but is not useful as chemiresistive one. The analysis based upon electronic structures, structural parameters and adsorption characteristics trace such behavior back to the hybridisation of molecular orbitals driven by the adsorption geometry. The discrepancy between the results of this computation and the experiment in the context of the performance of r-GO sensor is therefore, attributed to the limitations in the experimental method of reducing graphene.

In **Chapter IV** in order to expand the database of 2D sensors in the current context of

food technology, this chapter presents results of investigation into the sensing capabilities of free-standing silicene and Fluorine passivated (F-Silicene) nanosheets with regard to detection of the VOCs considered in the preceeding chapter. The results suggest that fluorine passivated silicene has significantly better sensitivity towards all six VOC molecules in comparison to pristine silicene. Like, r-GO, as chemiresistive sensor, F-silicene can discriminate between four VOCs, out of six. The sensitivities computed with F-silicene, in fact, turned out to be quantitatively better than r-GO. Here too,results are analysed based upon the microscopic mechanism by looking at the variations in the adsorption energy, charge transfer, and the electronic structures of the two systems considered.

MXenes with chemical formula $M_{n+1}X_nT_n$ (M=a transition metal, X=carbon or nitrogen, T= a surface functional group such as -O,-F,-OH, chalcogens, halogens etc, n=number of layers) constitute a new family of fascinating quasi-2D materials. The tunability with respect to composition, number of layers, surface functional groups make MXenes extremely flexible to make an in-depth study of structure-property relations. Moreover, upon construction of van der Waals heterostructure with transition metal dichalcogenides, class of materials where a stack of two or more different 2D materials are held by weak van der Waals interaction across the interfaces, are found to have enhanced transport across the interfaces. Motivated by these, in **Chapter V**, results on sensing abilities of Sc_2CO_2 MXene and its heterostructure with monolayer transition metal dichalcogenide WSe_2 towards four prominent VOCs considered in preceding two chapters are presented. Investigations are done by considering them as chemiresistive, work function and optical sensors. It is found that while Sc_2CO_2 is able to detect the four VOCs separately like F-silicene and GO do, the sensitivities are lower. However, the sensitivities increase substantially upon forming the heterostructure. Analyzing the DFT results, it is found that upon forming heterostructure, a huge charge transfer across the interface as compared to the case of bare MXene, happens. This coupled with significant changes in the work functions leads to much better sensitivities of the heterostructure based sensors.

Since the electronic properties of MXenes are controlled by the functional groups passivating their surfaces, it is worthwhile to address this in the context of sensing abilities of food material sensors. On the other hand, capability of sensors in the area of food technology should be investigated going beyond generic food products. In a bid to address both, in **Chapter VI** the capabilities of functionalized Sc_2CT_2 (T=-O,-F,-S) MXenes towards distinctive detection of four important volatile organic compounds (VOC)-3-carene, D-limonene, methylbutanoate, and methylhexanoate, emitted by papaya during various stages of ripening, are investigated. Assessment of these materials with regard to all three types of sensors is done in this chapter. It is found that out of the three, only Sc_2CS_2 is able to detect and separate the VOCs. Such outcome is connected to the geometry of molecular adsorption, electronic structure and charge transfer for the VOC-MXene complexes. This work is the first one that proposes a 2D material as potential nanosensor for detection of quality of papaya fruit. The results demonstrate a bigger scope towards exploration of MXenes as potential sensors for detection of quality of food products, something that has not been done yet.

The concluding **Chapter VII** summarises and proposes possible extensions of the work presented in this thesis. In summary, the chapters of this thesis highlight two aspects of 2D materials as potentials sensors for assessment of food quality: a) how functionalization of pristine compounds or putting them into heterostructures enhance their sensing abilities and b) comparative study of usefulness of a given material as sensors

working on different principles. Chapters 3-5 deal with the same set of food VOCs while the sensor material changes. These three chapters systematically show the similarities and differences in three different classes of potential sensor materials, keeping the VOCs same and generic. After building this tempo, chapter 6 focuses on a specific food item and a specific 2D material and examine the role of different surface passivation in affecting sensing capability of the material. This way the thesis covers a broader spectrum which can be useful in designing new sensors in laboratories.

Chapter 2

Methodology

This chapter describes the theoretical foundations employed in this thesis for the simulation of material properties. The work presented in this thesis is carried out by Density Functional Theory (DFT) based calculations. We provide a description of the Pseudopotential method and the projected augmented wave (PAW) as these implementations of DFT have been used in this thesis for evaluation of the ground state properties and electronic structure of the materials considered. A brief discussion on Non-Equillibrium Green Function Method (NEGF), which is used for the calculation of transmission function in nanoscale system. The chapter ends with a brief description of the ways to calculate adsorbtion energy, charge transfer, Charge density difference, work-function and optical properties.

2.1 The Many-Body Schrödinger Equation

Electrons in atoms, molecules, and solids interact to determine their physical and chemical properties. Understanding the electrical structure, especially the ground state, is crucial for determining material properties. Solving the many-body problem is hard due to the necessity to account for all particle interactions, making it computationally costly. The time-independent Schrödinger equation for a system of N electrons and N_s nuclei is as follows:

$$H\Psi(\mathbf{r}_1, \mathbf{r}_2, ..., \mathbf{r}_N, \mathbf{R}_1, \mathbf{R}_2, ..\mathbf{R}_{N_s}) = E\Psi(\mathbf{r}_1, \mathbf{r}_2, ..., \mathbf{r}_N, \mathbf{R}_1, \mathbf{R}_2, ..\mathbf{R}_{N_s}) \tag{2.1}$$

Here, H corresponds to the Hamiltonian operator, and E is the total energy associated with the system. The system consist of N electrons and N_s nuclei. The variables $\mathbf{r}_1, \mathbf{r}_2, ..., \mathbf{r}_N$ corresponds to the the electronic coordinates while $\mathbf{R}_1, \mathbf{R}_2, ..\mathbf{R}_{N_s}$ represents nuclear coordinates .The form of the Hamiltonian is given as:

$$H = \frac{-\hbar^2}{2m_e}\sum_e \Delta_i^2 + \frac{1}{2}\sum_{i\neq j}\frac{e^2}{\mid \mathbf{r}_i - \mathbf{r}_j \mid} - \frac{\hbar^2}{2M_n}\sum_I \Delta_I^2 - \sum_{i,I}\frac{Z_I e^2}{\mid \mathbf{r}_i - \mathbf{R}_I \mid} + \frac{1}{2}\sum_{i\neq j}\frac{Z_I Z_J e^2}{\mid \mathbf{R}_I - \mathbf{R}_J \mid} \tag{2.2}$$

The Hamiltonian above consists of five terms in total. The kinetic energy of the electrons and nuclei is represented by the first and third terms, respectively. Here, m_e and M_n denote the electrons and the nuclear mass, respectively. The columb interactions between the electrons (nuclei) are represented by the second (fifth) term. The interaction between electrons and nuclei is represented by the fourth term. Equation 2.2 for many electrons

is too complicated to solve and possible only for small systems like hydrogen atoms and molecules. Approximations are crucial for bigger systems, such as solids. Because of the massive mass differential between nuclei and electrons (a proton is 1836 times heavier than an electron), nuclei travel slower and are considered immobile in comparison to electrons. The Born-Oppenheimer approximation is proposed by taking the dynamics of electrons and nuclei independently [143].

2.2 The Born-Oppenheimer Approximation

In order to reduce the intricate many-body Hamiltonian regulating systems with both electrons and nuclei, Max Born and Robert Oppenheimer developed the Born-Oppenheimer approximation in 1927. The substantial mass difference between a system's nuclei and electrons is the basis of the approximation. Since the nuclei are substantially heavier than the electrons, they move much more slowly. This means that, from the perspective of the swiftly moving electrons, the nuclei appear almost motionless.As a result, the kinetic energy of the nuclei can be discarded, but the Coulomb interactions between the nuclei (which are independent of electronic motion) become constant. As a result, the situation is simplified to one in which electrons are viewed as moving in a set potential provided by immobile nuclei. Using this approximation, the electronic Hamiltonian has the form:

$$H = \frac{-\hbar^2}{2m_e}\sum_e \nabla_i^2 + \frac{1}{2}\sum_{i\neq j}\frac{e^2}{\mid \mathbf{r}_i - \mathbf{r}_j \mid} - \sum_{i,I}\frac{Z_I e^2}{\mid \mathbf{r}_i - \mathbf{R}_I \mid} \tag{2.3}$$

The first term is the electron's kinetic energy (T_e), the second term is the Coulomb interaction between electrons (V_{ee}), and the last term is the potential energy due to electron-nucleus interaction ($V_{external}$). The approach does not completely solve the difficulties associated with the many-body Schrödinger equation since the electronic wave function is still a many body one. In next couple of section, we discuss methods to take care of this.

2.3 Hartree and Hartee Fork Methods

The Hartree approach, invented by Douglas Hartree in 1928, is a first approximation used to characterise the behaviour of many-electron systems [144]. Instead of explicitly accounting for the complete many-body wave function, this approach treats each electron as moving independently in an average electric field produced by the other electrons. The approach approximates the electron wavefunctions as a product of single-particle wavefunctions, assuming that the electrons are uncorrelated. An average potential is used in place of the electron interactions, resulting in a set of self-consistent equations that describe how each electron moves in this effective field. For a system of N interacting electrons, the Hartree method leads to a set of N single-particle Schrödinger equations, which are given by:

$$\frac{-\hbar^2}{2m_e}\nabla_i^2 + V_H(\mathbf{r}_i)\Psi(\mathbf{r}_i) = \epsilon_i\Psi(\mathbf{r}_i) \tag{2.4}$$

V_H represents the effective potential, which includes both the Coulomb attraction to the nucleus and the average electrostatic repulsion from other electrons. This approximation

represents the system's wavefunction as a product of single-particle wavefunctions for each electron.:

$$\Psi(\mathbf{r}) = \Psi_1(\mathbf{r}_1).\Psi_2(\mathbf{r}_2).....\Psi_n(\mathbf{r}_n) \tag{2.5}$$

The Hartree-Fock approach was created as a natural extension of the Hartree method, which, although offering a good approximation for many-electron systems, overlooked key physical consequences[145]. Specifically, the Hartree method sees electrons as independent particles moving in an average field formed by the other electrons, ignoring the exchange interactions that occur as a result of the Pauli exclusion principle. This indicates that the Hartree method does not account for the antisymmetry of the many-electron wavefunction, which is required to describe electrons. The Hartree-Fock method was developed to address this issue by enforcing the wavefunction's antisymmetry via a Slater determinant. Using this, the wave function of an N-electron system can be represented as:

$$\Psi(\mathbf{r}) = \frac{1}{\sqrt{N!}} \begin{vmatrix} \Psi_1(\mathbf{r}_1) & \Psi_2(\mathbf{r}_1) & \cdots & \Psi_N(\mathbf{r}_1) \\ \Psi_1(\mathbf{r}_2) & \Psi_2(\mathbf{r}_2) & \cdots & \Psi_N(\mathbf{r}_2) \\ \vdots & \vdots & \ddots & \vdots \\ \Psi_1(\mathbf{r}_N) & \Psi_2(\mathbf{r}_N) & \cdots & \Psi_N(\mathbf{r}_N) \end{vmatrix} \tag{2.6}$$

While the approach allows for exchange interactions due to the Pauli exclusion principle, it misses important effects like electron-electron correlations. Moreover, it is only applicable to tiny systems with atoms on the order of tens as the method itself is computationaly expensive. In the following section, we describe Kohn and Sham's innovative approach, known as the Density Functional Theory, which addresses the shortcomings of these wave function based approaches and provide tracable solution.

2.4 Density Functional Theory

Density Functional Theory (DFT) is a sophisticated quantum mechanical technique for investigating the electronic structure of atoms, molecules, and solids. The accuracy and computational efficiency make it an excellent tool for studying electrical structures. The technique focuses on single-particle electron density rather than the many-body wavefunction. Unlike previous methods that require solving the difficult many-body Schrödinger equation to derive a system's wavefunction, DFT simplifies the issue by describing the system's energy as a function of electron density, which is far simpler to compute. Thomas and Fermi presented an early model based upon this philosophy [146, 147]. However, this model could not adequately explain electron interactions in multi-body systems. Kohn and Hohenberg devised the contemporary DFT formalism. The Hohenberg-Kohn theorems provided an exact theoretical foundation for tractable solution of an interacting many-body systems. The present form of DFT, known as Kohn-Sham DFT, emerged from their work [148].

2.4.1 Hohenberg-Kohn Theorem

Pierre Hohenberg and Walter Kohn proposed two theorems in 1964. These establish that the electron density alone completely determines the ground-state features of a many-electron system. They are as follows.:
(1) The external potential, $V_{external}$, or the ground state energy E, is a unique functional of density [149].
(2) The electron density that minimises the entire energy functional is the real ground-state density of the system[149]. Consequently, the energy functional provides the ground state of the interacting electrons at an external potential $V_{external}$:

$$E[\rho(\mathbf{r})] = F[\rho(\mathbf{r})] + \int V_{external}(\mathbf{r})\rho(\mathbf{r})d\mathbf{r} \tag{2.7}$$

where $F[\rho(\mathbf{r})]$ is a universal functional of electron density $\rho(r)$. DFT aims to determine the electron density $\rho(\mathbf{r})$ that minimises the total energy functional $E[\rho(\mathbf{r})]$, which corresponds to the system's genuine ground-state density.

2.4.2 The Kohn-Sham Framework in Density Functional Theory

The Hohenberg-Kohn theorems implied that all attributes of the ground state of a many-body system can be determined by $\rho(\mathbf{r})$. Inspite of making this important connection, the theorems do not provide information on how to explicitly formulate the universal functional $F[\rho(\mathbf{r})]$. Kohn and Sham proposed a formalism that worked around this issue. The Kohn-Sham (KS) approach provides a feasible method for applying DFT by using a collection of fictitious, non-interacting particles [122]. The electron density of these hypothetical particles is identical to that of the actual interacting system. By substituting non-interacting particles that travel in a unique potential, the complicated many-electron system is intended to be made simpler. This effective potential is produced to ensure that the electron density and the consequences of interactions between electrons are appropriately represented. Using an effective potential that follows a Schrödinger-like equation, this method transforms the multi-electron systems into effective single-electron ones:

$$(H_{KS} - \epsilon_i)\Phi_i(\mathbf{r}) = 0 \tag{2.8}$$

The Kohn-Sham Hamiltonian operator, denoted by H_{KS} in this Kohn-Sham equation, comprises the kinetic energy of the electrons as well as the effective potential that takes into consideration the external potential and electron-electron interactions.ϵ_i represents the energy eigenvalue of the i-th electron, and $\Phi_i(\mathbf{r})$ is the single-particle wavefunction (also known as the Kohn–Sham orbital) for the i-th electron. The mathematical representation of the Kohn-Sham Hamiltonian is given as:

$$H_{KS} = \frac{-\hbar^2}{2m_e}\nabla^2 + V_{eff} \tag{2.9}$$

The first term is the kinetic energy of the electron, and the second term is the effective potential.

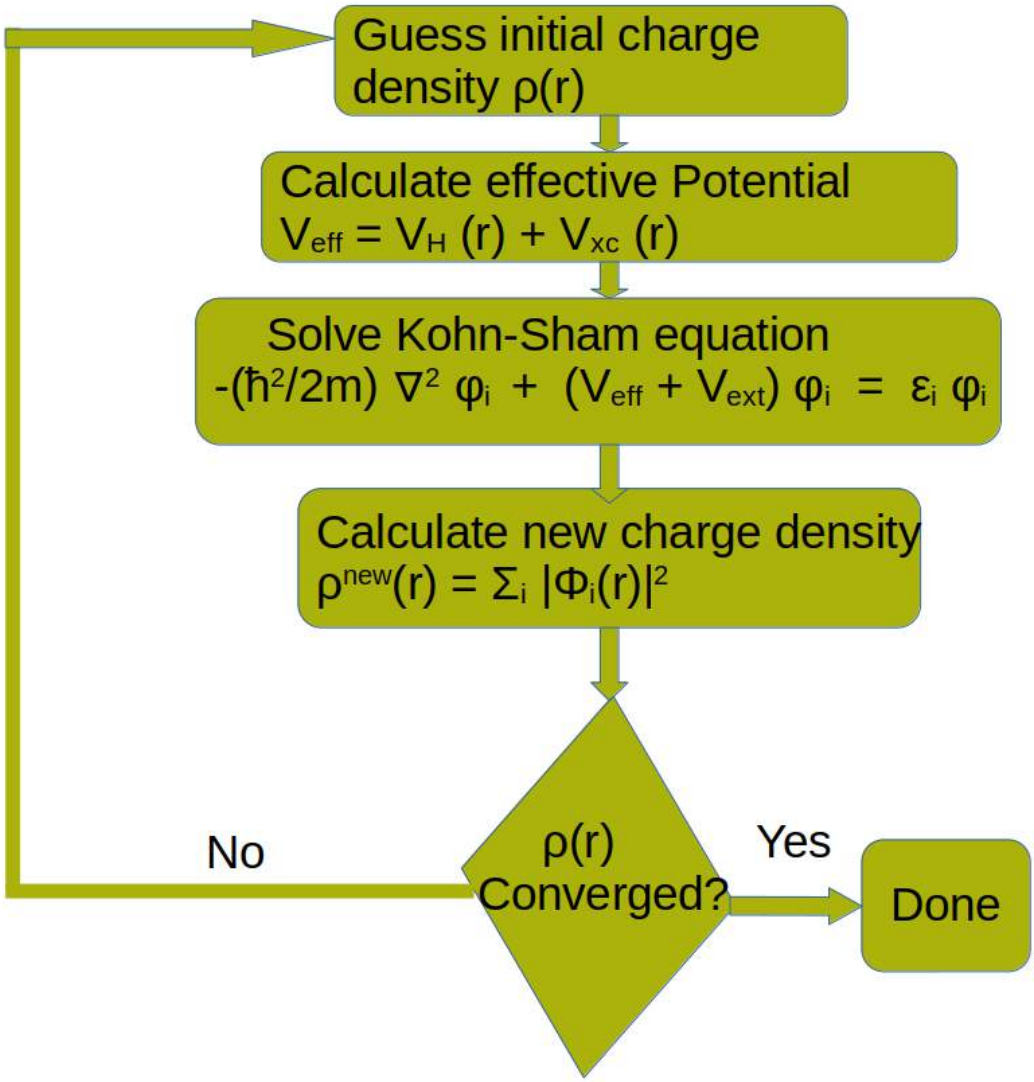

Figure 2.1: Flowchart for solving self-consistent Kohn Sham (KS) equation.

$$V_{eff} = V_{external}(\mathbf{r}) + V_H(\mathbf{r}) + V_{xc}(\mathbf{r}) \tag{2.10}$$

The first term is the external potential; the second is the Hartree potential; and the third is the exchange-correlation potential. The Hartree potential is expressed as:

$$V_H(\mathbf{r}) = \frac{1}{2}\int \frac{\rho(\mathbf{r})\rho(\mathbf{r'})\mathbf{drdr'}}{|\ \mathbf{r\text{-}r'}\ |} \tag{2.11}$$

and the exchange-correlation potential is given as :

$$V_{xc}(\mathbf{r}) = \frac{\delta E_{xc}(\mathbf{r})}{\delta \rho} \tag{2.12}$$

The density is expressed as a summation over the individual Kohn-sham orbitals, i.e.,

$$\rho(\mathbf{r}) = \sum_{i}^{N} \mid \Phi_i(\mathbf{r}) \mid^2 \tag{2.13}$$

By integrating this density, the total number of electrons is obtained, i.e.:

$$N = \int \rho(\mathbf{r}) d\mathbf{r} \tag{2.14}$$

The Kohn-Sham energy functional is given as :

$$E_{KS} = T_s(\rho) + \int V_{external}(\mathbf{r})\rho(\mathbf{r})d\mathbf{r} + E_H(\rho) + E_{xc}(\rho) \tag{2.15}$$

The Kohn-Sham equation is iteratively solved by offering a starting estimate for the electron density, $\rho(\mathbf{r})$, and the exchange-correlation functional, $E_{xc}([\rho(\mathbf{r})])$. Schematic for a DFT calculation is shown in Figure 2.1.

2.4.3 Exchange Correlation Energy Functional

In the aforementioned Kohn-Sham energy functional, the exact form of the exchange-correlation energy functional E_{xc} is unknown. To balance computing efficiency and accuracy, approximations to the exchange-correlation (xc) functional have been made. The correctness of DFT computations is solely dependent on the chosen form of E_{xc}. In the following, we briefly describe the two most widely used approximations to address the exchange and correlation effects in DFT.

2.4.3.1 Local Density Approximation (LDA)

The simplest approximation to E_{xc} is the local density approximation (LDA) [122]. Within LDA, the exchange-correlation energy at every point in space is only determined by the local electron density at that point, as if the density of the system were uniform. For a particular spatial point, the system is regarded as if it acts as a homogeneous electron gas with the same density as the local electron density at that place. Mathematically :

$$E_{xc}^{LDA}(\rho(\mathbf{r})) = \int \rho(\mathbf{r}) E_{xc}^{hom}(\rho(\mathbf{r}))d^3\mathbf{r} \tag{2.16}$$

E_{xc}^{hom} represents the exchange-correlation energy of a homogeneous electron gas with density $\rho(\mathbf{r})$. The E_{xc}^{hom} can be separated into two parts: exchange E_{xc} and correlation E_c terms. An analytical approach can be used to derive the exchange term E_{xc}, but the correlation term E_c remains unknown.Thus, E_c can be derived from the entire spectrum of Monte-Carlo (MC) simulations mixed with distinct interpolation methods[150]. The LDA formalism is found to work effectively in a variety of model systems. Also, the LDA formalism was expected to work for systems with slowly variable density, such as free electrons in metallic systems[151]. Nonetheless, current research indicates that LDA formalism is quite promising for other systems, such as semiconductors and insulators. Many experimentally significant physical parameters can be calculated precisely [152, 153]. However, it has some serious drawbacks: (i) it overestimates the cohesive and binding energy levels. (ii) Insufficient electron localisation in space, which is appropriate for s and p orbital electrons but not for d and f orbital electrons. (iii) The LDA formalism's excessively local nature prevents long-range effects, such as van der Waals (vdW) bonding.

2.4.3.2 Generalized-Gradient Approximation (GGA)

An attempt to improve the LDA is made by introducing both the electron density and the gradient of the local electronic density, $\bigtriangledown\rho(\mathbf{r})$[148] in formulating E_{xc}. The exchange-correlation energy in the GGA formalism is primarily produced by adjusting the LDA energy density and can be represented as shown below in equation.

$$E_{xc}^{GGA}(\rho(\mathbf{r})) = \int \rho(\mathbf{r}) E_{xc}^{hom}(\rho(\mathbf{r}), \bigtriangledown\rho(\mathbf{r}))d^3\mathbf{r} \tag{2.17}$$

Some of the well known Generalized Gradient Approximation (GGA) functionals are : PBE (Perdew-Burke-Ernzerhof) [154] , PW91 (Perdew-Wang 1991) [155] , BLYP (Becke-Lee-Yang-Parr) and PBEsol (PBE for solids) [156] . This thesis makes extensive use of PBE functionals throughout.

Finding the optimal balance between numerical accuracy and efficiency while solving the Kohn-Sham equations is one of the fundamental concerns in computational materials research. This makes it difficult to build numerical approaches that are both accurate and time efficient in modern computational material science, depending on the nature of the problem. Nowadays, three types of approaches are commonly used: pseudopotential (PP) methods, full potential (FP) methods, and Green's function-based methods.

2.5 Pseudopotential (PP) method

Bloch's theorem states that the wave function of an electron in a periodic potential can be represented as a discrete series of plane waves. We require a large number of plane waves to depict the strong core potential, which is marked by tightly bound core orbitals and wiggles in the wave functions of the core's valance electrons caused by the orthogonality of core and valance states. In PP techniques, instead of a strong core potential, a pseudopotential corresponding to a "Pseudo-Hamiltonian" is employed, so that outside of a cut-off radius, the ground state wave functions estimated in this manner approximate that of the all electron wavefunction. This approach is computationally tractable because it uses a smooth pseudo-wavefunction provided by a reasonable number of plane waves to decrease wiggles in the core region. The plane wave-based pseudopotential methods, which are commonly employed in electronic structure computations, are briefly presented in the following subsections.

2.5.1 Norm-Conserving Pseudopotentials (NCPP)

While creating the pseudo potentials, the main objectives are to (i) keep it as soft as possible, resulting in the use of fewer planewaves; (ii) keep it as transferable as possible, so that a pseudopotential for a given element can easily be applied in various situations; and (iii) generate a pseudo-charge density that mimics the valance charge density as accurately as possible.[157]. The earliest computationally tractable pseudopotentials were norm conserving pseudopotentials (NCPP). The NCPPs are designed so that the pseudo-wavefunctions (and potentials) resemble the genuine valance wavefunctions (and potentials) outside of a cut-off radius, which corresponds to the core radius r_c. Within the cut-off radius, the pseudo-wavefunctions and the actual wavefunctions differ but are forced to conserve the norm, i.e.

$$\int_0^{r_c} \varphi^{PS*}(r)\varphi^{PS}(r)r^2\,dr = \int_0^{r_c} \varphi^{AE*}(r)\varphi^{AE}(r)r^2\,dr \tag{2.18}$$

φ^{PS} and φ^{AE} represent the pseudo and all electron wavefunctions, respectively. This technique is effective for *sp* elements, but transition metals and rare earth elements with localised d and f states necessitate a very large plane wave basis set, making NCPP difficult.

2.5.2 Ultrasoft Pseudopotentials (USPP)

The pseudo-wavefunctions produced by the NCPP technique are limited to matching all electron wavefunctions outside of r_c. The norm-conservation inside r_c requires a huge plane wave basis set, which contradicts the criteria for fast convergence in planewave-based calculations. Vanderbilt et al. [158, 159, 160] proposed a new and radical approach by allowing the pseudo wavefunctions to be as soft as possible inside r_c, while the NCPP approach was maintained outside r_c. This approach significantly reduces the number of plane waves required to construct the basis set, but at the cost of introducing some complications. Three inherent complications in the construction of ultasoft pseudopotential are: (i) because the wavefunctions are not necessarily normalised, they present a significant overlapping element in the secular equation, (ii) the pseudo charge density can't just be calculated using $\sum \varphi^*\varphi$ as done in NCPP method. Nonetheless, USPPs have demonstrated their dependability in condensed matter calculations and have been employed in large-scale computations over the years. Most significantly, the cost of creating these pseudopotentials is low in comparison to the cost of the computations in which they are employed.

2.5.3 Projector Augmented Wave (PAW) Method

While the pseudopotential approach has some advantages, including reduced memory utilisation and processing needs, it also has some substantial downsides. One significant concern is that this approach compromises the true all-electron wavefunction near atomic nuclei by artificially smoothening the wavefunctions in the core region. This smoothening can cause errors in computed characteristics that rely strongly on the electronic structure near the nucleus, influencing quantities like hyperfine interactions, electric field gradients, and core-level spectra.The pseudopotential technique's dependence on numerous modifiable parameters throughout the generating process is another drawback. This means a pseudopotential customised for one specific enviroment may not be produce trustworthy in a different one, generating real questions over its transferability and consistency across multiple systems.

In 1994, Peter Blöchl proposed the Projector Augmented Wave (PAW) approach to solve these hurdles [161]. This unique method effectively blends pseudopotential and all-electron approaches. The PAW formalism employs a linear transformation to reconstruct the whole all-electron wavefunction from a simpler pseudo-wavefunction. It accomplishes this by separating the wavefunction into two different regions: a partial wave expansion within atom-centered augmentation spheres, which accurately represent both core and valence states, and smooth envelope functions in the interstitial space. A linear transformation connects these components at the spheres' boundaries.

Therefore, the PAW approach is particularly useful for determining desired material properties since it combines the accuracy of all-electron computations with the computing efficiency of pseudopotentials. We present a quick synopsis of the PAW formalism in this section.

The PAW approach represents the all-electron wavefunction $|\psi_n\rangle$ as a smooth auxiliary wavefunction $\left|\tilde{\psi}_n\right\rangle$ following a linear transformation with the operator T:

$$|\psi_n\rangle = T\left|\tilde{\psi}_n\right\rangle \tag{2.19}$$

An augmentation sphere is built around each atom so that $|\mathbf{r} - \mathbf{R}^a| < r_c^a$, where r_c^a is the cut-off radius, a is the atomic index, and $\mathbf{R}^a$ represents the position of atom a. In this approach, the linear transformation operator T can be represented as:

$$T = 1 + \sum_a T^a \tag{2.20}$$

where T^a only acts in the augmentation sphere. Inside this region, the smooth wavefunction is represented as a linear combination of smooth partial waves denoted by $\left|\tilde{\phi}_i^a\right\rangle$:

$$\left|\tilde{\psi}_n\right\rangle = \sum_{ia} c_{ni}^a \left|\tilde{\phi}_i^a\right\rangle \tag{2.21}$$

The all-electron wavefunction in the same way can be written as:

$$|\psi_n\rangle = \sum_{ia} c_{ni}^a |\phi_i^a\rangle \tag{2.22}$$

The smooth partial wave, upon application of the linear transformation operator, takes the form:

$$|\phi_i^a\rangle = T\left|\tilde{\phi}_i^a\right\rangle = (1 + T^a)\left|\tilde{\phi}_i^a\right\rangle \tag{2.23}$$

As T^a only acts inside the augmented sphere, at $r > r_c^a$

$$|\phi_i^a\rangle = \left|\tilde{\phi}_i^a\right\rangle \tag{2.24}$$

Now the true wavefunction is expressed as :

$$|\psi_n\rangle = \left|\tilde{\psi}_n\right\rangle - \sum_{ia} c_{ni}^a \left|\tilde{\phi}_i^a\right\rangle + \sum_{ia} c_{ni}^a |\phi_i^a\rangle \tag{2.25}$$

As the transformation operator T is linear, the coefficient c_{ni}^a of the smooth partial wave must be a scalar product. Thus,

$$c_{ni}^a = \left\langle \tilde{p}_i^a \middle| \tilde{\psi}_n \right\rangle \equiv \mathcal{P}_{ni}^a \tag{2.26}$$

where $\tilde{p}_i^a$ are some smooth projector functions. So the transformation operator T becomes

$$T = \sum_a \sum_i \left(|\phi_i^a\rangle - \left|\tilde{\phi}_i^a\right\rangle\right) \langle \tilde{p}_i^a| \tag{2.27}$$

After the transformation in Eq. 2.27, the Kohn-Sham wavefunction is

$$|\psi_n\rangle = \left|\tilde{\psi}_n\right\rangle + \sum_a \sum_i \left(|\phi_i^a\rangle - \left|\tilde{\phi}_i^a\right\rangle\right) \left\langle \tilde{p}_i^a \middle| \tilde{\psi}_n \right\rangle$$
$$= \left|\tilde{\psi}_n\right\rangle + \sum_a \left(\sum_i \left(|\phi_i^a\rangle \left\langle \tilde{p}_i^a \middle| \tilde{\psi}_n \right\rangle - \left|\tilde{\phi}_i^a\right\rangle \left\langle \tilde{p}_i^a \middle| \tilde{\psi}_n \right\rangle \right) \right) \tag{2.28}$$

From Eq. 2.28, the wavefunction can be broken down into the sum of the smooth wavefunctions (smooth everywhere) and the sum over the subtraction of the one-centered pseudo portion and one-centered all electron contribution. By replacing Equation 2.28 into Equation 2.19, one may get a more succinct formulation for various quantities in the PAW technique[162, 163, 164, 165]. Throughout the thesis, I have used PAW approach implemented in Vienna Ab Initio Simulation Package (VASP) [166], for computation of ground state properties and electronic structures of the systems considered.

2.6 Quantum Transport Theory

2.6.1 Quantum Transport System

Quantum transport theory outlines how electrons are transported via nanoscale structures. This thesis focusses on understanding electronic transport in nanodevices where determining the transport regime for a system an issue is crucial before starting computations [167]. Transport regimes have two distinct length scales: (a) Momentum relaxation length (L_m) and (b) Phase relaxation length (L_ϕ). The momentum relaxation length (L_m) measures the average distance an electron travels before losing its original momentum. The phase relaxation length (L_ϕ) is the average distance an electron can travel before its initial phase is eliminated. When the dimension of the conducting nanoscale device (L) is substantially longer than both L_m and L_ϕ, the conductance that depends on the device's length in accordance with the traditional Ohm's law, resulting in what is known as the 'Ohmic regime'. Advances in nanoscale device technologies at the single-molecule level have broadened electronic transport theories. To incorporate the quantum nature of electrons in nanoscale devices, in reference to these characteristic length scales, electron transport can be divided into three separate regimes. :

2.6.1.1 Ballistic Transport Regime ($L << L_m, L_\phi$):

In the ballistic transport phase, electrons go from one lead to another without encountering considerable scattering. This implies that momentum and phase relaxation are insignificant during the transfer process. Resistance is mostly caused by electron backscattering in contact areas. Ballistic conduction is most typically seen in quasi-one-dimensional (quasi-1D) structures like metallic nanowires and carbon nanotubes. In these architectures, conductance is quantised: $G_0 = \frac{2e^2}{h}$, where e represents the electron charge, and h represents Planck's constant. The conduction in this system remain independent of device length.

2.6.1.2 Elastic and Coherent Transport Regime ($L < L_m, L_\phi$):

Electrons in this domain can undergo elastic scattering within the device, preserving their energy and phase but changing their momentum. Elastic scattering reduces the

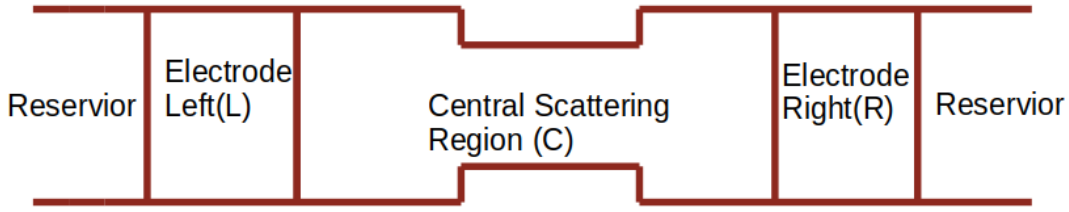

Figure 2.2: Schematic diagram of a nanoscale device with ballistic left/right electrodes connected to the central scattering region and reservoir

transmission function compared to ballistics, yet the electron wavefunction stays coherent during transport.

2.6.1.3 Inelastic and Incoherent Transport Regime ($L > L_m, L_\phi$):

In this domain, the device length L surpasses the momentum and phase relaxation lengths, causing considerable inelastic scattering with other electrons or phonons. These interactions alter electron momentum and phase, leading to a loss of phase coherence. Incoherent transport occurs during inelastic scattering and phase-breaking events.

2.6.2 Non-Equilibrium Green's Function (NEGF) Formalism

The NEGF technique [127] is a generalised approach of calculating the electron transport properties that is applicable for all three transport regimes. This section elaborates explains the NEGF formalism for evaluating current-voltage curves in nanoscale devices. The schematic of a nanoscale transport device is divided into three components as shown in Figure 2.2. The system is made up of a centre scattering zone(C) with semi-infinite left (L) and right (R) electrodes. The Hamiltonian (H) of the system can be represented as:

$$H = \begin{pmatrix} H_L & \tau_L & 0 \\ \tau_L^\dagger & H_C & \tau_R^\dagger \\ 0 & \tau_R & H_R \end{pmatrix} \tag{2.29}$$

H_C , $H_{L/R}$ denotes the Hamiltonian matrices of the central zone and L/R electrodes, respectively. $\tau_{L/R}$ indicates the matrix elements representing interactions among the L/R electrodes and the central area. We assume that there is no close connection (tunnelling) between the L/R electrodes. The retarded Green's function (G) corresponding to the Hamiltonian is given as

$$[E^+S - H]G = I \tag{2.30}$$

S corresponds to an overlap matrix,$E^+ = \lim_{\eta\to 0^+} E + i\eta$ and I the unit matrix. G can be conveniently represented as:

$$G = \begin{pmatrix} G_L & G_{CL} & 0 \\ G_{LC} & G_C & G_{RR} \\ 0 & G_{CR} & G_R \end{pmatrix} \tag{2.31}$$

To evaluate G, it's easier to separate the system into different parts since the process isn't taking place inside the electrode. Therefore, the central scattering zone is only connected to the electrode's surface. The interaction term ($\tau_{L/R}$) is expected to be significantly small compared to the diagonal elements in Equation 2.29. Putting 2.30 and 2.31 together, we get

$$\begin{pmatrix} E^+S_L - H_L & -\tau_L & 0 \\ -\tau_L^\dagger & E^+S_C - H_C & -\tau_R^\dagger \\ 0 & -\tau_R & E^+S_R - H_R \end{pmatrix} \begin{pmatrix} G_L & G_{CL} & 0 \\ G_{LC} & G_C & G_{RC} \\ 0 & G_{CR} & G_R \end{pmatrix} = \begin{pmatrix} I & 0 & 0 \\ 0 & I & 0 \\ 0 & 0 & I \end{pmatrix} = I \tag{2.32}$$

Therefore,

$$G = \begin{pmatrix} g_L\left(1 + \tau_L G_{LR}\right) & g_L\tau_L G_C & 0 \\ G_{LR} & 0 & G_{RC} \\ g_R\tau_R G_C & 0 & g_R\left(1 + \tau_R G_{RC}\right) \end{pmatrix} \tag{2.33}$$

here,$g_{L/R} = \frac{1}{(E^+S_L - H_C)} = (E^+S_L - H_C)^{-1}$ is the surface Green's function of the L/R electrode uncoupled to the central region.The final expression for retarded G of the central region can be expressed as,

$$G_C = \left[E^+S_c - H_C - \Sigma_L(E) - \Sigma_R(E)\right]^{-1} \tag{2.34}$$

where $\Sigma_L(E) = \tau_L^\dagger g_L \tau_L$ and $\Sigma_R(E) = \tau_R^\dagger g_R \tau_R$ are called the 'self-energies'. From, equation 2.34, we find that the infinite dimensional Hamiltonian is reduced to the dimension of the central region, where the self-energies,$\Sigma_{L/R(E)}$, includes all information on the semi-infinite properties of the electrodes. The central region interacts only with the surface region of the L/R electrodes [127]. As a result, we can solely focus on the G matrix of the central region and effective Hamiltonian (H_{eff}) can be described as

$$H_{eff} = H_C + \big(\Sigma_L(E) + \Sigma_R(E)\big) \tag{2.35}$$

2.6.3 The Schrödinger Equation

From equation 2.30 and because of self-adjoint Hamiltonian, we write retarded and advanced wave functions for the inhomogeneous Schrödinger equation as:

$$|\psi\rangle^R = -G\,|\nu\rangle \tag{2.36}$$

$$|\psi\rangle^A = -G^\dagger\,|\nu\rangle \tag{2.37}$$

Thus, we can describe the Schrödinger equation as

$$[E^+ - H]\,|\psi\rangle = -\,|\nu\rangle \tag{2.38}$$

Here, the difference $|\psi\rangle^R - |\psi\rangle^A$ is the solution to the homogeneous Schrödinger equation. Therefore, for any vector ($|\nu\rangle$), the vector representing wave function can be found as,

$$|\psi\rangle = A\,|\nu\rangle \tag{2.39}$$

where,

$$A = i(G - G^\dagger) = -2Im(G) \tag{2.40}$$

A is the spectral function, which used to solve the homogeneous Schrö dinger equation and the G can be described in terms of the eigen basis:

$$G = \sum_k \frac{|\Psi_k\rangle\langle\Psi_k|}{E + i\eta - E'_k} \tag{2.41}$$

After substituting the equation 2.41 into the equation 2.40, we obtain

$A(E) = i\sum_k |\Psi_k\rangle\langle\Psi_k| \left(\frac{1}{E+i\eta-E'_k} - \frac{1}{E-i\eta-E'_k}\right)$

$$A(E) = \sum_k |\Psi_k\rangle\langle\Psi_k| \left(\frac{2\eta}{(E - E'_k)^2 + \eta^2}\right) \tag{2.42}$$

Now let us assume η to be zero, then

$$A(E) = 2\pi \sum_k \delta(E - E'_k)\,|\psi\rangle_k\,\langle\Psi_k| \tag{2.43}$$

By using the spectral function (equation 2.40), we get,

$$A_C(E) = i(G_C - G_C^\dagger) = iG_C(G_C^{\dagger^{-1}} - G_C^{-1})G_C^\dagger \tag{2.44}$$

Further expanding, we get the following identity

$$A_C(E) = i\,G_C\big(E - H_C - \Sigma_L^\dagger(E) - \Sigma_R^\dagger(E) - E + H_C + \Sigma_L(E) + \Sigma_R(E)\big)G_C^\dagger, \tag{2.45}$$

$$A_C(E) = i\,G_C\big(\Gamma_L(E) + \Gamma_R(E)\big)\,G_C^\dagger = A_L(E) + A_R(E) \tag{2.46}$$

2.6.4 Solution to Electronic Transport Problem

Here, we will explain the transport problems through analysing the L to R transport. With the conventional screened approximate technique, the Schrödinger equation can be recast as,

$$\begin{pmatrix} H_L & \tau_L & 0 \\ \tau_L^\dagger & H_C & \tau_R^\dagger \\ 0 & \tau_R & H_R \end{pmatrix} \begin{pmatrix} |\Psi_L\rangle \\ |\Psi_C\rangle \\ |\Psi_R\rangle \end{pmatrix} = E \begin{pmatrix} |\Psi_L\rangle \\ |\Psi_C\rangle \\ |\Psi_R\rangle \end{pmatrix} = E|\Psi\rangle \tag{2.47}$$

where $|\psi_C>$, $|\psi_L>$, and $|\psi_R>$ represent the incoming wave function in each region. We first consider the solitary L electrode, which reflects incoming waves at its end. This yields the interaction term for the L electrode ($\tau_L = 0$). If $|\nu\rangle$ is the solution wave function, then,

$$\begin{pmatrix} H_L & 0 & 0 \\ 0 & H_C & \tau_R^\dagger \\ 0 & \tau_R & H_R \end{pmatrix} \begin{pmatrix} |\nu\rangle \\ |0\rangle \\ |0\rangle \end{pmatrix} = E' \begin{pmatrix} |\nu\rangle \\ |0\rangle \\ |0\rangle \end{pmatrix} = E'|\nu\rangle \tag{2.48}$$

After connecting the L electrode to the central region, we can evaluate the wave function of the whole system. The simple ansatz $|\psi\rangle + |\nu\rangle$ is placed into the Schrödinger equation as shown below,

$$\begin{pmatrix} H_L & \tau_L & 0 \\ \tau_L^\dagger & H_C & \tau_R^\dagger \\ 0 & \tau_R & H_R \end{pmatrix} \begin{pmatrix} |\Psi_L + \nu\rangle \\ |\Psi_C\rangle \\ |\Psi_R\rangle \end{pmatrix} = E \begin{pmatrix} |\Psi_L + \nu\rangle \\ |\Psi_C\rangle \\ |\Psi_R\rangle \end{pmatrix} \tag{2.49}$$

From equation 2.48 and 2.49,

$$\begin{pmatrix} H_L & \tau_L & 0 \\ \tau_L^\dagger & H_C & \tau_R^\dagger \\ 0 & \tau_R & H_R \end{pmatrix} |\Psi\rangle + \begin{pmatrix} 0 & \tau_L & 0 \\ \tau_L^\dagger & 0 & 0 \\ 0 & 0 & 0 \end{pmatrix} \begin{pmatrix} |\nu\rangle \\ |0\rangle \\ |0\rangle \end{pmatrix} = E|\Psi\rangle + (E - E') \begin{pmatrix} |\nu\rangle \\ |0\rangle \\ |0\rangle \end{pmatrix} \tag{2.50}$$

The form of Schrödinger equation is the following:

$$\begin{pmatrix} H_L & \tau_L & 0 \\ \tau_L^\dagger & H_C & \tau_R^\dagger \\ 0 & \tau_R & H_R \end{pmatrix} |\Psi\rangle = E|\Psi\rangle - \begin{pmatrix} (E - E')|\nu\rangle \\ \tau_L^\dagger|\nu\rangle \\ |0\rangle \end{pmatrix} \tag{2.51}$$

By solving equations 2.33 and 2.51 we obtain the wave functions for the electrodes and central region due to incoming wave as,

$$|\Psi_L\rangle = g_L\tau_L G_C\tau_L^\dagger + 1|\nu\rangle|\Psi_C\rangle = G_C\tau_L^\dagger + 1|\nu\rangle|\Psi_R\rangle = g_R\tau_R G_C\tau_L^\dagger + 1|\nu\rangle \tag{2.52}$$

Each one of these equation has some physical significance. Therefore, once we get the incoming solution for the electrode, we can obtain the total solution. Furthermore, after knowing the electron population in the contact regions, we can fill the system's different transport states.

2.6.5 The Charge Density

The charge density (ρ) can be described as,

$$\rho = e\big(\Sigma_k f(E_k, \mu)|\psi_k\rangle\langle\psi_k|\big) \tag{2.53}$$

f is the occupation of the states at energy E and with chemical potential μ of the electrode. The induced charge density (ρ_L) from the L electrode is given as,

$$\rho_L = e\big(\Sigma_k f(E_k, \mu_L)\, G_C\tau_L^\dagger\, |\nu_k\rangle\langle\nu_k|\, \tau_L G_C^\dagger\big) \tag{2.54}$$

In terms of δ-functions,

$$\rho_L = e\int dE\big(\Sigma_k f(E, \mu_L)\, G_C\tau_L^\dagger\, |\nu_k\rangle\, \delta(E - E_k)\, \langle\nu_k|\, \tau_L G_C^\dagger\big) \tag{2.55}$$

In equation 2.55, we can identify the spectral function from equation 2.43 for the L electrode as

$$a_L = 2\pi\big(\Sigma_k\, |\nu\rangle\, \delta(E - E_k')\langle\nu|\big) \tag{2.56}$$

Using the identity (Equation 2.46)

$$\tau_L^\dagger a_L\tau_L = i\tau_L^\dagger(g_L - g_L^\dagger)\tau_L = i(\Sigma_L - \Sigma_L^\dagger) = \Gamma_L \tag{2.57}$$

By substituting equations 2.56 and 2.57 into equation 2.55, we get,

$$\rho_L = \frac{e}{2\pi} \int dE\, f(E, \mu_L)\, G_C \Gamma_L G_C^\dagger \tag{2.58}$$

The total charge density is the sum over the L and R electrodes:

$$\rho = \frac{e}{2\pi} \int dE \sum_{i=L,R} f(E, \mu_i)\, G_C \Gamma_i G_C^\dagger \tag{2.59}$$

2.6.6 Calculation of electric current I

The flow of electric current through nanoscale devices depends on the difference in the chemical potentials (μ) of the electrodes/leads. In the steady state, the current probability does not change over time. Therefore, the probability of finding an electron in the system is conserved, as derived in equation 2.61:

$$\frac{\partial \langle \Psi_C | \Psi_C \rangle}{\partial t} = 0 \tag{2.60}$$

$$\frac{\partial \langle \Psi_C | \Psi_C \rangle}{\partial t} = \frac{\partial |\Psi_C\rangle}{\partial t} \langle \Psi_C| + |\Psi_C\rangle \frac{\partial \langle \Psi_C|}{\partial t} = 0 \tag{2.61}$$

Under experimental conditions, electrons flow continuously from one electrode to another. Hence, we assume that the electrodes are large enough to maintain a continuous electron flow. The time-dependent Schrödinger equation is:

$$i\hbar \frac{\partial |\Psi\rangle}{\partial t} = H|\Psi\rangle \tag{2.62}$$

Using equations 2.47, we obtain

$$i\hbar \frac{\partial |\Psi_C\rangle}{\partial t} = \tau_L^\dagger |\Psi_L\rangle + H_C |\Psi_C\rangle + \tau_R^\dagger |\Psi_R\rangle \tag{2.63}$$

After inserting equation 2.63 into 2.62, we obtain

$$i\hbar \big[- (\langle \Psi_L | \tau_L | \Psi_C \rangle - \langle \Psi_C | \tau_L^\dagger | \Psi_L \rangle) + (\langle \Psi_C | \tau_R^\dagger | \Psi_R \rangle - \langle \Psi_R | \tau_R | \Psi_C \rangle) \big] = 0 \tag{2.64}$$

In the above equation, the first term represents the incoming probability current from electrode L. The second term corresponds to the same but for electrode R. Now, we can write the electric current from an arbitrary contact j into the central scattering region as the charge times the probability current:

$$I_j = \frac{ie}{\hbar} \Big(\langle \Psi_C | \tau_j | \Psi_j \rangle - \langle \Psi_j | \tau_j^\dagger | \Psi_C \rangle \Big) \tag{2.65}$$

where j represents the L or R electrode, and I_j stands for the electric current from the j-th contact to the central region.

Further, to evaluate the electric current, we insert the wave functions of the contacts ($|\Psi_j\rangle$) and the central region ($|\Psi_C\rangle$) from equation 2.52 into equation 2.65. Therefore, the current through the system due to an incoming wave is given as

$$I_{\nu\to R} = \frac{ie}{\hbar}\left[\langle\nu|\tau_L G_C^\dagger \tau_R^\dagger g_R \tau_R G_C \tau_L^\dagger|\nu\rangle - \langle\nu|\tau_L G_C^\dagger \tau_R^\dagger g_R^\dagger \tau_R G_C \tau_L^\dagger|\nu\rangle\right] \tag{2.66}$$

$$I_{\nu\to R} = \frac{ie}{\hbar}\left[\langle\nu|\tau_L G_C^\dagger \tau_R^\dagger (g_R - g_R^\dagger) \tau_R G_C \tau_L^\dagger|\nu\rangle\right] \tag{2.67}$$

$$I_{\nu\to R} = \frac{e}{\hbar}\langle\nu|\tau_L G_C^\dagger \tau_R^\dagger \Gamma_R G_C \tau_L^\dagger|\nu\rangle \tag{2.68}$$

To obtain the total current through the device, we sum over the incoming states $|\nu_n\rangle$, (where n is a quantum number) and integrate over the energy E. Thus, the total current through the device is

$$I_{L\to R} = \frac{2e}{\hbar}\int_{-\infty}^{+\infty} dE \sum_n \mathrm{DOS}(E)\langle\nu_n|\tau_L G_C^\dagger \Gamma_R G_C \tau_L^\dagger|\nu_n\rangle \tag{2.69}$$

$$I_{L\to R} = \frac{2e}{\hbar}\int_{-\infty}^{+\infty} dE \sum_{m,n} \mathrm{DOS}(E)\langle\nu_n|\tau_L|m\rangle\langle m|G_C^\dagger \Gamma_R G_C \tau_L^\dagger|\nu_n\rangle \tag{2.70}$$

$$I_{L\to R} = \frac{2e}{\hbar}\int_{-\infty}^{+\infty} dE \sum_m \langle m|G_C^\dagger \Gamma_R G_C \tau_L^\dagger \left(\sum_n \mathrm{DOS}(E)|\nu_n\rangle\langle\nu_n|\right)\tau_L|m\rangle \tag{2.71}$$

$$I_{L\to R} = \frac{2e}{\hbar}\int_{-\infty}^{+\infty} dE \sum_m \langle m|G_C^\dagger \Gamma_R G_C \tau_L^\dagger A_L \tau_L|m\rangle \tag{2.72}$$

$$I_{L\to R} = \frac{e}{\pi\hbar}\int_{-\infty}^{+\infty} dE\, \mathrm{Tr}\left(G_C^\dagger \Gamma_R G_C \Gamma_L\right) \tag{2.73}$$

Here, DOS(E) represents the densities of states. A spin factor of 2 is also included. When the reservoirs are connected to the electrodes, the electrode states are filled according to the Fermi distribution. Thus, the total current through the device connected to two electrodes at μ_L and μ_R is

$$I_{L\to R} = \frac{e}{\pi\hbar}\int_{-\infty}^{+\infty} dE\, \mathrm{Tr}\left(G_C^\dagger \Gamma_R G_C \Gamma_L\right)\left[f(E-\mu_L) - f(E-\mu_R)\right] \tag{2.74}$$

$$= \frac{2e}{h}\int_{-\infty}^{+\infty} T(E)\left[f(E-\mu_L) - f(E-\mu_R)\right] \tag{2.75}$$

where, $T(E) = \mathrm{Tr}\left(G_C^{\dagger}\Gamma_R G_C \Gamma_L\right)$ is obtained from Landauer formalism[168, 169, 170].

In this thesis, electrical transport via the VOC-nanosheet complexes is examined using the NEGF approach in conjunction with DFT as implemented in the TRANSIESTA[171] package. The electrical current through the device with two metal electrodes under a finite bias voltage V_b is calculated as:

$$I(V_b) = \frac{2e}{h}\int T\left(E, V_b\right)\left(f_L\left(E-\mu_L\right) - f_R\left(E-\mu_R\right)\right) \tag{2.76}$$

e represents the electronic charge, h is Planck's constant,$T(E, V_b)$ the electronic transmission function calculated using Landauer formalism, $f_L(E-\mu_L)$ and $f_R(E-\mu_R)$ are the Fermi functions in the left (L) and right (R) electrodes, respectively. μ_L and μ_R are the chemical potentials of the left and right electrodes, respectively. The bias energy window is between $\mu_L = E_f - eV_b/2$ and $\mu_R = E_f + eV_b/2$; E_f, the average Fermi energy, is given by $\left(\mu_L + \mu_R\right)/2$.

2.7 Computation of physical quantities

In the following we briefly present the key quantities computed to understand the VOC-nanosensor interactions.

2.7.1 Adsorbtion Energy

Adsorption energy is a fundamental parameter governing the interaction between gas molecules and the sensing surface. It plays a decisive role in determining the sensitivity, selectivity, and response characteristics of a gas sensor. The adsorption energy ((E_{ad})) is calculated using the relation

$$E_{ad} = [E_{nanomaterial+VOC} - E_{nanomaterial} - E_{VOC}] \tag{2.77}$$

$E_{nanomaterial+VOC}$, $E_{nanomaterial}$ and E_{VOC} are the total energies of nanomaterial-VOC complex, isolated nanomaterial and isolated VOC molecule, respectively. A negative E_{ad} value indicates an exothermic and thermodynamically favorable adsorption process. Generally, weaker interactions (-0.05 to -0.5 eV) correspond to physisorption, dominated by van der Waals forces, enable rapid desorption and fast recovery times. Stronger interactions (-0.5 to -2.5 eV) indicate chemisorption, resulting in enhanced charge transfer and improved sensitivity, although sometimes at the cost of slower recovery. Adsorption energies that are excessively high ($<$ -3 eV) may trap gas molecules on the surface and degrade sensor reversibility. Therefore, an optimal adsorption energy range of approximately -0.3 to -1.0 eV is often considered desirable for practical gas sensing, as it provides a balance between strong enough interaction for high sensitivity and sufficiently weak binding to maintain good recoverability. This parameter, therefore, serves as a reliable indicator for evaluating and comparing the gas-sensing performance of different materials.

2.7.2 Work-function

In order to assess the utility of a sensing material to be used as a work function based sensor, the work function of the sensor is to be calculated before and after adsorption of

a VOC. The work function is defined as

$$\phi = V(\infty) - E_F \tag{2.78}$$

$V(\infty), E_F$ are the electrostatic potential to bring an electron from vaccum to the surface and the Fermi level, respectively. In order to evaluate $V(\infty)$, the planar-averaged electrostatic potential along the surface normal (z) is calculated using

$$\overline{V}(z) = \frac{1}{A} \iint_{\text{cell}} V(x, y, z)\, dx\, dy \tag{2.79}$$

A is the surface area of the 2D slab. $\overline{V}(z)$ at a large distance from the surface where it is essentially flat is considered as $V(\infty)$, and subsequently used to determine ϕ.

2.7.3 Total Charge and Charge Density Difference

For a chemiresistive sensor, in paticular, charge transfer between VOC and 2D material is an useful indicator. An accurate calculation of total charge associated with each constituent is therefore necessary. In this thesis, we have used Bader formalism to compute the total charges[172]. In Bader formalism, the space is divided into regions of zero-flux surfaces in the gradient of electron densities, that is surfaces defined by $\vec{\nabla}\rho(\vec{r}).\hat{n}(\vec{r}) = 0$; $\rho(\vec{r}), \hat{n}(\vec{r})$ are the charIge density and the unit vector normal to the zero-flux surface, respectively. In this construction, atoms are separated by regions defined through such surfaces. Once $\rho(\vec{r})$ in the volume associated with such a surface is obtained, the atomic charge q is obtained as $q = \int_V \rho(\vec{r})\, d\vec{r}$; V the volume associated with the zero-flux surface defining the atom in space.The charge transfer Q between the 2D sensor material and a VOC molecule adsorbed on it, is obtained as,

$$Q = \sum_i q_i^{2D} - \sum_j q_j^{VOC} \tag{2.80}$$

where, q_i^{2D} is the Bader atomic charge associated with constituent i of the 2D sensor, q_j^{VOC} is the Bader atomic charge associated with constituent j of the VOC. Thus,a negative charge transfer Q indicates a charge transfer from the molecule to the monolayer sheet, while a positive Q indicates that the molecule withdraws electrons from the sheet. To understand the details of charge transfer between VOC molecules and 2D system, isosurface plots of charge density differential $\delta\rho$ are also presented.

$$\delta\rho = \rho_{nanomaterial+VOC} - \rho_{nanomaterial} - \rho_{VOC} \tag{2.81}$$

where , $\rho_{nanomaterial+VOC}$, $\rho_{nanomaterial}$ and ρ_{VOC} are the total charge density of the VOC-adsorbed nanomaterial, pristine nanomaterial and isolated molecule, respectively.

2.7.4 Optical Properties

In optical sensors, absorption coefficient is one of the decisive quantities as it implies how strongly light is absorbed by the sensor material when an adsorbate interacts with it. The sensitivity and selectivity of a sensor working on optical excitation, therefore, depends on

the absorption coefficient. This, in turn, directly depends upon $\epsilon^{(2)}$, the imaginary part of the dielectric constant ϵ. $\epsilon^{(2)}$ is obtained by Kubo formalism [173]:

$$\varepsilon^{(2)}(\omega) = \frac{4\pi^2 e^2}{\Omega} \lim_{q\to 0} \frac{1}{q^2} \sum_{c,v,\mathbf{k}} 2\omega_{\mathbf{k}}\, \delta(E_{c,\mathbf{k}} - E_{v,\mathbf{k}} - \hbar\omega)\, \langle u_{c,\mathbf{k+q}} \mid u_{v,\mathbf{k}} \rangle \langle u_{v,\mathbf{k}} \mid u_{c,\mathbf{k+q}} \rangle \quad (2.82)$$

e is the electronic charge, Ω is the volume of the supercell, c and v denote the conduction and valance band states, respectively, ω is the frequency of the incident light. u_{ck} is the cell-periodic part of the orbitals at the point $\mathbf{k}$. The excitation is represented in terms of Dirac δ. The absorption coefficient can be obtained using $\epsilon^{(2)}(\omega)$ and it's real counterpart

$$I(\omega) = \sqrt{2}(\omega)[\sqrt{\epsilon^{(1)}(\omega)^2 + \epsilon^{(2)}(\omega)^2} - \epsilon^{(1)}(\omega)]^{1/2} \quad (2.83)$$

$\epsilon^{(1)}(\omega)$ and $\epsilon^{(2)}(\omega)$ are real and imaginary part of the dielectric function, respectively. These are calculated using the Kramers-Kronig transformation [174]. Further, the reflectance can be computed as,

$$R\,(\omega) = |\frac{\sqrt{\epsilon\,(\omega)} - 1}{\sqrt{\epsilon\,(\omega)} + 1}|^2 \quad (2.84)$$

2.7.5 Response/Recovery time

The re-usability of a sensor is dependent on how fast the desorption of a gas molecule takes place. This is quantified by sensor recovery time. Using Transition state theory and Arrhenius equation [175, 176], the expression for recovery time is given as

$$\tau = \nu_0^{-1} \exp(-E_{\mathrm{ad}}/k_B T), \quad (2.85)$$

ν_0 is the operating frequency, T the temperature, and k_B the Boltzmann constant. In order for a gas sensor to be reusable $\tau \lesssim 10^5$s[177].

Chapter 3

Investigations into the efficiencies of Graphene based gas sensors towards food VOCs

In this chapter we explore the sensing efficiencies of Graphene and Graphene derivatives towards sensing VOCs emitted from standard food products. Graphene, the prototype 2D material has been thoroughly investigated for use in biosensing and gas sensing applications [178, 179, 180, 181, 182, 183]. Graphene based nanomaterials have also been exploited to detect and differentiate various VOCs for breath analysis where they act as bio-markers for several terminal diseases [184] and to remove pollutants like NO_2 and SO_2 from atmosphere [185]. Nevertheless, the pristine graphene-based sensors are not very sensitive or selective to different VOCs[184]. One option to overcome this limitation is through its functionalisation with organic compounds, molecules, conducting polymers, introduction of dopants or through defect engineering [186, 187, 188, 189, 190]. The results obtained have been promising.

Graphene based nanocomposites have recently started to be used in food industry for variety of purposes associated with food safety[191]. However, there is limited work on exploration of Graphene based nanomaterials as sensors to detect stages of food degradation by detection of VOCs. Only recently, chemiresistive responses of reduced Graphene oxide (r-GO) and it's nanocomposites with polythiopene have been experimentally measured upon exposure to flows of VOCs[192]. Methanol (CH_3OH), Ethanol (C_2H_5OH), Acetone ($(CH_3)_2OC$), Methyl acetate ($(CH_3)_2OCO$), Dimethylsulfide ($(CH_3)_2S$) and Toluene ($C_6H_5CH_3$) vapours were tested since they are the prominent VOCs released from meat [193], fruits[194] and vegetables[195], making them markers of food quality. The sensitivity against a paticular VOC in this experiment was obtained from the resistance relative amplitude $A_r = \frac{R-R_0}{R_0}$, where $R(R_0)$ is the resistance of the sensor in presence of a particular gas(N_2 gas) vapour.The experimental results suggest that r-GO has poor selectivity that is it is unable to distinguish between the six VOCs.

Motivated by this result, in this chapter we have explored the changes in electronic structure and transport properties of pristine Graphene, Graphene oxide (GO) and reduced Graphene oxide(r-GO) upon adsorption of the above mentioned six VOCs released by standard food materials. Comparative study of sensing capabilities of these three compounds when used as both chemiresistive sensor and work function based sensor is

The contents of this chapter are published in 2025, THE EUROPEAN PHYSICAL JOURNAL B,(2025)98:208, DOI: 10.1140/epjb/s10051-025-01054-6.

being carried out in detail. Contrary to the experimental result, we find that rGO can distinguish between at least four VOCs when used as a chemiresistive sensor. We also find that Graphene, as either type of sensor shows poor selectivity while GO can distinguish several VOCs when used as a work function based sensor.

3.1 Methodology

3.1.1 Modeling GO and r-GO

While Graphene structure is made up of flat hexagonal network of sp^2 bonded Carbons (Figure 3.1(a)), the structure of Graphene oxide (GO) is made up of a carbon network with a large fraction (up to 67 %) of them sp^3 hybridized and covalently bonded with oxygen in the form of epoxy (-O-) and hydroxyl (-OH) groups[196, 197, 198, 199, 200].Based on a number of experimental and theoretical investigations[201, 202, 203, 204],several model structures of GO have been proposed since its discovery[205]. However, in a recent work[206], systematic first-principles calculations determined the energy diagram of GO as a function of oxygen and hydrogen chemical potentials and established that thermodynamically stable GOs can exist only under stringent growth conditions in the form of hydroxyl, epoxy or a mixture of these phases and that there is no mixed phase involving sp^2 carbons. It was also shown that these groups prefer to cluster along armchair direction and form one-dimensional chain configurations on the basal plane. The most stable GO structures, thus obtained, are later found to be the ones where -OH to -O ratio is 2:1[207]. A coverage percentage for such a structure can be defined as

$$R = 100\% N_{sp^3-C}/N_C \tag{3.1}$$

where N_{sp^3-C} is the number of sp^3 C atoms bonded to -OH and -O, N_C the total number of Carbon atoms. In this work, we have used such a stable structure for GO with $R = 41.6\%$ (Figure 3.1(c),(f)). The reason behind considering a GO structure with this value of R is the following : in the experiment[192] on sensing abilities of r-GO towards standard food, the GO sample is first prepared by Hummers method [208]. In the Hummers method of preparing GO, the ratio of C and O is typically in the range of 2-3. This translates to a R value between 33.3 and 50 %. We have chosen a R value in between these two extremes.

Upon reduction of GO prepared by Hummers method to obtain r-GO, the C:O can increase between 6 and 13.5. Thus consideration of a C:O ratio of 10:1 is a reasonable estimate. Accordingly, we have considered such a model of r-GO [209] (Figure 3.1(b),(e)) where the surface contains only epoxy groups. In this structure all pairs of C atoms attached to the epoxy groups are aligned in parallel and the functionalised C atoms form a cluster. This is the appropriate structure considered for earlier studies of using it as a molecular sensor [209] as r-GO can be in multilayer forms and only one side of the surface is, therefore, of interest.

3.1.2 Computational Details

The structural models of the 2D nanosheets are constructed using a $5 \times 5(4 \times 3)$, supercell for G and r-GO(GO).This resulted in 50(48) C atoms for G and r-GO(GO) sheets. The ground state structures and associated electronic properties of VOC adsorbed nanosheets are calculated using Density Functional Theory (DFT)[210] based Projector Augmented Wave (PAW)[161] method implemented in Vienna ab initio simulation

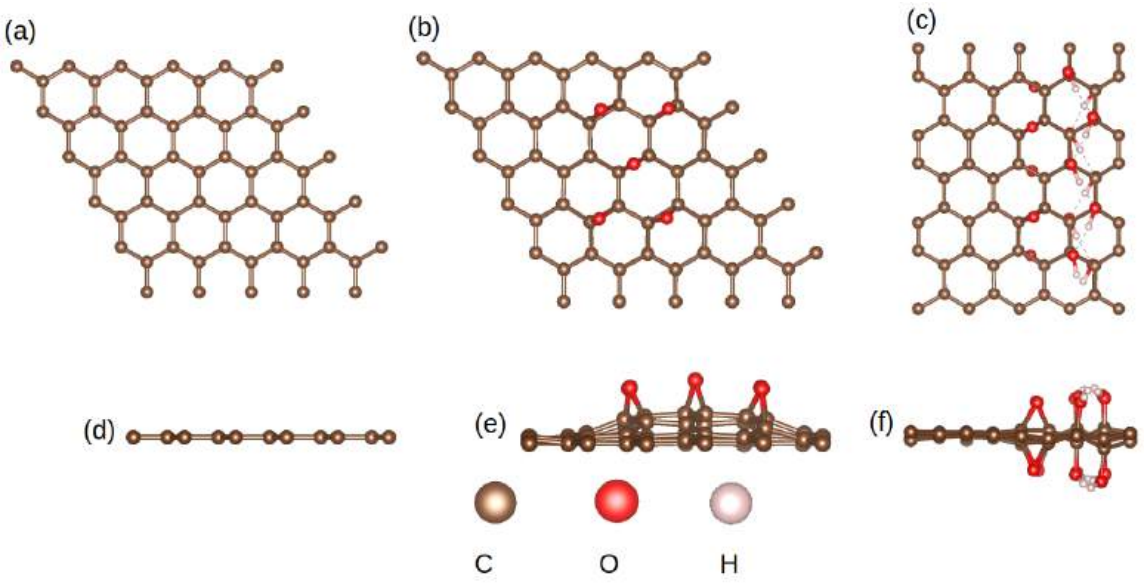

Figure 3.1: (a-c) Top View and (d-f) side view of Pristine Graphene, r-GO,and GO respectively.

package (VASP)[162, 211, 212]. The exchange and correlation part of the Hamiltonian is approximated using the generalized gradient approach (GGA)in the Perdew-Burke-Ernzerhof (PBE) parameterization[154]. A vacuum space of 30 Å, perpendicular to the 2D sheets, is incorporated to prevent unintended interactions between periodic images. To achieve the ground-state configurations while maintaining fixed cell volume and shape, we allow the ionic positions to relax without symmetry constraints. Full relaxation is done until the residual force on individual atoms and per-atom energy change converged to values smaller than 0.01 eV/Å and 0.1×10^{-6} eV, respectively. For optimizing the ground-state structure, a $5 \times 5 \times 1$ k-point mesh is used to sample the Brillouin zone[213]. For the calculation of the densities of states, a $17 \times 17 \times 1$ k-grid is used. Plane waves with energy upto 550 eV are considered. Throughout the calculations, Grimme's van der Waals (vdW)-corrected (DFT-D3) technique[214] is used.

For the electron wave function, a double-z polarised (DZP) basis set was employed. For electronic transport calculations, a mesh cutoff energy of 300 Hartree and a $10 \times 1 \times 100$ k-point mesh are used.

3.2 Results and Discussions

3.2.1 Structural properties

In Figure 3.1 we show the top and side views of optimised structures corresponding to pristine Graphene, r-GO and GO sheets constructed as described in the previous section. For pristine Graphene, the calculated lattice constants and C-C bond distance are found to be 2.46 Åand 1.42 Å, respectively. These values are fairly close to the experimental results [215]. In case of r-GO, we find the C-O bond distances to be 1.45 Å. In case of GO, the lattice constants a and b are 2.46 Åand 4.27 Årespectively. The calculated C-C and C-O bond distances are 1.40 Åand 1.44 Å, respectively. Thus, across the compounds C-C and C-O bond distances remain almost same.

The optimized configurations of the VOC-nanosheet complexes upon adsorption of VOC molecules on the nanosheets are computed by minimizing the total energies of the complexes with respect to the distances between surfaces of the 2D sheets and the molecules as well as their orientations. The optimized configurations are shown in Figures 3.2,3.3 and 3.4 for cases where Graphene, r-GO and GO is the 2D sheet, respectively. We find that in case of Graphene as the adsorbent, only Methylacetate is adsorped in a parallel orientation. Moreover,the hydrogen atoms are the closest ones to the surface for all cases. In case of adsorption at GO surface, the orientations of more VOCs are parallel to the surface with hydrogen closest to the oxygen atoms of GO. The trend remains same in case of r-GO as the adsorbent.

In order to validate our calculations regarding structural properties of VOC-nanosheet complexes, in Table 3.1, we report adsorption energies E_{ad},the equilibrium distance D between the adsorbate and the 2D sheets and compare them with existing results. Out of the three 2D systems, results on structural parameters are available for a few VOCs adsorbed on pristine Graphene only [216, 217, 218, 219]. We find that in Reference [216], the orientation of Acetone adsorbed on Graphene is similar to ours with $D = 2.86$ Å, slightly higher than ours. Accordingly, E_{ad} in Reference [216] is significantly smaller (-0.136 eV) in comparison with ours (-0.39 eV). Substantially good agreement is obtained with results from Ab initio molecular dynamics (AIMD) calculations and experiments [217]. E_{ad} obtained by the AIMD(the experiment) are -0.37(-0.34)eV,-0.31(-0.31)eV and -0.61(-0.58)eV for Acetone, Ethanol and Toluene adsorbed on pristine Graphene, respectively. In Reference [218], $E_{ad}(D)$ obtained by DFT total energy calculation are -0.31eV(2.80 Å) and -0.57eV(2.65 Å) for Ethanol and Toluene-adsorped pristine Graphene sheets. While the E_{ad} obtained in this work agree closely with our results, D for Toluene differ more than that in case of Ethanol. E_{ad} obtained from another DFT total energy calculation [219] are -0.29eV for Ethanol and -0.5 eV for Toluene adsorped on pristine Graphene. The approach taken in this work and Reference [219] differ from that taken in References [217, 218] is in approximation of the Exchange-correlation part of the Hamiltonian. While this work (and Reference [219]) incorporate the non-local van Der waals corrections in a semi-empirical, non self-consistent way, they were introduced in References [217, 218] self-consistently. The differences in the geometric configurations of the adsorped VOCs are probably due to this. In References [217, 218]the molecules were adsorped in near-parallel orientation with respect to Graphene. The agreement in E_{ad} between this work and the ones reported in References [217, 218],inspite of such differences indicates accuracy of our calculations and that the details of adsorption orientations of the molecules do not play a significant role in deciding the strengths of the interactions.

Due to lack of available results, we cannot compare our calculations with GO and r-GO as the adsorbents. However, the benchmark test of our results with Graphene indicate that results with GO and r-GO can be considered accurate and robust. Our results do not indicate any pattern in the variations of the E_{ad} as the 2D nano-sheet is changed. The common trend across the three adsorbents is that E_{ad} with Toluene is the strongest. This happens due to predominant $\pi - \pi$ stacking in Toluene. Across the three systems, equilibrium distance D varies between 2.31-3.05 Å, with the only exception of Ethanol on r-GO where D is 1.94 Å. This happens due to significant bending of the molecule in comparison with cases of other two surfaces. Neverthelss, the values of D indicate that the molecules are physisorped on all three surfaces.

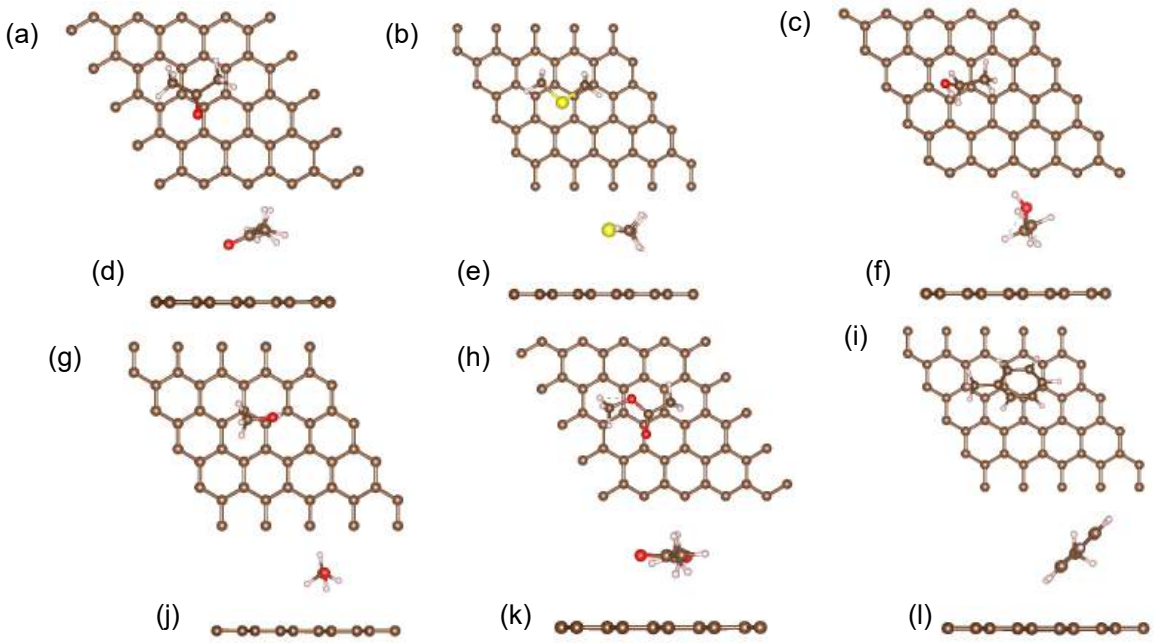

Figure 3.2: (a-c) Top and (d-f) side views of optimised geometries after (a,d) Acetone, (b,e) Dimethylsulfide, and (c,f)Ethanol physisorbed on Graphene nanosheet. (g-i)Top and (j-l) side views of optimised geometries after (g,j) Methanol, (h,k) Methylacetate and (i,l) Toluene physisorbed on Graphene nanosheet. Red, brown, white and yellow balls stand for O,C,H and S atoms respectively.

3.2.2 Electronic structure, charge transfer and work function

Better insights into the adsorption of VOCs on different nanosheets and their possible impacts on the electrical transport properties of the 2D materials when they are put into device forms to sense and separate different VOCs, can be obtained by analysing the electronic structures of the VOC adsorbed nanosheets. In Figures 3.5-3.7 we show the total and component projected densities of states (DOS) of the systems considered in this work. In each case, comparison is made with the DOS of isolated nanosheet and isolated VOC molecule.

In Figure 3.5, we show the DOS corresponding to different VOCs adsorbed on pristine Graphene sheet. We find the following general trends : (a) there is no remarkable change in the total DOS after VOC adsorption when compared with that of isolated Graphene (b) due to presence of the molecular states, the total DOS have additional peaks in the occupied parts of the spectra. However these modifications happen mostly away from the Fermi levels (c)only in case of Dimethylsulfide adsorption, additional peak occurs within an energy range of 1 eV below Fermi level (d)the DOS of the adsorbed molecules resemble closely to those of the isolated ones, that is the adsorbed molecular DOS are made up of isolated peaks only. The states are, however, lie deeper in the occupied parts of the spectra. This suggests weak interactions between the VOCs and the Graphene sheet. Smaller charge transfer and consequently insignificant differences in transport properties upon adsorption of different VOCs when Graphene is put into a sensing device form are expected. Our results for Ethannol and Toluene adsorbed Graphene agree very well with the results of Reference [218].

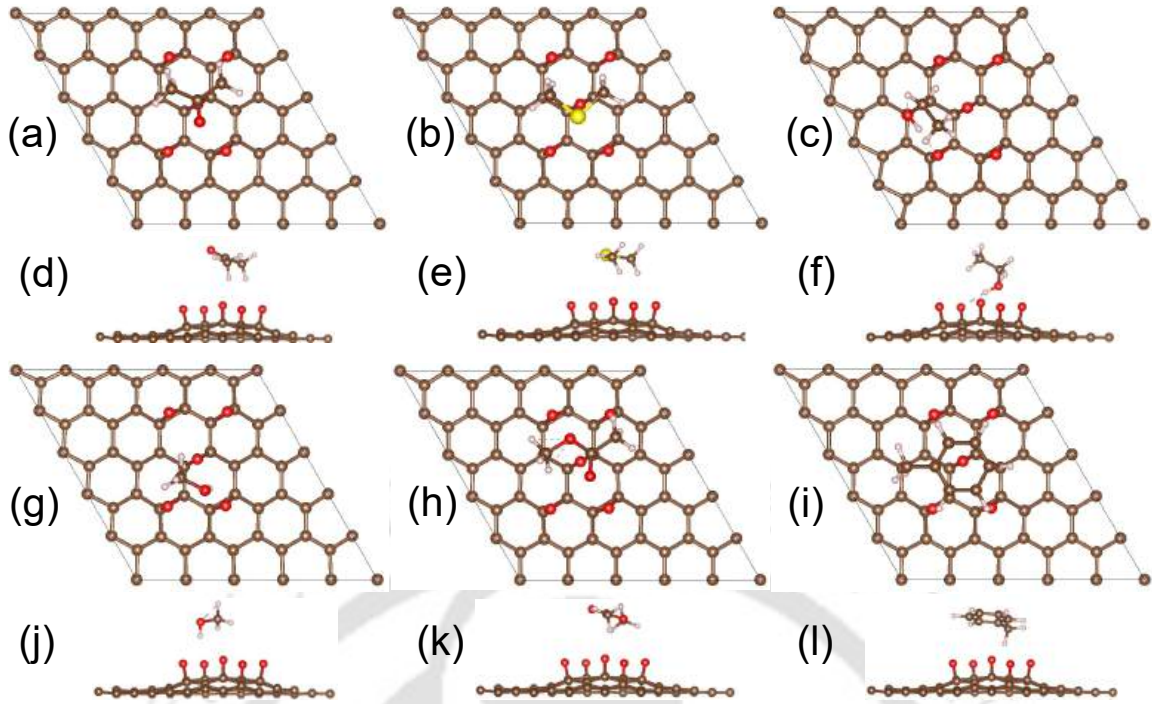

Figure 3.3: (a-c) Top and (d-f) side views of optimised geometries after (a,d) Acetone, (b,e) Dimethylsulfide, and (c,f)Ethanol physisorbed on r-GO nanosheet. (g-i)Top and (j-l) side views of optimised geometries after (g,j) Methanol, (h,k) Methylacetate and (i,l) Toluene physisorbed on r-GO nanosheet. Red, brown, white and yellow balls stand for O,C,H and S atoms respectively.

Significant changes in the electronic structures are observed when Graphene as the adsorbent is replaced with r-GO (Figure 3.6). First of all, like Graphene, r-GO too is a zero-gap semi-metal. Upon adsorption of these six VOCs, the electronic ground state of the composite systems change. The changes are, however, noteworthy for three VOCs-Acetone, Dimethylsulfide and Methanol. While the ground state is still a zero-gap one for the other three VOC adsorbed r-GO, the gap vanishes for these three. This difference is solely due to the frontier molecular orbitals of the concerned VOCs. Although, like the case of Graphene-VOC systems, the structures of the DOS are like those of isolated molecules, the frontier molecular orbitals are closer to the Fermi level. The positions of the molecular states close near the Fermi levels are responsible for the noticeable changes in the electronic ground states of the composite systems. Consequently, larger charge transfers between r-GO and VOCs, as well as charge transfers of different magnitudes with different VOCs are expected. From the point of view of sensing different VOCs and separating them out, r-GO is expected to perform better than Graphene.

Monolayer GO, unlike the other two nanosheets considered in this work, is a semiconductor. The DOS of VOC adsorbed GO along with isolated GO and isolated VOCs are presented in Figure 3.7. Our calculations show isolated GO a semiconductor with a band gap of 0.9 eV. The semiconducting nature is retained upon adsorption of the six VOC molecules. However, the band gaps change considerably. While the band gap of Dimethylsulfide adsorped GO (0.89 eV) remains nearly same as that of the isolated GO, it changes to 1.1 eV for Acetone-GO system and to 1.02 eV for the rest four. A detailed inspection of the DOS shows that upon adsorption of Ethanol, Methanol, Methylacetate

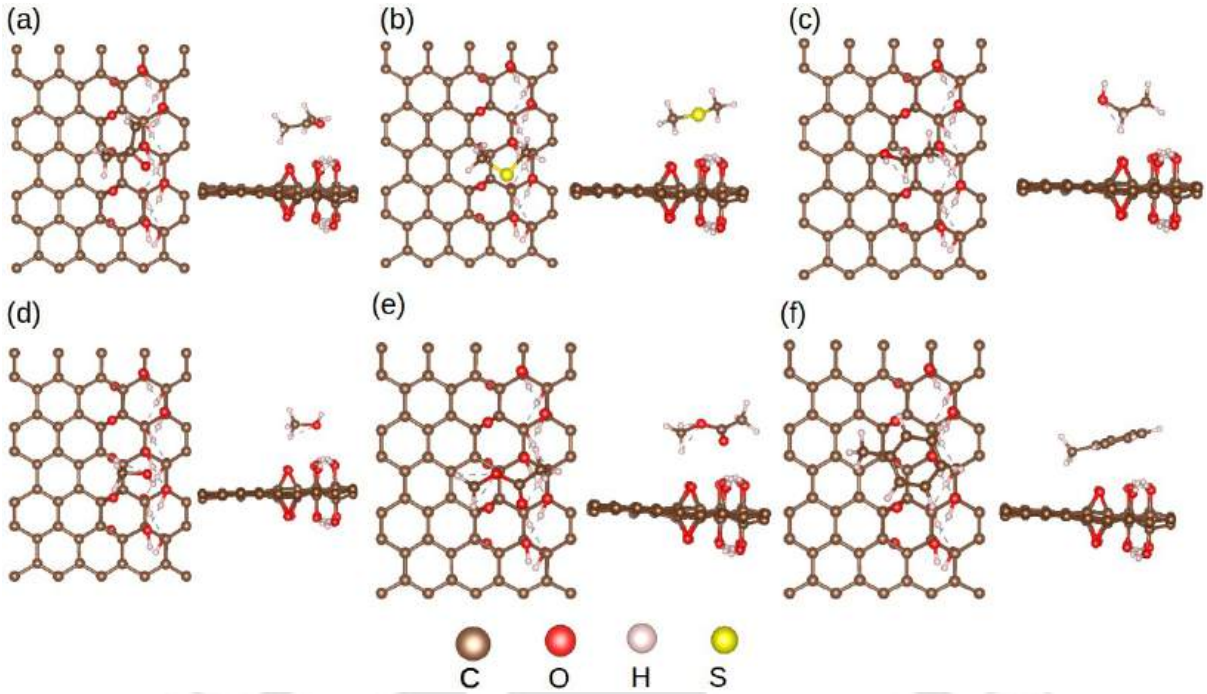

Figure 3.4: (a-c) Top and (d-f) side views of optimized geometries after (a,d) Acetone, (b,e) Dimethylsulfide, and (c,f)Ethanol physisorbed on GO nanosheet. (g-i)Top and (j-l) side views of optimised geometries after (g,j) Methanol, (h,k) Methylacetate and (i,l) Toluene physisorbed on GO nanosheet. Red, brown, white and yellow balls stand for O,C,H and S atoms respectively.

and Toluene, the DOS near Fermi level in the occupied part of the spectra hardly changes from that of isolated GO. This is due to the fact that the molecular states lie deeper in energy and thus the states near Fermi level are dominated by GO. For Acetone and Methylacetate, the molecular states are closer to the Fermi level and hybridise with the states of the 2D sheet. The valence band maxima in case of Methylacetate adsorbed GO is due to the molecular states. We expect a reflection of this in the charge transfer and work functions.

The features in the DOS are reflected in the quantitative values of charge transfer between the molecules and the 2D materials (Table 3.1). Our results agree well with results from other DFT based calculations using the same approximation for the Exchange correlation [219]. The value of Q obtained in Reference [219] for Ethanol(Toluene) is 0.01e(0.007e). The largest value of Q calculated in this work is for Dimethylsulfide. This is consistent with the largest change in the electronic structure observed in case of adsorption of Dimethylsulfide. However, the magnitudes of charge transfer in all cases are small, indicating weak interactions between the molecules and Graphene. Virtually no charge transfer happens in case of adsorption of Acetone, Ethanol and Toluene. This also is consistent with the deep lying molecular states as observed in their densities of states. In case of Dimethylsulfide adsorption on both r-GO and GO, Q is one order of magnitude larger than all other cases. This, once again is consistent with the differences in the features of DOS. In general, larger charge transfers are observed when the adsorbing surface is r-GO. This suggests that among the three 2D materials, r-GO will produce the best sensing performance. Though conventional wisdom suggests a linear correlation

Table 3.1: Adsorption Energy ($\mathbf{E}_{ad}$), equilibrium distance $\boldsymbol{D}$ (Å) between VOC and nano-sheet, charge transfer $\mathbf{Q(e)}$ between the sheet and the VOC molecule, recovery time $\boldsymbol{\tau}$**(s)** of the nano-sensors and Work function $\boldsymbol{\phi}$**(eV)** of differnt VOC-nanosheet complexes considered here.

2D material	**Molecule**	$\mathbf{E}_{ad}(eV)$	$\boldsymbol{D}$ (Å)	**Q(e)**	τ**(s)**	ϕ**(eV)**
Graphene	Acetone	-0.39	2.54	0.003	6.8×10^{-6}	4.13
	Dimethylsulfide	-0.40	2.68	-0.040	1.2×10^{-5}	4.26
	Ethanol	-0.35	2.89	0.006	1.4×10^{-6}	4.29
	Methanol	-0.28	3.05	0.018	9.04×10^{-8}	4.48
	Methylacetate	-0.48	2.49	0.014	2.5×10^{-4}	4.26
	Toluene	-0.60	2.90	0.004	2.8×10^{-2}	4.26
r-GO	Acetone	-0.35	2.47	-0.033	1.62×10^{-6}	5.19
	Dimethylsulfide	-0.31	2.53	-0.190	3.03×10^{-7}	4.75
	Ethanol	-0.47	1.94	-0.045	2.07×10^{-4}	5.02
	Methanol	-0.31	2.32	-0.021	2.42×10^{-7}	5.34
	Methylacetate	-0.33	2.58	-0.015	5.98×10^{-7}	5.21
	Toluene	-0.46	2.70	-0.059	1.02×10^{-4}	5.06
GO	Acetone	-0.31	2.50	-0.01	3.23×10^{-4}	5.26
	Dimethylsulfide	-0.39	2.83	-0.67	7.94×10^{-6}	4.94
	Ethanol	-0.27	2.76	-0.05	4.88×10^{-8}	5.17
	Methanol	-0.28	2.31	-0.01	6.94×10^{-8}	5.06
	Methylacetate	-0.31	2.68	-0.009	1.48×10^{-5}	5.03
	Toluene	-0.62	2.34	-0.03	7.00×10^{-2}	5.19

between E_{ad} and Q, we find a stark contradiction in this case. The best example is that of Dimethylsulfide. Irrespective of the adsorbent, it transfers the maximum charge. But the adsorption energies of Dimethylsulfide-2D complexes are similar to the systems where the adsorbate is different.The same pattern is observed when Dimethylsulfide is adsorbed on three different surfaces. To understand this apparent counter-intuitive result, we show, in Figure 3.8, the charge density difference isosurfaces when Dimethylsulfide is adsorbed on three different 2D adsorbent.We find good correlations between the natures of the isosurfaces and associated value of Q. The isosurface of Dimethylsulfide-Graphene shows small charge depletion(charge accumulation) around the molecule(the π states of Graphene). This suggests a small charge transfer from the molecule to the delocalised orbitals of Graphene.This is consistent with a small amount of Q. In case of Dimethylsulfide-r-GO, we find accumulation of electrons near the surface more pronounced and localised in comparison with the case of Graphene adsorbent. The depletion on the molecule in this case is clearly much larger than the case of Graphene adsorbent. This is due to the O atoms on the r-Go surface which act as localised acceptors. A greater Q in comparison with Dimethylsulfide-Graphene case is thus consistent. The largest charge transfer happens in case of Dimethylsulfide-GO compound. The isosurfaces in this case indicates stronger localised accumulation at O sites of GO, in comparison to those of r-GO.Larger depletion of charge density on the molecule corroborates this. Such large donation of electron density on to the acceptor sites on GO correlates well with the comparatively large Q. The strength of adsorption of molecules on surfaces, however, depend on energy costs due to factors like Coulomb interaction, structural relaxations, re-hybridisation and vdW interaction. Though all three surfaces in our case accept electrons from the adsorbate molecule, the nature of the acceptor states and the corresponding energy costs

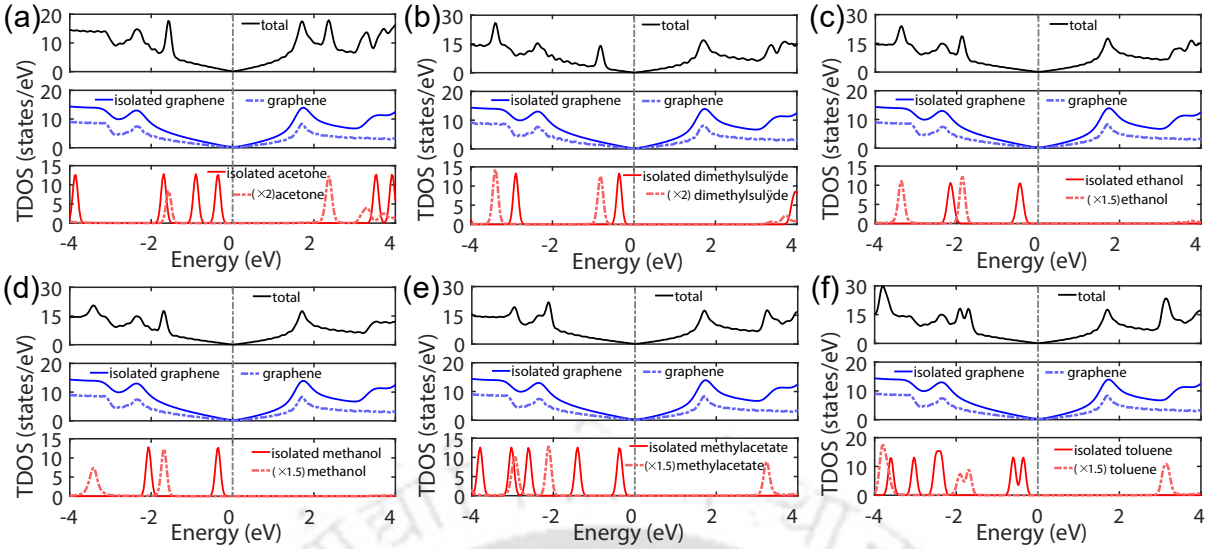

Figure 3.5: Total and component projected DOS for (a)Acetone, (b)Dimethylsulfide, (c)Ethanol, (d)Methanol, (e)Methylacetate and (f)Toluene) adsorbed Graphene monolayer. In each case, isolated Graphene (Graphene) stands for DOS of Graphene before (after) molecular adsorption. In the panels showing molecular DOS, isolated molecule (molecule) stands for DOS of molecule before(after)adsorption.

are responsible for absence of correlation between E_{ad} and Q. GO receives maximum charge but its E_{ad} is almost same as that of Graphene surface which receives one order of magnitude less charge. The difference lies in the following two factors: (a)the geometry of adsorption on Graphene suggests larger vdW contact and (b)the delocalised acceptor states of Graphene as opposed to the localised states of GO. Strong accumulation of electrons into highly localised acceptor sites give rise to possible re-hybridisation (as is clear from the densities of states) and strong Coulomb screening, both of which cost energy that reduces the stabilization per accepted electron. The favorable vdW contact and the delocalised states of the acceptors, on the other hand, is the reason for Graphene to bind the molecule with same strength, despite much smaller charge transfer. The situation of r-GO is somewhat in between these two extremes. The geometry of adsorption in this case probably produces the minimal vdW interaction. This along with the accumulation of large charge in localised orbitals producing an energy penalty causes reduction in strength of adsorption.

The changes in work function ϕ of the 2D nanosheet upon molecular adsorption is another measure of the substrates responses to the molecules that can be indicative of the sensing performance of the 2D material under consideration. The calculated work function ϕ_0 is 4.35 eV, 5.25 eV and 5.14 eV for isolated Graphene, r-Go and GO, respectively. For Graphene adsorbent, our result has reasonable agreement with calculations using self-consistent non-local corrections[218]; the calculated ϕ is 4.56eV. Agreements in $\Delta\phi = |\phi - \phi_0|$ between our results and those in [218, 219]are close too. After Ethanol adsorption, $\Delta\phi$ is 0.22 eV in this work while it is 0.21 eV(0.29eV) in [218]([219]). However, in case of Toluene adsorption, our results are in better agreement with Reference [218]; $\Delta\phi$=0.09 eV in our case while it is 0.16 eV using non-local van Der waals correction in a self-consistent manner. On the other hand, despite use of same approximation in treating the van Der waals corrections reported $\Delta\phi$ in Reference [219] is only 0.01eV.

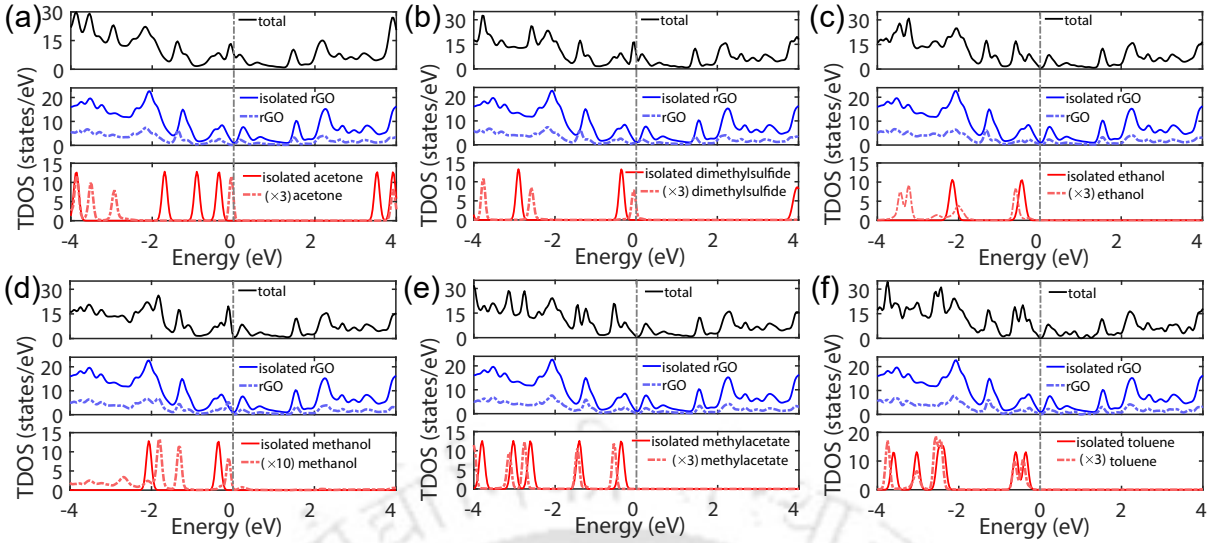

Figure 3.6: Total and component projected DOS for (a)Acetone, (b)Dimethylsulfide, (c)Ethanol, (d)Methanol, (e)Methylacetate and (f)Toluene) adsorbed r-GO monolayer. In each case, isolated rGO (rGO) stands for DOS of r-GO before (after) molecular adsorption. In the panels showing molecular DOS, isolated molecule (molecule) stands for DOS of molecule before(after)adsorption.

From the results of ϕ in Table 3.1, we find good correlation between variations in Q and ϕ across adsorped molecule-substrate systems. For Graphene substrate, ϕ changes little across the systems. For GO and r-GO substrates, the changes are significant; the maximum change happens in case of Dimethylsulfide. Since Dimethylsulfide donates maximum amount of charge, the work functions of the substrates are considerably different upon its adsorption in comparison to cases when other VOCs are adsorped. These imply that if sensing is based upon changes in work function, GO and r-GO will perform better in terms of discriminating different VOCs.

3.2.3 Sensing performances

A comparative assessment on sensing abilities of the three 2D materials under consideration is a validation of the insights obtained so far. We have computed the sensing properties of these materials when used both as a chemiresistive and a work function based sensor.

The chemiresistive nano-sensor is simulated by considering a two-probe model consisting of a central scattering region and two electrodes on either side of it. These electrodes act as source and drain of electrons. The adsorption of VOC molecules happen in the central scattering region. In Figure 3.9, such a setup is shown where the central scattering region made up of r-GO is joined smoothly to the Graphene electrodes in the transport direction z. Screening out the perturbations in the sensing region is taken care of by extending the electrodes into the central region.

In Figure 3.11(a) and (b), we present $I-V$ characteristics of Graphene and r-GO with and without adsorped VOCs, respectively. In case of Graphene sensor, we find $I-V$ characteristic curve is Ohmic. From Figure 3.10(a), we find that the maximum current is obtained when no VOC is adsorped. Upon adsorption of Ethanol, there is no

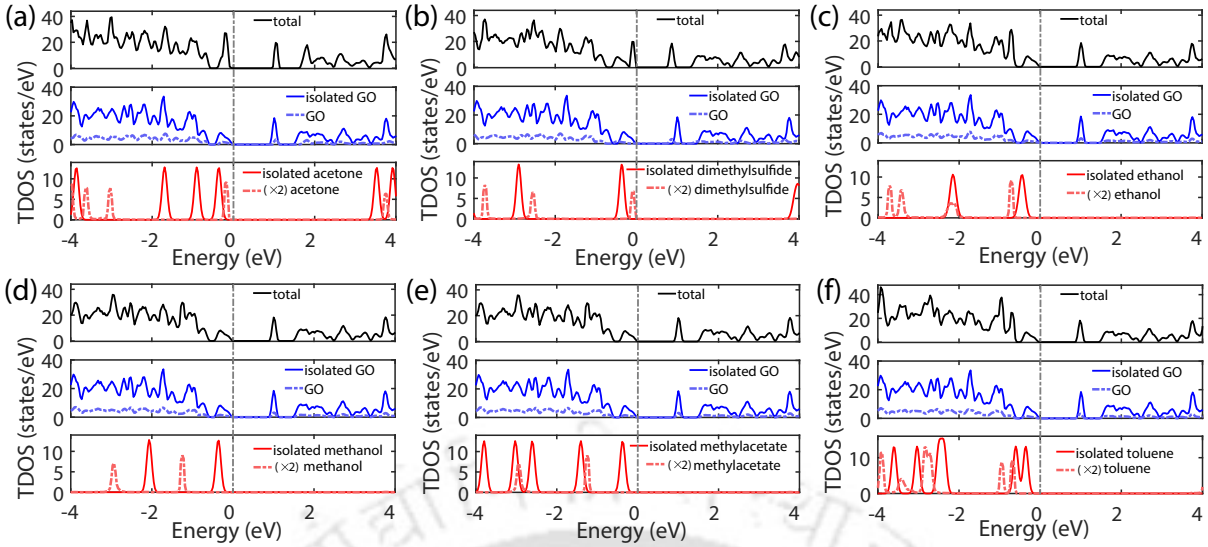

Figure 3.7: Total and component projected DOS for (a)Acetone, (b)Dimethylsulfide, (c)Ethanol, (d)Methanol, (e)Methylacetate and (f)Toluene) adsorbed GO monolayer. In each case, isolated GO (GO) stands for DOS of GO before (after) molecular adsorption. In the panels showing molecular DOS, isolated molecule (molecule) stands for DOS of molecule before(after)adsorption.

change in the current. Maximum change is obtained upon adsorption of Dimethylsulfide, followed by Methylacetate. For the other three VOCs, changes are nearly same. The $I-V$ relationship for r-GO based device is almost linear on the other hand. Like the Graphene based device, the $I-V$ curves corresponding to adsorption of different VOCs are separable around 0.2V and onward. Unlike Graphene, in this case the current increases upon adsorption of VOC except in cases of Ethanol and Methanol. Moreover, responses for each case can be identified separately. This suggests better sensing prospects with r-GO chemiresistive sensor.

Direct estimate of sensing capability and one-to-one correspondence to the experimental measurements can be done by calculation of differential conductances. The sensitivity $S^{gas}(\%)$ is given by

$$S^{gas} = \frac{|g - g_0|}{g_0} \times 100 \tag{3.2}$$

$g(g_0)$ is the zero-bias conductance of the sensor material when the VOC molecule is adsorbed(before the molecular adsorption). With a finite bias V_b, the conductance can be expressed as $g\,(V_b) = \frac{2e^2}{h} T\,(\mu = E_F - eV_b)$; T is the transmission coefficient, E_F the Fermi energy, h the Planck's constant and e the electronic charge. Conductance is a better measure than current because (i) the result is directly comparable to experiments where they measure differential resistance and (ii) it allows a better distinction of signal change as the conductance through sensor material changes by a quantum unit of $2e^2/h$ in its interaction with the VOC. Quantitative estimation of the sensor's ability to discriminate between the VOCs is done through selectivity. The selectivity towards molecule x is computed as $\mathrm{S}_h/\mathrm{S}_x$, where S_h is the highest sensitivity obtained in the group of molecules considered.

In Figure 3.11, we present the sensing parameters for Graphene and r-GO chemire-

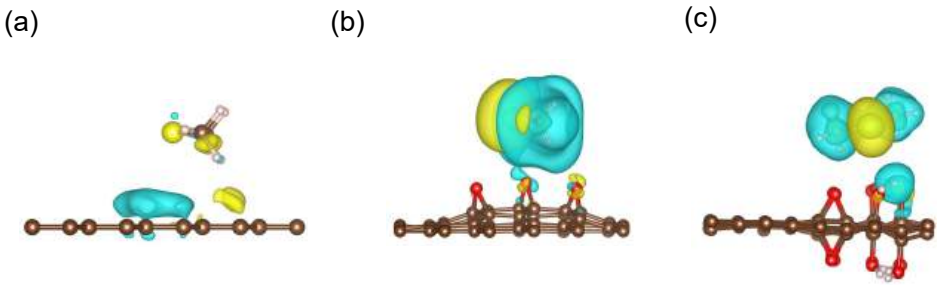

Figure 3.8: Charge density differential isosurfaces for Dimethylsulfide adsorbed on (a)Graphene, (b)r-GO, and (c)GO. Isosurface value is 0.0003 e/Å^3. Yellow(cyan) indicates charge accumulation(depletion).

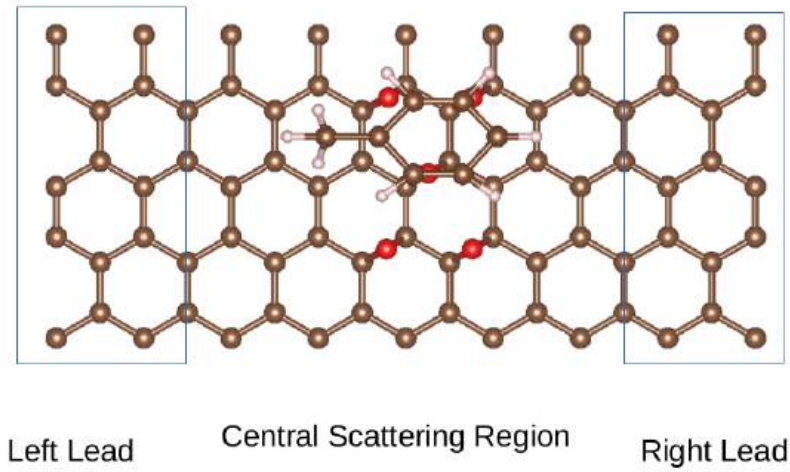

Figure 3.9: Schematic structural model of a gas sensor based on r-GO with two semi-infinite electrodes . The areas marked by square boxes represent semi-infinite electrodes.The central part of the figure where the molecule is physisorbed (Toluene is shown here) is the scattering region.

sistive sensors. As is expected from the DOS, the charge transfer and the $I-V$ results, Ethanol has almost zero sensitivity while maximum sensitivity is seen in sensing Dimethylsulfide (Figure 3.11(a)). The sensitivities corresponding to Toluene, Acetone and Methanol are comparable while sensitivity is slightly distinguishable for Methylacetate adsorption. This is reflected in the selectivity shown in Figure 3.11(b). Clearly Graphene sensor would be hardly able to distinguish signals due to adsorption of different molecules. Though it appears that it can sense Ethanol clearly as the selectivity value is distinct with respect to others, near zero sensitivity of Ethanol implies that it wouldn't be sensed at all. Thus, Graphene as chemiresistive sensor to assess the quality of deterioration of standard food items is undesirable. Results of Figure 3.11(c)-(d) on the other hand shows that r-GO sensor can distinguish between at least four VOCs: Toluene, Dimethylsulfide,Ethanol and Methylacetate. Maximum sensitivity is obtained for Toluene while that of Acetone and Methanol are same. As a result, r-GO sensor will not be able to distinguish between signals corresponding to adsorption of Acetone and

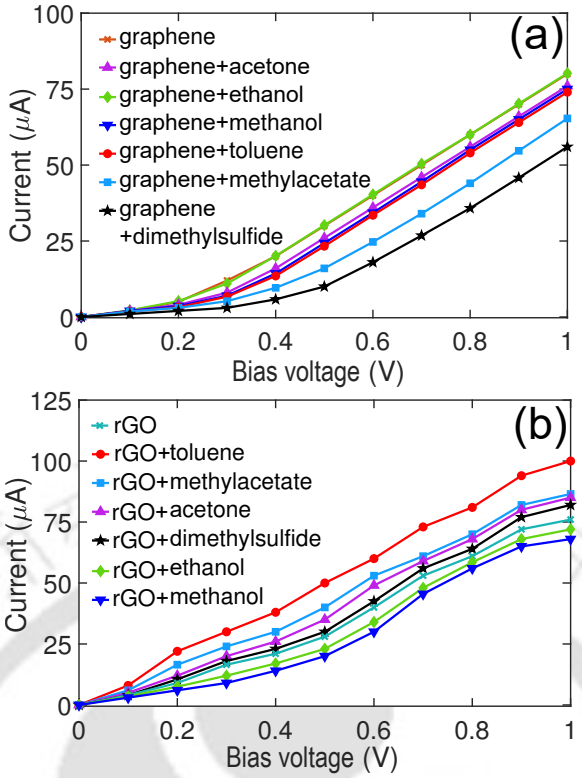

Figure 3.10: I-V characteristics for (a) Graphene (b) r-GO monolayer with and without adsorption of six VOCs separately.

Methanol. This result is in contrast with the experimental one [193] where the r-GO sensor could not distinguish between any of the six VOCs.

A quicker and easier qualitative estimation of the sensing parameters of a chemiresistive sensor can be done if the sensing material is a semiconductor. In this case, the sensitivity $S^{gas}(\%)$ is given as [220]

$$S^{gas} = |\frac{\sigma_{VOC} - \sigma_{pure}}{\sigma_{pure}}| \times 100\%, \tag{3.3}$$

where $\sigma_{VOC}(\sigma_{pure})$ represent the electrical conductivity of sensor material with(without) adsorbed VOC molecule. Since electrical conductivity (σ) of a semiconductor material correlates with its band gap [59]

$$\sigma \propto \exp(-E_g/2k_BT)$$

where E_g is the electronic band gap, k_B the Boltzmann constant, and T is the temperature (in K), the changes in its band gap upon adsorption of different VOC can be exploited to assess its sensing parameters. We use this approach to estimate sensing ability of a GO chemiresistive sensor at room temperature. The results are presented in Figure 3.12. As expected from the results of the DOS, GO has poor sensing ability in the present context. Sensitivity and consequently selectivity towards Ethanol, Methanol, Methylacetate and Toluene are same. Therefore, GO when used as chemiresistive sensor to detect VOCs from standard food,will be able to distinguish at most two out of the six VOCs.

In Figure 3.13, we show the sensing parameters of the three systems when used as a work function based sensor. The sensitivity S^{ϕ} of a work-function based sensor is

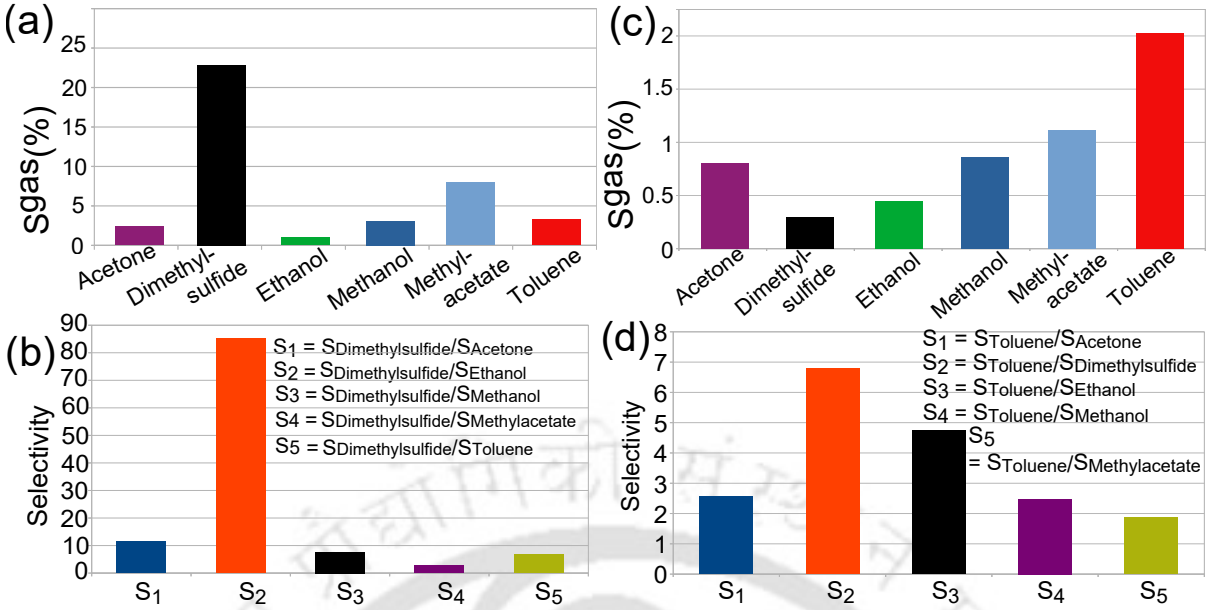

Figure 3.11: (a,b) Sensitivity and selectivity of Graphene (c,d) Sensitivity and selectivity of rGO monolayer along with different adsorbed VOC molecules

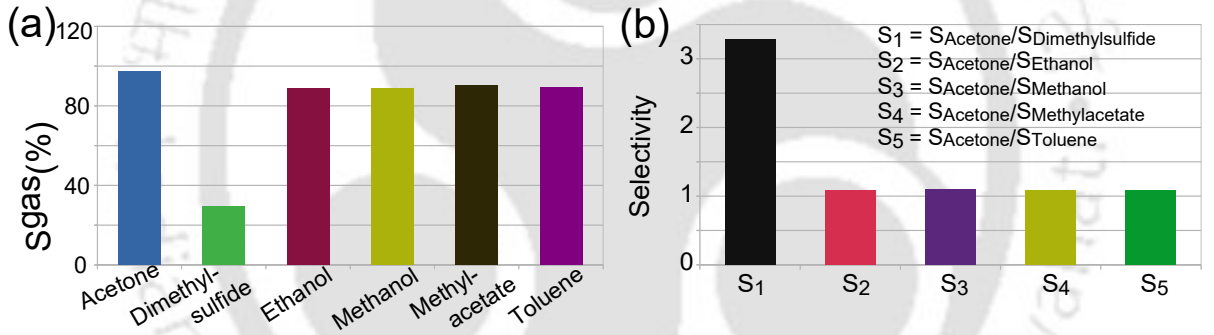

Figure 3.12: (a) Sensitivity and (b) Selectivity of GO Chemiresistive Sensor.

calculated as: $S^{\phi} = \frac{\phi - \phi_0}{\phi_0}$ where $\phi(\phi_0)$ is the Work function of the surface after(before) VOC adsorption. In this case, we find that Graphene can distinguish at most three VOCs while both GO and r-GO can distinguish four different VOCs : Acetone, Ethanol and Methanol in case of Graphene, Acetone, Dimethylsulfide, Methanol and Methylacetate in case of r-GO and Dimethylsulfide, Ethanol, Methanol and Toluene in case of GO. The relative sensitivities reflect the trends in the variations in ϕ and is consistent with the changes in the electronic structures as reflected in the DOS. We can, therefore, infer that Graphene and its two derivatives will function better in sensing the quality of food if used as work function sensors.

Finally, we investigate the recovery time of these sensors. In Table 3.1, we present results of sensor recovery time τ for Graphene, r-GO and GO. The results suggest that all three qualify to be reusable sensors for sensing VOCs from standard food materials. To further assess the capabilities as sensors, a comparison of τ obtained in case of other 2D materials in the context of sensing same VOCs is necessary. To this end, we focus particularly on r-GO since its sensing ability turns out to be consistent when used as

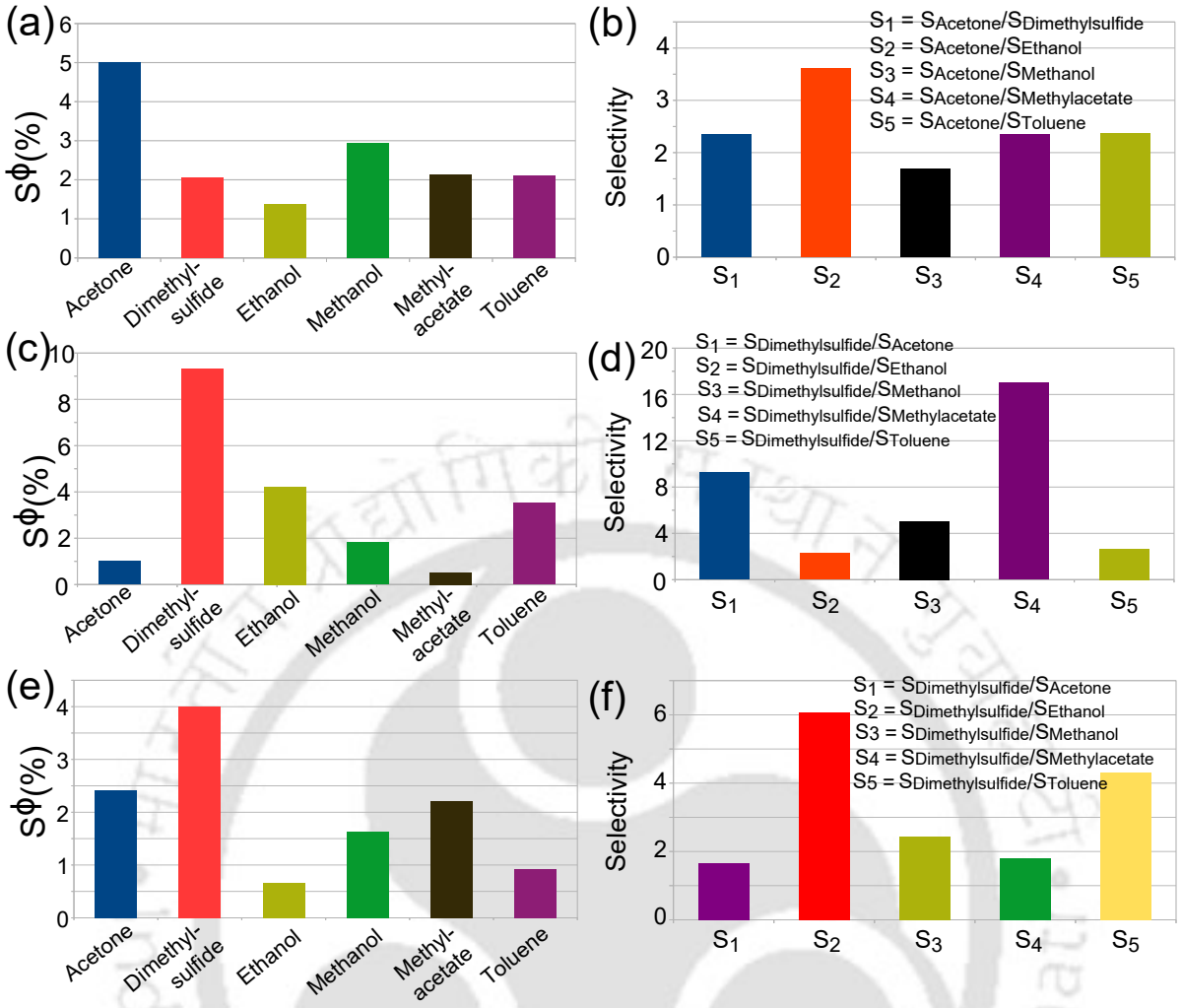

Figure 3.13: (a,b) Sensitivity and Selectivity of pristine Graphene (c,d) Sensitivity and Selectivity of r-GO and (e,f) Sensitivity and Selectivity GO work function based sensor.

either chemiresistive or as work function based sensor. We find that τ for r-GO in case of each VOC compare very well with F-silicene[221]. We also find that calculated values of τ for r-GO are orders of magnitude smaller compared to pristine and defected BC_6N [222] in case of Acetone, Ethanol, Methanol and Toluene desorption. This suggests that r-GO sensor will be as efficient or better in comparison to many other 2D material based sensor.

3.3 Conclusions

Motivated by a recent experiment on sensing capabilities of bare and polymerized r-GO for detection of stage of deterioration of standard food products, we have investigated monolayers of Graphene, r-GO and GO to assess their abilities in sensing the VOCs emerging from standard food components that are markers of stage of degradation. Using a combination of DFT and non-equilibrium Green's function technique, we have analyzed in detail the structural properties, the electronic structures, the transport properties and the sensing parameters associated with VOC-2D material complexes. Our results suggest that pristine Graphene is the worst performer among the three substrates considered

while r-GO perform reasonably well as both chemiresistive and work function based sensor. GO, on the other hand, can be used only as a work function based sensor. Such differences among the three materials can be attributed to the geometry of adsorption and the nature of the surface states that participate in the charge transfer with the VOC molecules.Our results suggest that, we could not find any trends in the adsorbtion energy among the molecules except that toluene shows maximum adsorbtion energy due to it's large size and parallel adsorbtion with the 2D material. The charge transfer value also indicate that only dimethylsulfide molecule shows maximum charge transfer due to it's localized charge distribution. We find that the sensing related performance of r-GO is comparable to those of other 2D materials like F-Silicene and BC_6N. However, in contrast with the experiment [192], we find r-GO to be able to discriminate between four of the six VOCs. The origin of this discrepancy can be in the differences between the model of r-GO used here and the experimental sample. During the reduction of GO to obtain r-GO by standard chemical route, the r-GO sheets tend to generate irreversible agglomerates that can decrease the effective surface area for adsorption, leading to lowering of sensitivity and selectivity. Such effects are not considered in the computational modeling. This might be the reason in obtaining better sensitivity and selectivity in our calculations. This work, thus may trigger attempts to obtain samples that are devoid of such limitations. Therefore, the results hold immense importance in future exploration of nano-materials in the area of food technology.

Chapter 4

Sensing Food Quality by Free-Standing Silicene Nanosheets

Due to the limitations posed by pure graphene and the structural complications associated with its various composites, researchers, particularly ones performing modeling and simulations, have explored other materials from the 2D family as potential gas sensors applicable to a wide spectrum of VOCs. A plethora of first-principles Density Functional Theory [210] based simulations have been carried out in recent times with pristine compounds like MoS_2 [137], phosphorene [223, 139, 140], black phosphorous [141], $HfTe_2$ [224] and BC_6N [222] as sensors for VOC and hazardous gas detection.

As an alternative to Graphene, silicene, among the single-component 2D materials, has shown substantial promise. In contrast to sp^2-hybridised Graphene, silicene has a mixture of sp^2 and sp^3 hybridisation and hence exhibits a buckled structure. The buckling turns out to be advantageous over the planar structure of Graphene as it provides tunability in the band gap upon application of an external electric field. Accordingly, silicene-based Field Effect Transistors (FETs) have been explored. It turns out that they demonstrate better efficiency than Graphene-based FETs [225]. Although unlike Graphene, majority of the work on Silicene are with Silicene grown on a substrate due to challenges in growing free-standing silicene, of late there has been some success in growth of free-standing silicene. Subsequently, The material has been extensively investigated with regard to biosensing applications through computational modeling. To this end, silicene nanosheets and nanoribbons as bio-sensors have been investigated for DNA sequencing [226, 227, 228, 229] and sensing of important bio-molecules like uric acid [230], paracetamol [231] and pyrazinamide, the organic molecule used to treat tuberculosis [232]. Silicene nanosheets have also been used for sensing hazardous gases [233]. The band structure of silicene changes significantly upon surface passivation by functional groups. Hydrogenation is the passivation of surface dangling bonds by hydrogen, changes the zero gap semiconductor to an insulator [234] while fluorine functionalization yields a moderate band gap of 0.45 eV [235, 236]. This poses a possibility of band gap modulation upon adsorption of different VOCs and its connection to differential responses, giving rise to discrimination between VOCs, which is the desired goal. This certainly is an advantage over Graphene or r-GO as a sensing material.

In what follows, in this work, using DFT and non-equilibrium Green's function (NEGF) [237] technique, we have investigated the changes in the structural and electronic prop-

The contents of this chapter are published in 2025, Phys. Status Solidi B 2025, 262, 2400578 DOI: 10.1002/pssb.202400578.

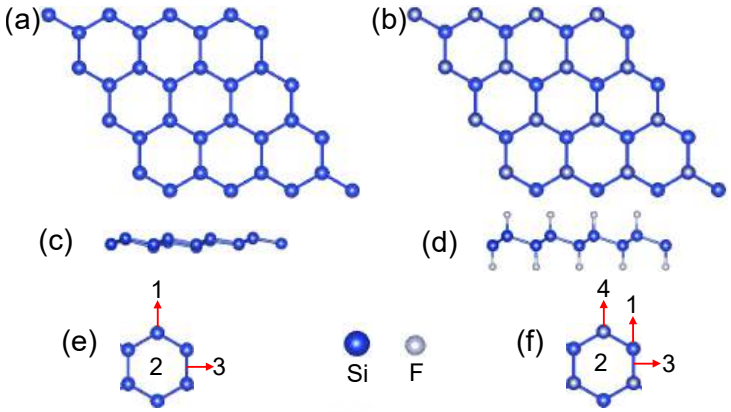

Figure 4.1: Relaxed structure of silicene: (a)top view, (c)side view. Relaxed structure of F-silicene: (b) top view and (d) side view. Sites of adsorption for (e) silicene and (f)F-silicene are shown.

erties as well as sensing capabilities of pristine and Fluorine (-F) functionalized free-standingsilicene (F-silicene) nanosheets upon adsorption of six prominent VOCs (mentioned in the previous chapter)that are indicators of degradation of food products. Our modeling simulates the situation for either a free-standing silicene or where the interactions with the substrates are weak so that the effect of the substrate on the properties of silicene can be ignored. The modifications in the electronic structures, associated charge transfers, and work functions of the gas-adsorbed nanosheets, as well as the differences in these properties/parameters between bare and functionalized nanosheets, provide necessary insights into their comparative capabilities as sensors to ascertain the degree of deterioration of food. The ideas obtained are tested by simulating the sensing device and calculating transport parameters that are directly related to the experimental quantities, like sensitivity and selectivity. We find that both sensitivity and selectivity of silicene increase upon -F functionalization at a moderate bias voltage. This demonstrates that functionalized silicene can be a sensor, an alternative to Graphene-based ones, that addresses the quality of food products.

4.1 Computational Details

Long-range van der Waals (vdW) interactions are considered by employing corrections proposed by Grimme[238]. $4 \times 4 \times 1$ fully relaxed supercells are used for the pristine and -F functionalized silicene nanosheets (Figure 4.1). In order to avoid interaction between two layers along z-direction, a vacuum of 30 Åis used. The geometry optimization of the composite system of a molecule adsorbed on the nanosheet is carried out using the conjugate gradient method. A plane wave basis set up to 550 eV is considered. Convergence criteria for total energy and force are kept at 10^{-6} eV and 0.04 eV/ Å, respectively. A $4\times4\times1$ Monkhorst-Pack [213] k-point grid is used to sample the Brillouin zone for self-consistent calculations. A $17 \times 17 \times 1$ k-mesh is used for calculations of electronic structures.

Nanosheets of size $5 \times 3 \times 1$ and k-point grids of size $10 \times 1 \times 100$ are used for all transport calculations.

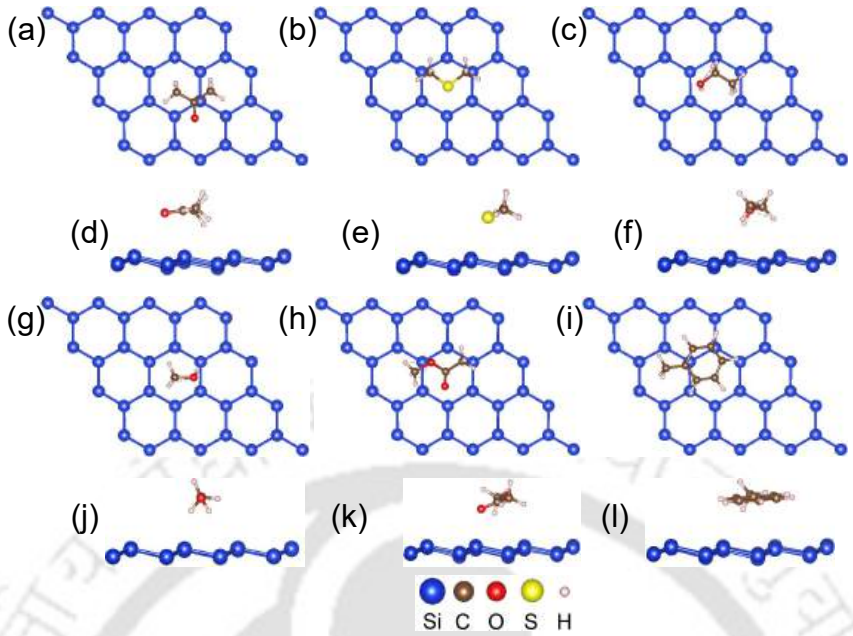

Figure 4.2: (a-c) Top and (d-f) side views of optimised geometries after (a,d) Acetone, (b,e) Dimethylsulfide, and (c,f)Ethanol physisorbed on silicene nanosheet. (g-i)Top and (j-l) side views of optimised geometries after (g,j) Methanol, (h,k) Methylacetate and (i,l) Toluene physisorbed on silicene nanosheet.

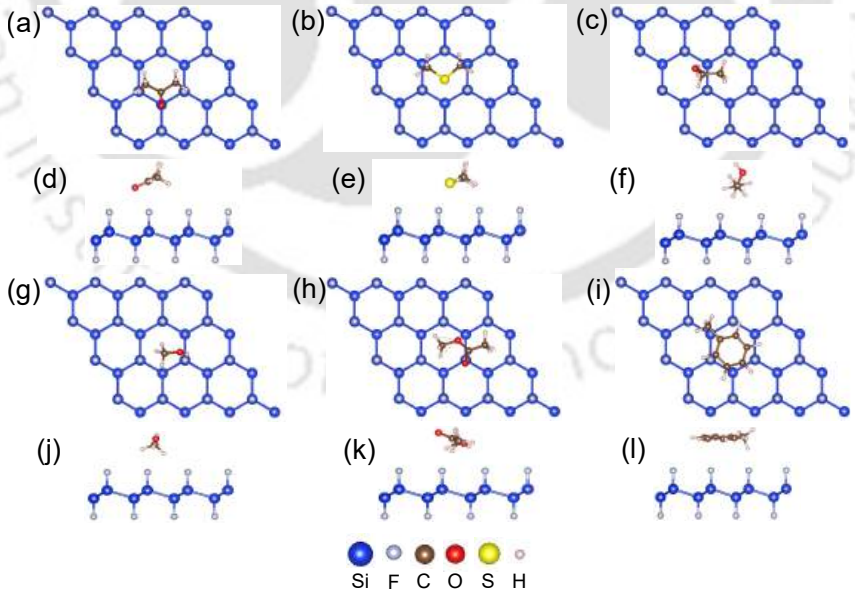

Figure 4.3: (a-c) Top and (d-f) side views of optimised geometries after (a,d) Acetone, (b,e) Dimethylsulfide, and (c,f)Ethanol physisorbed on F-silicene nanosheet. (g-i)Top and (j-l) side views of optimised geometries after (g,j) Methanol, (h,k) Methylacetate and (i,l) Toluene physisorbed on F-silicene nanosheet.

Table 4.1: Site of adsorption, Adsorption Energy (E_{ad}) and equilibrium distance between 2D sheet and VOC Molecule(D) for the systems considered in this work.

Adsorped molecule	2D sheet	Adsorption site	$\boldsymbol{E}_{ad}$ (eV)	$\boldsymbol{D}$ (Å)
Acetone	silicene	1	-0.34	3.43
	F-silicene	1	-0.32	3.97
Dimethylsulfide	silicene	2	-0.42	3.55
	F-silicene	2	-0.35	3.09
Ethanol	silicene	2	-0.32	2.76
	F-silicene	3	-0.24	2.6
Methanol	silicene	2	-0.25	2.89
	F-silicene	3	-0.17	2.3
Methylacetate	silicene	2	-0.39	2.92
	F-silicene	3	-0.35	3.36
Toluene	silicene	3	-0.64	3.18
	F-silicene	3	-0.48	3.91

4.2 Results and Discussions

4.2.1 Structural properties

In Figure 4.1 (a) and (c), the top and side views of the optimized pristine silicene sheet are shown. Corresponding structures for F-silicene are shown in Fig 4.1 (b) and (d). The calculated lattice constant (Si-Si bond length) of pristine silicene sheet is 3.84(2.27) Å, in good agreement with existing results [239, 236]. In the case of F-silicene, the optimized Si-Si bond length doesn't change much; the optimized Si-F bond length is 1.6 Å, in agreement with other works [236, 240]. The buckling parameter, in either case, is 0.47 Å, in excellent agreement with the existing result of 0.4 Å[241]. There are three sites of adsorption, marked as 1-3 in Figure 4.1 (e) in a pristine silicene sheet. For F-silicene, there is one extra site available due to the -F functional site (Figure 4.1(f)). For each of the six VOC molecules, we optimize the geometry of the nanosheet-VOC complex and obtain the preferred site of binding and the orientation of the gas molecule

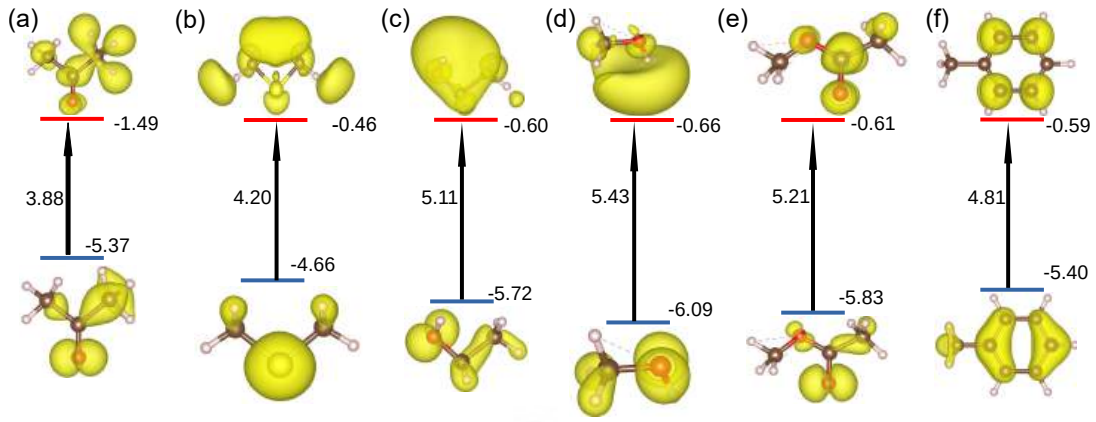

Figure 4.4: HOMO and LUMO of (a) Acetone (b) Dimethylsulfide (c) Ethanol (d) Methanol (e) Methylacetate (f) Toluene molecules. The energies are in eV.

with respect to the nanosheet. The sites of adsorption and the orientations of the six VOC molecules with respect to the pristine silicene(F-silicene) sheet are shown in Figure 4.2(Figure4.3). Associated binding energies, sites of adsorption as numbered in Figure 4.1, and the distances of the molecules from the sheets are tabulated in Table 4.1.

Upon inspecting the calculated E_{ad}, the adsorption energy, we find the following trends: first, the interaction strength for all six VOCs is weaker with F-silicene as the sensor material, and second, irrespective of the 2D sensor material, the interaction strength in the ascending order is Methanol, Ethanol, Acetone, Methylacetate, Dimethylsulfide, Toluene. The adsorption energy varies over a wide range: from -0.17 eV for Methanol on F-silicene to -0.64 eV for Toluene on silicene. The values suggest that except Toluene, all other molecules are moderately physisorbed on the silicene and F-silicene nanosheets. The adsorption energies compare well with existing results obtained for different 2D adsorbent materials. Our results on Acetone are either better in the case of adsorbent being MoS_2(-0.14 eV)[137], blue phosphorene (-0.25 eV)[140] or agree closely when the adsorbent is black phosphorous(-0.32 eV)[141] and BC_6N (-0.3 eV)[222]. For Ethanol, our results agree closely too (-0.21 eV for MoS_2 [137], -0.2 eV for blue phosphorene [140], -0.24 eV for black phosphorous [141] and -0.38 eV for BC_6N [222]). In the case of Toluene and Methanol, our results differ substantially when compared with results with BC_6N adsorbent (-0.91 eV for Toluene and -0.31 eV for Methanol) [222]. However, with black phosphorous as the nanosheet, our results are in good agreement for Toluene (-0.5 eV) [141]. It is, therefore, expected that the performance of silicene and F-silicene as sensors will be comparable to the standard 2D gas sensors.

In order to understand the trends in the adsorption energies, we look at the optimized structures of the VOC molecules on two different nanosheets. From Table 4.1, we find that except for Methanol and Methyl acetate, the molecules prefer the same adsorption site, irrespective of the adsorbent. Acetone prefers one of the Si-sites of the hexagon. Dimethylsulfide prefers the center of the hexagon, while Toluene prefers a bridge site. Ethanol, Methanol, and Methyl acetate prefer the center of the hexagon(bridge site) when the sensing material is pristine silicene (F-silicene). When physisorbed on pristine silicene, the acetone molecule prefers an orientation almost parallel to the nanosheet, with the oxygen atom closest to the sheet and at a distance of 3.43 Å. When the adsorbent is F-silicene, the molecule prefers the same orientation but is at a greater distance of 3.97 Åfrom the nanosheet. The interaction distance D increases substantially when the

nanosheet is F-silicene, which is also observed in the case of Methylacetate and Toluene. For the other three, the trend is the opposite. While Toluene molecules are adsorbed in an orientation parallel to the sheet for both nanomaterials, with the H atom closest to the adsorbent, Methylacetate is adsorbed with a tilted orientation with respect to the nanosheets. When the nanomaterial is pristine silicene, the O atom is the closest to it. The orientation changes in the case of F-silicene, bringing H closest to the adsorbent. The other three molecules prefer tilted orientations with respect to both adsorbents. While the H atom remains the closest to the nanosheet in the case of Ethanol and Methanol, it is the S atom in the case of Dimethylsulfide.

Among the six molecules, Toluene has the highest adsorption energy when physisorped on Silicene. Toluene consists of a Benzene ring where the electron density is distributed throughout. The highest occupied molecular orbital (HOMO) of bare Toluene molecule shown in Figure 4.4(f) demonstrates this. Such delocalisation of electron density gives rise to $\pi-\pi$ stacking. Since the Toluene molecule is adsorped almost parallel to the nanosheet, the strong $\pi - \pi$ interactions with electron cloud of Silicene becomes the strongest due to large adsorption area. On the other hand, the weakest adsorption strength is in case of Methanol. From Figure 4.2(j), we see that Methanol, the smallest molecule is adsorped such that the interaction area with the surface is the smallest. Methanol has an asymmetric charge distribution where the presence of hydroxyl group gives rise to accumulation of electron density on it in the C-(OH) bond. The other three C-H bond do not give rise to such asymmetry. We see this clearly from it's HOMO (Figure 4.4(d)). Among these, the H atom having the least electron density is closest to the interface. The non-polar bond being in the proximity of the non-polar Silicene surface coupled with smallest interaction area gives rise to the weakest interaction among the group. Comparing with Ethanol, we find that the interaction area of Ethanol with Silicene is greater than that of Methanol. Moreover the hydroxyl group is closest to the surface. The greater concentration of electron density on it (HOMO of Ethanol is shown in Figure 4.4(c)) makes the interaction stronger in comparison with that in case of Methanol. Thus, the interaction area and the asymmetric charge distribution are responsible for greater adsorption energy in case of Ethanol. The presence of Carbonyl groups in Acetone and Methylacetate make these two molecules more polar than the others. HOMO of these two molecules (Figure 4.4(a),(e)) show accumulation of electrons around the O atom in the carbonyl group. This may give rise to an attaractive dipole-dipole interaction with the Silicene surface, making their physisorptions stronger than Ethanol and Methanol. This, coupled with their orientations when adsorped on Silicene (Figure 4.2) where the O in the carbonyl group is the closest to the surface,thus leading to a possible large interaction of charge densities of molecule and nanosheet, can be correlated with their larger energies of adsorption. In case of dimethylsulfide, there is substantial asymmetric charge distribution among the constituents of the molecule. The HOMO of this molecule (Figure 4.4(b)) show accumulation of electron density on the S atom. This atom being closest to the surface would make the interaction between the adsorbate and adsorbant very strong. This explains higher adsorption energy of this molecule as compared to the four others. We find the same trend in adsorption energies when the nanosheet is -F passivated Silicene. However, the adsoption in case of -F passivated silicene is weaker. This can be understood the following ways: when the silicene surface is functionalized with -F, very strong Si-F covalent bonds are formed. Since -F is highly electronegative, a protective layer is created on the silicene surface that prevents silicene from reacting with VOC molecules. The strong Si-F bonds, too, make it difficult for VOC molecules to

react. Thus, the binding of VOCs is relatively weak when the nanosheet is -F passivated silicene.

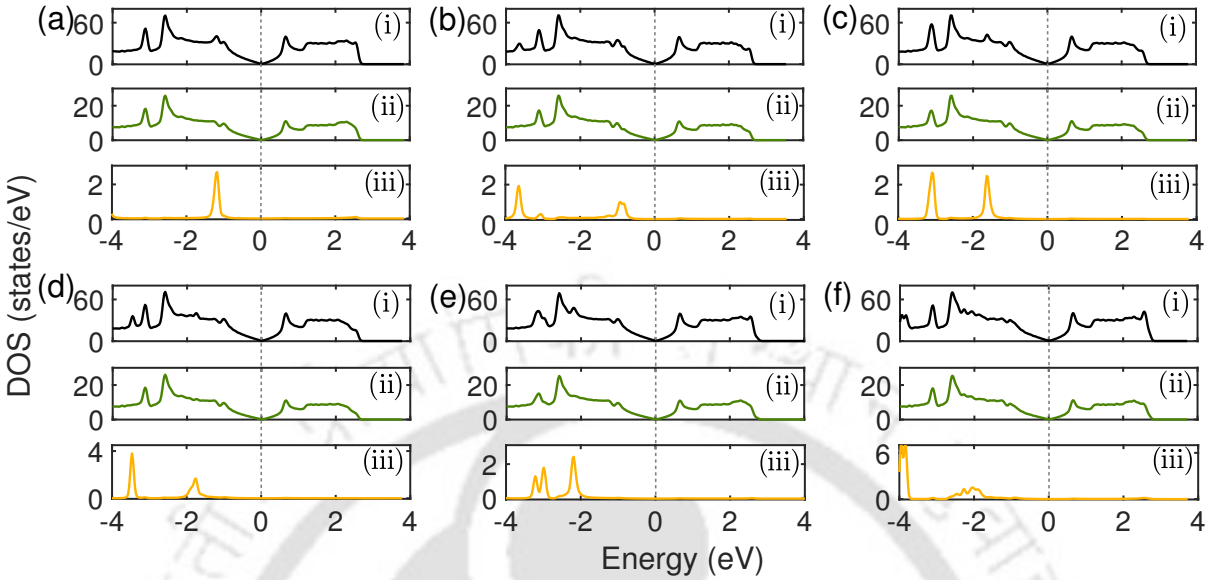

Figure 4.5: i) Total DOS (ii) DOS of silicene and (iii) DOS of VOC molecule in (a)Acetone-silicene (b)Dimethylsulfide-silicene (c)Ethanol-silicene (d)Methanol-silicene (e)Methylacetate-silicene and (f)Toluene-silicene systems.

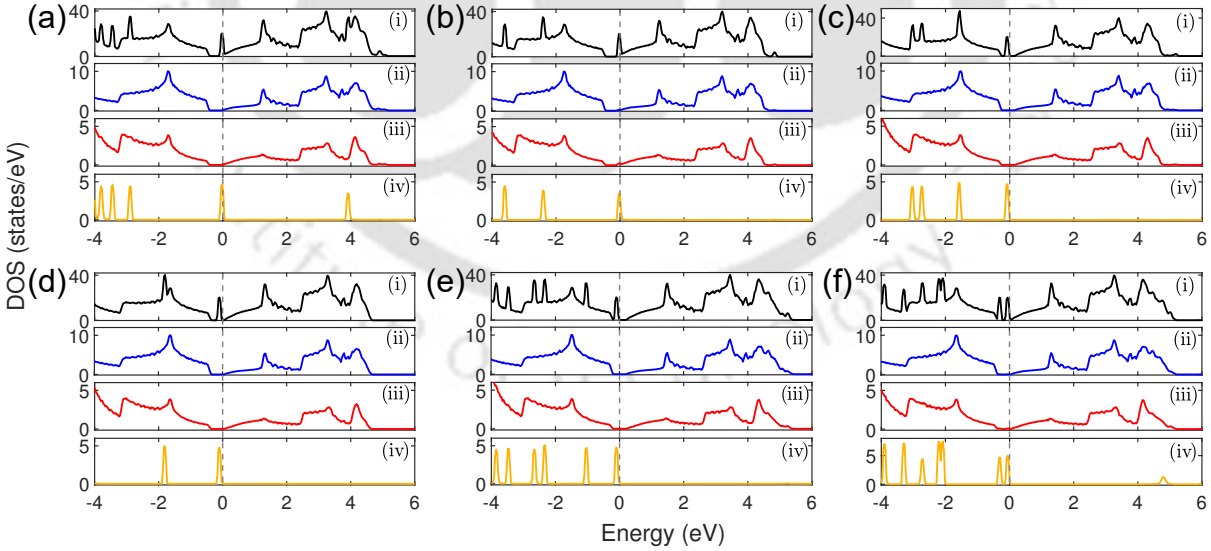

Figure 4.6: (i) Total DOS (ii) DOS of silicene (iii) DOS of F and (iv) DOS of VOC molecule in (a)Acetone-F-silicene (b)Dimethylsulfide-F-silicene (c)Ethanol-F-silicene (d)Methanol-F-silicene (e)Methylacetate-F-silicene and (f)Toluene-F-silicene systems.

4.2.2 Electronic Structure

A more profound understanding of VOC adsorption on the nanosheets and their possible consequences with regard to the sensing abilities of these 2D materials can be obtained by analyzing the electronic structures of the VOC-nanomaterial complexes.In Figures 4.5 and 4.6 we show the total and component-projected densities of states(DOS) of the systems considered in this work.Comparison with DOS of isolated VOC molecules (Figure 4.7(a)) and bare Silicene molecules (Figure 4.8(a)) show that upon formation of adsorbate-adsorbent complexes, only the electronic structure of the VOC molecules change considerably. The noticeable effect in all cases is that the DOS consisting of sharp peaks as seen in the cases of isolated molecules, give way to broader peaks that are less in number. The states as a whole are pushed towards lower energies. The Total densities of states of the VOC complexes with silicene as the adsorbent (Figure 4.5) show that there is very little change in the electronic structure, particularly close to the Fermi level, upon adsorption of different VOCs. The significant difference in the total DOS occurs around -1 eV to -2 eV and between -3 eV to -4 eV due to the states of the VOC molecules. For all cases, the VOC states are contributed by the valence states of all constituent atoms (Figure 4.9). The structure around -1 eV for the Acetone-silicene complex (Figure 4.5(a)) is due to the hybridization of Si, C, and O p and C and H s states. The presence of two -CH_3 functional groups symmetrically networked with the C-O bond leads to near-equal contributions of all atoms of the molecule. In the case of adsorbed Dimethylsulfide, its states near -1 eV are contributed largely by the $3p$ states of S and s states of the two H atoms connected to the two C atoms and are closer to the surface of the nanosheet. The deeper states around -4 eV have contributions from valence orbitals of all atoms in the molecule. For Ethanol, upon adsorbed in silicene, the states around -2 eV are contributed by p orbitals of O, p orbitals of C, and the s orbitals of two H attached to them, situated closer to the sheet after relaxation (Figure 4.2(c) and (f)). For the adsorbed Methanol, the states around -2 eV are similarly contributed by the O p and s states from the two H atoms attached to the C atom (Figure 4.2(g) and (j)) while p states of O closer to silicene surface and those of two C atoms connected (Figure 4.2(h) and (k)) are the major contributors to the states near -2 eV for Methylacetate-silicene complex. The DOS of toluene-adsorbed silicene is somewhat different from the rest. This is due to weak contributions from toluene around -2 eV. The major contributions from the constituents of the Toluene molecule are located deeper in the valence band. The features in the densities of states imply that the charge transfer between the VOC and the nanosheet will be maximum for Acetone and least for Toluene VOC. Also, since there are no noteworthy changes in the electronic structures upon adsorption of different VOCs, the selectivity of the silicene sensor may be poor.

The electronic structure of F-Silicene undergoes considerable changes in comparison with bare Silicene (Figure 4.8(b)). The presence of -F functional groups modify Silicene electronic structure near the Fermi level, leading to opening of an energy gap. Hybridisation with p orbitals of F pushes the unoccupied states of Silicene to higher energies resulting in the energy gap. Consequently, the adsorption of VOCs on the F-silicene sheet produces remarkable changes in the DOS of the adsorbate-adsorbent complexes (Figure 4.6). A common feature found in all six cases is that the projected DOS of the molecules displays features of an isolated molecule. The molecular DOS now consists of sharp, discrete peaks. This is an artifact of the weak reactivity with the nanosheet due to the protective layer formed by the -F functional group, as discussed in the previous subsection. However, in this case, we find significant changes in the DOS of the systems.

Table 4.2: Energies of the Highest Occupied Molecular Orbital (HOMO), and the Lowest Unoccupied Molecular Orbital (LUMO) along with HOMO-LUMO gap for different adsorbate-adsorbant complexes considered in this work are shown.

Adsorped molecule	2D sheet	E_{HOMO} (eV)	E_{LUMO} (eV)	ΔE (eV)
-	silicene	-3.34	-2.54	0.80
	F-silicene	-4.16	-3.22	0.93
Acetone	silicene	-3.29	-2.44	0.85
	F-silicene	-3.38	-3.08	0.29
Dimethylsulfide	silicene	-3.20	-2.44	0.75
	F-silicene	-3.28	-3.16	0.12
Ethanol	silicene	-3.38	-2.49	0.89
	F-silicene	-3.72	-3.35	0.36
Methanol	silicene	-3.29	-2.46	0.83
	F-silicene	-3.72	-3.44	0.27
Methylacetate	silicene	-3.07	-2.15	0.83
	F-silicene	-3.78	-3.38	0.39
Toluene	silicene	-3.16	-2.31	0.85
	F-silicene	-3.46	-3.29	0.16

Table 4.3: Charge Transfer(Q) and Work function(ϕ) for different VOC-2D sheet combination considered in this work.

Adsorped molecule	2D sheet	**Q(e)**	ϕ (eV)
Acetone	silicene	0.055	4.58
	F-silicene	-0.058	5.81
Dimethylsulfide	silicene	-0.042	4.51
	F-silicene	-0.192	5.73
Ethanol	silicene	0.047	4.59
	F-silicene	-0.020	6.12
Methanol	silicene	0.043	4.60
	F-silicene	-0.012	6.15
Methylacetate	silicene	0.046	4.58
	F-silicene	-0.016	6.23
Toluene	silicene	0.006	4.57
	F-silicene	-0.055	5.96

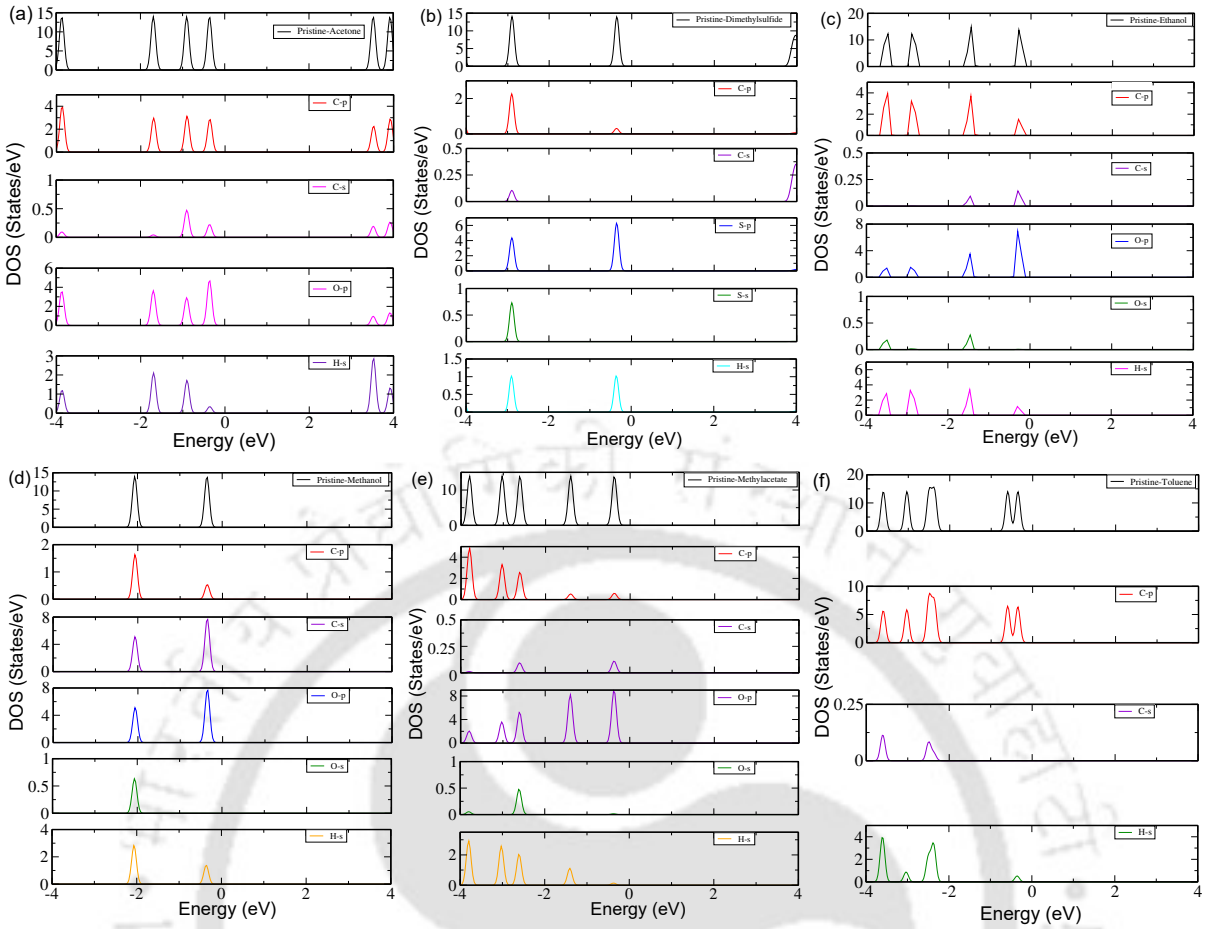

Figure 4.7: Total, atom and orbital projected densities of states of isolated (a) Acetone (b) Dimethylsulfide (c) Ethanol (d) Methanol (e) Methylacetate (f) Toluene molecule.

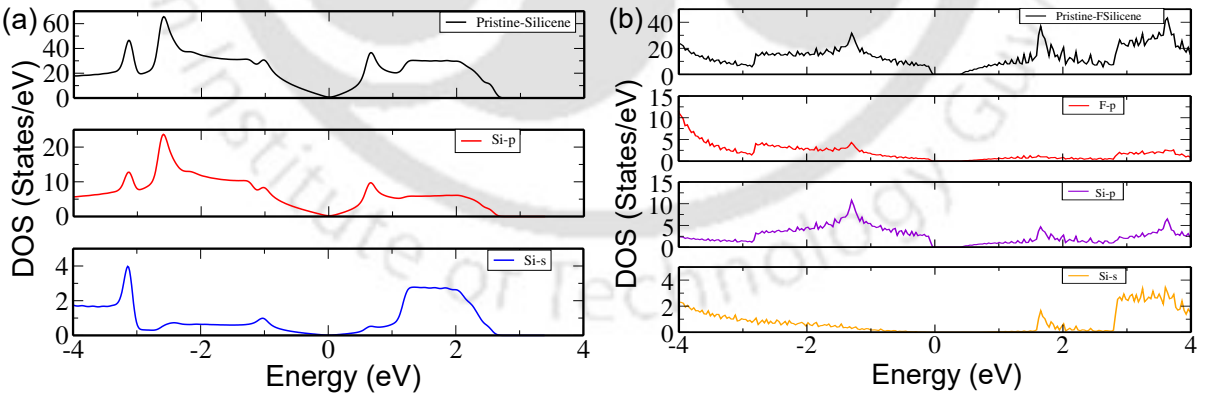

Figure 4.8: Total, atom and orbital projected densities of states of (a) Bare Silicene (b) Bare F-Silicene.

As mentioned earlier, functionalization by -F opens up a semiconducting gap. The adsorption of different VOC molecules produces discrete molecular states (contributed by the valence states of the constituents aligned closer to the surface of the nano-material) that are very close to the Fermi levels of the systems (Figure 4.10). The position of this

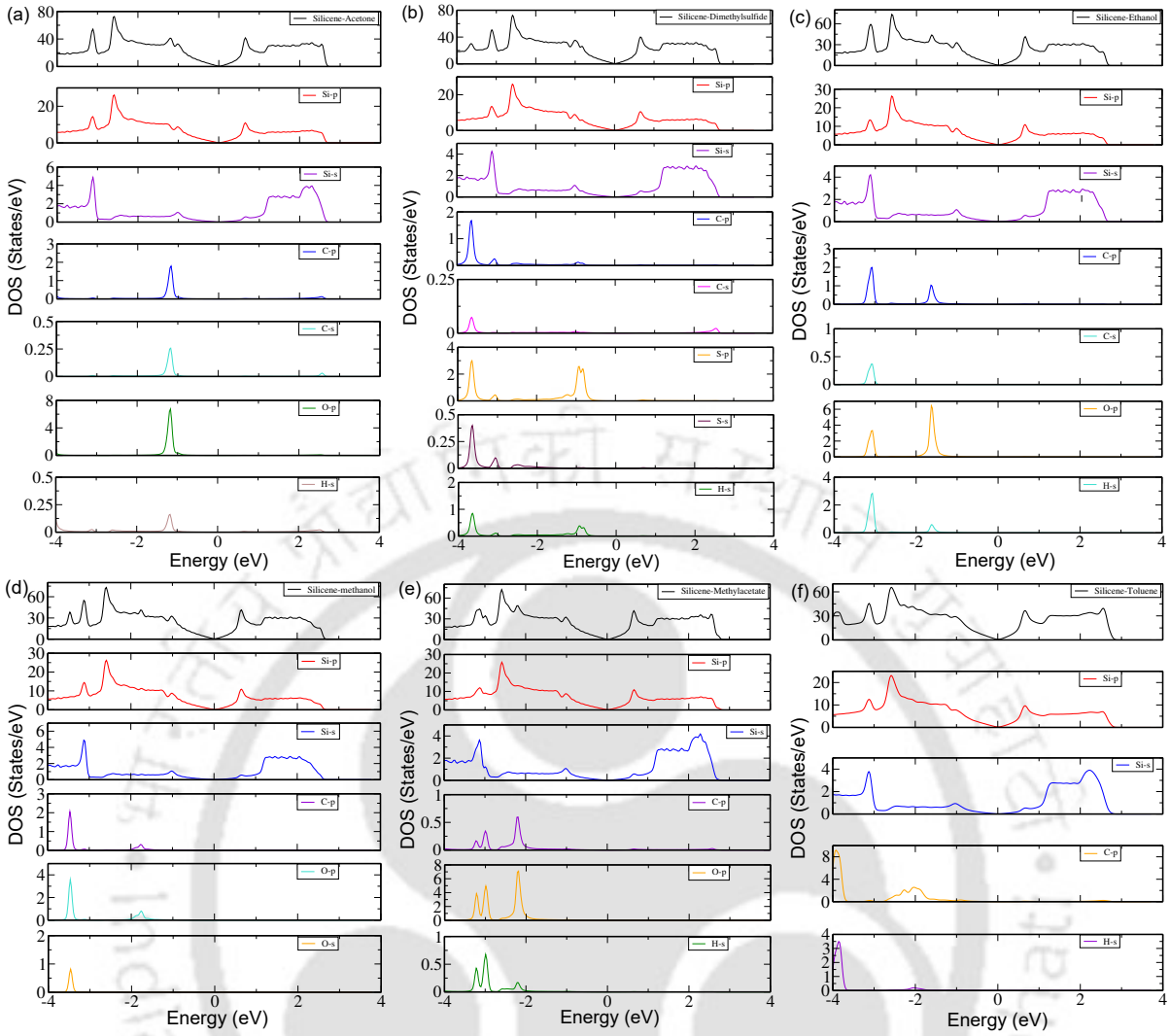

Figure 4.9: Total, atom and orbital projected densities of states of (a) Acetone (b) Dimethylsulfide (c) Ethanol (d) Methanol (e) Methylacetate (f) Toluene molecule adsorped on the Silicene nanosheet.

isolated state creates a noticeable difference between the electronic structures of different VOC-F-silicene complexes. This feature can be quite useful from the perspective of differences in charge transfers and sensitivity when F-silicene is used as a sensor material. The band structures of the six compounds presented in Figure 4.11 demonstrate this more clearly. In all cases, an isolated flat band appears below the Fermi level. This band represents the highest occupied molecular orbital (HOMO) of a given complex. This acts as a shallow donor state [139], reducing the band gap of the systems substantially, rendering the systems like an n-type semiconductor. The new band gap E_n, calculated as the energy difference between the conduction band minimum and the HOMO, is 0.055, 0.053, 0.281, 0.195, 0.346, and 0.137 eV for Acetone, Dimethylsulfide, Ethanol, Methanol, Methyl acetate, and Toluene adsorbed F-silicene, respectively. Such considerable reductions in the band gap imply lower activation energies required for the electrons in the shallow donor states for charge transport.

More understanding of the changes in the electronic states after molecular adsorption

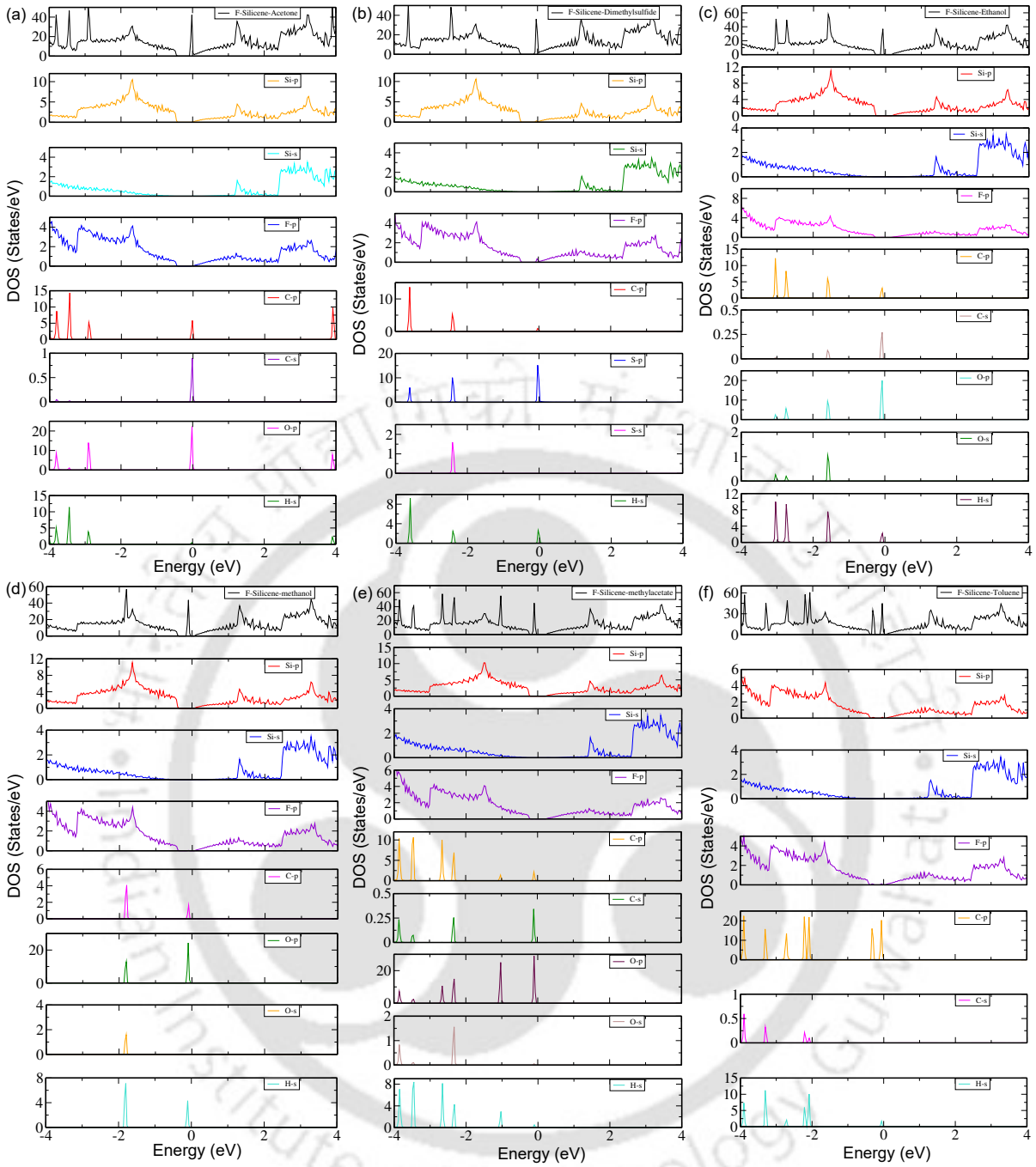

Figure 4.10: Total, atom and orbital projected densities of states of (a) Acetone (b) Dimethylsulfide (c) Ethanol (d) Methanol (e) Methylacetate (f) Toluene molecule adsorped on the F-Silicene nanosheet.

can be obtained from HOMO and LUMO of the adsorped systems. In Figures 4.12 and 4.13, we show the HOMO and LUMO of the VOC-nanosheet complexes for F-Silicene and Silicene substrates, respectively. The numerical values are presented in Table 4.2. The major observations are : (a)the positions of HOMO, LUMO when molecules are adsorped on Silicene do not change substantially. As a result, HOMO-LUMO gap varies between 0.75-0.89 eV while the gap for Silicene before molecular adsorption is 0.8 eV. This implies greater stability for these adsorbate-adsorbent complexes, (b) in contrast,

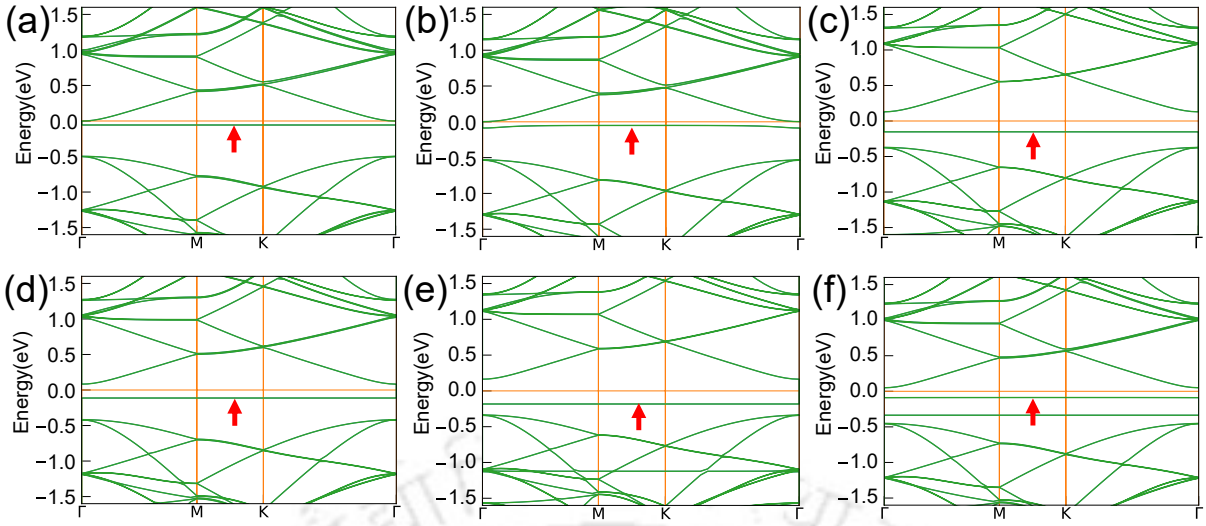

Figure 4.11: Band Structure of (a) Acetone-F-silicene (b)Dimethylsulfide-F-silicene (c)Ethanol-F-silicene (d)Methanol-F-silicene (e) Methylacetate-F-silicene and (f)Toluene-F-silicene systems.The shallow donor state in each case is marked by arrow.

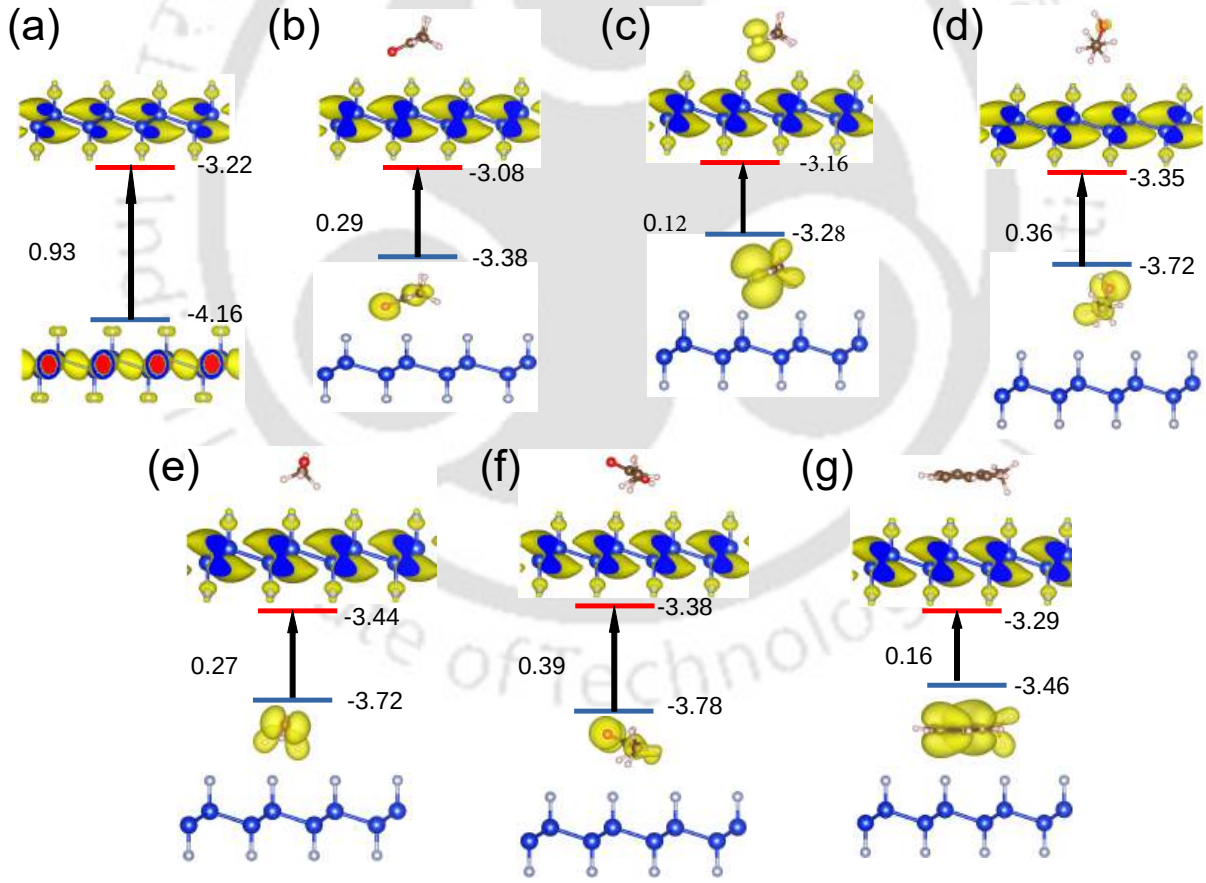

Figure 4.12: HOMO-LUMO orbitals of pristine F-Silicene is shown in (a). Same are shown after adsorption of (b) Acetone (c) Dimethylsulfide (d) Ethanol (e) Methanol (f) Methylacetate (g) Toluene molecule. The energies are in eV.

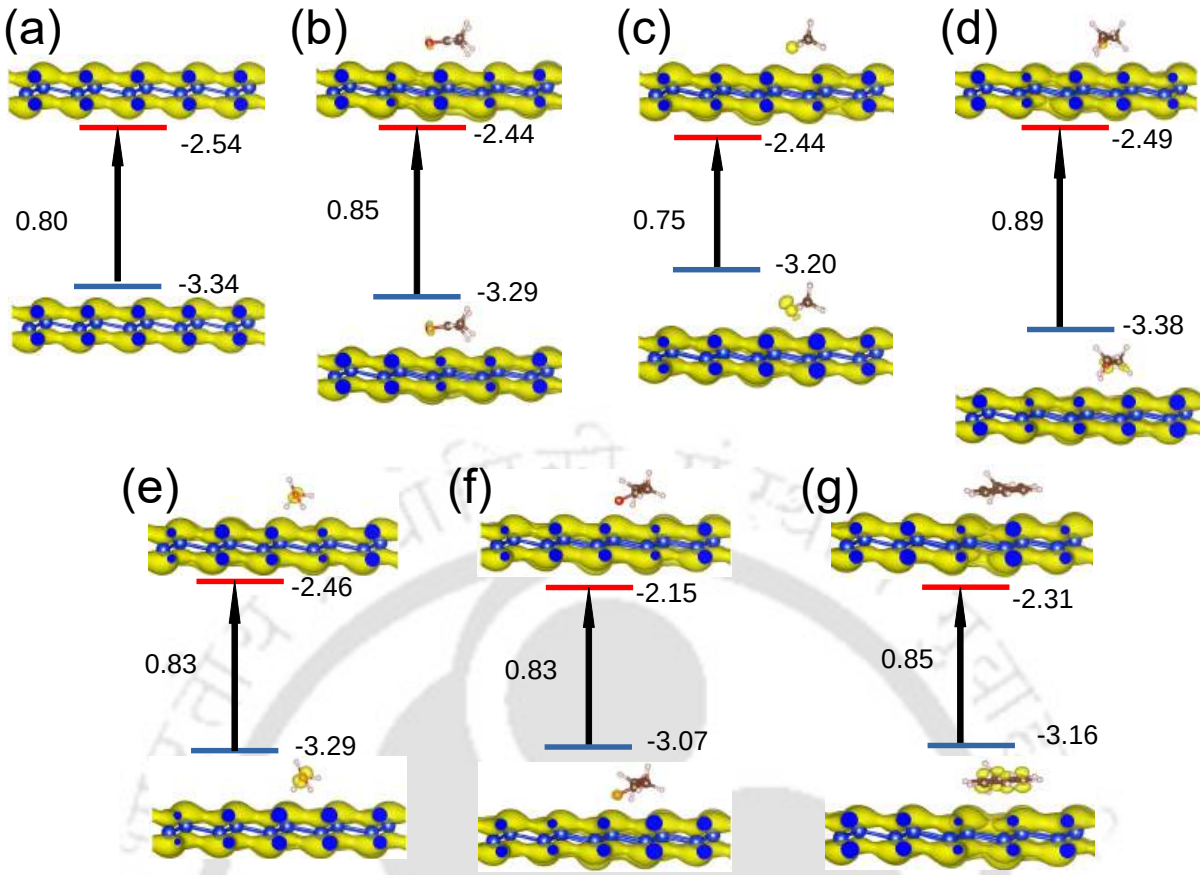

Figure 4.13: HOMO-LUMO orbitals of pristine Silicene is shown in (a). Same are shown after adsorption of (b) Acetone (c) Dimethylsulfide (d) Ethanol (e) Methanol (f) Methylacetate (g) Toluene molecule. The energies are in eV.

the positions of HOMO,LUMO and the size of the HOMO-LUMO gap undergoes large change and variation across molecules when the substrate for adsorption is F-Silicene. Largest variation in HOMO-LUMO gap occurs for Toluene and Dimethylsulfide. This implies that among the six molecules, the interaction strength of these two with F-Silicene are the highest. This agrees perfectly with the trends in the adsorption energies. (c)In case of F-Silicene-VOC complexes, larger variation occurs in HOMO as compared with variation in LUMO. This indicates the electron donating character of the molecules. This is consistent with the donor states seen in the band structures (Figure 4.11). The opposite is observed for cases when substrate is Silicene, though the degree of variation is less. This implies the electron accepting character of the molecules. In both cases it agrees with the directions of charge transfer, discussed later, (d)For F-Silicene-VOC complexes, the HOMO of all are completely form the molecular states while the LUMO are completely from the states of the nanosheet. This is in perfect agreement with the DOS discussed above. This also indicates that the charge transfer in this case will be from the molecule to the nanosheet. For Silicene-VOC complexes, both HOMO and LUMO are contributed by the Silicene and the molecules. However, the states are mostly concentrated on Silicene. This is in agreement with the features in the DOS discussed above that is across the molecules, there is very little changes in the electronic structures.

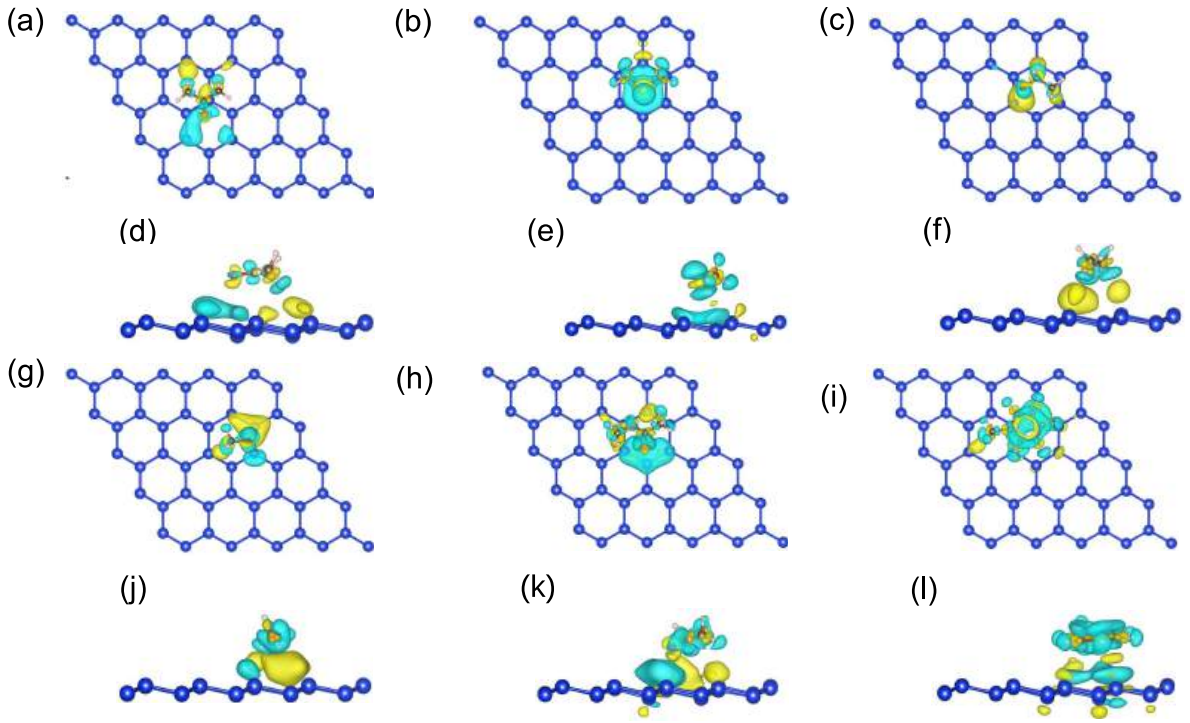

Figure 4.14: (a-c)Top and (d-f)side view of iso-surface charge density plots of acetone, dimethylsulfide, ethanol adsorped in Silicene nanosheet, respectively. (g-i) Top and (j-l)side view of iso-surface charge density plots of methanol, methylacetate and toluene adsorbed on Silicene nanosheet, respectively. Isosurface value is 0.0003 $e/^3$. Yellow and cyan colors represent charge accumulation and depletion regions, respectively.

4.2.3 Charge transfer and Work function

In order to substantiate the inferences drawn from analysis of the electronic structures of the VOC-nanosheet complexes, we first present, in Fig 4.14 and 4.15, the differential charge densities for VOC-Silicene and VOC-F-Silicene complexes, respectively. In both cases, the natures of differential charge densities imply physisorption as no signature of strong bond formation is observed. In case of Silicene as the nanosheet, there are more depletion than accumulation on the sheet. This indicates a charge transfer from the nanosheet to the molecule. In case of Toluene adsorption, there are accumulation and depletion regions of equal intensity in and around Silicene. The charge density on the molecule is accumulated(depleted) on the aromatic ring (outer bonds). This implies very little charge transfer. Larger charge transfers are expected in cases of Ethanol, Methanol and Methylacetate. The accumulation pattern in these three cases indicate a possibility of hydrogen bond formation in them. With F-Silicene as the nanosheet, the nature of charge transfer changes drastically. The figures in 4.15, indicate that the magnitude of charge transfer is much less compared to the case when Silicene is the substrate for adsorption.

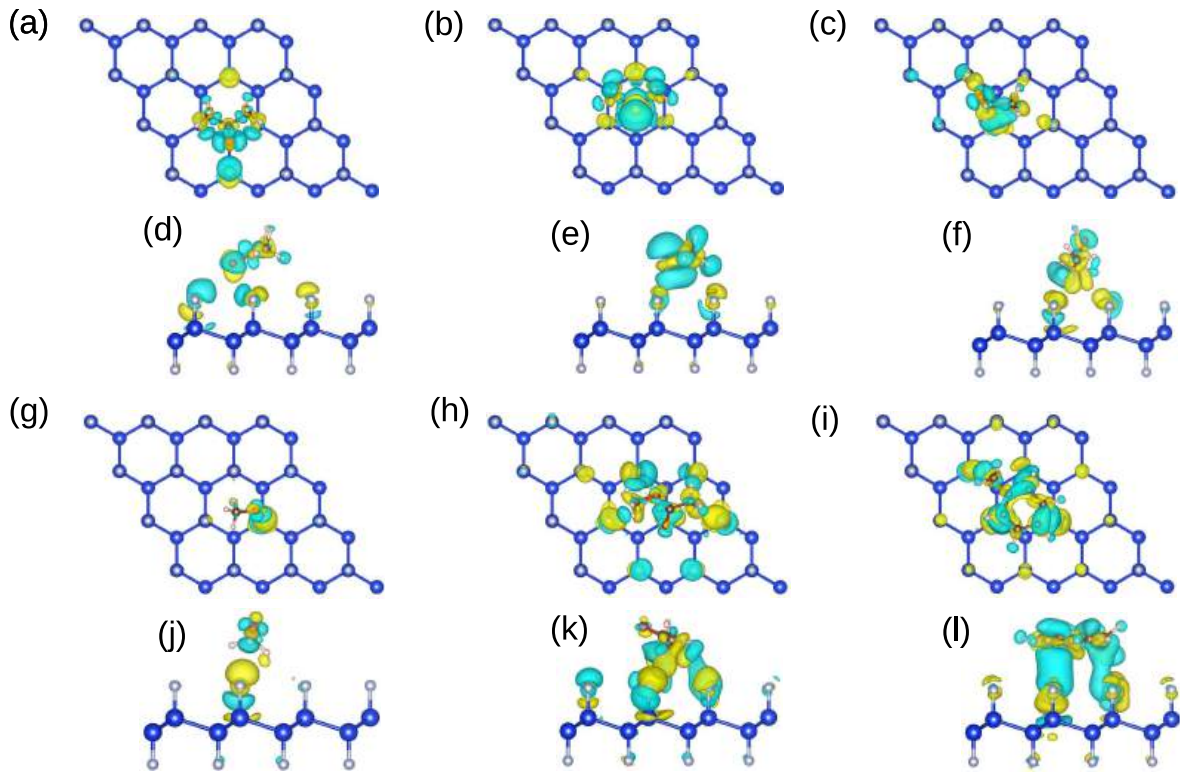

Figure 4.15: (a-c)Top and (d-f)side view of iso-surface charge density plots of acetone, dimethylsulfide, ethanol adsorped on F-Silicene nanosheet, respectively. (g-i) Top and (j-l)side view of iso-surface charge density plots methanol, methylacetate and toluene adsorbed on F-Silicene nanosheet, respectively. Isosurface value is 0.0003 $e/^3$. Yellow and cyan colors represent charge accumulation and depletion regions, respectively.

Significant accumulation on the -F functional group indicates that in this case, charge is transferred from the molecule. To substantiate the observations from differential charge densities, in Figure 4.16, we present the results of charge transfer Q and work function ϕ for VOCs adsorbed on both silicene and F-silicene nanosheets. $Q < (>)0$ indicates charge transfer from the molecule(nanosheet) to the nanosheet (molecule). Analyzing the trends in Q, we find that the charge transfers, in general, are small, irrespective of the nanosheet. This is consistent with the observations made from differential charge densities and the fact that the adsorption in the present context is physisorption only. The other noticeable features are the following: (a) $Q < 0$ when the nanosheet is F-silicene. This corroborates the donor levels obtained in the band structures and the inferences from Figure 4.15. (b)With silicene as the nanosheet, $Q > 0$ for all cases except the adsorption of Dimethylsulfide. Dimethylsulfide has two lone pairs coming from S. As a result, it acts as a donor instead of the acceptor. This is consistent with the HOMO and LUMO for this system. (c) Q is greater in magnitude when the nanosheet is F-silicene. This is consistent with the fact that the molecular electronic states lie deeper in energies (Figure 4.4) when molecules are adsorbed in pristine silicene. The greater

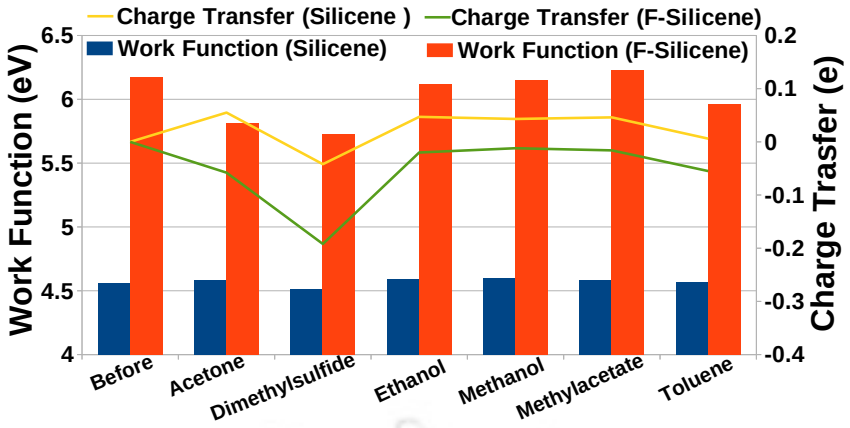

Figure 4.16: Charge Transfer and Work functions before and after adsorption of different VOCs on silicene and F-silicene.

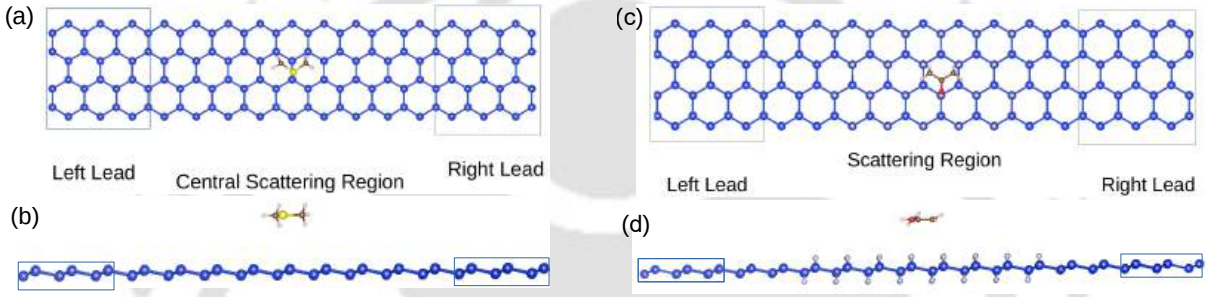

Figure 4.17: (a) Top and (b) side views of the schematic structural model of a gas sensor based on silicene with two semi-infinite electrodes . The areas marked by square boxes represent semi-infinite electrodes.The central part of the figure where the molecule is physisorped (Dimethylsulfide is shown here) is the scattering region. (c) and (d) represent the same but for F-silicene gas sensor. The physisorbed molecule shown in the schematics is Acetone.

charge transfer for F-silicene is also an artifact of the presence of highly electronegative -F on the surface of the 2D material. (d) With silicene as the adsorbent, there is hardly any charge transfer between Toluene and silicene ($Q = 0.006e$), while it is maximum in the case of Acetone adsorbate ($Q = 0.055e$). For the other four molecules, Q varies between 0.042 and 0.047. This corroborates the implications stated by the analysis of the DOS. (e) For both adsorbents, Dimethylsulfide enforces the largest charge transfer. (f) In the case of the F-silicene nanosheet, charge transfer amounts are almost identical when Acetone and Toluene are adsorbed ($Q = -0.058e, -0.055e$ for Acetone and Toluene, respectively). Qualitatively, the same is seen when the other three VOCs are adsorbed. However, Q is less in their cases: -0.012e, -0.020e, and -0.016e for Methanol, Ethanol, and Methylacetate, respectively. Once again, such qualitative behavior validates the conclusions from the electronic structures. It is to be noted that the appreciable changes in the charge transfers upon adsorption of different molecules on an adsorbate are supposed to affect its resistance, which can be experimentally measured and is directly connected to the sensitivity when used as a sensor.

In an adsorbate-adsorbent complex, if the absorbate is an acceptor (donor), the Fermi

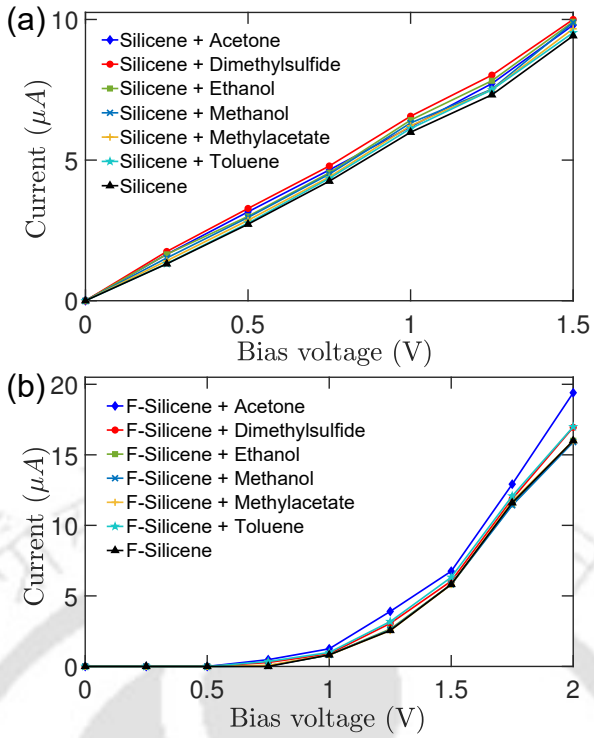

Figure 4.18: I-V characteristic of (a)silicene and (b)F-silicene sensors with and without adsorption of the six VOCs separately.

energy of the system is lowered(elevated), increasing (decreasing) the work function as a consequence. The work function ϕ of pristine silicene (F-silicene) is 4.56 eV (6.17 eV). Higher ϕ of F-silicene is due to strong Si-F bonds as opposed to an unpassivated silicene surface. From Figure 4.16 and Table 4.3, we find that ϕ of the compounds after adsorption of VOCs on pristine silicene increase only slightly (4.57 eV for Toluene adsorped to 4.61 for Methanol adsorped silicene); the only exception is Dimethylsulfide where ϕ=4.51 eV. This is understandable as the molecule is a donor. Large changes in ϕ are observed when the adsorbent is F-silicene. The changes are hardly noticeable (with respect to ϕ of F-silicene before adsorption) for Methyl acetate, Ethanol, and Methanol. Large changes are observed in the case of the other three molecules: ϕ=5.73 eV, 5.82 eV, and 5.96 eV for Dimethylsulfide, Acetone, and Toluene, respectively. This trend of ϕ correlates with Q; the larger the Q, the lower the work function. The results, therefore, indicate the possible selectivity of these three molecules when F-silicene is used as a sensing material. On the other hand, the results imply that silicene, when used as a sensor for these VOCs, may not be able to discriminate between them as has been inferred from the electronic structure.

4.2.4 Sensing performances

In Figure 4.17 (a) and (b), we show the device setup with pristine and F-silicene, respectively. The central region is smoothly joined to the periodic electrodes in the transport direction (z in this case). To screen out the perturbations in the sensing regions, the electrode regions are extended into the central scattering region. The $I-V$ characteristics with and without gas adsorptions by silicene and F-silicene are shown in Figure 4.18 (a)

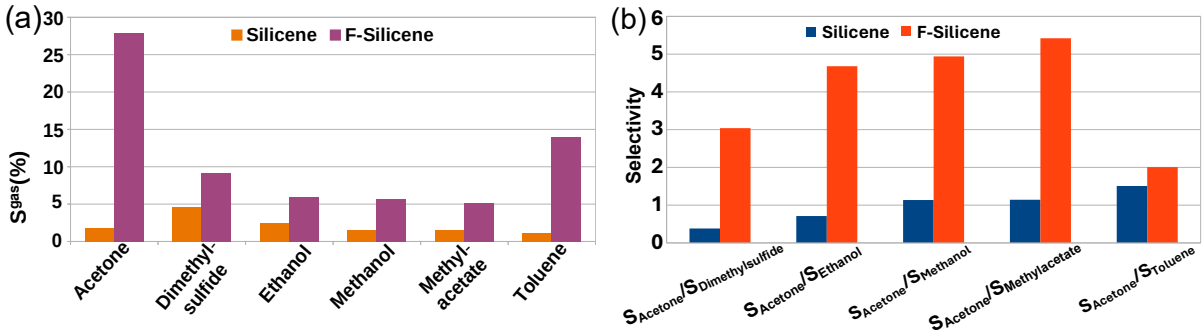

Figure 4.19: (a) Sensitivity of silicene and F-silicene towards the six VOCs considered in this work (b) Selectivity of silicene and F-silicene for detection of Acetone.

and (b), respectively. Application of a bias voltage V_b to the device elevates the Fermi level of the left electrode with respect to the right electrode. When V_b supersedes the threshold voltage at which the conduction band minimum of the right electrode matches with the valence band maximum of the left electrode, the current starts to flow. As seen in Figure 4.18, this threshold is 0V(0.5 V) for pristine silicene (F-silicene). The values are consistent with the electronic band gaps of the bare materials. $I-V$ characteristics curves for VOC adsorped silicene are linear, while those for F-silicene are parabolic. In a pristine silicene device, the curves are barely separable from one another. The current for VOC-adsorbed silicene is always higher than that of bare silicene. The current reaches a maximum of 10 μA at 1.5 V when Dimethylsulfide is adsorbed. The lowest current is observed in the case of Toluene adsorption.

For the F-silicene device, the current curves corresponding to each VOC-complex start to get separated from each other around a bias voltage of 0.75V. For each VOC-F-silicene complex, the maximum current is higher than the one corresponding to the pristine silicene device. This suggests a better sensing capability of F-silicene, as predicted in earlier sub-sections. Here, the highest current is observed for the Acetone-F-silicene system with a maximum of 19.4 μA at 2V. Toluene and Dimethylsulfide are the two recording the next highest currents. The $I-V$ curves for the other three VOC complexes are barely separable from one another and the bare F-silicene. This behavior is consistent with the qualitative trends in charge transfer and work functions.

In Figure 4.19(a), we compare the sensitivities of silicene and F-silicene sensors with regard to the six food VOC molecules. The results presented are for $V_b = 1.23$ V. For the silicene gas sensor, the maximum sensitivity of only about 5 % is obtained for Dimethyl-sulfide. The lowest sensitivity is obtained for Toluene ($\sim$ 1 %). The sensitivities for Acetone, Methanol, and Methylacetate are almost the same. The sensitivity of Ethanol is slightly higher. The trend is consistent with the behavior of charge transfer and DOS of VOC-silicene complexes. Low and near identical sensitivity for all six systems can be correlated to the near identical DOS with respect to each other and in comparison with bare Silicene. A remarkable improvement is obtained in the case of the F-silicene sensor. The sensitivity for Acetone increases nearly 16 times, reaching nearly 30%. The sensitivities of Toluene and Dimethylsulfide, too, improved significantly, reaching nearly 14 % and 10 %, respectively. For the other three VOCs, too, sensitivities improve to near 5%. Here too, the sensitivities can be directly correlated to the qualitative nature of variations in charge transfer which in turn can be connected to the features of their DOS.

Table 4.4: Recovery time τ (in s)of silicene and F-silicene gas sensors to sense food VOCs. The calculations are done at room temperature (T = 300K) and under visible light ($\nu_0 = 10^{12}$ s^{-1}).

Molecule	silicene	F-silicene
Acetone	1.15×10^{-7}	3.89×10^{-7}
Dimethylsulfide	2.29×10^{-5}	7.57×10^{-7}
Ethanol	4.38×10^{-7}	1.58×10^{-8}
Methanol	3.27×10^{-8}	1.13×10^{-9}
Methylacetate	5.95×10^{-6}	1.2×10^{-6}
Toluene	0.18	2.85×10^{-4}

For example, larger charge transfers in Toluene and Acetone lead to greater sensitivities compared to the other four as the relative conductances (with respect to bare F-Silicene) are greater.Our results with F-silicene as the sensor compare well the experimental result with r-GO where the sensitivities are found to vary between 5 and 25 % [192].The sensitivities with regard to Acetone and Toluene, obtained in our calculations, are either better or comparable with respect to DFT+NEGF results obtained with other 2D sensors. For example, sensitivity for Acetone and Toluene with BC_6N sensor are 6.1 % and 14.7 % while those with defective-BC_6N are 1.7 % and 8.8 % only [222]. For Ethanol and methanol, the sensitivity of the F-silicene sensor is somewhat poor compared to the sensitivity obtained by DFT+NEGF calculations on other 2D materials. With BC_6N, the sensitivity for Ethanol and Methanol are 14.7 % and 9.5 %, respectively. It is 61 % and 8.8 % with defective BC_6N, 21 % for both with $MoSe_2$ [242], 52 % for both with Graphyne [243], 5% for both with Green phosphorene [244] and 9 % for Ethanol with Black Phosphorene[141].

In Figure 4.19(b), we show the comparative abilities of silicene and F-silicene sensors in discriminating the molecules. The sensitivity of Acetone has been considered the reference, and the ratio of its sensitivity to that of another molecule is considered a quantitative measure of the selectivity of that molecule. The selectivity using a silicene sensor is poor in comparison with F-silicene. In fact, silicene sensors cannot separate Methanol and Methyl acetate at all. On the contrary, F-silicene can clearly distinguish between Acetone, Dimethylsulfide, Toluene, and Methylacetate. The selectivities of Ethanol and Methanol are very close, 4.6 and 4.9, respectively. Therefore, we can conclude that F-silicene can separate out at least four VOCs emitted by food products. The performance is significantly better than r-GO sensors [193], which could not discriminate between any of the six VOCs.

In Table 4.4, we present calculated values of sensor recovery time τ for both silicene and F-silicene sensors. The results suggest that both silicene and F-silicene can work as reusable sensors for sensing the VOCs from food materials. Calculated recovery times for silicene-based sensors turn out to be smaller than those for pristine and defected-BC_6N [222]. τ of pristine(defected) BC_6N sensors in case of Acetone, Ethanol, Methanol and Toluene desorption are 2.6×10^{-6}(740) s, 2.3×10^{-6}(4.9) s, 2.1×10^{-7}(4.2) s and 2×10^{3}(6.8×10^{3}) s, respectively, orders of magnitude higher than silicene based sensors. Thus, the silicene and F-silicene nanosheets will function more efficiently as sensors than many other 2D materials.

4.3 Conclusions

Using a combination of the based first-principles method and non-equilibrium Green's function technique, we have investigated in detail the sensing abilities of two-dimensional silicene and -F functionalized silicene nanosheets for standard VOCs emitted by canonical food products like meat, fruits, and vegetables. We have systematically analyzed the structural parameters, the energetics, the electronic structures, and charge transfers when silicene-based 2D materials are used to adsorb the VOC molecules. Based on these, we have concluded that F-silicene is a better candidate as a sensor. Our insights from such analysis of microscopic physics are then put to the test by modeling sensor devices and making a direct comparison with the experimental quantities. We find that F-silicene indeed has a much better sensitivity than pristine silicene as far as VOCs from food products are concerned. This is due to the presence of highly electronegative -F atoms on the surfaces makes it highly reactive, enabling greater electron trasfer between the substrate and the molecules. The sensitivities for select molecules obtained by using F-silicene as the sensing material compare well with the available results using other 2D materials as sensors. Moreover, silicene-F is able to clearly discriminate between at least four molecules: Acetone, Dimethylsulfide, Methyl acetate, and Toluene. The selectivity is comparable to the other two. Finally, we establish the re-usability of silicene-based sensors to detect these VOCs by computing the desorption time under excitation by visible light. We find that the physisorption of the adsorbates actually helps in faster desorption of molecules. This, in turn, should enhance the sensor's re-usability [245]. The results with F-Silicene, upon comparison with Graphene based ones presented in the pervious chapter, demonstrates greater sensitivities when used as chemiresistive sensor. So, F-Silicene could be used as a chemiresistive sensor due to it's charge trasfer property, work-function difference, large shifting of HOMO-LUMO shifts makes it a good sensing material. Thus F-Silicene can be considered as an alternative to Graphene based sensors in the context of monitoring food degradation.

Chapter 5

Understanding the sensing potentials of MXene Sc_2CO_2 and Sc_2CO_2/WSe_2 MXene/TMDC heterostructure towards VOCs of standard food products

In this chapter we explore sensing capabilities of Sc_2CO_2 and Sc_2CO_2/WSe_2 heterostructure towards VOCs of standard food products, the markers of their stages of degradation, considered in the previous two chapters. Among the family of 2D materials, MXenes, the class of materials with the general formula $M_{n+1}X_nT_x$, (M an early transition metal, X is C or N, T a surface passivating group, $n > 0$,an integer) offer excellent metallic conductivity, hydrophilicity, and large interlayer spacing that make them ideal for surface interactions and rapid electron transfer.The flexibility in their structure and composition make them explorable towards improvements in sensing applications. Subsequently,several MXenes have turned out to be significantly sensitive towards different VOCs [246, 247, 38, 248, 249, 220, 250, 38, 251, 252]. Transition metal dichalcogenides(TMDCs) is another family of materials found to be useful as chemiresistive sensors for VOC sensing[253, 254, 142, 255, 256, 137, 257, 258, 259, 260, 261].

Van der Waals(vdW) heterostructures built out of 2D materials from different families can have a quick transition between their building blocks with an abrupt inclination of carrier concentration over the interface [262]. The possibility of synergistic contribution from the constituents having different electronic attributes (band structures, Work functions) can lead to a regulated band alignment of the heterostructure enabling easy transport of carriers and efficient separation of electrons and holes [263]. This would lead to improved sensing and selectivity towards VOCs when adsorbed on them [264, 265].

Differences in surface activities, Work functions and electronic properties of a MXene and a TMDC can be exploited in an advantageous way by building a heterostructure with these two as constituents. The differences in their properties can induce new features at the interface and give rise to novel properties. This has been observed in the context of memory device applications, for example in Sc_2CO_2/VSe_2 heterostructure[266]. Improved sensing properties with regard to gas molecules including VOCs in MXene/TMDC heterostructures have also been observed both computationally and experimentally [267, 268, 269]. For example, $Ti_3C_2T_x/WSe_2$ shows significantly improved NO sensitivity

[270], attributable to optimized Work-function alignment, efficient charge transfer at the heterointerface, and suppression of metal-induced gap states. $MoS_2/Ti_3C_2T_x$ heterostructures deliver rapid carrier transport via conductive MXene channels and abundant adsorption sites on MoS_2, leading to heightened sensitivity and fast response to different gases [271].Due to presence of WSe_2 in WSe_2/V_2C heterostructure,the sensing performance towards detection of ammonia is found to improve considerably [272]. A recent computational study of Sc_2CO_2, Sc_2CO_2/WSe_2 and $Sc_2CO_2/MoSe_2$ TMDs demonstrated improved sensitivity towards detecting phosgene ($COCl_2$) due to formation of MXene/TMDC heterostructure [273].

Exploration of potentials of MXene, TMDC and their heterostructure as sensors towards applications in the area of food quality assessment is practically absent. Apart from a recent computational study [38] that investigated the efficiencies of several M_2CT_x MXene sensors in detecting the VOCs associated with spoilage of meat, there is no other work available. Using Density Functional Theory(DFT) based calculations, in this work, we perform a detailed study into the sensing abilities of MXene Sc_2CO_2 and its heterostructure with TMDC WSe_2 towards the VOCs that are markers of degradation of generic fruit, meat and vegetables [193, 194, 195].A total of six VOCs - Acetone, Dimethylsulfide, Ethanol, Methonol, Methylacetate and Toluene, are the ones that make distinction between different stages of spoilage of these food products possible. Results from previous two chapters show that r-GO and F-Silicene can clearly distinguish Acetone, Dimethylsulfide, Ethanol and Toluene from a mixture of these six [274, 275]. We, therefore, choose these four for the present study. Sc_2CO_2 MXene is chosen for the following reasons: (a) among all MXenes, it possesses highest surface area per unit weight making it attractive for gas sensor applications [220], (b)it is among a handful of Mxenes that are synthesised [276] and (c)it is one of the rare semiconductors in the MXene family having a large electronic band gap. As major changes in its electronic structure, most notably in the electronic band gap, are anticipated upon interactions with VOCs, this opens the door for microscopic comprehension of the expected variations in its response following adsorption of various VOCs. The reasons for choosing WSe_2 for making heterostructure with Sc_2CO_2 are its complimentary electronic properties, compatible 2D layered structure, possibility to form a type-II heterojunction facilitating the charge separation enabling improved sensing performance. This uniqueness of WSe_2 has already been exploited in sensing applications [277, 278].

Subsequently, in this chapter, we explore the impacts on structural, electronic, optical and adsorption characteristics of Sc_2CO_2 and its heterostructure with WSe_2 upon interaction with the four VOCs mentioned above. By analyzing the variations in adsorption energy, charge transfer, electronic structure, Work function and optical properties due to VOC exposure, we provide insights into the fundamental mechanisms governing VOC sensing and identify key descriptors for sensor optimization. The findings of our study highlight the outstanding suitability of the Sc_2CO_2/WSe_2 heterostructure for VOC sensing applications. This study offers theoretical guidance for the development of high-performance VOC sensors based on 2D MXene-TMD heterostructures, and underscore the critical role of interfacial engineering in enhancing the sensitivity and selectivity of VOC sensors.

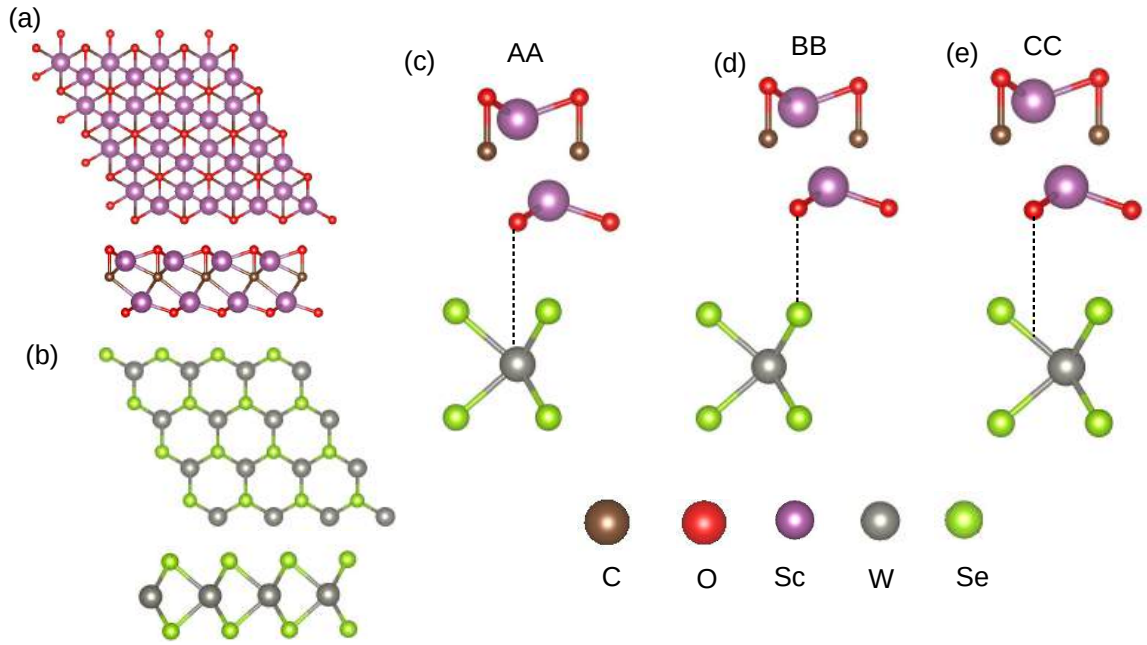

Figure 5.1: Top and side views of optimized structures of (a)Sc_2CO_2 and (b)WSe_2 monolayer Top and side views of optimized Sc_2CO_2/WSe_2 heterostructure in (c)AA,(d)BB,and (e)CC arrangements.

5.1 Methodology

The structural relaxations are done using the Conjugate-gradient method by setting the energy and force convergence limits as 10^{-4} eV and 10^{-2} ev Å^{-1}, respectively. The systems are modeled by $3 \times 3 \times 1$ supercells where a vacuum of 15 Åalong z-direction is kept throughout so that interactions between periodic images can be avoided. Plane waves upto energy of 450 eV are considered to ensure convergences in computed quantities. During self-consistent calculations, Brillouin zone is sampled with a Γ-centered $3 \times 3 \times 1$ k-point mesh. A denser mesh of $17 \times 17 \times 1$ is used for computation of electronic structures.

5.2 Results and Discussions

5.2.1 Structural and electronic properties of MXene and TMDC /MXene heterostructure

Optimized ground state structure of Sc_2CO_2 MXene monolayer is shown in Figure 5.1(a). The inversion symmetry is broken in the structure due to asymmetric nature of surface functionalization: the O-atom on one of the surfaces occupies the hollow site associated with the Sc atom while on the other surface, it occupies the hollow site associated with the C-atom. Consequently, $Sc^{(2)}$, the Sc atom on the lower surface in Figure 5.1(a) is in an octahedral crystal field, while $Sc^{(1)}$, the Sc atom on the top surface is in a trigonal prismatic crystal field. The calculated lattice parameter is 3.43 Å, in excellent agreement with the reported results [279]. The ground state structure of WSe_2 is shown in Figure 5.1(b). WSe_2 crystallizes in a honeycomb-like structure where each W atom is in a

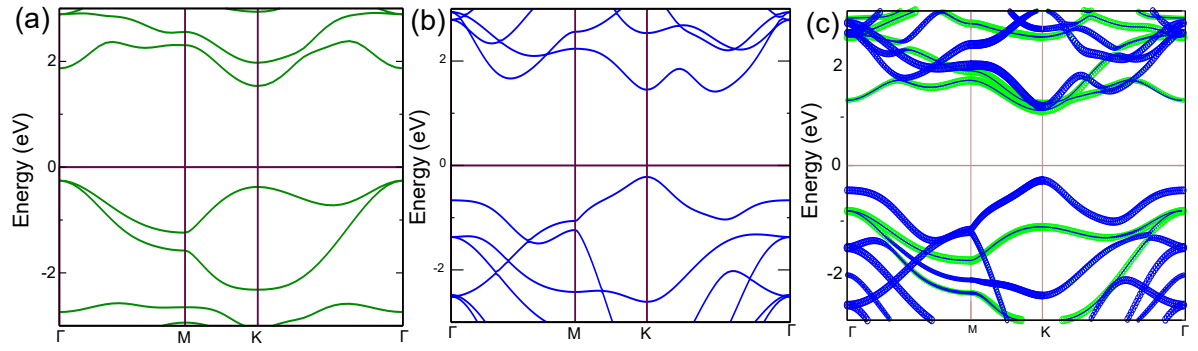

Figure 5.2: Band structure of (a)Sc_2CO_2,(b)WSe_2 and (c)Sc_2CO_2/WSe_2 heterostructure in CC arrangement. In (c)blue(green) bands correspond to WSe_2 (Sc_2CO_2).

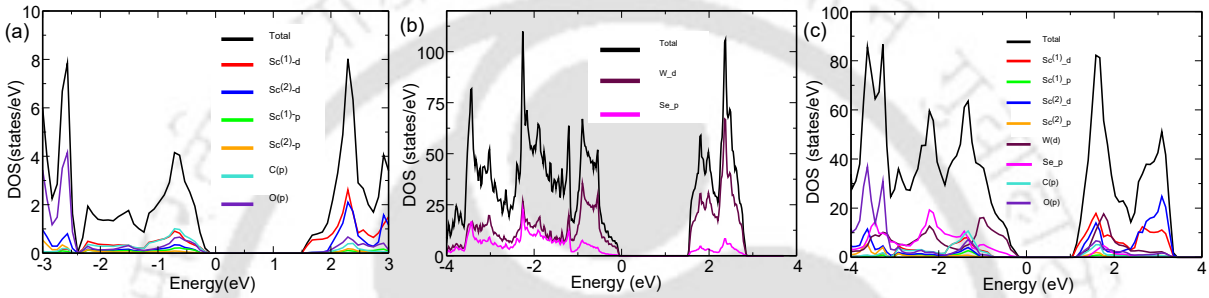

Figure 5.3: Total, atom-projected and orbital-projected densities of states (DOS) of (a)Sc_2CO_2,(b)WSe_2 and (c)Sc_2CO_2/WSe_2 heterostructure in CC arrangement.

trigonal prismatic crystal field formed by surrounding Se atoms. The calculated lattice constant of WSe_2 is 3.31 Å, in good agreement with existing results [280].

Since the mismatch between computed lattice parameters of Sc_2CO_2 and WSe_2 monolayers is only 3.6%, they can be stacked vertically to create a 2D vdW heterostructure. In Figure 5.1(c), we show three possible arrangements: AA where the O atom of Sc_2CO_2,closest to WSe_2 is directly above the W atom, BB where the O atom closest to WSe_2 is directly above the Se atom and CC where the O atom closest to WSe_2 is above a W-Se bond in WSe_2. The stability of the heterostructures is assessed by calculating their binding energies

$$E_b = [E_{hetero} - E_{Sc_2CO_2} - E_{WSe_2}] \tag{5.1}$$

E_{hetero} is the total energy of the heterostructure. E_{WSe_2} and $E_{Sc_2CO_2}$ are the energies of pristine monolayers of WSe_2 and Sc_2CO_2, respectively. The results are presented in Table 5.1. Significant negative values in each stacking arrangement implies that this heterostructure can be grown. We find that the binding is strongest in case of CC arrangement. This is consistent with earlier findings [273]. The interlayer distance also matches exactly to the results of Reference [273]. We,therefore,use the CC arrangement only for further investigations into the heterostructure.

In Figure 5.2 and 5.3, respectively, we present the electronic band structures and the densities of states(DOS) of the MXene, the TMDC and the heterostructure formed by them. We find excellent agreement with the existing results. Our calculated band gaps

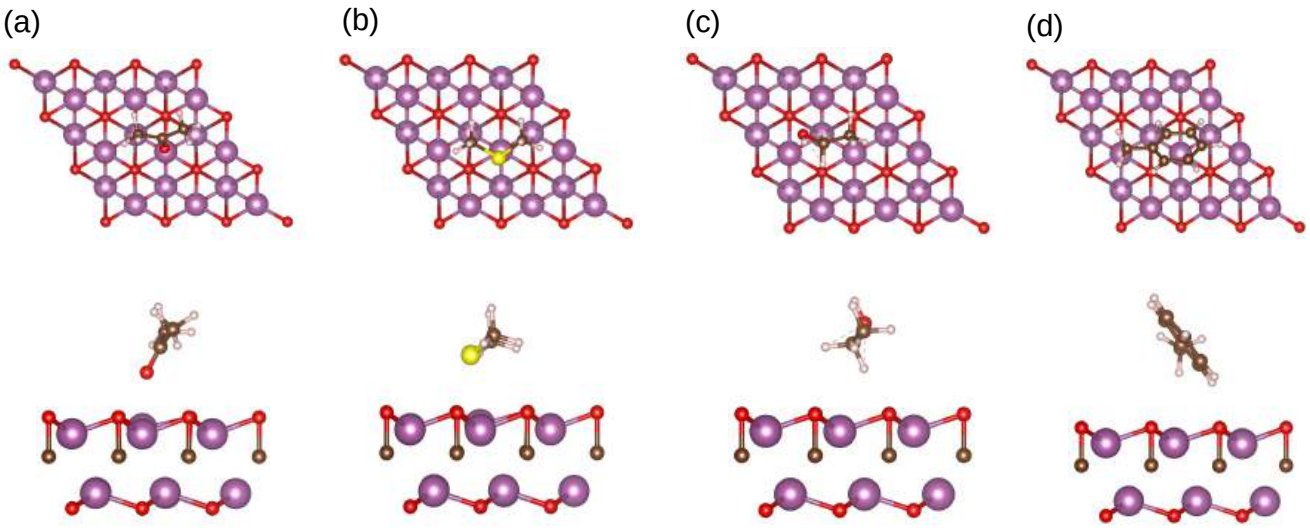

Figure 5.4: Optimized geometries of (a) acetone, (b) dimethylsulfide, (c) ethanol and (d)toluene adsorbed on Sc_2CO_2. The top(bottom) row of the figure stand for top(side) views of the adsorption configurations. Purple,brown,red,white and yellow balls represent Sc,C,O,H and S atoms.

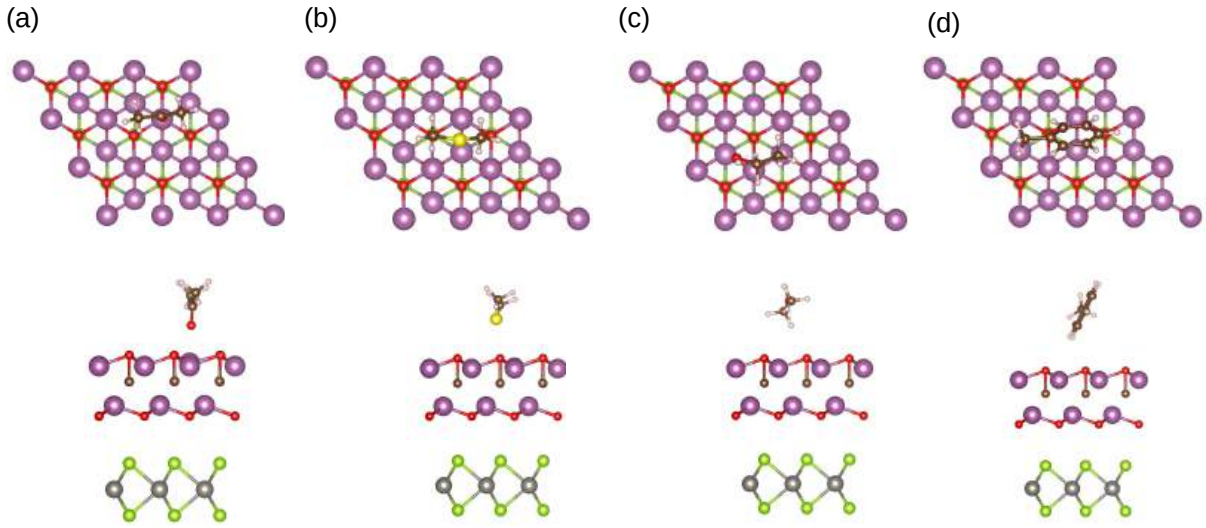

Figure 5.5: Optimized geometries of (a) acetone, (b) dimethylsulfide, (c) ethanol and (d)toluene adsorbed on Sc_2CO_2/WSe_2 heterostructure. The top(bottom) row of the figure stand for top(side) views of the adsorption configurations. Purple,brown,grey, silver,red,white and yellow balls represent Sc,C,W,Se,O,H and S atoms.

of Sc_2CO_2 and WSe_2 monolayers are 1.85 eV and 1.63 eV,respectively. They match well with the existing values [279, 280]. The band structure of the heterostructure(Figure 5.2)(c) shows that it is essentially a superposition of bands from the constituents, typical characteristic of 2D vdW heterostructures with weak coupling between layers. It is a direct band semiconductor with gap of 1.35 eV. The reduction in band gap with it being transformed from indirect (in Sc_2CO_2) to direct is due to the WSe_2 layer.The valence band maxima of the heterostructure is totally contributed by WSe_2 while the conduction

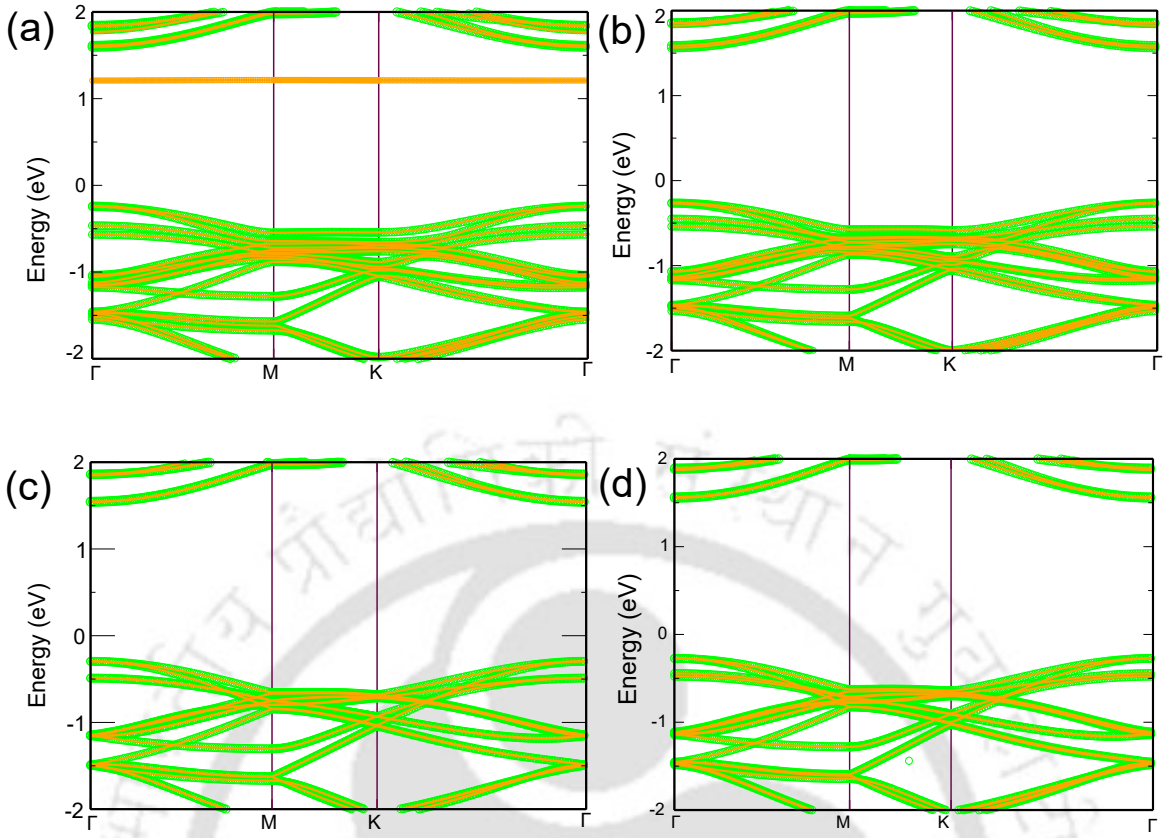

Figure 5.6: Band structures of (a) acetone, (b) dimethylsulfide, (c) ethanol, and (d) toluene -adsorbed Sc_2CO_2 surface. In each case, the green(orange) lines correspond to the contribution from Sc_2CO_2(molecules).

Table 5.1: Interlayer distance **d(Å)**, binding Energy $\boldsymbol{E_b}$ (eV) and band gap **(eV)** in case of different arrangements of constituents in $\mathbf{Sc_2CO_2}$/$\mathbf{WSe_2}$ heterostructure.

Arrangement	**d**	$\boldsymbol{E_b}$	**Band gap**
AA	3.39	-63.95	1.45
BB	3.41	-63.99	1.43
CC	3.55	-64.04	1.35

band minima is due to Sc_2CO_2. This enables efficient separation of electron-hole pairs at the heterointerface. The sensory response is expected to be enhanced as a consequence.

Total, atom-projected and orbital-projected electronic densities of states corresponding to Sc_2CO_2, WSe_2 and the heterostructure are shown in Figure 5.3(a)-(c),respectively. In Sc_2CO_2, d-states of $Sc^{(1)}$ contribute substantially to the band edges. While there is strong hybridisation of $Sc^{(1)} - d$,O$-p$ and C$-p$ orbitals making up the valence band maxima, the conduction band minima is contributed by $Sc^{(1)}$ only. In WSe_2, strong hybridisation of W$-d$ and Se$-p$ make up both band edges. Upon formation of heterostructure, the contributions from the constituents do not mix near the top of the valence band. It is d-orbitals of W and p-orbitals of Se that fill up the states available near Fermi level in the occupied part of the spectrum. The opposite happens at the bottom of the conduction band. Exactly like pristine Sc_2CO_2, the states at the bottom of the conduction band are

due to $Sc^{(1)}$ alone. This implies the transport of carriers across the interface.

5.2.2 Adsorption of VOCs on surfaces

5.2.2.1 Structural and electronic Properties

The optimized geometries of VOC-nanosheet complexes after adsorption are shown in Figures 5.4(for Sc_2CO_2 surface) and 5.5(for WSe_2/Sc_2CO_2 surface). The adsorption energy E_{ad} and D, the distance between surface and VOC, are presented in Table 5.2. The results suggest physisorption of VOCs. Analyzing them together, we find that there is a correlation between them. Acetone adapts the closest approach to the Sc_2CO_2 surface positioning its strongly polar C=O group directly above electronegative surface O atoms. This gives rise to strong electrostatic coupling between molecular dipole and surface, producing highest adsorption energy among the four. In case of physisorption on different surfaces like r-GO [275] and F-Silicene [274], Toluene had the largest adsorption energy among the same molecules considered in this work.In those cases, the molecule was adsorbed almost parallel to the surfaces leading to the strongest interactions between π electrons of the molecule and surfaces. In contrary, the Toluene molecule on Sc_2CO_2 is adsorbed in a near perpendicular manner. Despite this, the adsorption energy in this case is next to that of Acetone adsorption. Upon inspecting the geometry, we find that the origin of large E_{ad} is the strong interaction between hydrogen atoms on the benzene ring of toluene and O atoms on the surface of Sc_2CO_2. The electron rich benzene ring polarizes the surface electrons as the molecular polarizability of toluene is substantial; this promotes stronger vdW attraction, compared to the other two molecules, etahnol and dimethylsulfide. Thus, even without a favorable π-surface contact with Sc_2CO_2, the large polarizable π electron cloud of Toluene contributes to strong binding via dispersion and multipole interactions. Among Ethanol and Dimethylsulfide, the former binds at a shorter distance from the surface, yet the adsorption energy is lower. In comparison to Acetone and Toluene, E_{ad} of Dimethylsulfide is less because of its weaker molecular dipole and less effective overlap of the S lone pair with the surface atoms. The weakest adsorption seen in case of Ethanol is due to its orientation during adsorption. Figure 5.4(c) shows that the optimized configuration is where the -OH group is closest to the surface. This limits strong hybridisation and restricts interactions to moderate hydrogen bond-like electrostatic forces.

Table 5.2: Adsorption Energy E_{ad} (eV), distance between VOC and surface $\boldsymbol{D}$ (Å), chrage transfer $\boldsymbol{\Delta Q(e)}$ of VOC-nanosheet complexes

Nanosheet	**VOC**	$\mathbf{E}_{ad}$	$\boldsymbol{D}$	$\boldsymbol{\Delta Q}$
Sc_2CO_2/WSe_2	Acetone	-0.688	2.28	-0.738
	Dimethylsulfide	-0.580	2.20	-0.330
	Ethanol	-0.361	2.64	-0.178
	Toluene	-0.637	2.53	-0.361
Sc_2CO_2	Acetone	-0.587	2.38	-0.040
	Dimethylsulfide	-0.518	2.88	-0.057
	Ethanol	-0.340	2.73	-0.101
	Toluene	-0.579	2.40	-0.004

The same trend is observed in case of WSe_2/Sc_2CO_2 heterostructure. The only difference is that the E_{ad} in each case is larger in comparison with cases of adsorption on

Sc_2CO_2. This indicates that the presence of WSe_2 makes the binding stronger. From Table 5.2, we find that the largest change is E_{ad} happens in case of Acetone, followed by Dimethylsulfide. The adsorption geometries shown in Figure 5.5 explain this. For both cases, the molecules are adsorbed perpendicularly on the surface, reducing their distances. This makes the interactions, same as when the surface was pristine Sc_2CO_2, stronger. The orientations for the other two cases are hardly different from the respective cases of adsorption on pristine Sc_2CO_2, explaining the trends in E_{ad} completely. Moreover, presence of WSe_2 produces an internal electric field which makes the polarization stronger leading to higher binding energies.

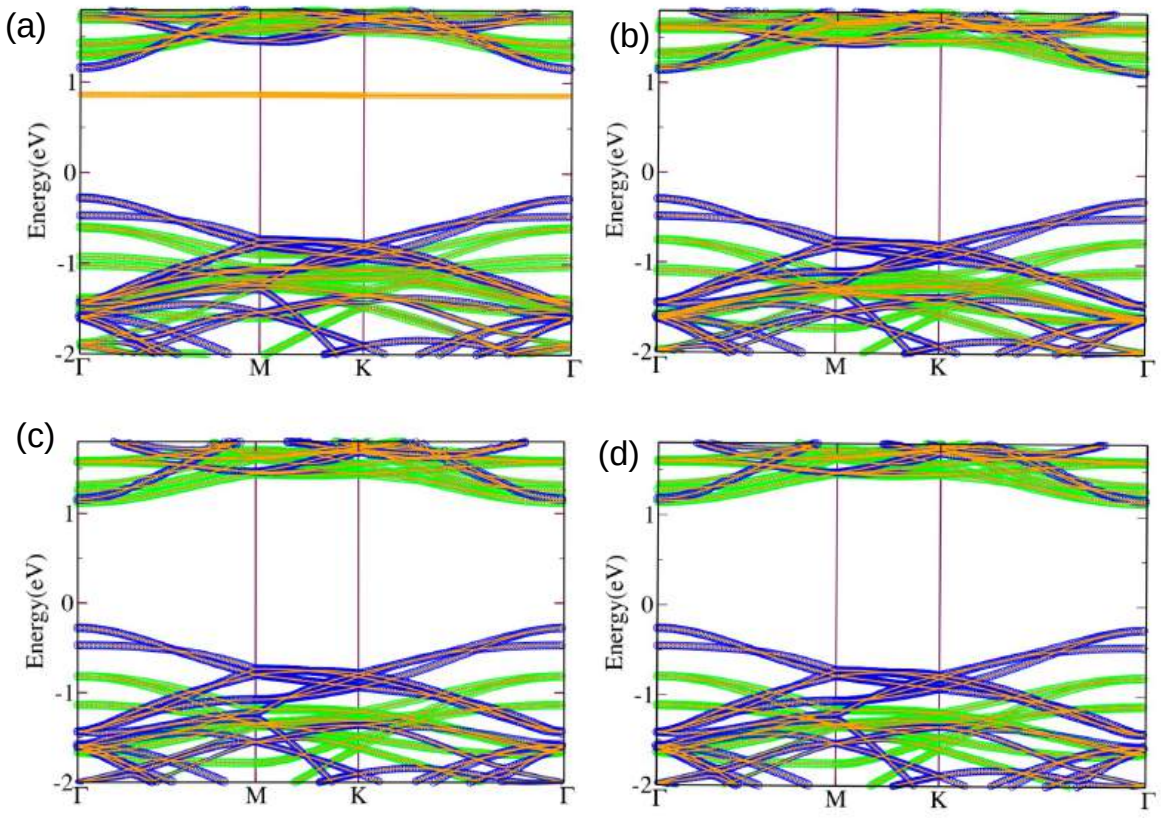

Figure 5.7: Band structures of (a) acetone, (b) dimethylsulfide, (c) ethanol, and (d) toluene-adsorbed Sc_2CO_2/WSe_2 heterostructure. The blue (green)lines are contributions from WSe_2 (Sc_2CO_2).The orange lines are contributions from the molecules.

The changes in electronic structures upon adsorption of VOC molecules in pristine Sc_2CO_2 and its heterostructure are important to investigate as it can provide insights into sensing characteristics of the surfaces qualitatively. In Figures 5.6 and 5.7, we show the band structures of VOC-adsorbed Sc_2CO_2 and WSe_2/Sc_2CO_2, respectively. We find that molecular adsorption brings in noticeable change in the band structure of the Sc_2CO_2. Irrespective of the molecule adsorbed, the valence band maxima and conduction band minima both shift to the Γ point. Moreover, the valence bands near Fermi energy are flatter along M-K direction. We find significant contributions from the molecular states along this direction. The band structures are very similar across different VOC-Sc_2CO_2 complexes; only in case of Acetone, a flat band, completely due to the molecule, appears in the conduction region. This reduces the electronic band gap of this system significantly

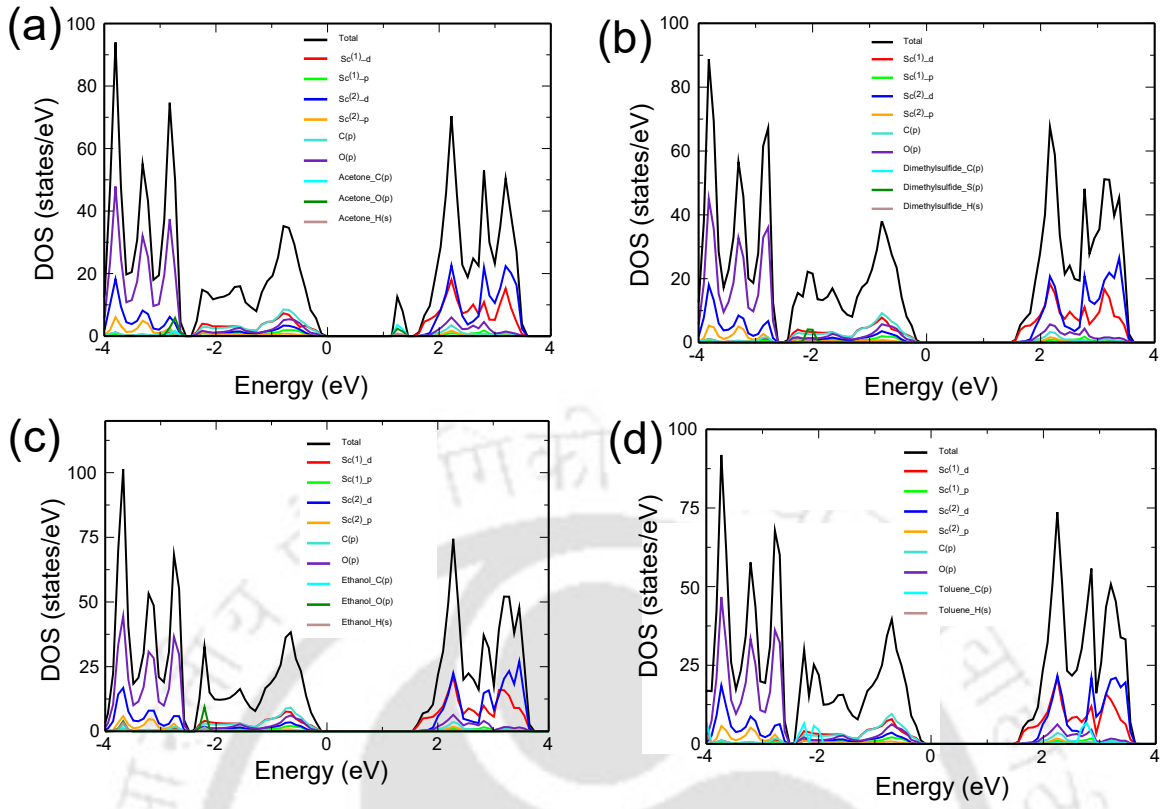

Figure 5.8: The total,atom-projected and orbital-projected densities of states (DOS) of (a) acetone-, (b) dimethylsulfide-, (c) ethanol- and (d) toluene- adsorbed Sc_2CO_2.

in comparison with other three VOC-MXene complexes. In case of these three, the band gap decreases by 1.5-2.6 % only. This happens due to shift of the conduction band edge towards lower energies. Similar changes in the band gaps occur when the adsorbent is the heterostructure of WSe_2 and Sc_2CO_2 (Figure 5.7). However, contrary to the case when Sc_2CO_2 is the adsorbent, the band gap increases for all cases except adsorption of Acetone (Table 5.3). Like the case of Sc_2CO_2 adsorbent, a flat band due to molecular states, appear in the conduction part when Acetone is adsorbed on the heterostructure surface (Figure 5.7(a)) leading to reduction in the band gap. The increase in the band gaps in other three cases (in comparison to that in pristine heterostructure) is due to shifting of both valence band maxima and conduction band minima to Γ point; the contributions to them still coming from same components of the heterostructure as is seen in case of pristine surface. This suggests that except for the case of Acetone, adsorption does not affect the band structures drastically upon changing the adsorbate, implying physisorption in all cases.

To understand features observed in the band structures in a finer and comprehensive way, we present the total, atom-projected and orbital-projected densities of states (DOS) of VOC adsorbed Sc_2CO_2 and WSe_2/Sc_2CO_2 monolayers in Figure 5.8 and 5.9, respectively. From Figure 5.8, we find that in the occupied part, the states at the band edges are mostly contributed by the C-p of the VOC, $Sc^{(1)} - d$,O-p and C-p states of Sc_2CO_2 monolayer. The O-p of Acetone, S-p of Dimethylsulfide, O-p and H-s of Ethanol and H-s states of Toluene lie deeper into the valence band signifying strong adsorption. The con-

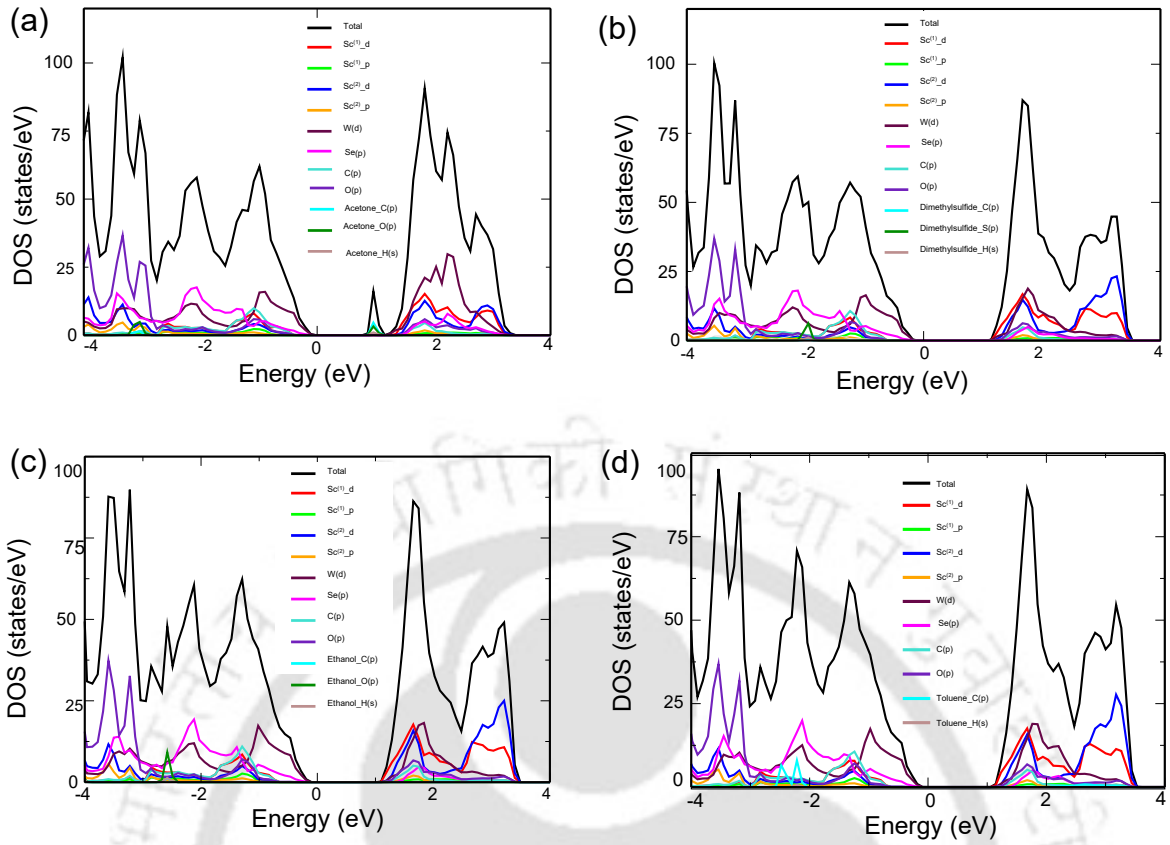

Figure 5.9: The total, atom-projected and orbital-projected densities of states (DOS) of (a) acetone-, (b) dimethylsulfide-, (c) ethanol- and (d) toluene-adsorbed Sc_2CO_2/WSe_2 heterostructure.

duction band edge in all cases are made up of $Sc^{(1)}$-d orbitals. In case of Acetone-Sc_2CO_2, however, we find impurity-like states due to C-*p* and O-*p* orbitals of Acetone in the gap, corroborating the band structure (Figure 5.6(a)). The positions of the band edges in the other three cases are near identical to that observed in pristine Sc_2CO_2 monolayer (Figure 5.3(a)),consistent with the reductions in the band gaps reported in Table 5.3.The densities of states of VOC-heterostructures show that the states near the valence band edges are contributed by W-*d* and Se-*p* orbitals alone. The contributions of MXene and molecular orbitals contribute at lower energy values. In the unoccupied part of the spectrum, though the band edge is from $Sc^{(1)}$, the states near show strong hybridisation with WSe_2 and the molecular orbitals.The band edge positions for Ethanol and Toluene adsorbed systems are identical while they shift slightly to lower energies in case Dimethylsulfide adsorbed heterostructure. The band gap values reported in Table 5.3 are consistent with this. In case of Acetone adsorption,an isolated molecular state, like the one observed in case of only Sc_2CO_2 being the adsorbent, is found which corroborates the band structure (Figure 5.7(a)).

5.2.2.2 Charge transfer and charge density difference

Charge re-distribution and subsequent transfer due to adsorption of VOCs are directly related to the sensing abilities of adsorbent 2D materials when proposed as chemiresis-

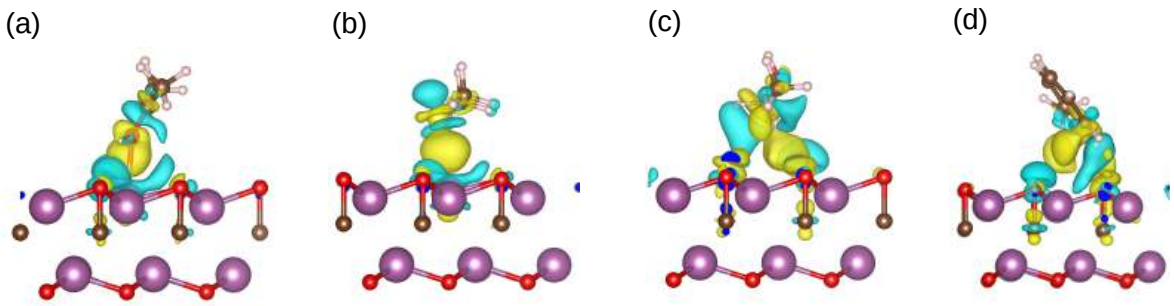

Figure 5.10: Isosurface charge density plots of (a)acetone-, (b)dimethylsulfide-, (c)ethanol- and (d)toluene-adsorbed Sc_2CO_2. Yellow and cyan represent charge accumulation and depletion,respectively. The isosurface value is taken to be 0.0004 e/^{3} .

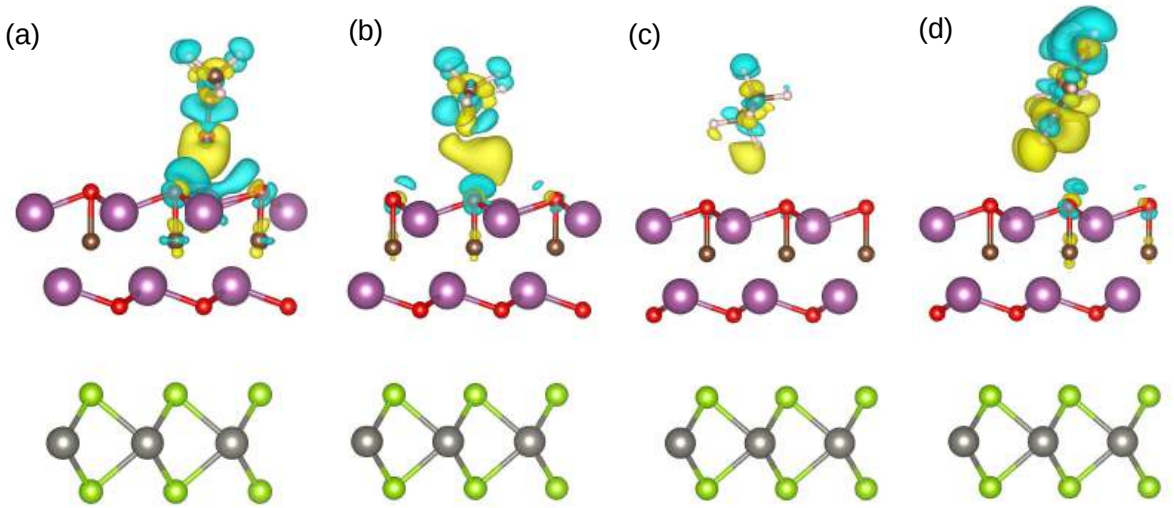

Figure 5.11: Isosurface charge density plots of (a)acetone-, (b)dimethylsulfide-, (c)ethanol- and (d)toluene-adsorbed Sc_2CO_2/WSe_2 heterostructure. Yellow and cyan represent charge accumulation and depletion,respectively. The isosurface value is taken to be 0.0004 e/^{3} .

tive sensors. These can be correlated with the changes in the electronic structures and the strength of adsorption. In Figures 5.10 and 5.11 we present the isosurface plots of charge density differentials for VOC-adsorbed Sc_2CO_2 and Sc_2CO_2/WSe_2, reespectively. These plots show the pattern of charge distribution with change in VOC and the adsorbent.Q,the amount of total charge transfers between surface and VOC are shown in Table 5.2. CDD for Acetone on Sc_2CO_2 shows small localised depletion around the O of C=O bond of the molecule and weak accumulation on the surface. This suggests weak dipole-induced physisorption,that is, mainly electrostatic polarisation between the two. This is supported by small amount of charge transfer from molecule to the surface. In case of Dimethylsulfide on Sc_2CO_2, we find small charge patches around the S atom of the VOC and the closest Sc atom, suggesting interaction between the lone pair of S

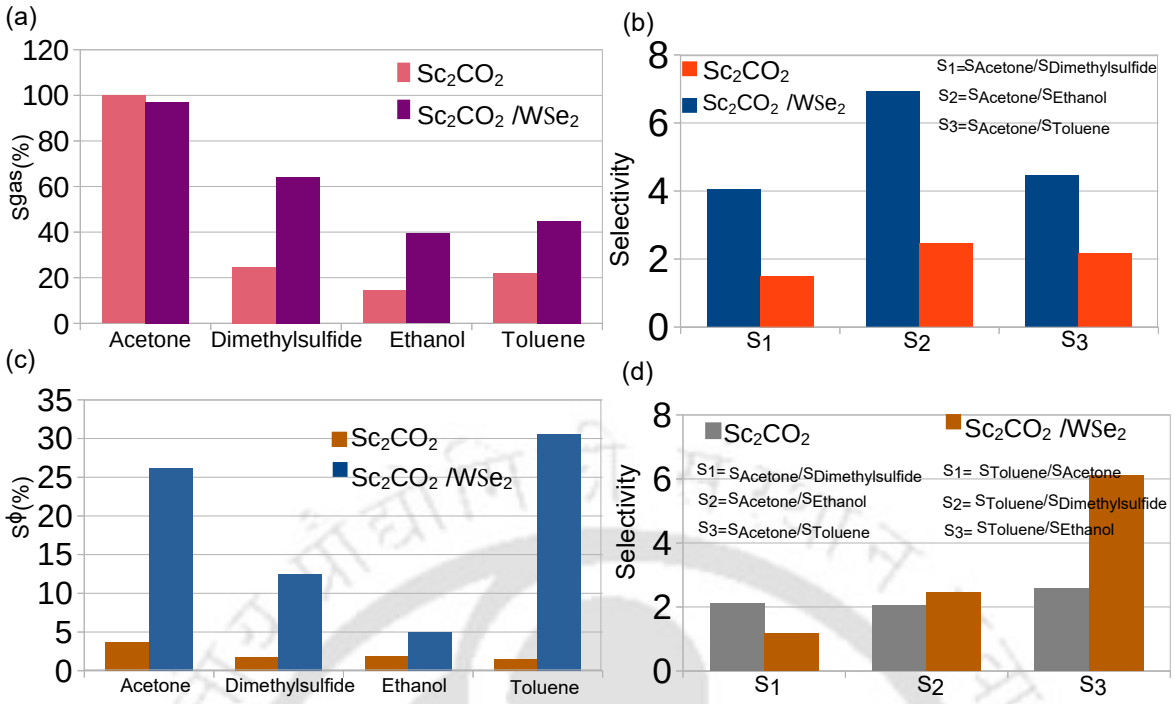

Figure 5.12: Calculated (a)sensitivity (S^{gas}) and (b)selectivity of Sc_2CO_2 and Sc_2CO_2/WSe_2 Chemiresistive sensors. Calculated (c)sensitivity (S^{ϕ}) and (d)Selectivity of them when used as Work-function based sensor.

and the surface. Q value of only -0.06e indicates weak physisorption in this case too. In case of Toluene adsorption on Sc_2CO_2, we find minimal charge re-distribution suggested by isosurfaces confined mostly on the surface. This is supported by almost no charge transfer as seen in the computed value of Q. The largest Q found in case of Ethanol adsorption on Sc_2CO_2 can be understood from more visible depletion around the -OH group of the molecule facing the surface. The isosurface structure suggests a hydrogen bonding like interaction with a noticeable electron polarisation.

Heterostructure of Sc_2CO_2 and WSe_2 as the adsorbent surface brings in substantial changes in the charge-redistribution and amount of charge transferred to the surface.Highlights of the isosurfaces for Acetone-heterostructure system are massive depletion around the molecule along with patches of accumulation on C and O of the surface, suggesting strong charge transfer to the surface. The largest Q in this case supports this. Larger accumulation around the S atom ,vanishing of depletion regions from the surface and an order of magnitude larger Q, in comparison with those in case of adsorption on Sc_2CO_2,when Dimethylsulfide is adsorbed on the heterostructure, indicates a stronger donation through the S lone pair. Substantial re-distribution of charges can be seen in case of Toluene. Larger accumulation in the contact region of VOC and the surface along with vanishing depletion on the surface indicate larger charge transfer enabled by the heterostructure in comparison to MXene surface.Computed Q value of -0.361e justifies this. Q in case of Ethanol adsorbed on the heterostructure, like others, though increase with respect to adsorption on pristine Sc_2CO_2, the increment is not as substantial. Accumulation of depletion around -OH of the VOC, with moderate depletion on the surface O atoms suggests that the moderate increase in Q is solely due to heterostructure induced polarisation.

The results provide us with an overall picture regarding the influence of WSe_2 in the heterostructure. The formation of an interface by bringing in WSe_2, introduces an in-built electric field which is responsible for strong polarisation. Due to this, molecules can transfer charge more efficiently. WSe_2 provides additional scope of orbital hybridisation, the effect of which is seen in case of significant changes in the band gap for Dimethylsulfide adsorbed surface. The charge–density difference isosurfaces and corresponding Bader charge analysis reveal a clear correlation between interfacial charge redistribution and molecular adsorption strength for VOCs on both surfaces. On pristine Sc_2CO_2, only small amounts of charge transfer occur (–0.004e to –0.10e), consistent with weak to moderate adsorption energies and predominantly physisorptive interactions driven by dipole polarization (Acetone, Ethanol) or polarization induced van der Waals forces (Toluene). In contrast, the heterostructure induces substantially larger charge transfer (–0.18e to –0.74e), accompanied by significantly enhanced and spatially extended charge accumulation/depletion at the adsorption interface, indicating stronger orbital hybridization and stronger bonding. This heterostructure-enabled charge-transfer amplification is expected to improve the sensitivity, particularly towards Acetone and Toluene.

Table 5.3: Band gap E_g(eV), Workfunction ϕ(eV) and recovery time τ(s) of differnt VOC-nanosheet complex.

Nanosheet	**VOC**	$\mathbf{E}_g$	ϕ	τ
Sc_2CO_2/WSe_2	Acetone	1.138	3.573	6.01×10^{-8}
	Dimethylsulfide	1.436	4.238	7.44×10^{-9}
	Ethanol	1.400	5.082	1.07×10^{-10}
	Toluene	1.407	3.361	2.24×10^{-8}
Sc_2CO_2	Acetone	1.446	5.550	8.52×10^{-9}
	Dimethylsulfide	1.824	5.445	2.24×10^{-9}
	Ethanol	1.835	5.447	7.15×10^{-11}
	Toluene	1.827	5.428	7.30×10^{-9}

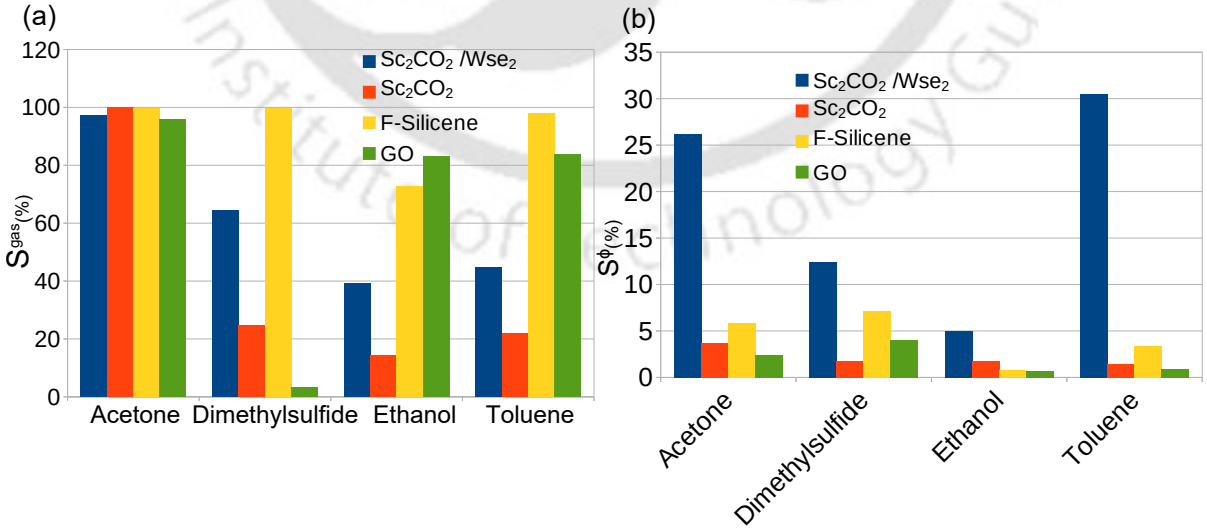

Figure 5.13: Sensitivity (a)S^{gas} and (b)S^{ϕ} of various 2D materials. The results are presented for comparison.

5.2.3 Sensing abilities of Sc_2CO_2 and its heterostructure with WSe_2

As discussed in chapter 3, a qualitative estimate of relative sensitivities of a sensor material can be obtained if it is a semiconductor. In this case one can exploit the relation $\sigma \propto exp\,(E_g/2k_BT)$; σ, E_g, k_B, T the conductivity, electronic band gap, Boltzmann constant and temperature, to compute the sensitivity from changes in E_g due to adsorption of VOC. An appropriate normalized expression for sensitivity S^{gas} is given as[281]

$$S^{gas}(\%) = |\frac{\sigma_{VOC} - \sigma_{pure}}{\sigma_{VOC} + \sigma_{pure}}| \times 100\%, \tag{5.2}$$

$\sigma_{VOC}(\sigma_{pure})$ is the estimated conductivity of the surface after(before) VOC-adsorption.

In Figure 5.12(a),we compare S^{gas} of Sc_2CO_2 and Sc_2CO_2/WSe_2 monolayers towards the four VOCs considered. We find that for both cases, S^{gas} is highest for Acetone. This is understandable from the variations in electronic band gaps. Strong polarization induced by Acetone makes charge transport easier leading to the highest sensitivity. For Sc_2CO_2 monolayer, the sensitivities towards Dimethylsulfide and Toluene are the same. The system has least sensitivity towards Etahnol. This can be attributed to weakest adsorption strength in this case. Sensitivities in all cases are amplified when the sensing material is the TMDC/MXene heterostructure, as was expected from the charge density distributions and adsorption energies. Moreover, all four sensitivities are distinctly different. This is reflected in the selectivity presented in Figure 5.12(b). While Ethanol and Toluene can not be separately recognized by Sc_2CO_2 sensor, the heterostructure makes it possible.Thus, formation of the heterostructure with WSe_2 makes the performance of Sc_2CO_2 sensor improved.

In Figure 5.12(c), we compare S^{ϕ}, the sensitivity when these two 2D materials are used as Work function based sensor.Computed ϕ_0 for Sc_2CO_2 and Sc_2CO_2/WSe_2 heterostructure is 5.35 eV and 4.84 eV, respectively. In Table 5.3, we show the ϕ values after adsorption of different VOCs. While ϕ increases irrespective of the VOC when they are adsorbed on Sc_2CO_2, opposite trend is observed when the adsorbent is the heterostructure. In this case, except for Ethanol, adsorption reduces ϕ substantially with Acetone and Toluene adsorption registering large changes. Accordingly, we find low and comparable S^{ϕ} for all molecules adsorbed on Sc_2CO_2 while distinguishible S^{ϕ} across VOCs is obtained for adsorption on the heterostructure. This is aptly reflected in the associated selectivity (Figure 5.12(d)). While Sc_2CO_2 Work function sensor cannot discriminate between Dimethylsulfide and Ethanol, the heterostructure one distinguishes all four VOCs considered. Like the chemiresistive one, this result too demonstrates the superior performance of Sc_2CO_2 sensor when it is put into a heterostructure form with WSe_2.

In Figure 5.13(a) and (b), respectively, we compare S^{gas} and S^{ϕ} of the two 2D systems considered here with those of two other materials, F-Silicene and GO, ones that have been investigated with regard to sensing these four VOCs [274, 275] in the previous chapters. We find that as chemiresistive sensor, Sc_2CO_2/WSe_2 heterostructure performance is comparable to that of F-Silicene, the best performer, with regard to sensing Acetone. Overall, it is the only one, other than F-Silicene, that can discriminate between the four VOCs clearly. As a Work function based sensor, it performs far better than the other three with substantial sensitivities towards Ethanol and Acetone. Therefore, this heterostructure, in comparison to other sensors considered for assessing their potentials

in detecting these four VOCs, can be considered as a potentially useful sensor material in all counts.

In Table 5.3, we present the results of τ for the two sensors.The results suggest that both can be used as reusable sensor since re-usability requires $\tau \leq 10^5$s [177]. Moreover, the shorter recovery time in both cases, in comparison with GO and F-Silicene [274, 275], suggest faster desorption of the gas molecules, enhancing its utility.

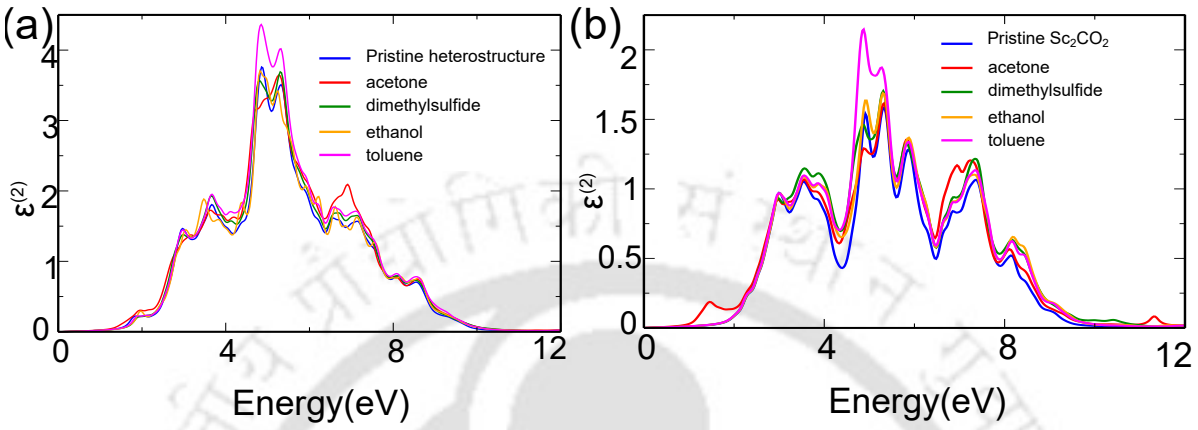

Figure 5.14: Variations in the imaginary part of the dielectric function $\epsilon^{(2)}$ with photon energy for pristine and VOC-adsorbed (a) Sc_2CO_2/WSe_2 and (b) Sc_2CO_2.

Finally, we examine the potential of these two 2D materials as optical sensors in the context of sensing these four molecules. Unlike the gas sensors,direct calculation of sensitivity is not possible with optical sensors.Only qualitative understanding of sensitivity is possible through computation of the imaginary part of the dielectric function [282, 283],as is discussed earlier. In Figure 5.14, we, therefore, present results on $\epsilon^{(2)}$, the imaginary part of the dielectric constant. We show the changes in $\epsilon^{(2)}$, upon adsorption of the four VOC molecules on a given surface. We find that with either adsorbent, the energy range of 3.5-7 eV can be considered relevant. We find that in case of Sc_2CO_2 better distinguishibility is obtained in the range of 3.75-5 eV, where curves corresponding to pristine and different VOC-adsorbed Sc_2CO_2 can be identified. This is not so in case of the heterostructure.Therefore, as optical sensor in the UV region of the electromagnetic spectrum, performance of Sc_2CO_2 trumps its heterostructure counterpart. .

5.3 Conclusions

MXenes are a relatively new class of 2D materials that have shown their immense potential in many applications including sensing of environmental gases, and biomolecules that are markers of terminal disease. In comparison, exploration of MXenes as sensors to detect the state of deterioration of food products remain untouched. On the other hand, heterostructures of MXenes with other 2D materials like TMDCs have been found to enhance functinalities in various applications. In this work, we have investigated the sensing abilities of semiconducting MXene Sc_2CO_2 and its heterostructure with well known TMDC WSe_2 towards four important VOC molecules emitted by standard food products during various stages of their degradation. Using DFT, we have studied in detail the nature of microscopic interactions at the adsorbate-adsorbent interfaces and

subsequent impacts on properties associated with sensing. We find that the incorporation of the TMDC layer significantly enhances the sensing ability of the MXene by amplifying the adsorption strength through making available the scope for more orbital hybridisation and the charge transport through the interface due to an internal electric field arising out of substantially different Work functions of the constituents of the heterostructure.The results suggest the heterostructure performs better than the bare MXene in sensing and distinguishing the VOCs when it is considered a chemiresistive as well as a Work function based sensor. The bare MXene works better as an UV optical sensor. We also find that this MXene-TMDC Work function sensor outperforms F-Silicene and GO, two other 2D semiconductors investigated as sensors for the same purpose. As a chemiresistive sensor too, its performance in comparison to these two are reasonably well. The full potential of this MXene and its heterostructure in the context of food technology can be explored in future by computing the transport properties in a model device setup as has been done recently [274, 275]. This work is the first that explores a MXene and its heterostructure in the area of food quality assessment. The encouraging results make way for future investigations with different MXenes, their heterostructures and different VOCs associated with specific food products, a field of materials research,hitherto uncharted.

Chapter 6

Sc_2CT_2 (T = O, S, F) MXenes as nanosensors for detection of biomarkers of papaya fruit

6.1 Introduction

One of the most widely consumed and significant tropical fruits in terms of commerce is papaya which is a member of the Caricaceae family.They are commonly utilised to make a variety of food products, or they can be eaten raw as a vegetable or matured fresh for table use [284, 285].Papaya contains health-promoting phytochemicals like carotenoids [286], phenolics [287], sugars [288], vitamins A, C, E, and B complex [289], minerals like magnesium and potassium [285], and the enzyme papain (especially in green papaya) [289]. They also contain anticancer glucosinolates and cyanogenic glucosides [290].Their distinct color and flavor are due to emission of a complex variety of volatile organic compounds (VOCs). Over 300 VOCs[284] consisting of esters, alcohols, and aldehydes, contributing significantly towards its aroma [291]. Out of these, six biomarker VOCs that can efficiently distinguish between the ripening stages, have been identified in a recent work [292]. As VOCs are being used as a non-invasive identifier to identify plant phenotypes, cultivar kinds, and fruit sensory qualities [293, 294],the VOCs released by papaya fruits during their ripening process may be utilised as a real-time, non-invasive marker to describe their nutritional content and the stage of maturity. However, no gas sensor, working on the principles of electronic nose [295] that can exploit these biomarkers for non-evasive monitoring of ripening stages and the nutritional values of papaya, is yet realized.

In this chapter, we seize this opportunity and perform a computational study on interaction between Papaya VOCs and a 2D material to assess its performance as a monitoring device for Papaya degradation. The 2D material of our choice for this work is Sc_2CT_2 MXenes where T is the functional group that passivates the surface of Sc_2C MXene while exfoliated from it's precursor MAX phase, an inevitable phenomenon, discussed in chapter 1. Since MXene surfaces can be passivated with different T(depending

The contents of this chapter are published in 2026, Phys. Scr. 101 (2026) 115903 DOI: 10.1088/1402-4896/ae4dc8

upon the synthesis), this offers a lot of flexibility in its composition which can be used to our advantage by exploiting structure-property variations. In the previous chapter, we have observed the potential of Sc_2CO_2 Mxene in sensing and discriminating among standard VOCs associated with generic food materials.Therefore, while investigating a specific food product like Papaya fruit, we are motivated to explore this particular MXene and its compositional flexibility.

In what follows, we have investigated the utility of Sc_2CT_2 (T=O,F,S) MXenes in detection and separation of prominent VOCs emitted by Papaya fruit during its stages of maturing. Out of the six biomarker VOCs (Methyl hexanoate, ethyl butanoate, methyl butanoate,3-carene, longifolene and D-limonene), methyl hexanoate, 3-carene and longifolene were found to display a valid correlation with the ripening associated changes in select fruit nutritional parameters as their concentrations increased [292].Therefore, in this study we have considered two out of these three VOCs (methyl hexanoate and 3-carene) and two from the rest three (methyl butanoate and D-limonene) for our investigation. By computing the electronic structure, charge transfer, work function changes, optical and electronic transport properties with the help of first-principles Density Functional Theory (DFT) [210] and non-equilibrium Green's function method (NEGF)[237], we have estimated the efficacy of Sc_2CT_2 MXenes as chemiresistive, work function based and optical sensors. We find that only Sc_2CS_2, as a chemiresistive sensor, can clearly distinguish between them with reasonable sensitivity. The uniqueness of this work and subsequent novelty stems from the fact that unlike almost all computational and even experimental investigations into the sensing abilities of various two-dimensional sensor materials which dealt with relatively smaller and structurally simpler molecules, this work has investigated sensing abilities of a material upon adsorption of large and complex molecules (complexities of the structures are detailed in the next sections) that are extremely relevant in daily lives of people in the real world.

6.2 Methodology

.In order to make sure the physical quantities are not affected by periodic image interactions, a supercell of $4 \times 4 \times 1$ and a vacuum space of 30 Åperpendicular to the 2D sheet is used all along. The relaxation of the ionic positions are done by the conjugate gradient method. The structures underwent full relaxation until the residual force on individual atoms and per-atom energy change are smaller than 0.01 eV/Å and 10^{-7} eV, respectively.A $5 \times 5 \times 1$ Monkhorst-Pack special k-point mesh [213] is used to sample the Brillouin zone during self-consistent calculations. For calculations of electronic structures, a $17 \times 17 \times 1$ k-point grid is sampled. The plane wave cut-off energy is taken to be 550 eV. Throughout the calculations, we use Grimme's van der Waals (vdW)-corrected DFT-D3 dispersion correction technique [238]to take into account long-range van der Waals interactions.

6.3 Results and Discussions

Unlike the bulk of literature on gas molecule adsorption on 2D materials, the molecules considered here are bigger and complex. 3-carene and D-limonene are cyclic monoterpenes with chemical formula $C_{10}H_{16}$, while both methyl butanoate and methyl hexanoates are esters; the former with chemical formula $C_5H_{10}O_2$ and the later with $C_7H_{14}O_2$. In Figure

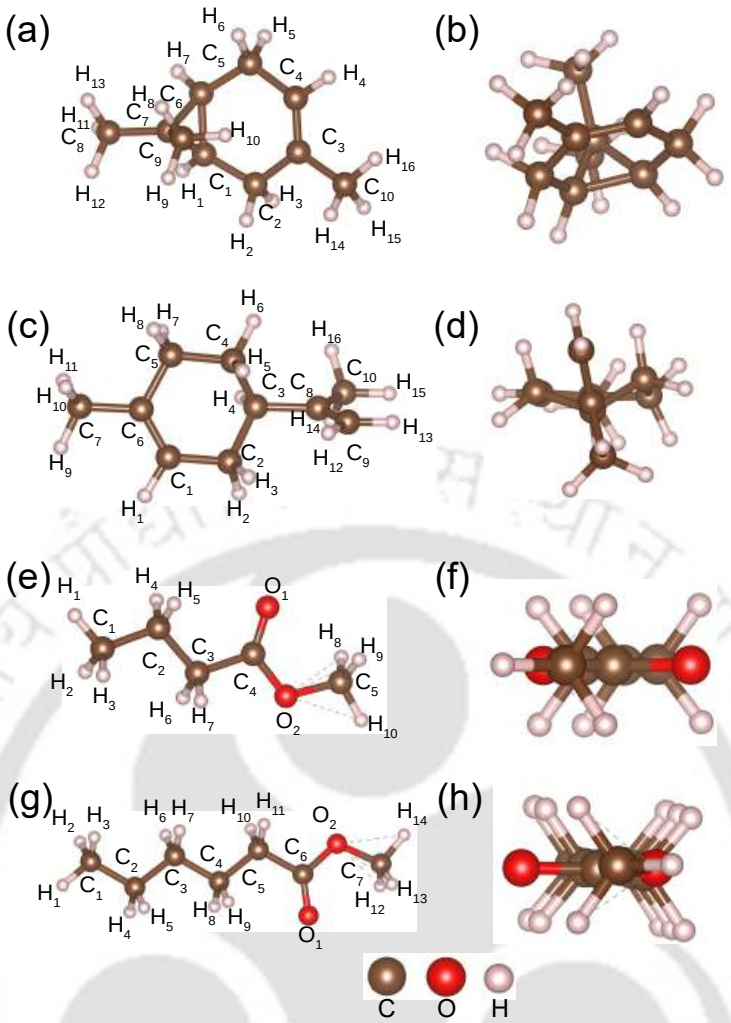

Figure 6.1: Optimised structure of isolated 3-Carene((a) top view, (b) side view), D-Limonene ((c) top view, (d) side view, Methylbutanoate ((e) top view, (f) side view),and Methylhexanoate ((g) top view, (h) side view).

6.1 we show the optimized structures of the molecules. 3-carene consists of a cyclohexene ring with a C-C double bond (C_3-C_4 in Figure 6.1(a)); a cyclopropane ring (the vertices are made up of C_1, C_6 and C_7 in Figure 6.1(a)) fused onto it. Three methyl (CH_3) groups, one on the double bonded Carbon C_3 and two at the bridgehead Carbon C_7 are attached to the main rings. The computed C-C bond lengths associated with the double bond, cyclohexane and cyclopropane rings are 1.34-1.36 Å, 1.52-1.54 Åand 1.50 Å, respectively. The C-H bond length is 1.09 Å. The corresponding bond angles are 120°, 107.5°-109.5° and 60°, respectively. There is no available experimental or theoretical results on the structural parameters of 3-carene. However, since it is a hydrocarbon with one C-C double bond fused to a cyclopropane, its bond lengths and bond angles can be well approximated by standard values for these motifs. With that approximation, we find that our results agree reasonably well with the available structural data [296].

The structure of D-limonene consists of a cyclohexane ring, a methyl group (C_7−H_9−H_{10}−H_{11} in Figure 6.1(c)), an isopropenyl group ((CH_2)=C(CH_3); the three C atoms are C_8,C_9,C_{10} in Figure 6.1(c)). There are two C-C double bonds - one inside the ring (C_1-C_6 in Figure 6.1(c)) and one in the isopropenyl group (C_8-C_9 in Figure

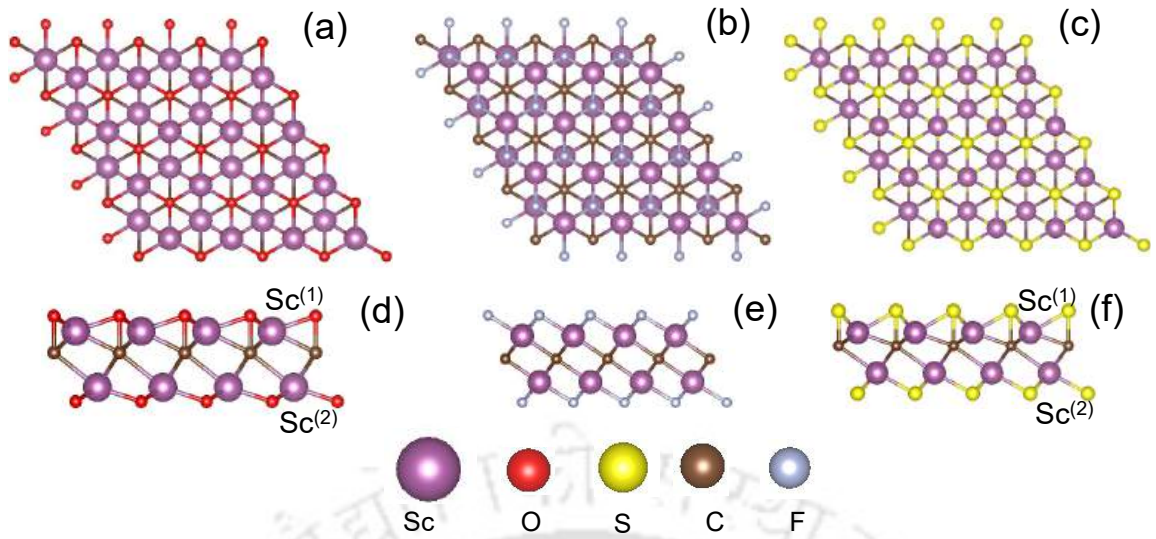

Figure 6.2: (a)-(c): Top View of Pristine Sc_2CO_2, Sc_2CF_2, Sc_2CS_2 respectively. (d)-(f): Side view of Pristine Sc_2CO_2, Sc_2CF_2, Sc_2CS_2 respectively.

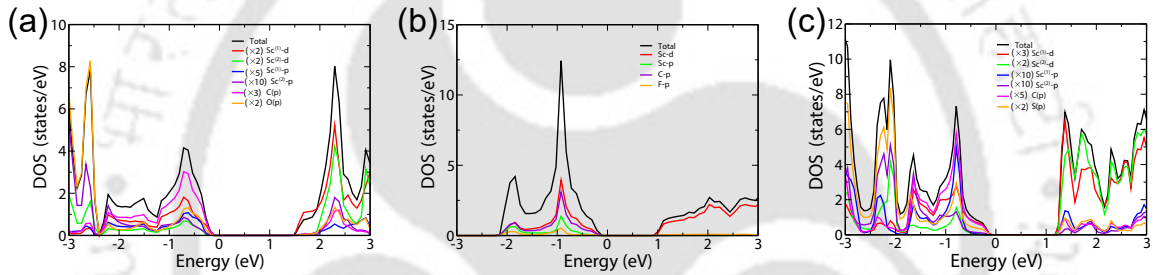

Figure 6.3: (a)-(c) Densities of states (DOS)for Sc_2CO_2, Sc_2CF_2, Sc_2CS_2, respectively.

6.1(c)). The computed C-C bond lengths associated with the double bonds, C atoms inside the cyclohexane ring and the bonds connecting cyclohexane ring and the methyl groups are 1.34 Å, 1.52-1.54 Åand 1.47-1.50 Årespectively. The corresponding bond angles are 120°,107.5 °-109.5° and 120°, respectively. The results agree very well with the available experimental and theoretical estimations [297].

Methyl butanoate and methyl hexanoate have near identical structures. The structure consists of a carbon chain containing 4(6)carbon atoms for the former(later). On one end the chains are terminated by a carbonyl group (C=O); an ester functional group O-CH_3 is attached to the carbonyl group (Figures 6.1(e),(g)). For Methyl butanoate, the C=O bond distance (C_4-O_1 in Figure 6.1(e)), the C-O bond distance (C_4-O_2 in Figure 6.1(e), for example) and C-C bond distance in the carbon chain are 1.22 Å, 1.36-1.42 Åand 1.51-1.52 Å, respectively.The corresponding bond angles are 123.2°,116°-119° and 109.5°-112.5° respectively. The corresponding bond distances in methyl hexanoate are 1.20-1.22 Å, 1.33-1.39 Åand 1.51-1.52 Å, respectively. The bond angles are near identical to those in methyl butanoate. Our calculated results agree very well with the available experimental results [298, 299].

In Figure 6.2, we show the optimized structures of the MXene nanosheets. The structures are obtained by minimizing the total energy of each compound with respect to the positions of the surface passivating functional groups. In Sc_2C MXene, a functional

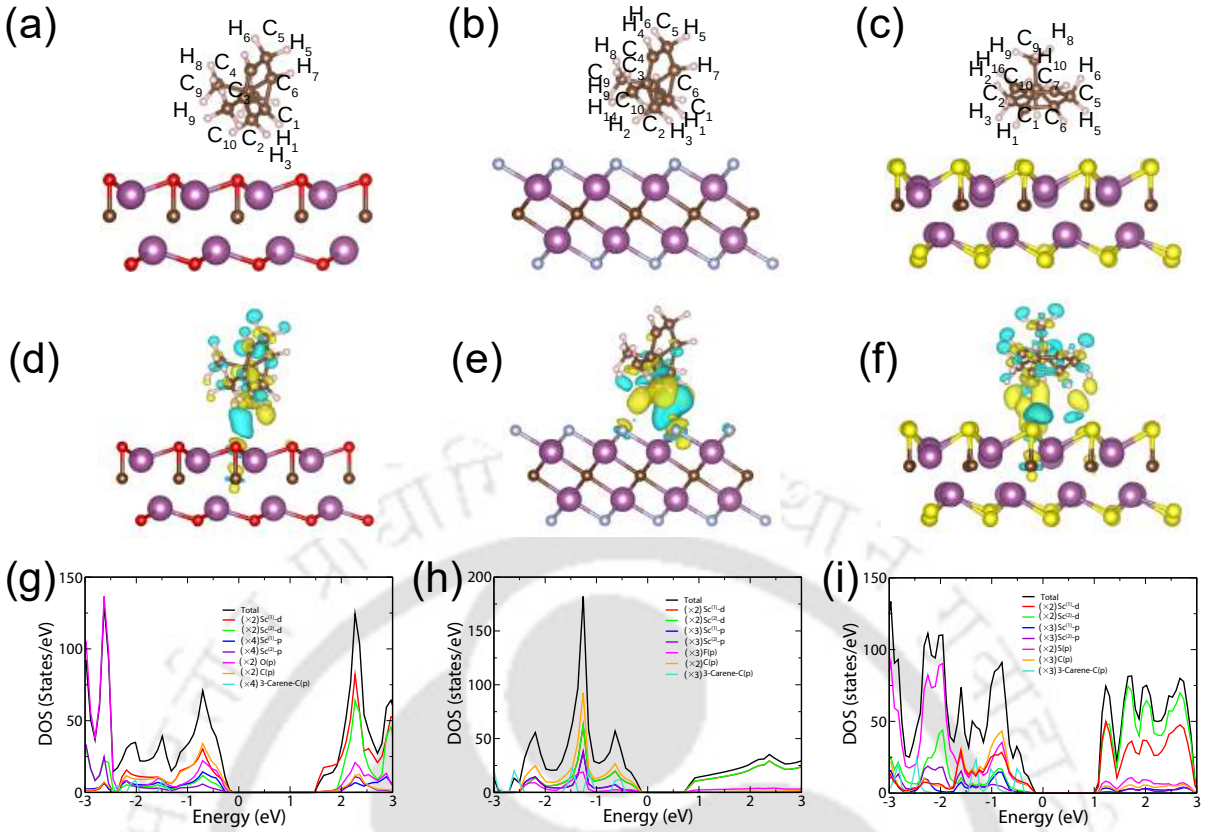

Figure 6.4: (a)-(c)optimized geometries, (d)-(f) iso-surface charge density plots, (g)-(i)total, atom and orbital projected densities of states (DOS) of 3-Carene adsorbed on Sc_2CO_2, Sc_2CF_2 and Sc_2CS_2, respectively. In (a)-(c), purple, silver, yellow, red, brown and pink stand for Sc,F,S,O,C and H atoms respectively. In (d)-(f), yellow and cyan colours indicate charge accumulation and depletion, respectively. The isosurface value is taken to be 0.0003 e/Å^3.

group -T can occupy three different positions on a given surface : position H (hollow site above Sc associated with the opposite surface), position C (hollow site above C) and position T (site directly above Sc associated with the same surface). Accordingly, several configurations arising out of different combinations of occupying sites for -T are possible. We find that while the minimum energy configuration for Sc_2CF_2 is HH (both -F atoms are in H position), the symmetry is broken for the other two. For both cases, the configuration is CH, making the two Sc atoms inequivalent. Hence, the Sc atom at the top (along 001 direction)surface is marked as $Sc^{(1)}$ while the one at the bottom (along 00-1 direction) surface is marked as $Sc^{(2)}$. The lattice constant, Sc-O bond length and C-O bond lengths of Sc_2CO_2 nanosheet are 3.41 Å, 2.08 Åand 1.64 Å, respectively. The bond-angle of O-Sc-O is 109.95°. The computed structural parameters are in good agreement with the existing results[300]. In case of Sc_2CF_2, the lattice constant, Sc-F bond length and C-F bond length are 3.26 Å,2.19 Åand 3.04 Å, respectively, the bond-angle of F-Sc-F is 56.07°, in excellent agreement with existing results[301]. Corresponding structural parameters of Sc_2CS_2 are 3.76 Å, 2.48 Åand 1.95 Å, the bond-angle of S-Sc-S is 98.21°.also in good agreement with the existing results[300].

In Figure 6.3, we show the total, atom and orbital projected densities of states for

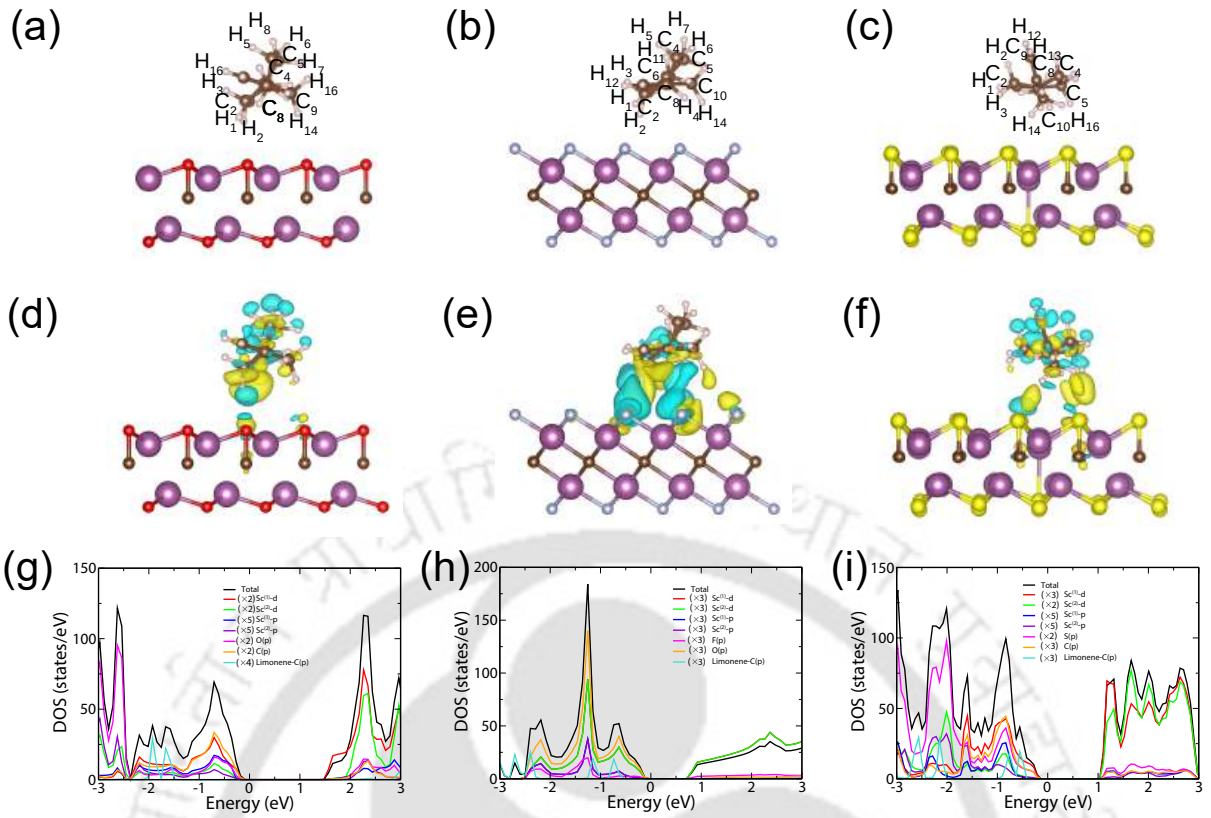

Figure 6.5: (a)-(c)optimized geometries, (d)-(f) iso-surface charge density plots, (g)-(i)total, atom and orbital projected densities of states (DOS) of D-limonene adsorbed on Sc_2CO_2, Sc_2CF_2 and Sc_2CS_2, respectively. In (a)-(c), purple, silver, yellow, red, brown and pink stand for Sc,F,S,O,C and H atoms respectively. In (d)-(f), yellow and cyan colours indicate charge accumulation and depletion, respectively. The isosurface value is taken to be 0.0003 e/Å^3.

the three MXenes considered in this work. Only d and p-orbitals of Sc and p-orbitals of C and functional group atoms are shown.The ground states of all three compounds are semiconducting with band gaps of 1.788 eV, 1.011 eV and 1.499 eV for Sc_2CO_2, Sc_2CF_2 and Sc_2CS_2, respectively. The results agree well with the existing ones [300, 301]. We find that the valence band maxima and conduction band minima of Sc_2CO_2 are due to $Sc^{(1)}$ d states. There is strong hybridisation between Sc, O and C states. Similar features are observed in Sc_2CF_2. However, unlike Sc_2CO_2, the states are more localised in the occupied part and de-localised in the unoccupied part. The densities of states of Sc_2CS_2 largely resembles Sc_2CO_2, except that there is strong hybridisation of Sc states near conduction band minima and that in comparison with Sc_2CO_2, the states in the unoccupied part are more delocalised and are pushed towards lower energies. Moreover, the S p-states in Sc_2CS_2 occupy higher energies in comparison with O p-states in Sc_2CO_2.

In Figures 6.4(a)-(c), we show the optimized geometry of 3-carene after adsorption on Sc_2CO_2, Sc_2CF_2 and Sc_2CS_2, respectively. The optimised geometries of D-limonene, methyl butanoate and methyl hexanoate after adsorption on the three MXenes are presented in Figures 6.5-6.7(a)-(c), respectively. The optimized geometry in each case is obtained by calculating total energies of various different orientations of the molecules with respect to the MXene, and after relaxation of bond lengths and bond angles. In case

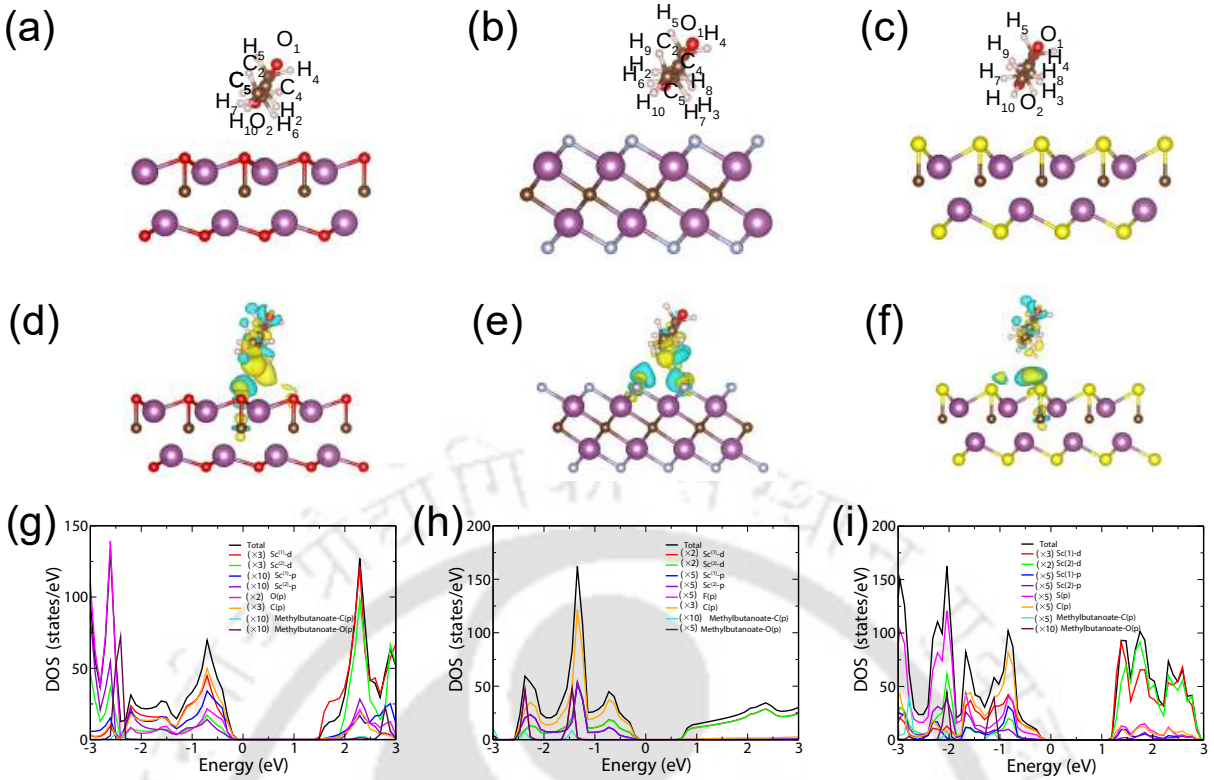

Figure 6.6: (a)-(c)optimized geometries, (d)-(f) iso-surface charge density plots, (g)-(i)total, atom and orbital projected densities of states (DOS) of methylbutanoate adsorbed on Sc_2CO_2, Sc_2CF_2 and Sc_2CS_2, respectively. In (a)-(c), purple, silver, yellow, red, brown and pink stand for Sc,F,S,O,C and H atoms respectively. In (d)-(f), yellow and cyan colours indicate charge accumulation and depletion, respectively. The isosurface value is taken to be 0.0003 e/Å^3.

of 3-carene and D-limonene, we find the preferred orientation is the one where the cyclohexane rings of the molecules are perpendicular to the Sc_2CO_2 surface. Both molecules prefer a parallel orientation of the cyclohexane ring with respect to Sc_2CS_2 nanosheet. The situation is mixed in case of Sc_2CF_2 as adsorbent. While cyclohexane ring of 3-carene prefers a perpendicular orientation, that of D-limonene prefers to be adsorbed parallel to Sc_2CF_2. In case of methyl butanoate and methyl hexanoate, the orientations are similar for all three adsorbents : the ester (carbonyl)group being closest to the surface for the former(later). The structural parameters of 3-carene do not change much after their adsorption on either of the three MXenes. The bond lengths remain intact while the bond angle associated with C-C double bonds is now dispersed, with variations being 2°-3° with respect to the value obtained for the isolated molecule. Additionally, the C-C-C bond angle associated with the cyclohexane ring reduces by 2° when the molecule is adsorbed on Sc_2CF_2. For D-limonene, only the C-C-C bond angle associated with the cyclohexane ring reduces by 2°-3° (with respect to those in isolated molecule) when adsorbed on Sc_2CO_2 and Sc_2CF_2. The bond angle associated with the ester group in methylbutanoate reduces significantly, irrespective of the adsorbent; the changes are as large as 4°-6°. The bond angles between C atoms in the carbon chain of methyl hexanoate, on the other hand, increase by 2°-3°, irrespective of the adsorbent nanosheet.

These structural features can be correlated with the strength of adsorption reflected in

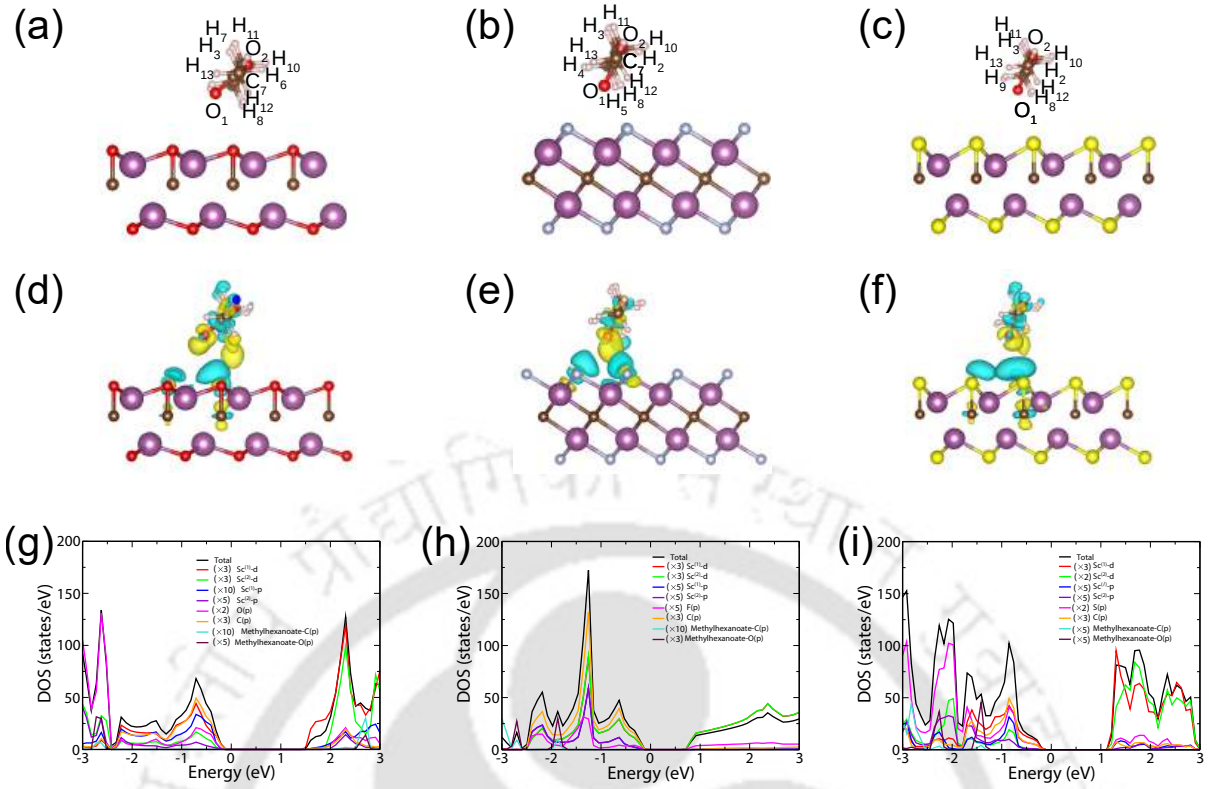

Figure 6.7: (a)-(c)optimized geometries, (d)-(f) iso-surface charge density plots, (g)-(i)total, atom and orbital projected densities of states (DOS) of methylhexanoate adsorbed on Sc_2CO_2, Sc_2CF_2 and Sc_2CS_2, respectively. In (a)-(c), purple, silver, yellow, red, brown and pink stand for Sc,F,S,O,C and H atoms respectively. In (d)-(f), yellow and cyan colors indicate charge accumulation and depletion, respectively. The isosurface value is taken to be 0.0003 e/Å^3.

E_{ad}, the adsorption energy. The results on E_{ad} and D, the distance between the nanosheet and the molecule, presented in Table 6.1, suggest that the molecules are physisorbed on MXene sheets. The weakest adsorption, quantified by the smallest E_{ad}, is found to be for methylbutanoate adsorption. D too, in this case, turns out to be the largest. This can be correlated with reduction in the bond angle associated with the ester group attached to the molecule,the one that is closest to the surface. In case of adsorption of 3-carene and D-limonene on either of the three MXene nanosheets, E_{ad} values are substantially larger than in case of adsorption of the other two VOCs. Moreover, the values are close to each other. These indicate that the adsorption of 3-carene and D-limonene are qualitatively different than the other two. Across the three adsorbent nanomaterials, qualitative variations of E_{ad} correlate with D, as is clear from Table 6.1.

The highest values of E_{ad} are obtained in cases of 3-carenene and D-limonene adsorption on Sc_2CS_2. When these two molecules are adsorbed on Sc_2CO_2, like in case of Sc_2CS_2, E_{ad} are very close.When the adsorbent is Sc_2CF_2, larger E_{ad} is obtained in case of D-limonene adsorption. We find a correlation between the configurations of the molecules during adsorption and the corresponding E_{ad}. On Sc_2CS_2, both molecules adsorb in a parallel orientation. This increases the region of contact with the nanosheet and provides more sites of adsorption in comparison with cases where the orientations of the molecules are different. Comparatively smaller and near identical E_{ad} when these two

molecules are adsorbed on Sc_2CO_2 can be correlated with the perpendicular orientations of the molecules with respect to the MXene nanosheet during adsorption. This is further corroborated by the fact that E_{ad} is larger when D-limonene is adsorbed on Sc_2CF_2 in a parallel orientation in comparison with adsorption of 3-carene in a perpendicular orientation with respect to the Sc_2CF_2 surface.

In Figures 6.4-6.7(d)-(f), we show the corresponding isosurfaces of charge density differential $\delta\rho$. These, along with total charge transfer Q, presented in Table 6.1, provide insights into the interactions between the VOC and the nanosheets. We find that in case of VOC-Sc_2CO_2 complexes, charge is mostly accumulated on the molecules, suggesting the charge transfer between the components are small. This is supported by relatively small values of Q in those cases. In case of VOC-Sc_2CF_2, less charges are accumulated on the molecules in all cases as is observed from the Figures 6.4-6.7(e). This is reflected in $Q < 0$ in all cases. Significant amount of charge accumulation is observed in the region between the MXene and the VOC molecule in case of 3-carene and D-limonene adsorption on Sc_2CS_2. In contrast, charges are concentrated on the VOC in case of methylbutanoate and methylhexanoate adsorbed on this MXene. This is consistent with the VOC-nanosheet interactions being the strongest in cases of 3-carene-Sc_2CS_2 and D-limonene-Sc_2CS_2.

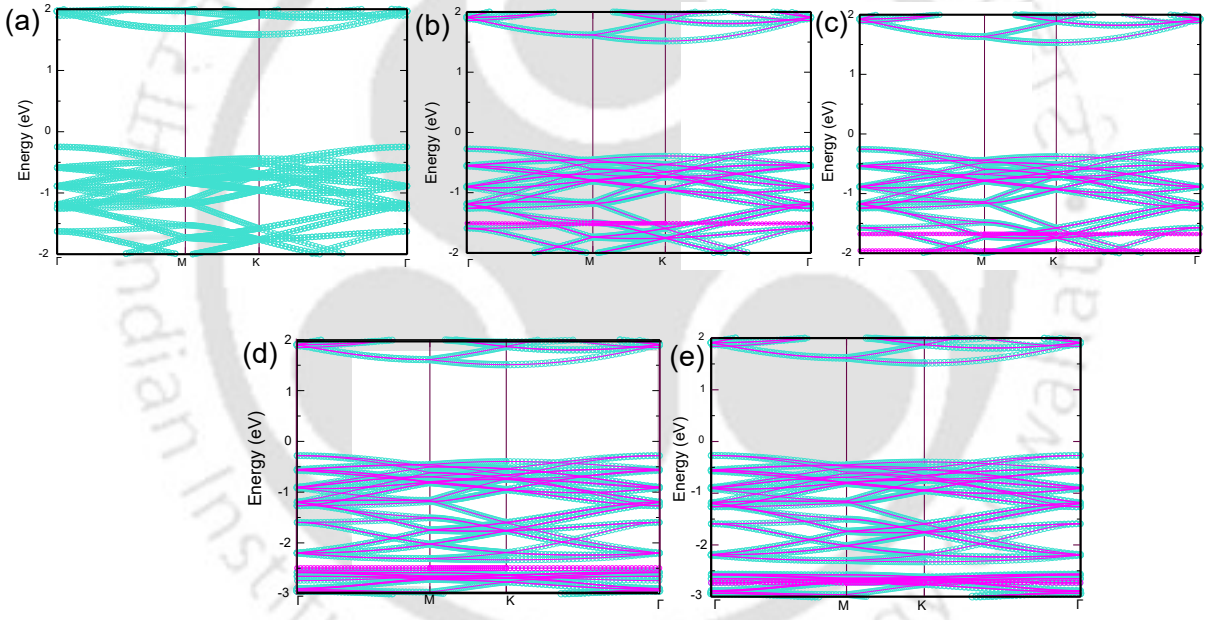

Figure 6.8: Band structure of (a) Pristine (b) 3-Carene (c) D-Limonene (d) Methylbutanoate (e) Methylhexanoate adsorbed Sc_2CO_2.The turquoise (magenta)lines correspond to the contributions from Sc_2CO_2 (molecule) bands.

To get more insights, we take recourse to the total, and atom projected densities of states (DOS) of the VOC-MXene complexes. The results are shown in Figures 6.4-6.7(g)-(i). The band structures before and after adsorption of VOC are also presented in Figures 6.8-6.10. Upon comparing Figures 6.4 (g)-(f), we find significant differences in the electronic structures of the complexes when same VOC 3-carene is adsorbed on different MXenes. Like pristine Sc_2CO_2, the VBM and CBM of the 3-carene-Sc_2CO_2 complex are due to $Sc^{(1)}$ atoms.The positions of the VBM and CBM remain almost identical, with negligible modification in the electronic band gap(Table 6.1). The dominant p-states of the VOC hybridise with the Sc d, C p and O p states of the MXene significantly, thus

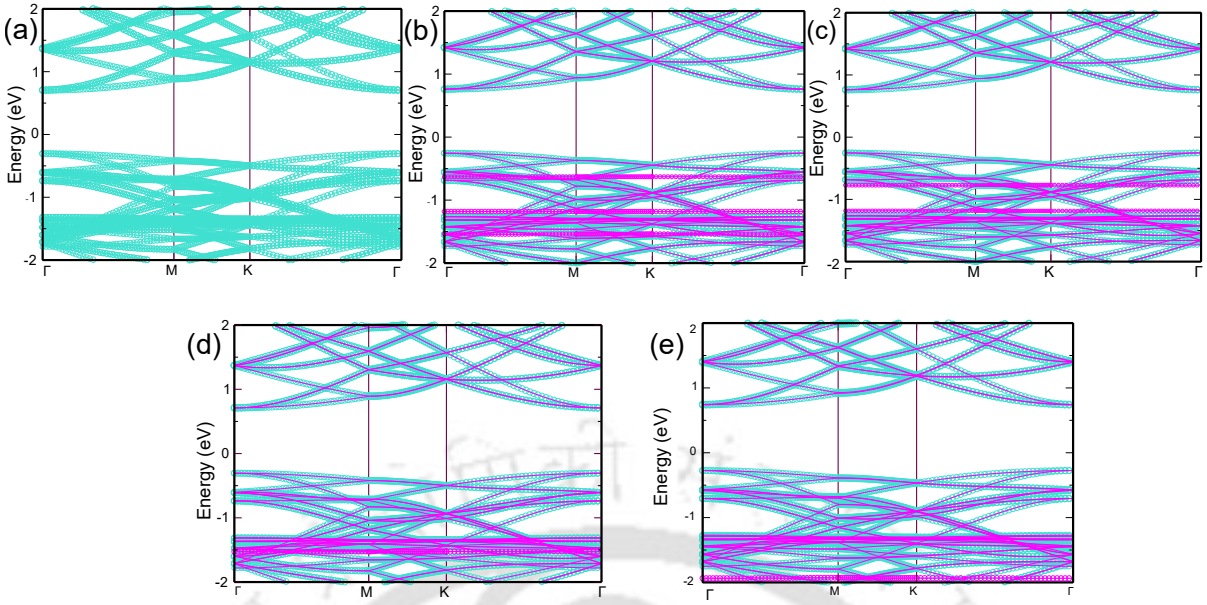

Figure 6.9: Band structure of (a) Pristine (b) 3-Carene (c) D-Limonene (d) Methylbutanoate (e) Methylhexanoate adsorbed Sc_2CF_2.The turquoise (magenta)lines correspond to the contributions from Sc_2CF_2 (molecule) bands.

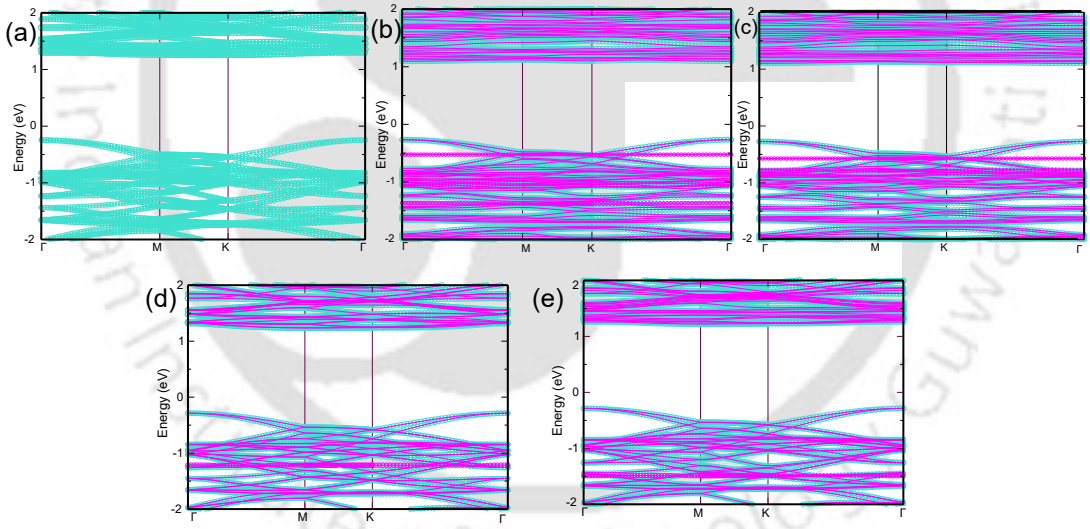

Figure 6.10: Band structure of (a) Pristine (b) 3-Carene (c) D-Limonene (d) Methylbutanoate (e) Methylhexanoate adsorbed Sc_2CS_2.The turquoise (magenta)lines correspond to the contributions from Sc_2CS_2 (molecule) bands.

lending no substantial impact on the electronic structure in comparison with that of bare MXene. There is some visible change in the densities of states, in comparison with that of bare Sc_2CF_2 when 3-carene is adsorbed. A new peak at around -0.5 eV appears in the occupied part of the spectrum. This is due to hybridisation of p states of C in the cyclohexane ring of the VOC with the d states of Sc and p states of C and F of the Mxene. The unoccupied part remains unchanged. However, despite appearance of the molecular states,no changes are observed in the positions of the VBM and CBM, leaving

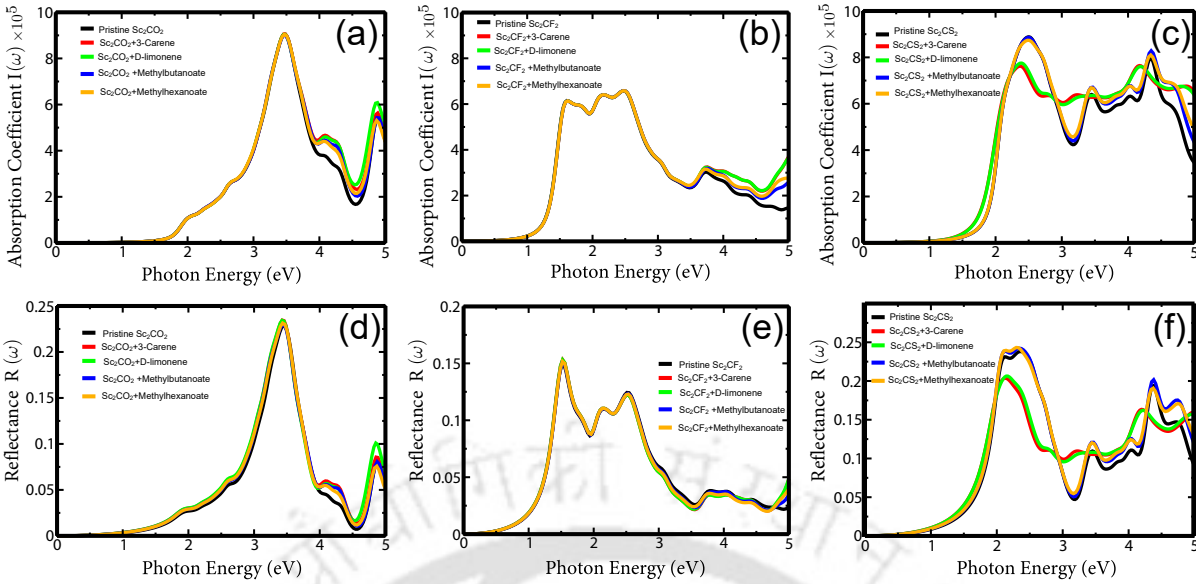

Figure 6.11: (a)-(c) Optical absorption co-efficients and (d)-(e) reflectances of bare and VOC-adsorbed Sc_2CO_2, Sc_2CF_2, Sc_2CS_2 respectively.

the band gap nearly unchanged. Significant changes are observed when the nanosheet is Sc_2CS_2. We find a shallow peak around -0.5 eV solely due to the p states of C atoms associated with the cyclohexane ring of 3-carene. Moreover, the conduction band is pulled substantially towards lower energy. This reduces the electronic band gap by 0.138 eV. This suggests stronger interactions between the VOC and the nanosheet that re-distributes the electronic states significantly. This is consistent with the adsorption energy and charge density distribution discussed earlier. The densities of states of each D-limonene-Sc_2CT_2 complex (Figure 6.5(g)-(i)) is near identical to the corresponding 3-carene-Sc_2CT_2 compound. This goes with the variations in the adsorption energy, and charge distribution. The only noticeable difference is in case of Sc_2CF_2 where the p states of C belonging to the cyclohexane ring in D-limonene are deeper than those in 3-carene-Sc_2CF_2. This is consistent with the variations in the adsorption energy and points towards an artifact of stronger interaction between the VOC and the nanosheet due to the geometry of adsorption. The densities of states of methylbutanoate-Sc_2CT_2 compounds (Figure 6.6(g)-(i)) show that the molecular states (p states of C and O in the ester group)have distinct isolated molecule like states deep inside the valence band. The states are the deepest in case of Sc_2CO_2 (between -2 eV and -3 eV). Distinct peaks due to states occupied by these two constituents of the molecule are found around -1.5 eV and -2.5 eV when it is adsorbed on Sc_2CF_2. These states are further up in energies when Sc_2CS_2 is the adsorbent. For this system, the unoccupied part is pushed towards higher energies, thus affecting the band gap only slightly (by 0.025 eV). The changes in the band gaps are one order of magnitude less when the molecule is adsorbed on the other two MXenes. This suggests weaker interaction between the VOC and the MXenes, in comparison with the previous two cases and is consistent with the qualitative variations in the adsorption energy and charge density distributions. The densities of states are very similar for all cases when methylhexanoate is adsorbed (Figure 6.7(g)-(i)).Our analysis therefore suggests that impacts due to adsorption of 3-carene and D-limonene are very similar and is qualitatively different from the effects due to adsorption of the other two

(which have significant similarity among themselves) on MXene surfaces. Moreover, out of the three, Sc_2CS_2 is more responsive in comparison with the other two when different VOCs are adsorbed on its surface. In the following we check this by computations of quantities related to sensing ability of a material.

Table 6.1: Variations in the Adsorption Energy $(\mathbf{E}_{ad})$, Distance between nanosheet and VOC $\boldsymbol{D}$, Chrage transfer between VOC and nanosheet $\mathbf{Q}$, electronic band gap $(\mathbf{E}_g)$, Workfunction $\boldsymbol{\phi}$ and sensitivity of work function based sensor $\mathbf{S}^{\phi}$of VOC-MXene complexes.

Nanosheet	**VOC**	$\mathbf{E}_{ad}(eV)$	$\boldsymbol{D}$ (Å)	**Q(e)**	$\mathbf{E}_g(eV)$	ϕ**(eV)**	$\mathbf{S}^{\phi}(\%)$
Sc_2CO_2	-	-	-	-	1.788	5.354	-
	3-carene	-0.960	2.28	0.0007	1.789	5.347	0.1
	D-limonene	-0.956	2.20	0.0066	1.787	5.290	1.02
	Methylbutanoate	-0.640	2.64	0.0064	1.791	5.299	1.03
	Methylhexanoate	-0.904	2.53	0.0044	1.787	5.329	0.46
Sc_2CF_2	-	-	-	-	1.011	4.799	-
	3-Carene	-0.938	2.79	-0.0171	1.013	4.731	1.4
	D-Limonene	-1.015	2.53	-0.0300	1.012	4.748	1.07
	Methylbutanoate	-0.581	2.32	-0.0111	1.014	4.725	1.56
	Methylhexanoate	-0.837	2.86	-0.0291	1.012	4.753	0.96
Sc_2CS_2	-	-	-	-	1.499	5.902	-
	3-Carene	-1.175	2.68	0.0049	1.361	5.773	2.2
	D-Limonene	-1.133	2.75	-0.0110	1.375	5.792	1.89
	Methylbutanoate	-0.515	3.18	0.0076	1.524	5.732	2.96
	Methylhexanoate	-0.740	2.97	0.0021	1.507	5.779	2.1

First, we investigate the effectiveness of these three MXenes as work function based sensors towards these four biomarkers for papaya. In Table 6.1, we present the results for ϕ, ϕ_0 and S^{ϕ}. We find the sensitivities of all the systems are quite low. Highest sensitivity (between 2-3 %) is obtained for Sc_2CS_2. In this case, D-limonene and methyl butanoate can be distinctly recognized. The close values of S^{ϕ} for the other two makes it difficult to distinguish them. The worst performance is found for Sc_2CO_2 where sensitivity is nearly zero for 3-carene and methyl hexanoate while they are almost identical for the other two. This makes use of Sc_2CO_2 as work function based sensor for papaya VOCs ineffective. The situation is somewhat better in case of Sc_2CF_2. The qualitative nature of the work function variation and resulting sensitivity is consistent with the variations in the electronic structures of the VOC-MXene complexes where Sc_2CS_2 is more reactive towards the VOCs in comparison to the other two.

We next explore the possibility of using these MXenes as optical sensors to detect the papaya VOCs. The results for the absorption coefficients and reflectances are presented in Figure 6.11. Analysing the absorption coefficients of three MXenes before and after VOC adsorption (Figure 6.11(a)-(c)), we find that the following: (a)For Sc_2CO_2 and Sc_2CF_2, the absorption spectra of four different VOC-MXene complexes are barely distinguishable in the UV region of the electromagnetic spectrum which accounts for only 7% of solar energy. On the contrary, spectrum of all four can be distinguished in the energy range of 2.23-3.2 eV when the VOCs are adsorbed on Sc_2CS_2. Since this energy range is in the visible part of the spectrum, this can be utilised far more effectively for detection of the VOCs using optical probe. The computed reflectances (Figure 6.11(d)-(f)) too follow this trend. We, therefore, conclude that only Sc_2CS_2 can be utilised as an optical sensor to

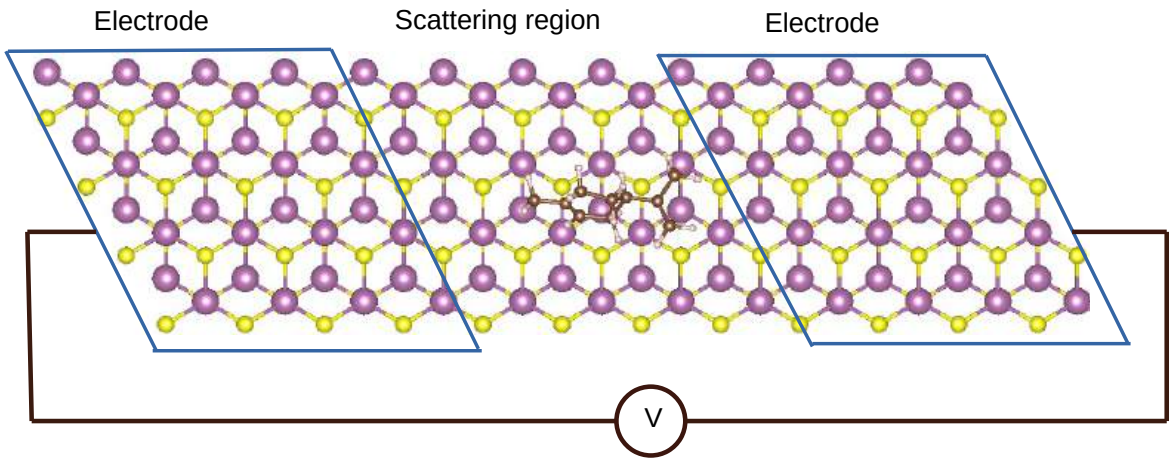

Figure 6.12: Schematic illustration of the nanodevice setup in Sc_2CS_2 nanosheet. The device consists of semi-infinite electrodes on left and right (rectangular area), and a central scattering region where the VOCs are adsorbed.

detect and separate biomarkers of papaya.

Subsequently, we investigate only Sc_2CS_2 for chemiresistive sensor application by computing the transport properties using NEGF method. The sensor is simulated by considering a two-probe model that consists of a central scattering region and two electrodes on either side of it.The electrodes act as the source and the drain while the VOCs are adsorbed in the central scattering region through which the transport takes place along z-direction. The setup is shown in Figure 6.12.

In Figure 6.13 we show the transmission coefficients $T(E)$ of the four VOC-Sc_2CS_2 compounds, as a function of energy E, calculated using Equation(5). The results are obtained with zero bias voltage ($V_b = 0$). Clear distinctions between the transmission coefficients of certain complexes at positive energies can be seen.From the inset of the figure, we find that transmission co-efficients due to 3-carene and D-limonene adsorbed Sc_2CS_2 are clearly separable while the contributions due to methylbutanoate and methylhexanoate are near identical and almost same as that of bare Sc_2CS_2.This indicates that sensitivities of 3-carene and D-limonene will be distinctively different. In Figure 6.14, we show computed values of S^{gas}, the chemiresistive sensitivity, for Sc_2CS_2. As expected and discussed throughout the chapter, 3-carene and D-limonene can be separated out from the mixture of VOCs. The other two, too, are separable but their sensitivities are extremely low. The results indicate that Sc_2CS_2 can be an useful chemiresistive sensor to detect and separate biomarkers of papaya. The low sensitivities obtained in this calculation may raise doubts about its utility in a real application. However, this calculation has been done considering the smallest amount of each VOC, that is a single molecule. In a realistic set-up, there are more molecules present and therefore the possibility of getting higher sensitivities is bright as has been established elsewhere [222]. Finally, in Table 6.2,

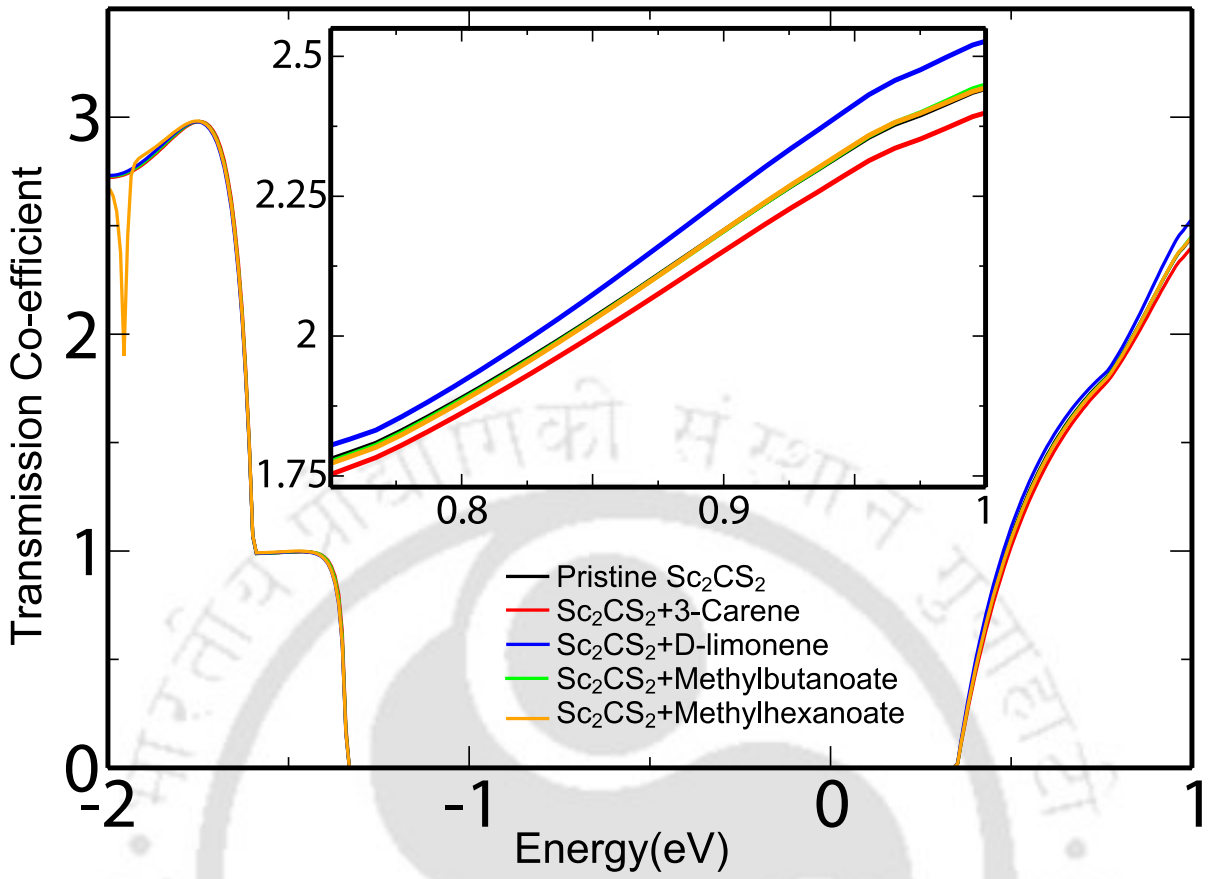

Figure 6.13: Zero bias transmission coefficients of bare and VOC-adsorbed Sc_2CS_2 MXene sheets. Inset shows results around the Fermi level)

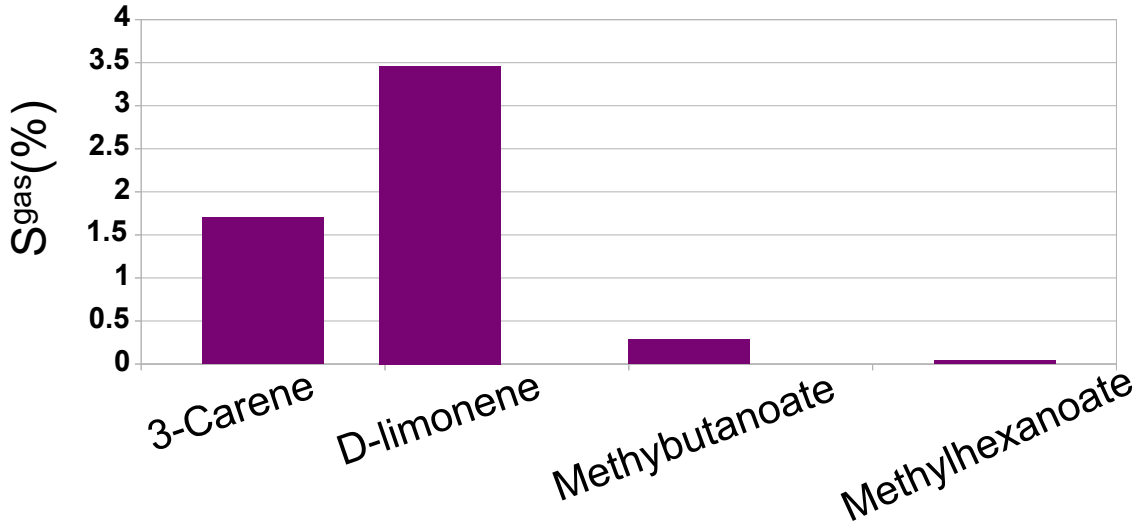

Figure 6.14: Sensitivity of chemiresistive Sc_2CS_2 towards papaya VOCs.

Table 6.2: Calculated response time τ (in s) of Sc_2CT_2 gas sensors. The calculations are done at room temperature ($T = 300$K) and under visible light ($\nu_0 = 10^{13}$ s^{-1}).

Molecule	Sc_2CO_2	Sc_2CF_2	Sc_2CS_2
3-Carene	1.15×10^{-5}	7.56×10^{-6}	7.40×10^{-4}
D-Limonene	1.07×10^{-5}	3.35×10^{-5}	3.28×10^{-4}
Methylbutanoate	2.37×10^{-8}	7.58×10^{-9}	2.11×10^{-9}
Methylhexanoate	3.91×10^{-6}	1.07×10^{-6}	1.64×10^{-7}

we present the results of τ for the three MXene sensors.The results suggest that all three MXene can be used as reusable sensor for sensing papaya VOCs.

6.4 Conclusions

Papaya, a fruit consumed heavily and having numerous health benefits, emit six major VOCs that can act as its biomarkers. In this work, using a combination of DFT and NEGF, we have investigated the sensing abilities of Sc_2CT_2 2D MXene compounds towards detection of four prominent VOCs emitted by papaya. We have explored the potentials of these systems as work function, optical and chemiresistive sensor. We find that Sc_2CS_2 stands out in sensing the VOCs in a distinctive manner. It performs well both as work-function and optical sensor but it's sensitivity is low as a chemiresistive sensor. Although the computed sensitivities are low but they can be improved under realistic conditions where more than one VOC molecule of each type are present simultaneously during the experiments. We have shown that the comparative sensing abilities can be understood from the geometry of adsorption and resulting electronic structures. To our knowledge, this is the first ever work to model a sensor for detection of papaya biomarkers. The results are expected to open up possibilities to investigate other 2D materials based sensors for detection of ripening stage of papaya, a need of the hour. A bigger picture placing MXenes as potential 2D sensors for detection of quality of various food products, also emerges from this study.

Chapter 7

Summary and future direction

7.1 Summary

In this dissertation, different 2D materials and VOCs from generic and specific food items have been considered with the motivation to assess the potentials of the 2D materials as sensors towards detecting VOCs. This has significance with regard to discovering useful sensors that can help monitor the quality of food products in a non- evasive and smart way. Computational study in this area of research is relatively new and under-explored.The work in this thesis is a comprehensive presentation on microscopic understanding of sensing in the area of food technology using state of the art computational techniques. The thesis has covered three prominent class of materials with regard to their interaction with quality markers of generic as well as specific food products. Each work follows a specific structure: first the understanding of VOC-2D material interactions and their consequences at the electronic level and then computations of sensing parameters that can be directly compared with experiments. The combinations of 2D material and the food quality markers(VOCs) used in this thesis provide significant insights into interaction of the two, based upon which systematic choice on sensors materials can be made judiciously. This work, to our knowledge, is first of its kind since the strategies adopted throughout, which not only enables understanding of complex interactions at the electronic level, but also mimics a real device and computationally characterizes it, in the field of food technology. The summary of each chapter is as follows.

In **Chapter 3**, we have investigated the potentials of Graphene and its two derivatives GO and r-GO with regard to sensing and discriminating six VOCs that act as biomarkers for stages of degradation of standard food item like fish, meat and vegetables. The assessment is done for using them as chemiresistive and work function based sensors. The work is motivated by an experiment which discarded r-GO as an inefficient sensor material as it could not seperate the VOCs. On the contrary our calculations stood r-GO in good stead. Both as a chemiresistive sensor and as a work function based sensor, it could differentiate between four VOCs, each with reasonable sensitivity. Pristine Graphene turned out be much less useful while GO turned out to be workable as a work function based sensor.

In **Chapter 4** we considered free-standing silicene and Fluorine passivated Silicene(F-Silicene) as the possible sensing materials and explored their performances as chemiresistive sensor with regard to the same set of VOCs considered in chapter 3. With the help of adsorption energy, charge transfer and positions of HOMO and LUMO of the VOC-2D material complexes, we assessed their potentials before performing device simulation.

The sensing parameters derived from device simulation corroborated the assessments from electronic structure calculations and understanding based upon the quantities calculated before device simulation. F-Silicene turned out to be sensitive and selective to four(out of six) VOCs, a performance at par with r-GO observed in chapter 3. The sensitivity of F-Silicene is found to be far superior than that of r-GO. This poses F-Silicene as an alternative to Graphene based ones, as a sensor for monitoring food degradation.

In **Chapter 5** , another set of materials are investigated with regard to detection of the four VOCs which both r-GO and F-Silicene could conclusively segregate. Sc_2CO_2 MXene and it's heterostructure with WSe_2, a TMDC, are considered for this investigation. The exciting outcome of this work is significant gain in the sensitivity due to formation of the heterostructure. A combination of two materials with different electronic properties led to an electric field across the interface of the heterostructure enabling easy charge transport, amplifying sensitivity as a consequence. A comparative sensing performance of Sc_2CO_2 and Wse_2/Sc_2CO_2 are presented with reference to F-Silicene and r-GO. It turns out that the MXene/TMDC heterostructure can be as useful as F-Silicene when used as a chemiresistive sensor and outperforms others as a Work function one.

In **Chapter 6**, we exploit the compositional flexibility of MXene family to assess the sensing performance of Sc_2C MXene, passivated with three different functionals:-O, -F and -S , each realizable in experiments, with regard to prominent VOCs from Papaya. Unlike the previous three chapters, the uniqueness of this work is in picking up a specific food product and much complicated VOCs associated with it. The investigation based on electronic structure related parameters and device simulation, showed that out of three, only Sc_2CS_2 can be considered as a chemiresistive sensor, that can discriminate between the VOCs released by Papaya. This work paves the way to use the strategy adopted throughout the thesis to be used in connection with detection of complex VOCs associated with specific food products.

7.2 Future Direction

Few directions that can make natural extension of this thesis are:

- Metallic MXenes like $Ti_3C_2T_x$, V_2CT_x and $Nb_3C_2T_x$ can be explored with regard to both specific and generic food VOC detection and segregation.

- TMDC, despite being investigated and with promising outcome, towards sensing hazardous gases and biomarkers of terminal diseases, have never been used in the context of sensing VOCs from food items. This thesis opens up the scope for exploring members from TMDC family as sensors for food quality assessment.

- TMDC-MXene heterostructure is another class of materials that can be excellent in sensing as is exemplified in this work. Future investigation can explore this direction.

- r-GO, F-Silicene and newly discovered metallic monolayers like Goldene can be assessed as sensors with regard to VOCs from specific food items. Like the case of

Papaya, VOCs from pear fruit, banana or tomato are large and complex molecules. One direction of future work can therefore be about testing grounds of these 2D materials when interacted with complex molecules.

References

[1] Margaret Kosek, Caryn Bern, and Richard L Guerrant. The global burden of diarrhoeal disease, as estimated from studies published between 1992 and 2000. *Bulletin of the world health organization*, 81:197–204, 2003.

[2] World Health Organization. *Tracking universal health coverage: 2023 global monitoring report*. World Health Organization, 2023.

[3] Bharat H Desai. 14. united nations environment programme (unep). *Yearbook of International Environmental Law*, 31(1):319–325, 2020.

[4] Helen Canton. Food and agriculture organization of the united nations—fao. In *The Europa directory of international organizations 2021*, pages 297–305. Routledge, 2021.

[5] Shiv Dutta Lawaniya, Anjali Awasthi, Prashanth W Menezes, and Kamlendra Awasthi. Detection of foodborne pathogens through volatile organic compounds sensing via metal oxide gas sensors. *Advanced Sensor Research*, 4(1):2400101, 2025.

[6] Yuxue Cui, Haijing Zhang, Jingwen Zhang, Baoyi Lv, and Bing Xie. The emission of volatile organic compounds during the initial decomposition stage of food waste and its relationship with the bacterial community. *Environmental Technology & Innovation*, 27:102443, 2022.

[7] Anastasia E Lytou, Efstathios Z Panagou, and George-John E Nychas. Volatilomics for food quality and authentication. *Current Opinion in Food Science*, 28:88–95, 2019.

[8] Hao Lin, Hao Jiang, Selorm Yao-Say Solomon Adade, Wencui Kang, Zhaoli Xue, Muhammad Zareef, and Quansheng Chen. Overview of advanced technologies for volatile organic compounds measurement in food quality and safety. *Critical Reviews in Food Science and Nutrition*, 63(26):8226–8248, 2023.

[9] EN Frankel. Volatile lipid oxidation products. *Progress in lipid research*, 22(1):1–33, 1983.

[10] Fereidoon Shahidi and Ying Zhong. Lipid oxidation and improving the oxidative stability. *Chemical society reviews*, 39(11):4067–4079, 2010.

[11] George-John E Nychas, Panos N Skandamis, Chrysoula C Tassou, and Konstantinos P Koutsoumanis. Meat spoilage during distribution. *Meat science*, 78(1-2):77–89, 2008.

[12] Małgorzata Starowicz. Analysis of volatiles in food products. *Separations*, 8(9):157, 2021.

[13] O David Sparkman, Zelda Penton, and Fulton G Kitson. *Gas chromatography and mass spectrometry: a practical guide*. Academic press, 2011.

[14] Kateřina Maštovská and Steven J Lehotay. Practical approaches to fast gas chromatography–mass spectrometry. *Journal of Chromatography A*, 1000(1-2):153–180, 2003.

[15] Patricia M Medeiros. Gas chromatography–mass spectrometry (gc–ms). In *Encyclopedia of geochemistry*, pages 530–535. Springer, 2018.

[16] Ghenadii Korotcenkov. Metal oxides for solid-state gas sensors: What determines our choice? *Materials Science and Engineering: B*, 139(1):1–23, 2007.

[17] Seon Ju Park, Soo Min Lee, Mi-Hwa Oh, Yoon Suk Huh, and Ho Won Jang. Food quality assessment using chemoresistive gas sensors: achievements and future perspectives. *Sustainable Food Technology*, 2(2):266–280, 2024.

[18] Michael G Campbell, Sophie F Liu, Timothy M Swager, and Mircea Dinca. Chemiresistive sensor arrays from conductive 2d metal–organic frameworks. *Journal of the American Chemical Society*, 137(43):13780–13783, 2015.

[19] Ruixian Tang, Yongji Shi, Zhongyu Hou, and Liangming Wei. Carbon nanotube-based chemiresistive sensors. *Sensors*, 17(4):882, 2017.

[20] Won-Tae Koo, Hee-Jin Cho, Dong-Ha Kim, Yoon Hwa Kim, Hamin Shin, Reginald M Penner, and Il-Doo Kim. Chemiresistive hydrogen sensors: fundamentals, recent advances, and challenges. *ACS nano*, 14(11):14284–14322, 2020.

[21] Parthasarathy Srinivasan, Madeshwari Ezhilan, Arockia Jayalatha Kulandaisamy, K Jayanth Babu, and John Bosco Balaguru Rayappan. Room temperature chemiresistive gas sensors: challenges and strategies—a mini review. *Journal of Materials Science: Materials in Electronics*, 30(17):15825–15847, 2019.

[22] Eric Bakker and Martin Telting-Diaz. Electrochemical sensors. *Analytical chemistry*, 74(12):2781–2800, 2002.

[23] Grady Hanrahan, Deepa G Patil, and Joseph Wang. Electrochemical sensors for environmental monitoring: design, development and applications. *Journal of environmental monitoring*, 6(8):657–664, 2004.

[24] Jon R Askim, Morteza Mahmoudi, and Kenneth S Suslick. Optical sensor arrays for chemical sensing: the optoelectronic nose. *Chemical Society Reviews*, 42(22):8649–8682, 2013.

[25] Ramaier Narayanaswamy and Otto S Wolfbeis. *Optical sensors: industrial environmental and diagnostic applications*, volume 1. Springer Science & Business Media, 2003.

[26] Briliant Adhi Prabowo, Agnes Purwidyantri, and Kou-Chen Liu. Surface plasmon resonance optical sensor: A review on light source technology. *Biosensors*, 8(3):80, 2018.

[27] Pedro Jesús Rodríguez de Rivera, Miriam Rodríguez de Rivera, Fabiola Socorro, and Manuel Rodríguez de Rivera. Measurement of human body surface heat flux using a calorimetric sensor. *Journal of thermal biology*, 81:178–184, 2019.

[28] J Lerchner, D Caspary, and G Wolf. Calorimetric detection of volatile organic compounds. *Sensors and Actuators B: Chemical*, 70(1-3):57–66, 2000.

[29] Kiran Kumar Sappati and Sharmistha Bhadra. Printed acoustic sensor for low concentration volatile organic compound monitoring. *IEEE Sensors Journal*, 21(8):9808–9818, 2021.

[30] Dongsheng Li, Boyi Zhu, Kai Pang, Qian Zhang, Mengjiao Qu, Weiting Liu, YongQing Fu, and Jin Xie. Virtual sensor array based on piezoelectric cantilever resonator for identification of volatile organic compounds. *ACS sensors*, 7(5):1555–1563, 2022.

[31] Hongfei Zu, Huiyan Wu, and Qing-Ming Wang. High-temperature piezoelectric crystals for acoustic wave sensor applications. *IEEE transactions on ultrasonics, ferroelectrics, and frequency control*, 63(3):486–505, 2016.

[32] Hirofumi Shintaku, Takayuki Nakagawa, Dai Kitagawa, Harto Tanujaya, Satoyuki Kawano, and Juichi Ito. Development of piezoelectric acoustic sensor with frequency selectivity for artificial cochlea. *Sensors and Actuators A: Physical*, 158(2):183–192, 2010.

[33] Deniz Sadighbayan, Mohammad Hasanzadeh, and Ebrahim Ghafar-Zadeh. Biosensing based on field-effect transistors (fet): Recent progress and challenges. *TrAC Trends in Analytical Chemistry*, 133:116067, 2020.

[34] Shun Mao, Jingbo Chang, Haihui Pu, Ganhua Lu, Qiyuan He, Hua Zhang, and Junhong Chen. Two-dimensional nanomaterial-based field-effect transistors for chemical and biological sensing. *Chemical Society Reviews*, 46(22):6872–6904, 2017.

[35] Weiwei Cheng, Xiaozhi Tang, Yan Zhang, Di Wu, and Wenjian Yang. Applications of metal-organic framework (mof)-based sensors for food safety: Enhancing mechanisms and recent advances. *Trends in Food Science & Technology*, 112:268–282, 2021.

[36] Hessamaddin Sohrabi, Shahin Ghasemzadeh, Zahra Ghoreishi, Mir Reza Majidi, Yeojoon Yoon, Nadir Dizge, and Alireza Khataee. Metal-organic frameworks (mof)-based sensors for detection of toxic gases: A review of current status and future prospects. *Materials Chemistry and Physics*, 299:127512, 2023.

[37] Camilla Maria Cova, Esther Rincón, Eduardo Espinosa, Luis Serrano, and Alessio Zuliani. Paving the way for a green transition in the design of sensors and biosensors for the detection of volatile organic compounds (vocs). *Biosensors*, 12(2):51, 2022.

[38] Hakkim Vovusha, Hyeonhu Bae, Seunghan Lee, Jusang Park, Ali Raza, Komsilp Kotmool, Tanveer Hussain, and Hoonkyung Lee. Density functional theory studies of mxene-based nanosensors for detecting volatile organic compounds in meat spoilage assessment. *ACS Applied Nano Materials*, 6(19):18592–18601, 2023.

[39] Shih-Wen Chiu and Kea-Tiong Tang. Towards a chemiresistive sensor-integrated electronic nose: a review. *Sensors*, 13(10):14214–14247, 2013.

[40] Alphus D Wilson and Manuela Baietto. Applications and advances in electronic-nose technologies. *sensors*, 9(7):5099–5148, 2009.

[41] S Ampuero and JO Bosset. The electronic nose applied to dairy products: a review. *Sensors and Actuators B: Chemical*, 94(1):1–12, 2003.

[42] Frank Röck, Nicolae Barsan, and Udo Weimar. Electronic nose: current status and future trends. *Chemical reviews*, 108(2):705–725, 2008.

[43] Shadman Khan, Amid Shakeri, Simrun Tariq, Yingfu Li, and Tohid Fatanat Didar. Monitoring food contamination in real time using printable dnazyme sensors. In *Electrochemical Society Meeting Abstracts 240*, number 55, pages 1577–1577. The Electrochemical Society, Inc., 2021.

[44] Muhammad Khatib and Hossam Haick. Sensors for volatile organic compounds. *ACS nano*, 16(5):7080–7115, 2022.

[45] Deepak Goyal, Chandra Prakash Goyal, David Chidambaram, Yuvaraj Sivalingam, Hiroya Ikeda, S Ponnusamy, and Niranjan S Ramgir. No2 and nh3 detection using work function measurement of solvothermal synthesised zno–nio nanocomposites: a case study. *Journal of Materials Science: Materials in Electronics*, 35(14):960, 2024.

[46] Seo Yun Park, Yeonhoo Kim, Taehoon Kim, Tae Hoon Eom, Soo Young Kim, and Ho Won Jang. Chemoresistive materials for electronic nose: Progress, perspectives, and challenges. *InfoMat*, 1(3):289–316, 2019.

[47] B Bala Subbanna, Kuldeep Choudhary, Sonika Singh, and Santosh Kumar. 2d material-based optical sensors: a review. *ISSS Journal of Micro and Smart Systems*, 11(1):169–177, 2022.

[48] Hailong Zhang, Fuchao Tian, Yu Zhang, and Yuntao Liang. Research progress of temperature and pressure compensation method of industrial environment gas sensor. *Physics of Fluids*, 37(5), 2025.

[49] Tejaswini Sahoo and Paresh Kale. Work function-based metal–oxide–semiconductor hydrogen sensor and its functionality: A review. *Advanced Materials Interfaces*, 8(23):2100649, 2021.

[50] Shengming Li, Yusheng Zhou, Yunlong Zi, Gong Zhang, and Zhong Lin Wang. Excluding contact electrification in surface potential measurement using kelvin probe force microscopy. *ACS nano*, 10(2):2528–2535, 2016.

[51] Yuwei Shen, Antoine Tissot, and Christian Serre. Recent progress on mof-based optical sensors for voc sensing. *Chemical Science*, 13(47):13978–14007, 2022.

[52] Sulaiman Khan, Stéphane Le Calvé, and David Newport. A review of optical interferometry techniques for voc detection. *Sensors and Actuators A: Physical*, 302:111782, 2020.

[53] Minzhen Ma, Xinting Yang, Xiaoguo Ying, Ce Shi, Zhixin Jia, and Boce Jia. Applications of gas sensing in food quality detection: A review. *Foods*, 12(21):3966, 2023.

[54] Tabli Ghosh, GVS Bhagya Raj, and Kshirod Kumar Dash. A comprehensive review on nanotechnology based sensors for monitoring quality and shelf life of food products. *Measurement: Food*, 7:100049, 2022.

[55] Warren Rosario, Pravin Kumar Singh, Ashutosh Tiwari, Utkarsh Jain, Devesh Kumar Avasthi, and Nidhi Chauhan. Nanomaterial-based voc sensing applications and a deep dive into their developmental trends. *Journal of Materials Chemistry A*, 12(17):9979–10011, 2024.

[56] Murendeni I Nemufulwi, Hendrik C Swart, and Gugu H Mhlongo. Advances of nano-enabled znfe2o4 based-gas sensors for voc detection and their potential applications: a review. *Processes*, 11(11):3122, 2023.

[57] Stefano Veronesi, Ylea Vlamidis, Letizia Ferbel, Carmela Marinelli, Chiara Sanmartin, Isabella Taglieri, Georg Pfusterschmied, Markus Leitgeb, Ulrich Schmid, Fabio Mencarelli, et al. Three-dimensional graphene on a nano-porous 4h-sic backbone: a novel material for food sensing applications. *arXiv preprint arXiv:2309.13431*, 2023.

[58] Zheng Meng, Robert M Stolz, Lukasz Mendecki, and Katherine A Mirica. Electrically-transduced chemical sensors based on two-dimensional nanomaterials. *Chemical reviews*, 119(1):478–598, 2019.

[59] Mengqi Zeng, Yao Xiao, Jinxin Liu, Kena Yang, and Lei Fu. Exploring two-dimensional materials toward the next-generation circuits: from monomer design to assembly control. *Chemical reviews*, 118(13):6236–6296, 2018.

[60] Ivan V Vlassiouk, Yijing Stehle, Pushpa Raj Pudasaini, Raymond R Unocic, Philip D Rack, Arthur P Baddorf, Ilia N Ivanov, Nickolay V Lavrik, Frederick List, Nitant Gupta, et al. Evolutionary selection growth of two-dimensional materials on polycrystalline substrates. *Nature Materials*, 17(4):318–322, 2018.

[61] Guozheng Yang, Hao Kong, Yun Chen, Bin Liu, Danzhu Zhu, Lei Guo, and Gang Wei. Recent advances in the hybridization of cellulose and carbon nanomaterials: Interactions, structural design, functional tailoring, and applications. *Carbohydrate polymers*, 279:118947, 2022.

[62] Bo Tang, Haiqun Chen, Haoping Peng, Zhengwei Wang, and Weiqiu Huang. Graphene modified tio2 composite photocatalysts: Mechanism, progress and perspective. *Nanomaterials*, 8(2):105, 2018.

[63] Kirill I Bolotin, KJ Sikes, Zhifang Jiang, M Klima, G Fudenberg, James Hone, Phaly Kim, and Horst L Stormer. Ultrahigh electron mobility in suspended graphene. *Solid state communications*, 146(9-10):351–355, 2008.

[64] Yilin Wang, Yanan Chen, Steven D Lacey, Lisha Xu, Hua Xie, Tian Li, Valencia A Danner, and Liangbing Hu. Reduced graphene oxide film with record-high conductivity and mobility. *Materials Today*, 21(2):186–192, 2018.

[65] Alexander Grüneis, Claudio Attaccalite, Ludger Wirtz, Hidetsugu Shiozawa, R Saito, Thomas Pichler, and Angel Rubio. Tight-binding description of the quasiparticle dispersion of graphite and few-layer graphene. *Physical Review B—Condensed Matter and Materials Physics*, 78(20):205425, 2008.

[66] Tao Zhang, Jilun Liu, Cheng Wang, Xuanye Leng, Yao Xiao, and Lei Fu. Synthesis of graphene and related two-dimensional materials for bioelectronics devices. *Biosensors and Bioelectronics*, 89:28–42, 2017.

[67] Il-Yung Sohn, Duck-Jin Kim, Jin-Heak Jung, Ok Ja Yoon, Tien Nguyen Thanh, Trung Tran Quang, and Nae-Eung Lee. ph sensing characteristics and biosensing application of solution-gated reduced graphene oxide field-effect transistors. *Biosensors and Bioelectronics*, 45:70–76, 2013.

[68] Zhongjian Xie, Yanhong Duo, Zhitao Lin, Taojian Fan, Chenyang Xing, Li Yu, Renheng Wang, Meng Qiu, Yupeng Zhang, Yonghua Zhao, et al. The rise of 2d photothermal materials beyond graphene for clean water production. *Advanced Science*, 7(5):1902236, 2020.

[69] Jishan Wu, Wojciech Pisula, and Klaus Müllen. Graphenes as potential material for electronics. *Chemical reviews*, 107(3):718–747, 2007.

[70] Elochukwu Stephen Agudosi, Ezzat Chan Abdullah, Arshid Numan, Nabisab Mujawar Mubarak, Mohammad Khalid, and Nurizan Omar. A review of the graphene synthesis routes and its applications in electrochemical energy storage. *Critical Reviews in Solid State and Materials Sciences*, 45(5):339–377, 2020.

[71] Yuxin Liu, Xiaochen Dong, and Peng Chen. Biological and chemical sensors based on graphene materials. *Chemical Society Reviews*, 41(6):2283–2307, 2012.

[72] MF Hossain and Jae Y Park. An enzymatic hybrid electrode platform based on chemically modified reduced graphene oxide decorated with palladium and platinum alloy nanoparticles for biosensing applications. *Journal of The Electrochemical Society*, 162(7):B185, 2015.

[73] Nabilah Mohammad Yusof, Suriani Ibrahim, and Shaifulazuar Rozali. Advances on graphene-based gas sensors for acetone detection based on its physical and chemical attributes. *Journal of Materials Research*, 37(2):405–423, 2022.

[74] Yun Chen, Guozheng Yang, Bin Liu, Hao Kong, Zhong Xiong, Lei Guo, and Gang Wei. Biomineralization of zro2 nanoparticles on graphene oxide-supported peptide/cellulose binary nanofibrous membranes for high-performance removal of fluoride ions. *Chemical Engineering Journal*, 430:132721, 2022.

[75] Xiaowen Yu, Huhu Cheng, Miao Zhang, Yang Zhao, Liangti Qu, and Gaoquan Shi. Graphene-based smart materials. *Nature Reviews Materials*, 2(9):1–13, 2017.

[76] Houk Jang, Yong Ju Park, Xiang Chen, Tanmoy Das, Min-Seok Kim, and Jong-Hyun Ahn. Graphene-based flexible and stretchable electronics. *Advanced Materials*, 28(22):4184–4202, 2016.

[77] Xiao-Lin Wei, Yuan-Ping Chen, Wen-Liang Liu, and Jian-Xin Zhong. Enhanced gas sensor based on nitrogen-vacancy graphene nanoribbons. *Physics Letters A*, 376(4):559–562, 2012.

[78] Tanveer Hussain, Puspamitra Panigrahi, and Rajeev Ahuja. Enriching physisorption of h 2 s and nh 3 gases on a graphane sheet by doping with li adatoms. *Physical Chemistry Chemical Physics*, 16(17):8100–8105, 2014.

[79] Fang Niu, Jin-Mei Liu, Li-Ming Tao, Wei Wang, and Wei-Guo Song. Nitrogen and silica co-doped graphene nanosheets for no 2 gas sensing. *Journal of Materials Chemistry A*, 1(20):6130–6133, 2013.

[80] Viet Bac T Phung, Thi Nhan Tran, Quang Huy Tran, Thi Theu Luong, and Van An Dinh. Graphene as a sensor for lung cancer: insights into adsorption of vocs using vdw dft. *ACS omega*, 9(2):2302–2313, 2024.

[81] Vardan Galstyan, Elisabetta Comini, Iskandar Kholmanov, Andrea Ponzoni, Veronica Sberveglieri, Nicola Poli, Guido Faglia, and Giorgio Sberveglieri. A composite structure based on reduced graphene oxide and metal oxide nanomaterials for chemical sensors. *Beilstein journal of nanotechnology*, 7(1):1421–1427, 2016.

[82] Baishu Liu, Yan Huang, Kenneth WL Kam, Wai-Fung Cheung, Ni Zhao, and Bo Zheng. Functionalized graphene-based chemiresistive electronic nose for discrimination of disease-related volatile organic compounds. *Biosensors and Bioelectronics: X*, 1:100016, 2019.

[83] Bannur Nanjunda Shivananju, Wenzhi Yu, Yan Liu, Yupeng Zhang, Bo Lin, Shaojuan Li, and Qiaoliang Bao. The roadmap of graphene-based optical biochemical sensors. *Advanced Functional Materials*, 27(19):1603918, 2017.

[84] Miguel Hernaez, Carlos R Zamarreño, Sonia Melendi-Espina, Liam R Bird, Andrew G Mayes, and Francisco J Arregui. Optical fibre sensors using graphene-based materials: A review. *Sensors*, 17(1):155, 2017.

[85] Hao Kong, Yun Chen, Guozheng Yang, Bin Liu, Lei Guo, Yan Wang, Xin Zhou, and Gang Wei. Two-dimensional material-based functional aerogels for treating hazards in the environment: synthesis, functional tailoring, applications, and sustainability analysis. *Nanoscale Horizons*, 7(2):112–140, 2022.

[86] Mohamed A Helal, HM El-Sayed, Ahmed A Maarouf, and Mohamed M Fadlallah. Metal dichalcogenide nanomeshes: Structural, electronic and magnetic properties. *Physical Chemistry Chemical Physics*, 23(37):21183–21195, 2021.

[87] Shaswat Barua, Hemant Sankar Dutta, Satyabrat Gogoi, Rashmita Devi, and Raju Khan. Nanostructured mos2-based advanced biosensors: a review. *ACS Applied Nano Materials*, 1(1):2–25, 2017.

[88] Jiacheng Cao, Qian Chen, Xiaoshan Wang, Qiang Zhang, Hai-Dong Yu, Xiao Huang, and Wei Huang. Recent development of gas sensing platforms based on 2d atomic crystals. *Research*, 2021.

[89] Masaro Yoshida, Jianting Ye, Yijin Zhang, Yasuhiko Imai, Shigeru Kimura, Akihiko Fujiwara, Terukazu Nishizaki, Norio Kobayashi, Masaki Nakano, and Yoshihiro Iwasa. Extended polymorphism of two-dimensional material. *Nano Letters*, 17(9):5567–5571, 2017.

[90] Hui Chen, Jiwei Zhang, Dongxiao Kan, Jiabei He, Mengshan Song, Jianhua Pang, Songrui Wei, and Kaiyun Chen. The recent progress of two-dimensional transition metal dichalcogenides and their phase transition. *Crystals*, 12(10):1381, 2022.

[91] Damien Voiry, Aditya Mohite, and Manish Chhowalla. Phase engineering of transition metal dichalcogenides. *Chemical Society Reviews*, 44(9):2702–2712, 2015.

[92] Hai Li, Gang Lu, Zongyou Yin, Qiyuan He, Hong Li, Qing Zhang, and Hua Zhang. Optical identification of single-and few-layer mos2 sheets. *Small*, 8(5):682–686, 2012.

[93] Min Wu, Yonghong Xiao, Yang Zeng, Yuanliang Zhou, Xiangbin Zeng, Lining Zhang, and Wugang Liao. Synthesis of two-dimensional transition metal dichalcogenides for electronics and optoelectronics. *InfoMat*, 3(4):362–396, 2021.

[94] Arvind Mukundan, Shih-Wei Feng, Yu-Hsin Weng, Yu-Ming Tsao, Sofya B Artemkina, Vladimir E Fedorov, Yen-Sheng Lin, Yu-Cheng Huang, and Hsiang-Chen Wang. Optical and material characteristics of mos2/cu2o sensor for detection of lung cancer cell types in hydroplegia. *International Journal of Molecular Sciences*, 23(9):4745, 2022.

[95] Hai Li, Zongyou Yin, Qiyuan He, Hong Li, Xiao Huang, Gang Lu, Derrick Wen Hui Fam, Alfred Iing Yoong Tok, Qing Zhang, and Hua Zhang. Fabrication of single-and multilayer mos2 film-based field-effect transistors for sensing no at room temperature. *small*, 8(1):63–67, 2012.

[96] Goki Eda, Takeshi Fujita, Hisato Yamaguchi, Damien Voiry, Mingwei Chen, and Manish Chhowalla. Coherent atomic and electronic heterostructures of single-layer mos2. *ACS nano*, 6(8):7311–7317, 2012.

[97] Muharrem Acerce, Damien Voiry, and Manish Chhowalla. Metallic 1t phase mos2 nanosheets as supercapacitor electrode materials. *Nature nanotechnology*, 10(4):313–318, 2015.

[98] Si Young Lee, Un Jeong Kim, JaeGwan Chung, Honggi Nam, Hye Yun Jeong, Gang Hee Han, Hyun Kim, Hye Min Oh, Hyangsook Lee, Hyochul Kim, et al. Large work function modulation of monolayer mos2 by ambient gases. *ACS nano*, 10(6):6100–6107, 2016.

[99] Nirav Joshi, Takeshi Hayasaka, Yumeng Liu, Huiliang Liu, Osvaldo N Oliveira Jr, and Liwei Lin. A review on chemiresistive room temperature gas sensors based on metal oxide nanostructures, graphene and 2d transition metal dichalcogenides. *Microchimica Acta*, 185(4):213, 2018.

[100] Maryam Nayeri, Mahdi Moradinasab, and Morteza Fathipour. The transport and optical sensing properties of mos2, mose2, ws2 and wse2 semiconducting transition metal dichalcogenides. *Semiconductor Science and Technology*, 33(2):025002, 2018.

[101] Narendra Pal, Jitendra Bahadur Maurya, Yogendra Kumar Prajapati, and Santosh Kumar. Lif-ag-si-tmds based long-range spr sensor in visible and nir spectrum. *Optik*, 274:170556, 2023.

[102] Olha Mashtalir, Michael Naguib, Vadym N Mochalin, Yohan Dall'Agnese, Min Heon, Michel W Barsoum, and Yury Gogotsi. Intercalation and delamination of layered carbides and carbonitrides. *Nature communications*, 4(1):1716, 2013.

[103] Maria R Lukatskaya, Olha Mashtalir, Chang E Ren, Yohan Dall'Agnese, Patrick Rozier, Pierre Louis Taberna, Michael Naguib, Patrice Simon, Michel W Barsoum, and Yury Gogotsi. Cation intercalation and high volumetric capacitance of two-dimensional titanium carbide. *Science*, 341(6153):1502–1505, 2013.

[104] Mohammad Khazaei, Masao Arai, Taizo Sasaki, Chan-Yeup Chung, Natarajan S Venkataramanan, Mehdi Estili, Yoshio Sakka, and Yoshiyuki Kawazoe. Novel electronic and magnetic properties of two-dimensional transition metal carbides and nitrides. *Advanced Functional Materials*, 23(17):2185–2192, 2013.

[105] Michael Naguib, Murat Kurtoglu, Volker Presser, Jun Lu, Junjie Niu, Min Heon, Lars Hultman, Yury Gogotsi, and Michel W Barsoum. Two-dimensional nanocrystals produced by exfoliation of ti3alc2. In *MXenes*, pages 15–29. Jenny Stanford Publishing, 2023.

[106] Qiuming Peng, Jianxin Guo, Qingrui Zhang, Jianyong Xiang, Baozhong Liu, Aiguo Zhou, Riping Liu, and Yongjun Tian. Unique lead adsorption behavior of activated hydroxyl group in two-dimensional titanium carbide. *Journal of the American Chemical Society*, 136(11):4113–4116, 2014.

[107] Michael Ghidiu, Maria R Lukatskaya, Meng-Qiang Zhao, Yury Gogotsi, and Michel W Barsoum. Conductive two-dimensional titanium carbide 'clay'with high volumetric capacitance. In *MXenes*, pages 379–399. Jenny Stanford Publishing, 2023.

[108] Olha Mashtalir, Michael Naguib, Boris Dyatkin, Yury Gogotsi, and Michel W Barsoum. Kinetics of aluminum extraction from ti3alc2 in hydrofluoric acid. *Materials Chemistry and Physics*, 139(1):147–152, 2013.

[109] Michel W Barsoum and Tamer El-Raghy. The max phases: Unique new carbide and nitride materials: Ternary ceramics turn out to be surprisingly soft and machinable, yet also heat-tolerant, strong and lightweight. *American scientist*, 89(4):334–343, 2001.

[110] Andrey N Enyashin and Alexander L Ivanovskii. Structural and electronic properties and stability of mx enes ti2c and ti3c2 functionalized by methoxy groups. *The Journal of Physical Chemistry C*, 117(26):13637–13643, 2013.

[111] Yu Xie and PRC Kent. Hybrid density functional study of structural and electronic properties of functionalized\ce {Ti_ {n+ 1} X_n}(x= c, n) monolayers. *arXiv preprint arXiv:1306.6936*, 2013.

[112] Sevda Hasanova, Ayşe Boyraz, Minaya Mammadzada, and Erhan Zor. Mxene-based sensors on pharmaceutical and environmental assays. *Essential Chem*, 1(1):1–25, 2024.

[113] Thorsten Schultz, Peer Bärmann, Elena Longhi, Rahul Meena, Yves Geerts, Yury Gogotsi, Stephen Barlow, Seth R Marder, Tristan Petit, and Norbert Koch. Work function and energy level alignment tuning at ti 3 c 2 t x mxene surfaces and interfaces using (metal-) organic donor/acceptor molecules. *Physical Review Materials*, 7(4):045002, 2023.

[114] Hongyue Jing, Benzheng Lyu, Yingqi Tang, Sungpyo Baek, Jin-Hong Park, Byoung Hun Lee, Jin Yong Lee, and Sungjoo Lee. β-mercaptoethanol-enabled long-term stability and work function tuning of mxene. *Small Science*, 2(11):2200057, 2022.

[115] VR Sudheer, SR Sarath Kumar, and S Sankararaman. Ultrahigh sensitivity surface plasmon resonance–based fiber-optic sensors using metal-graphene layers with ti3c2tx mxene overlayers. *Plasmonics*, 15(2):457–466, 2020.

[116] Leiming Wu, Xixi Yuan, Yuxuan Tang, S Wageh, Omar A Al-Hartomy, Abdullah G Al-Sehemi, Jun Yang, Yuanjiang Xiang, Han Zhang, and Yuwen Qin. Mxene sensors based on optical and electrical sensing signals: from biological, chemical, and physical sensing to emerging intelligent and bionic devices. *PhotoniX*, 4(1):15, 2023.

[117] Ángel Millán and Marta Retamosa. Consumer assessment of pork loin quality: How important are sensory attributes, pig breed, and familiarity? *Foods*, 14(15):2587, 2025.

[118] Longyi Chen, Eugene Hwang, and Jin Zhang. Fluorescent nanobiosensors for sensing glucose. *Sensors*, 18(5):1440, 2018.

[119] Lakshmipathy Muthukrishnan. An overview on the nanotechnological expansion, toxicity assessment and remediating approaches in agriculture and food industry. *Environmental Technology & Innovation*, 25:102136, 2022.

[120] Tran Thanh Tung, Mickael Castro, Tae Young Kim, Kwang S Suh, and Jean-François Feller. Graphene quantum resistive sensing skin for the detection of alteration biomarkers. *Journal of Materials Chemistry*, 22(40):21754–21766, 2012.

[121] Komal Kushwaha, Shashank Sagar Saini, Bhairavnath Waghmode, Mariam Gaid, Pawan Kumar Agrawal, Partha Roy, and Debabrata Sircar. Volatile components in papaya fruits are the non-invasive biomarkers to monitor the ripening stage and the nutritional value. *European Food Research and Technology*, 247(4):907–919, 2021.

[122] Walter Kohn and Lu Jeu Sham. Self-consistent equations including exchange and correlation effects. *Physical review*, 140(4A):A1133, 1965.

[123] Mohammad Ubaid, A Aziz, and Bhalchandra S Pujari. Indium doped phosphorene as a potential gas sensor: a study using density functional theory. *Electronic Structure*, 2(3):035001, 2020.

[124] R Keerthi Bhavadharani, V Nagarajan, and R Chandiramouli. Silicene nanosheet to discriminate the quality of pear fruit based on volatiles adsorption—a dft application. *arXiv preprint arXiv:1910.00886*, 2019.

[125] V Nagarajan and R Chandiramouli. Interaction of volatile organic compounds (vocs) emitted from banana on stanene nanosheet—a first-principles studies. *Structural Chemistry*, 29(5):1321–1332, 2018.

[126] U Srimathi, V Nagarajan, and R Chandiramouli. Interaction of imuran, pentasa and hyoscyamine drugs and solvent effects on graphdiyne nanotube as a drug delivery system-a dft study. *Journal of Molecular Liquids*, 265:199–207, 2018.

[127] Supriyo Datta. Nanoscale device modeling: the green's function method. *Superlattices and microstructures*, 28(4):253–278, 2000.

[128] Fredrik Schedin, Andrei Konstantinovich Geim, Sergei Vladimirovich Morozov, Ew W Hill, Peter Blake, Mi I Katsnelson, and Kostya Sergeevich Novoselov. Detection of individual gas molecules adsorbed on graphene. *Nature materials*, 6(9):652–655, 2007.

[129] Jeremy T Robinson, F Keith Perkins, Eric S Snow, Zhongqing Wei, and Paul E Sheehan. Reduced graphene oxide molecular sensors. *Nano letters*, 8(10):3137–3140, 2008.

[130] Jesse D Fowler, Matthew J Allen, Vincent C Tung, Yang Yang, Richard B Kaner, and Bruce H Weiller. Practical chemical sensors from chemically derived graphene. *ACS nano*, 3(2):301–306, 2009.

[131] Ganhua Lu, Leonidas E Ocola, and Junhong Chen. Reduced graphene oxide for room-temperature gas sensors. *Nanotechnology*, 20(44):445502, 2009.

[132] Weiran Wang, Hengjie Su, Yuxiang Wu, Teng Zhou, and Ting Li. Biosensing and biomedical applications of graphene: a review of current progress and future prospect. *Journal of The Electrochemical Society*, 166(6):B505, 2019.

[133] Anindya Nag, Arkadeep Mitra, and Subhas Chandra Mukhopadhyay. Graphene and its sensor-based applications: A review. *Sensors and Actuators A: physical*, 270:177–194, 2018.

[134] Kumud Malika Tripathi, TaeYoung Kim, Dusan Losic, and Tran Thanh Tung. Recent advances in engineered graphene and composites for detection of volatile organic compounds (vocs) and non-invasive diseases diagnosis. *Carbon*, 110:97–129, 2016.

[135] Vanish Kumar, Yoon-Seo Lee, Jae-Won Shin, Ki-Hyun Kim, Deepak Kukkar, and Yiu Fai Tsang. Potential applications of graphene-based nanomaterials as adsorbent for removal of volatile organic compounds. *Environment international*, 135:105356, 2020.

[136] SM Aghaei, A Aasi, S Farhangdoust, and B Panchapakesan. Graphene-like bc6n nanosheets are potential candidates for detection of volatile organic compounds (vocs) in human breath: A dft study. *Applied Surface Science*, 536:147756, 2021.

[137] Xiao-Qing Tian, Lin Liu, Xiang-Rong Wang, Ya-Dong Wei, Juan Gu, Yu Du, and Boris I Yakobson. Engineering of the interactions of volatile organic compounds with mos_2. *Journal of Materials Chemistry C*, 5(6):1463–1470, 2017.

[138] Liangzhi Kou, Thomas Frauenheim, and Changfeng Chen. Phosphorene as a superior gas sensor: selective adsorption and distinct i–v response. *The journal of physical chemistry letters*, 5(15):2675–2681, 2014.

[139] Ruiqi Zhang, Bin Li, and Jinlong Yang. A first-principles study on electron donor and acceptor molecules adsorbed on phosphorene. *The Journal of Physical Chemistry C*, 119:2871, 2015.

[140] Suyang Sun, Tanveer Hussain, Wei Zhang, and Amir Karton. Blue phosphorene monolayers as potential nano sensors for volatile organic compounds under point defects. *Applied Surface Science*, 486:52–57, 2019.

[141] Pengfei Ou, Pengfei Song, Xinyu Liu, and Jun Song. Superior sensing properties of black phosphorus as gas sensors: a case study on the volatile organic compounds. *Advanced Theory and Simulations*, 2(1):1800103, 2019.

[142] Dwaipayan Chakraborty and Priya Johari. First-principles investigation of the 1t-hfte2 nanosheet for selective gas sensing. *ACS Applied Nano Materials*, 3(6):5160–5171, 2020.

[143] M Born and R Oppenheimer. Zur quantentheorie der molekeln annalen der physik, v. 84. 1927.

[144] Douglas R Hartree. The wave mechanics of an atom with a non-coulomb central field. part i. theory and methods. In *Mathematical Proceedings of the Cambridge Philosophical Society*, volume 24, pages 89–110. Cambridge university press, 1928.

[145] Vladimir Fock. Näherungsmethode zur lösung des quantenmechanischen mehrkörperproblems. *Zeitschrift für Physik*, 61:126–148, 1930.

[146] Llewellyn H Thomas. The calculation of atomic fields. In *Mathematical proceedings of the Cambridge philosophical society*, volume 23, pages 542–548. Cambridge University Press, 1927.

[147] Elliott H Lieb and Barry Simon. Thomas-fermi theory revisited. *Physical Review Letters*, 31(11):681, 1973.

[148] Pierre Hohenberg and Walter Kohn. Inhomogeneous electron gas. *Physical review*, 136(3B):B864, 1964.

[149] Matt Probert. Electronic structure: Basic theory and practical methods, by richard m. martin: Scope: graduate level textbook. level: theoretical materials scientists/condensed matter physicists/computational chemists, 2011.

[150] David M Ceperley and Berni J Alder. Ground state of the electron gas by a stochastic method. *Physical review letters*, 45(7):566, 1980.

[151] Aleš Zupan, Peter Blaha, Karlheinz Schwarz, and John P Perdew. Pressure-induced phase transitions in solid si, sio 2, and fe: Performance of local-spin-density and generalized-gradient-approximation density functionals. *Physical Review B*, 58(17):11266, 1998.

[152] Robert O Jones and Olle Gunnarsson. The density functional formalism, its applications and prospects. *Reviews of Modern Physics*, 61(3):689, 1989.

[153] Jeffrey C Grossman, Lubos Mitas, and Krishnan Raghavachari. Structure and stability of molecular carbon: importance of electron correlation. *Physical review letters*, 75(21):3870, 1995.

[154] John P Perdew, Kieron Burke, and Matthias Ernzerhof. Generalized gradient approximation made simple. *Phys. Rev. Lett.*, 77(18):3865, 1996.

[155] John P Perdew, P Ziesche, and H Eschrig. Electronic structure of solids' 91, 1991.

[156] John P Perdew, Adrienn Ruzsinszky, Gábor I Csonka, Oleg A Vydrov, Gustavo E Scuseria, Lucian A Constantin, Xiaolan Zhou, and Kieron Burke. Restoring the density-gradient expansion for exchange in solids and surfaces. *Physical review letters*, 100(13):136406, 2008.

[157] David J Singh and Lars Nordström. *Planewaves, pseudopotentials and the LAPW method*. Springer, 2006.

[158] David Vanderbilt. Soft self-consistent pseudopotentials in a generalized eigenvalue formalism. *Physical review B*, 41(11):7892, 1990.

[159] Kari Laasonen, Roberto Car, Changyol Lee, and David Vanderbilt. Implementation of ultrasoft pseudopotentials in ab initio molecular dynamics. *Physical Review B*, 43(8):6796, 1991.

[160] Kari Laasonen, Alfredo Pasquarello, Roberto Car, Changyol Lee, and David Vanderbilt. Car-parrinello molecular dynamics with vanderbilt ultrasoft pseudopotentials. *Physical Review B*, 47(16):10142, 1993.

[161] Peter E Blöchl. Projector augmented-wave method. *Physical review B*, 50(24):17953, 1994.

[162] Georg Kresse and Jürgen Furthmüller. Efficiency of ab-initio total energy calculations for metals and semiconductors using a plane-wave basis set. *Computational materials science*, 6(1):15–50, 1996.

[163] Georg Kresse and Jürgen Hafner. Ab initio molecular dynamics for liquid metals. *Physical review B*, 47(1):558, 1993.

[164] Georg Kresse and Jürgen Hafner. Ab initio molecular-dynamics simulation of the liquid-metal–amorphous-semiconductor transition in germanium. *Physical Review B*, 49(20):14251, 1994.

[165] Stefaan Cottenier et al. Density functional theory and the family of (l) apw-methods: a step-by-step introduction. *Instituut voor Kern-en Stralingsfysica, KU Leuven, Belgium*, 4(0):41, 2002.

[166] Georg Kresse and J Furthmüller. Vienna ab-initio simulation package (vasp). *Vienna: Vienna University*, 2001.

[167] Woo Youn Kim, Young Cheol Choi, Seung Kyu Min, Yeonchoo Cho, and Kwang S Kim. Application of quantum chemistry to nanotechnology: electron and spin transport in molecular devices. *Chemical society reviews*, 38(8):2319–2333, 2009.

[168] Yigal Meir and Ned S Wingreen. Landauer formula for the current through an interacting electron region. *Physical Review letters*, 68(16):2512, 1992.

[169] Markus Buttiker. Coherent and sequential tunneling in series barriers. *IBM Journal of Research and Development*, 32(1):63–75, 1988.

[170] Rolf Landauer. Spatial variation of currents and fields due to localized scatterers in metallic conduction. *IBM Journal of research and development*, 1(3):223–231, 1957.

[171] Mads Brandbyge, José-Luis Mozos, Pablo Ordejón, Jeremy Taylor, and Kurt Stokbro. Density-functional method for nonequilibrium electron transport. *Physical Review B*, 65(16):165401, 2002.

[172] Min Yu and Dallas R Trinkle. Accurate and efficient algorithm for bader charge integration. *The Journal of chemical physics*, 134(6), 2011.

[173] GJ Morgan and HB Ghassib. The kubo-greenwood formula and local field corrections. *Solid state communications*, 67(11):1035–1037, 1988.

[174] Huimin Wang, Guangzhao Qin, Jiayue Yang, Zhenzhen Qin, Yagang Yao, Qiang Wang, and Ming Hu. First-principles study of electronic, optical and thermal transport properties of group iii–vi monolayer mx (m= ga, in; x= s, se). *Journal of Applied Physics*, 125(24), 2019.

[175] George H Vineyard. Frequency factors and isotope effects in solid state rate processes. *Journal of Physics and Chemistry of Solids*, 3:121, 1957.

[176] Tevis D B Jacobs, Bernd Gotsmann, Mark A Lantz, and Robert W Carpick. On the application of transition state theory to atomic-scale wear. *Tribol Letters*, 39:257, 2010.

[177] Y Yong, H Cui, Q Zhou, X Su, Y Kuang, and X Li. Adsorption of gas molecules on a graphitic gan sheet and its implications for molecule sensors. *RSC Advances*, 7:51027, 2017.

[178] F Schedin, A K Geim, S V Morozov, E W Hill, P Blake, M I Katsnelson, and K S Novoselov. Detection of individual gas molecules adsorbed on graphene. *Nature Materials*, 6:652, 2007.

[179] J T Robinson, F K Perkins, E S Snow, Z Wei, and P E Sheehan. Reduced graphene oxide molecular sensors. *Nano Letters*, 8:3137, 2008.

[180] J D Fowler, M J Allen, V C Tung, Y Yang, R B Kaner, and B H Weiller. Practical chemical sensors from chemically derived graphene. *ACS Nano*, 3:301, 2009.

[181] G Lu, L E Ocola, and J Chen. Reduced graphene oxide for room temperature gas sensors. *Nanotechnology*, 20:445502, 2009.

[182] W Wang, H Su, Y Wu, T Zhou, and T Li. Biosensing and biomedical applications of graphene: a review of current progress and future prospect. *Journal of Electrochemical Society B*, 166:505, 2019.

[183] A Nag, A Mitra, and S C Mukhopadhyay. Graphene and its sensor based applications: a review. *Sensors and Actuators A*, 270:177, 2018.

[184] K M Tripathi, T Kim, D Losic, and T T Tung. Recent advances in engineered graphene and composites for detection of volatile organic compounds (vocs) and noninvasive disease diagnosis. *Carbon*, 110:97, 2016.

[185] V Kumar, Y S Lee, J W Shin, K H Kim, D Kukkar, and Y F Tsang. Potential applications of graphene-based nanomaterials as adsorbent for removal of volatile organic compounds. *Environment International*, 135:105356, 2020.

[186] Karolina Z Milowska and Jacek A Majewski. Graphene-based sensors: Theoretical study. *The Journal of Physical Chemistry C*, 118:17395, 2014.

[187] Karolina Z Milowska and Jacek A Majewski. Selective detection of acetone and hydrogen sulfide for the diagnosis of diabetes and halitosis using sno_2 nanofibres functionalised with reduced graphene oxide nanosheets. *ACS Applied Materials and Interfaces*, 6:2588, 2014.

[188] Sananda Nag, Lindsay Duarte, Emilie Bertrand, Veronique Celton, Mickael Castro, Veena Choudhary, Philippe Guegan, and Jean-Francois Feller. Ultrasensitive qrs made by supramolecular assembly of functionalised cyclidextrins and graphene for detection of lung cancer voc bio-markers. *Journal of Materials Chemistry B*, 2:6571, 2014.

[189] Seon-Jin Choi, Bong-Hoon Jang, Seo-Jin Lee, Byoung Koun Min, Avner Rothschild, and Il-Doo Kim. Fast responding exhaled-breath sensors using wo_3 hemitubes functionalised by graphene-based electronic sensitizers for diagnosis of diseases. *ACS Applied Materials and Interfaces*, 6:9061, 2014.

[190] A S Rad. First principles study of al-doped graphene as nanostructure adsorbent for no_2 and n_2o: Dft calculations. *Applied Surface Science*, 357:1217, 2015.

[191] Ashok Kumar Sundramoorthy and Sundaram Gunasekaran. Applications of graphene in quality assurance and safety of food. *Trends in Analytical Chemistry*, 60:36, 2014.

[192] Tran Thanh Tung, Mickael Castro, Tae Young Kim, Kwang S Suh, and Jean-Francois Feller. Graphene quantum resistive sensing skin for the detection of alteration biomarkers. *Journal of Materials Chemistry*, 22:21754, 2012.

[193] P Bhattacharjee, S Panigraphi, D Lin, C M Logue, J S Sherwood, C Doetkott, and M Marchello. A comparative qualitative study of the profile of volatile organic compounds associated with salmonella contamination of packaged aged and fresh beef by hs-spme/gc-ms. *Journal of Food Science and Technology*, 48:1, 2011.

[194] M E Fleming-Jones and R E Smith. Volatile organic compounds in foods: a five year study. *Journal of Agriculture and Food Chemistry*, 51:8120, 2003.

[195] M E Fleming-Jones and R E Smith. Comparison of tomatillo and tomato volatile compounds in the headspace by selected ion flow tube mass spectrometry (sift-ms). *Journal of Food Science C*, 75:268, 2010.

[196] Chun Hung Lui, Li Liu, Kin Fai Mak, George W Flynn, and Tony F Heinz. Ultraflat graphene. *Nature*, 462(7271):339–341, 2009.

[197] Tamás Szabó, Ottó Berkesi, Péter Forgó, Katalin Josepovits, Yiannis Sanakis, Dimitris Petridis, and Imre Dékány. Evolution of surface functional groups in a series of progressively oxidized graphite oxides. *Chemistry of materials*, 18(11):2740–2749, 2006.

[198] Daniel C Elias, Rahul Raveendran Nair, TMG Mohiuddin, SV Morozov, P Blake, MP Halsall, Andrea Carlo Ferrari, DW Boukhvalov, MI Katsnelson, AK Geim, et al. Control of graphene's properties by reversible hydrogenation: evidence for graphane. *Science*, 323(5914):610–613, 2009.

[199] Goki Eda, Cecilia Mattevi, Hisato Yamaguchi, HoKwon Kim, and Manish Chhowalla. Insulator to semimetal transition in graphene oxide. *The Journal of Physical Chemistry C*, 113(35):15768–15771, 2009.

[200] Cristina Gómez-Navarro, R Thomas Weitz, Alexander M Bittner, Matteo Scolari, Alf Mews, Marko Burghard, and Klaus Kern. Electronic transport properties of individual chemically reduced graphene oxide sheets. *Nano letters*, 7(11):3499–3503, 2007.

[201] Daniel R Dreyer, Sungjin Park, Christopher W Bielawski, and Rodney S Ruoff. The chemistry of graphene oxide. *Chemical society reviews*, 39(1):228–240, 2010.

[202] Anton Lerf, Heyong He, Michael Forster, and Jacek Klinowski. Structure of graphite oxide revisited. *The Journal of Physical Chemistry B*, 102(23):4477–4482, 1998.

[203] Rodney S Ruoff. Personal perspectives on graphene: New graphene-related materials on the horizon. *MRS bulletin*, 37(12):1314–1318, 2012.

[204] Wei Gao, Lawrence B Alemany, Lijie Ci, and Pulickel M Ajayan. New insights into the structure and reduction of graphite oxide. *Nature chemistry*, 1(5):403–408, 2009.

[205] Kostya S Novoselov, Andre K Geim, Sergei V Morozov, De-eng Jiang, Yanshui Zhang, Sergey V Dubonos, Irina V Grigorieva, and Alexandr A Firsov. Electric field effect in atomically thin carbon films. *science*, 306(5696):666–669, 2004.

[206] Lu Wang, Y Y Sun, Kyuho Lee, D West, Z F Chen, J J Jhao, and S B Zhang. Stability of graphene oxide phases from first-principles calculations. *Physical Review B*, 82:161406(R), 2010.

[207] Xue Jiang, Jawad Nisar, Biswarup Pathak, Jijun Zhao, and Rajeev Ahuja. Graphene oxide as a chemically tunable 2-d material for visible-light photocatalyst applications. *Journal of catalysis*, 299:204–209, 2013.

[208] William S Hummers and Richard E Offeman. Preparation of graphitic oxide. *Journal of American Chemical Society*, 80:1339, 1958.

[209] Kittiya Prasert and Thana Sutthibutpong. Unveiling the fundamental mechanisms of graphene oxide selectivity on the ascorbic acid, dopamine, and uric acid by density functional theory calculations and charge population analysis. *sensors*, 21:2773, 2021.

[210] W Kohn and L J Sham. Self-consistent equations including exchange and correlation effects. *Phys. Rev.*, 140:A1133, 1965.

[211] Hong-Jian Feng, Kan Wu, and Zun-Yi Deng. Predicting inorganic photovoltaic materials with efficiencies$>$ 26% via structure-relevant machine learning and density functional calculations. *Cell Reports Physical Science*, 1(9), 2020.

[212] Georg Kresse and Daniel Joubert. From ultrasoft pseudopotentials to the projector augmented-wave method. *Phys. Rev. B*, 59(3):1758, 1999.

[213] Hendrik J Monkhorst and James D Pack. Special points for brillouin-zone integrations. *Physical Review B*, 13(12):5188, 1976.

[214] Stefan Grimme. Semiempirical gga-type density functional constructed with a long-range dispersion correction. *Journal of computational chemistry*, 27(15):1787–1799, 2006.

[215] Antonio H Castro Neto, Francisco Guinea, Nuno MR Peres, Kostya S Novoselov, and Andre K Geim. The electronic properties of graphene. *Reviews of modern physics*, 81(1):109–162, 2009.

[216] Indranil Maity, Soubarno Chatterjee, and Souvik Bhanja. Acetone sensing perfprmance of pristine and gold doped graphene sheet: a comparative analysis. *28th International Symposium on VLSI Design and Test (VDAT), Vellore, India*, page 1, 2024.

[217] Petr Lazar, Frantisek Karlicky, Petr Jurecka, Mikulas Kocman, Eva Otyepkova, Klara Safarova, and Michal Otyepka. Adsorption of small organic molecules on graphene. *Journal of American Chemical Society*, 135:6372, 2013.

[218] Viet Bac T Phung, Thi Nhan Tran, Quang Huy Tran, Thi Theu Luong, and Van Ahn Din. Graphene as a sensor for lung cancer: insights into adsorption of vocs using vdw dft. *ACS Omega*, 9:2302, 2024.

[219] Li Chen, David Bodesheim, Ahmad Ranjbar, Arezoo Dianat, Robert Biele, Rafael Gutierrez, Mohammad Khazaei, and Gianaurelio Cuniberti. Computational design of the electronic response for volatile organic compounds interacting with doped graphene substrates. *Nanomaterials*, 14(22):1778, 2024.

[220] Rence Painappallil Reji, Sarath Kumar Chedharla Balaji, Yuvaraj Sivalingam, Yoshiyuki Kawazoe, and Surya Velappa Jayaraman. First-principles density functional theory calculations on the potential of sc2co2 mxene nanosheets as a dual-mode sensor for detection of volatile organic compounds in exhaled human breath. *ACS Applied Nano Materials*, 6(7):5345–5356, 2023.

[221] Madhumita Kundu and Subhradip Ghosh. Sensing food quality by free-standing silicene nanosheets: a combined density functional theory and nonequilibrium green's function method study. *Physica Status Solidi b*, 262:2400578, 2025.

[222] S M Aghaei, A Aasi, S Farhangdoust, and B Oanchapakesan. Graphene-like bc_6n nanosheets are potential candidates for detection of volatile organic compounds (vocs) in human breath: a dft study. *Applied Surface Science*, 536:147756, 2021.

[223] Liangzhi Kou, Thomas Fraunheim, and Chen Changfeng. Phosphorene as a superior gas sensor: selective adsorption and distinct i-v response. *Journal of Physical Chemistry Letters*, 5:2675, 2014.

[224] Dwaipayan Chakraborty and Priya Johari. First-principles investigation of the 1t-$hfte_2$ nanosheet for selective gas sensing. *ACS Applied Nano Materials*, 3:5160, 2020.

[225] Supriya Ghosal, Arka Bandyopadhyay, Suman Chowdhury, and Debnarayan Jana. A review on transport characteristics and bio-sensing applications of silicene. *Reports on Progress in Physics*, 86:096502, 2023.

[226] T Hussain, H Vovusha, T Kaewmaraya, V Amornkitbamrung, and R Ahuja. Adsorption characteristics of dna nucleobases, aromatic amino acids and heterocyclic molecules on silicene and germanene monolayers. *Sensors and Actuators B*, 255:2713, 2018.

[227] M B Henry, M Tumbapo, and B O Tayo. Identification of dna bases using nanopores created in finite-size nanoribbons from graphene, phosphorene and silicene. *AIP Advances*, 11:035324, 2021.

[228] S Alesheikh, N Shahtahmassebi, M R Roknabadi, and R P Shahri. Silicene nanoribbon as a new dna sequencing device. *Physics Letters A*, 382:595, 2018.

[229] Q Li, H Liu, Y Tian, J Guo, G Chen, and J Y Lee. Methylation detection and dna sequencing based on adsorption of nucleobases on silicene nanoribbon. *Journal of Physical Chemistry C*, 124:10823, 2020.

[230] T Tarun, D K K Randhawa, P Singh, B C Choudhary, G K Walia, and N Kaur. Analysis of uric acid adsorption on armchair silicene nanoribbons: a dft study. *Journal of Molecular Modelling*, 26:63, 2020.

[231] U Saikia, N Saikia, K Waters, R Pandey, and M B Sahariah. Electronic properties of acetaminophen adsorbed on 2d clusters: a first principles density functional study. *ChemistrySelect*, 2:3613, 2017.

[232] N Saikia, M Seel, and R Pandey. Stability and electronic properties of 2d nanomaterials conjugated with pyrazinamide chemotheraputic: a first-principles cluster study. *Journal of Physical Chemistry C*, 120:20323, 2016.

[233] Jariyanee Prasongkit, Rodrigo G Amorim, Sudip Chakraborty, Rajeev Ahuja, Ralph H Scheicher, and Vittaya Amornkitbamrung. Highly sensitive and selective gas detection based on silicene. *The Journal of Physical Chemistry C*, 119(29):16934, 2015.

[234] Tim H Osborn, Amir A Faraijan, Olga V Pupysheva, Rachel S Aga, and L C Lew Yan Voon. Ab initio simulations of silicene hydrogenation. *Chemical Physics Letters*, 511:101, 2011.

[235] Tian-Tian Jia, Meng-Meng Zheng, Xin-Yu Fan, Yan Su, Shu-Juan Li, Hai-Ying Liu, Gang Chen, and Yoshiyuki Kawazoe. Band gap on/off switching of silicene superlattice. *The Journal of Physical Chemistry C*, 119:20747, 2015.

[236] Esmaeil Zaminpayma and Nayebi Payman. Band gap engineering in silicene: A theoretical study of density functional tight-binding theory. *Physica E*, 84:555, 2016.

[237] Supriyo Dutta. Nanoscale device modeling: the green's function method. *Superlattices and Microstructures*, 28:253, 2000.

[238] Stefan Grimme. Semiempirical gga-type density functional constructed with a long-range dispersion correction. *Journal of computational chemistry*, 27(15):1787–1799, 2006.

[239] Tanveer Hussain, Thanayut Kaewmaraya, Sudip Chakraborty, and Rajeev Ahuja. Defect and substitution-induced silicene sensor to probe toxic gases. *The Journal of Physical Chemistry C*, 120:25256, 2016.

[240] Ning Lu, Zhenyu Li, and Jinlong Yang. Electronic structure engineering via on-plane chemical functionalisation: a comparison study of two-dimensional polysilane and graphene. *Journal of Physical Chemistry C*, 113:16741, 2009.

[241] Khaerul Umam, Sholihun, Pekik Nurwantoro, Moh Adib Ulil Absor, Ari Dwi Nugraheni, and Romy H S Budhi. Bi-axial strain effects on the electronic properties of silicene: the density-functional-theory based calculations. *Journal of Physics Conference Series*, 1011:012074, 2018.

[242] V Nagarjan and R Chandiramouli. $Mose_2$ nanosheets for detection of methanol and ethanol vapors. *Journal of Molecular Graphics and Modelling*, 81:97, 2018.

[243] V Nagarjan, S Dharani, and R Chandiramouli. Density functional studies on the binding of methanol and ethanol molecules to graphyne nanosheets. *Computational and Theoretical Chemistry*, 1125:86, 2018.

[244] B Swetha, V Nagarjan, and R Chandiramouli. Interaction studies of methanol and ethanol vapors on green phosphorene sheets: a first-principles study. *ChemistrySelect*, 4:14237, 2019.

[245] S M Aghaei, M M Monshi, and I A Calizo. A theoretical study of gas adsorption on silicene nanoribbons and its appliction in a highly sensitive molecular sensor. *RSC Advances*, 6:94417, 2016.

[246] Winston Yenyu Chen, Connor Daniel Sullivan, Sz-Nian Lai, Chao-Chun Yen, Xiaofan Jiang, Dimitrios Peroulis, and Lia A Stanciu. Noble-nanoparticle-decorated ti3c2t x mxenes for highly sensitive volatile organic compound detection. *ACS omega*, 7(33):29195–29203, 2022.

[247] Puspamitra Panigrahi, Hakkim Vovusha, Yash Pal, Hyeonhu Bae, Hoonkyung Lee, Thanayut Kaewmaraya, Shahid Nazir, Muhammad JA Shiddiky, and Tanveer Hussain. Identification of lung cancer biomarkers by nanosensors based on titanium carbide (ti3c2t x) mxenes. *ACS Applied Nano Materials*, 6(23):22117–22127, 2023.

[248] Yitong Wang, Yuhua Wang, Min Jian, Qinting Jiang, and Xifei Li. Mxene key composites: a new arena for gas sensors. *Nano-Micro Letters*, 16(1):209, 2024.

[249] Maciej J Szary. Computational study of the intercalation of no2 between bilayer mote2. *Applied Surface Science*, 611:155514, 2023.

[250] Sadegh Mehdi Aghaei, Aref Aasi, and Balaji Panchapakesan. Experimental and theoretical advances in mxene-based gas sensors. *ACS omega*, 6(4):2450–2461, 2021.

[251] Qingting Li, Yanqiong Li, and Wen Zeng. Preparation and application of 2d mxene-based gas sensors: A review. *Chemosensors*, 9(8):225, 2021.

[252] Wadha Alfalasi, Tanveer Hussain, and Nacir Tit. Ab initio investigation of functionalization of titanium carbide ti3c2 mxenes to tune the selective detection of lung cancer biomarkers. *Scientific reports*, 14(1):1403, 2024.

[253] Atanu Bag and Nae-Eung Lee. Gas sensing with heterostructures based on two-dimensional nanostructured materials: a review. *Journal of Materials Chemistry C*, 7(43):13367–13383, 2019.

[254] Wadha Alfalasi, Ibrahim Alghoul, Tanveer Hussain, Amna Al-Ali, Aaesha Albalooshi, Mazoun Aldhanhani, Hednna Al-Sayari, Hagar Ibrahim, and Nacir Tit. Efficient detection of lung cancer biomarkers using functionalized transition metal dichalcogenides (mos2) monolayers: Dft study. *FlatChem*, 45:100651, 2024.

[255] Weizhong Xiao, Zixuan Wang, and Yingang Gui. Adsorption properties of metal atom (co, v, w, zr)-modified mote2 for co, ch3cho, and c6h6 gases: A dft study. *Molecules*, 29(21):5086, 2024.

[256] Abdul Kaium Mia, M Meyyappan, and PK Giri. Two-dimensional transition metal dichalcogenide based biosensors: from fundamentals to healthcare applications. *Biosensors*, 13(2):169, 2023.

[257] Ravindra Kumar Jha, Jostin Vinroy D'Costa, Neha Sakhuja, and Navakanta Bhat. Mose2 nanoflakes based chemiresistive sensors for ppb-level hydrogen sulfide gas detection. *Sensors and Actuators B: Chemical*, 297:126687, 2019.

[258] Puspamitra Panigrahi, Tanveer Hussain, Amir Karton, and Rajeev Ahuja. Elemental substitution of two-dimensional transition metal dichalcogenides (mose2 and mote2): implications for enhanced gas sensing. *ACS sensors*, 4(10):2646–2653, 2019.

[259] Nirav Joshi, Maria Luisa Braunger, Flavio Makoto Shimizu, Antonio Riul Jr, and Osvaldo Novais Oliveira Jr. Two-dimensional transition metal dichalcogenides for gas sensing applications. In *Nanosensors for environmental applications*, pages 131–155. Springer, 2020.

[260] Tianyan Jiang, Wentao Zhang, Tao Zhang, Haoxiang Yuan, Maoqiang Bi, and Xin Zhou. Adsorption and gas-sensing performances of c2h2, c2h4, co, h2 in transformer oil on pt-doped mote2 monolayer: A dft study. *Physica E: Low-dimensional Systems and Nanostructures*, 146:115568, 2023.

[261] Miaolin Wang, Sihan Cheng, Wen Zeng, and Qu Zhou. Adsorption of toxic and harmful gas co on tm (ni, pd, pt) doped mote2 monolayer: A dft study. *Surfaces and Interfaces*, 31:102111, 2022.

[262] Deep Jariwala, Vinod K Sangwan, Lincoln J Lauhon, Tobin J Marks, and Mark C Hersam. Emerging device applications for semiconducting two-dimensional transition metal dichalcogenides. *ACS nano*, 8(2):1102–1120, 2014.

[263] Zhihong Feng, Buyun Chen, Shuangbei Qian, Linyan Xu, Liefeng Feng, Yuanyuan Yu, Rui Zhang, Jiancui Chen, Qianqian Li, Quanning Li, et al. Chemical sensing by band modulation of a black phosphorus/molybdenum diselenide van der waals hetero-structure. *2D Materials*, 3(3):035021, 2016.

[264] Nguyen Minh Triet, Le Thai Duy, Byeong-Ung Hwang, Adeela Hanif, Saqib Siddiqui, Kyung-Ho Park, Chu-Young Cho, and Nae-Eung Lee. High-performance schottky diode gas sensor based on the heterojunction of three-dimensional nanohybrids of reduced graphene oxide–vertical zno nanorods on an algan/gan layer. *ACS applied materials & interfaces*, 9(36):30722–30732, 2017.

[265] Jiale Shen, Zhi Yang, Yatong Wang, Li-Chun Xu, Ruiping Liu, and Xuguang Liu. Organic gas sensing performance of the borophene van der waals heterostructure. *The Journal of Physical Chemistry C*, 125(1):427–435, 2020.

[266] Himangshu Sekhar Sarma and Subhradip Ghosh. Consequences of magneto-electrical coupling in multiferroic vse_2/sc_2co_2 heterostructures. *Journal of Physical Chemistry C*, 129:6466, 2025.

[267] Winston Yenyu Chen, Xiaofan Jiang, Sz-Nian Lai, Dimitrios Peroulis, and Lia Stanciu. Nanohybrids of a mxene and transition metal dichalcogenide for selective detection of volatile organic compounds. *Nature communications*, 11(1):1302, 2020.

[268] Sikandar Aftab, Muhammad Zahir Iqbal, Sajjad Hussain, Hosameldin Helmy Hegazy, Fahmid Kabir, Syed Hassan Abbas Jaffery, and Ganesh Koyyada. New developments in gas sensing using various two-dimensional architectural designs. *Chemical Engineering Journal*, 469:144039, 2023.

[269] Hao Yan, Lihua Chu, Ze Li, Changxu Sun, Yuxin Shi, and Jing Ma. 2h-mos2/ti3c2tx mxene composites for enhanced no2 gas sensing properties at room temperature. *Sensors and Actuators Reports*, 4:100103, 2022.

[270] Yi Xia, Sufang He, Junming Wang, Liexing Zhou, Jing Wang, and Sridhar Komarneni. Mxene/ws 2 hybrids for visible-light-activated no 2 sensing at room temperature. *Chemical Communications*, 57(72):9136–9139, 2021.

[271] Rusen Tian, Yongling Ding, Qi Wang, and Peng Song. Designing advanced 2d/2d heterojunctions of mos2 nanosheets/ti3c2tx mxene in gas-sensing applications. *Vacuum*, 222:112991, 2024.

[272] Banalata Maji and Sushmee Badhulika. Fully flexible wse2/v2c mxene heterostructure-based gas sensor: A detailed sensing analysis for ppb level detection of ammonia at room temperature. *Journal of Alloys and Compounds*, 1017:179079, 2025.

[273] Julaiba T Mazumder, Mohammed M Hasan, Fahim Parvez, Tushar Shivam, Dobbidi Pamu, Alamgir Kabir, Mainul Hossain, and Ravindra K Jha. Unlocking the sensing and scavenging potential of sc 2 co 2 and sc 2 co 2/tmd heterostructures for phosgene detection. *Physical Chemistry Chemical Physics*, 27(20):10506–10522, 2025.

[274] Madhumita Kundu and Subhradip Ghosh. Sensing food quality by free-standing silicene nanosheets: A combined density functional theory and nonequilibrium green's function method study. *physica status solidi (b)*, page 2400578, 2025.

[275] Madhumita Kundu and Subhradip Ghosh. Combined density functional theory and non-equilibrium green's function method study on graphene-based gas sensors for detection of food quality. *The European Physical Journal B*, 98(10):208, 2025.

[276] Qiran Chen, Daohua Zhang, Jisheng Pan, and Weijun Fan. Optical properties of two-dimensional semi-conductive mxene sc2cox produced by sputtering. *Optik*, 219:165046, 2020.

[277] Siyu Zhang, Lin Tao, Han Zhang, Hongwei Zhao, Fang Di, Lixiang Li, and Baigang An. Theoretical study of metal-doped wse2 sensors for no detection in human exhalation. *Surfaces and Interfaces*, page 107553, 2025.

[278] Zheng Lu, Ying Zhai, Qizong Liang, and Wei Wu. Promoting sensitivity and selectivity of no2 gas sensor based on metal (pt, re, ta)-doped monolayer wse2: A dft study. *Chemical Physics Letters*, 755:137737, 2020.

[279] Shuhong Ma, Dongyu Yuan, Zhaoyong Jiao, Tianxing Wang, and Xianqi Dai. Monolayer sc2co2: a promising candidate as a so2 gas sensor or capturer. *The Journal of Physical Chemistry C*, 121(43):24077–24084, 2017.

[280] Do Muoi, Nguyen N Hieu, Huong TT Phung, Huynh V Phuc, B Amin, Bui D Hoi, Nguyen V Hieu, Le C Nhan, Chuong V Nguyen, and PTT Le. Electronic properties of ws2 and wse2 monolayers with biaxial strain: a first-principles study. *Chemical Physics*, 519:69–73, 2019.

[281] Francis Opoku and Penny P Govender. Adsorption behaviour of si anchored on g-c3n4/graphene van der waals heterostructure for selective sensing of toxic gases: Insights from a first-principles study. *Applied Surface Science*, 525:146590, 2020.

[282] Jane Hodgkinson and Ralph P Tatam. Optical gas sensing: a review. *Measurement science and technology*, 24(1):012004, 2012.

[283] Chanyoung Yim, Maria O'Brien, Niall McEvoy, Sinéad Winters, Inam Mirza, James G Lunney, and Georg S Duesberg. Investigation of the optical properties of mos2 thin films using spectroscopic ellipsometry. *Applied Physics Letters*, 104(10), 2014.

[284] Hasim Kelebek, Serkan Selli, Hamide Gubbuk, and Esma Gunes. Comparative evaluation of volatiles, phenolics, sugars, organic acids and antioxidant properties of sel-42 and tainung papaya varieties. *Food chemistry*, 173:912–919, 2015.

[285] Pranav D Pathak, Sachin A Mandavgane, and Bhaskar D Kulkarni. Waste to wealth: a case study of papaya peel. *Waste and Biomass Valorization*, 10:1755–1766, 2019.

[286] Ralf M Schweiggert, Rachel E Kopec, Maria G Villalobos-Gutierrez, Josef Högel, Silvia Quesada, Patricia Esquivel, Steven J Schwartz, and Reinhold Carle. Carotenoids are more bioavailable from papaya than from tomato and carrot in humans: a randomised cross-over study. *British Journal of Nutrition*, 111(3):490–498, 2014.

[287] Dulce M Rivera-Pastrana, Elhadi M Yahia, and Gustavo A González-Aguilar. Phenolic and carotenoid profiles of papaya fruit (carica papaya l.) and their contents under low temperature storage. *Journal of the Science of Food and Agriculture*, 90(14):2358–2365, 2010.

[288] Farhan Saeed, Muhammad Umair Arshad, Imran Pasha, Rabia Naz, Rizwana Batool, Ammar Ahmed Khan, Muhammad Adnan Nasir, and Bilal Shafique. Nutritional and phyto-therapeutic potential of papaya (carica papaya linn.): an overview. *International Journal of Food Properties*, 17(7):1637–1653, 2014.

[289] Lidiani F Santana, Aline C Inada, Bruna Larissa Spontoni do Espirito Santo, Wander FO Filiú, Arnildo Pott, Flávio M Alves, Rita de Cássia A Guimarães, Karine de Cássia Freitas, and Priscila A Hiane. Nutraceutical potential of carica papaya in metabolic syndrome. *Nutrients*, 11(7):1608, 2019.

[290] David J Williams, Sharon Pun, Mridusmita Chaliha, Pieter Scheelings, and Timothy O'Hare. An unusual combination in papaya (carica papaya): The good (glucosinolates) and the bad (cyanogenic glycosides). *Journal of food composition and analysis*, 29(1):82–86, 2013.

[291] Jorge A Pino, Karina Almora, and Rolando Marbot. Volatile components of papaya (carica papaya l., maradol variety) fruit. *Flavour and fragrance journal*, 18(6):492–496, 2003.

[292] Komal Kushwaha, Shashank Sagar Saini, Bhairavnath Waghmode, Mariam Gaid, Pawan Kumar Agarwal, Partha Roy, and Debabrata Sircar. Volatile components in papaya fruits are the non evasive biomarkers to monitor the ripening stage and the nutritional value. *European Food Research and Technology*, 247:907, 2021.

[293] B Niederbacher, JB Winkler, and JP Schnitzler. Volatile organic compounds as non-invasive markers for plant phenotyping. *Journal of experimental botany*, 66(18):5403–5416, 2015.

[294] Xiaoyang Zhu, Qiumian Li, Jun Li, Jun Luo, Weixin Chen, and Xueping Li. Comparative study of volatile compounds in the fruit of two banana cultivars at different ripening stages. *Molecules*, 23(10):2456, 2018.

[295] Peris Miguel and Laura Escuder-Gilabert. A 21st century technique for food control: Electronic noses. *Analytical Chimica Acta*, 638:1, 2009.

[296] Georges Brugger, Hans-Martin Frey, Patrick Steinegger, Franziska Balmer, and Samuel Leutwyler. Accurate determination of the structure of cyclohexane by femtosecond rotational coherence spectroscopy and ab initio calculations. *Journal of Physical Chemistry A*, 115:9567, 2011.

[297] Hayat El Ouafy, Tarik El Ouafy, Mustapha Oubenali, Aziz El Haimouti, Ahmed Gamouh, and Mohamed Mbarki. Analysis of the chemical reactivity of limonene by the functional density theory method using global descriptors. *Journal of Chemical Health Risks*, 11:213, 2021.

[298] Alicia O Hernandez-Castillo, Chamara Abeysekara, Brian M Hays, Isabela Kleiner, Ha Vinh Lam Nguyen, and Timothy S Zwier. Conformational preferences and internal rotation of methyl butyrate by microwave spectroscopy. *Journal of Molecular Spectroscopy*, 337:51, 2017.

[299] Nhu-Ngoc Dang, Hoang-Nam Pham, Isabelle Kleiner, Martin Schwell, Jens-Uwe Grabow, and Ha Vinh Lam Nguyen. Methyl internal rotation in fruit esters: Chain-length effect observed in the microwave spectrum of methyl hexanoate. *Molecules*, 27:2639, 2022.

[300] Mo Li, Olamide Omisakin, and Joshua Young. Effect of chemical substitution and external strain on phase stability and ferroelectricity in two dimensional m 2 ct 2 mxenes. *Nanoscale*, 14(18):6970–6980, 2022.

[301] Erdem Balcı, Ünal Özden Akkuş, and Savas Berber. Band gap modification in doped mxene: Sc 2 cf 2. *Journal of Materials Chemistry C*, 5(24):5956–5961, 2017.

List of Publications

A. Published

• **Madhumita Kundu** and Subhradip Ghosh, *Combined Density Functional Theory and Non−equilibrium Green's Function method study on Graphene based gas sensors for detection of food quality*,2025, Eur.Phys.J.B,98:208.

• **Madhumita Kundu** and Subhradip Ghosh, *Sensing Food Quality by Free − Standing Silicene Nanosheets: A Combined Density Functional Theory and Nonequilibrium Green's Function Method Study*, 2025, physica status solidi(b),2400578.

• **Madhumita Kundu** and Subhradip Ghosh, Sc_2CT_2 $(T = O, S, F)$ *MXenes as nanosensors for detection of biomarkers of papaya fruit: first principles modeling and simulation*, 2026, Phys. Scr.115903

B. Under review

• **Madhumita Kundu** and Subhradip Ghosh, *Density Functional Theory based computations of MXene and MXene-TMDC heterostructures sensors properties towards assessing quality of food.*

7.3 Coneferences attended

• Delivered a talk titled "Electronic and Transport Properties of Two-Dimensional Silicene Nanosheets for Selective Detection of Meat VOC's: Effect of On-Plane Chemical Functionalization" at International conference ″**Emerging phenomena in Quantum materials**″, December 11-15, 2023, organized jointly by Uppsala University and Savitribai Phule Pune University, at Bharatpur, India.

• Presented a poster titled “Superior Sensing Properties of geaphene and it’s derivative(rGO and GO) as Gas Sensors: A Case Study on the Volatile Organic Compounds.” at the **International Conference on 60 Years of DFT**: **Advancements in Theory and Computation** held on July 21-26, 2024, at IIT Mandi.

• Presented a poster titled “Sensing food quality by silicene nanosheets : a Density Functional Theory study" at **7th Annual Conference on Quantum Condensed Matter** (**QMAT – 2024**) held during December 20-23, 2024, at IIT Guwahati.